Liquid Refractive Index Measurements using a Terahertz Vector Network Analyser

RHIANNON LEES

How to cite:

LEES, RHIANNON (2022) Liquid Refractive Index Measurements using a Terahertz Vector Network Analyser. Doctoral thesis, Durham University.

Liquid Refractive Index Measurements using a Terahertz Vector Network Analyser

Rhiannon Lees

A Thesis presented for the degree of
Doctor of Philosophy

Department of Engineering
Durham University
UK

July 2022

Liquid Refractive Index Measurements using a Terahertz Vector Network Analyser

Rhiannon Lees

Submitted for the degree of Doctor of Philosophy
July 2022

Abstract

A lack of coherent sources has led the terahertz region of the electromagnetic spectrum to remain relatively unexplored as compared to its neighbouring frequencies. Over recent decades the development of these sources along with coherent detectors has led to the rapid development of terahertz technologies. To characterise and use materials within this region a database of material knowledge must be built up.

This thesis aims to outline various methods of material characterisation using a vector network analyser. It considers and overcomes issues to do with data collection using the vector network analyser within the frequency domain and secondly problems due to strong absorptions associated with water based samples within the terahertz region.

Two novel cuvette measurement methods are presented which use rotational stages to enable the vector network analyser to extract material data. A self-referencing technique rotating the test liquid and another self-referencing technique using a known refractive index reference liquid are shown. The latter is a fast and precise measurement technique which is as accurate as the known reference and could potentially be used for in-flow testing.

The use of paper at terahertz frequencies is explored with a particular interest in the use of paper for sensing. A range of metamaterial designs are simulated, fabricated and tested to develop a metamaterial device which can be used for liquid sensing. It was found that soaked filter paper in contact with the metamaterial surface is able to distinguish between different soaking liquids.

Serum samples of seven different tumour markers have been tested to determine if

the metamaterial in contact with serum soaked filter paper could provide an indication of tumour marker concentration. The outcome of this feasibility study suggested possible relations between absorption peak position frequency and marker concentration for five of the seven tested markers.

Declaration

The work in this thesis is based on research carried out at the Durham University Department of Engineering, England. No part of this thesis has been submitted elsewhere for any other degree or qualification and it is all my own work unless referenced to the contrary in the text.

Acknowledgements

Thank you to all of my friends who have become family to me: Oshrun, Phetven, Sconzo, Chomp, Razzy, Ell-bow, Muju, Bainsey and Roblet. Thanks to Dom for getting me through the toughest parts. Thanks Emma for always sticking around (8 years is a long time).

To my actual family who are always there when I need them. Love you mum and dad.

Thanks to my office mates: Polly for always being an amazing friend and colleague, Jonathan for helping solve the problems no-one else could solve, Heather for asking too many questions and also Timon (why?). Victor for being my spirit animal.

Thanks to my amazing supervisors. Andrew for his relentless optimism which always seems to catch and make you feel like everything is going to be ok even if youre in a nuclear apocalypse. Claudio for his endless stream of weird, wacky and wonderful ideas.

Finally, I'd like to thank myself for smashing out this thesis ... What a legend!

Publications

Journal Articles

Rhiannon Lees, Michael Cooke, Claudio Balocco and Andrew Gallant, *Computer Aided Patterning Design for Self-Assembled Microsphere Lithography (SA-MSL)*, Scientific Reports, (2019).

Conference Papers

Rhiannon Lees, Michael D. Cooke, Claudio Balocco and Andrew J. Gallant, *Quantifying Nail Varnish Drying Using a THz Vector Netowrk Analyer*, IEEE 2020 45th International Conference on Infrared, Millimeter, and Terahertz Waves, Buffalo, USA, (virtual), (IRMMW-THz), (2020).

Rhiannon Lees, Heather Sanders, Michael D. Cooke, Claudio Balocco and Andrew J. Gallant, *Chemical Smoothing as Method to Manufacture High Quality 3D Printed Optical Components*, IEEE 2020 45th International Conference on Infrared, Millimeter, and Terahertz Waves, Buffalo, USA, (virtual), (IRMMW-THz), (2020).

Rhiannon Lees, Michael Cooke, Claudio Balocco and Andrew J. Gallant, *Chemical Smoothing as Method to Manufacture High Quality 3D Printed Optical Components*, IEEE 2019 44th International Conference on Infrared, Millimeter, and Terahertz Waves, Paris, France, (IRMMW-THz), (2019).

Rhiannon Lees, Andreas Klein, Michael Cooke, Claudio Balocco and Andrew J. Gallant, *Rotational Cuvette Measurements for Refractive Index Testing using a THz Vector Network Analyser*, IEEE 2019 44th International Conference on Infrared, Millimeter, and Terahertz Waves, Paris, France, (IRMMW-THz), (2019).

Rhiannon Lees, Polina S. Stefanova, Andreas Klein, Claudio Balocco and Andrew J. Gallant, *Paper-based Optical Components for the THz Region*, IEEE 2018 43rd International Conference on Infrared, Millimeter, and Terahertz Waves, Nagoya, Japan, (IRMMW-THz), (2018).

Non-first Author Publications

Vanessa Fenlon, Rhiannon Lees, Polina S. Stefanova, Andreas K. Klein, Andrew J. Gallant and Claudio Balocco, *Evolutionary Optimisation of THz components*, IEEE 2018 43rd International Conference on Infrared, Millimeter, and Terahertz Waves, Nagoya, Japan, (IRMMW-THz), (2018).

Polina Stefanova, Andreas K. Klein, Rhiannon Lees, Andrew J. Gallant and Claudio Balocco. *Optically Controlled THz Metamaterial Modulators*, IEEE 2018 43rd International Conference on Infrared, Millimeter, and Terahertz Waves, Nagoya, Japan, (IRMMW-THz), (2018).

Contents

Chapter 1

Introduction

1.1 Terahertz Radiation

The term ‘terahertz radiation’ generally encompasses the region of the electromagnetic spectrum between 100 GHz (3 mm) and 10 THz (30 µm). This region of the electromagnetic spectrum is typically referred to as the terahertz ‘gap’ due to a historical lack of knowledge of terahertz radiation and its potential uses. Where technologies have been rapidly advancing across its neighbouring areas of the electromagnetic spectrum, the terahertz region has been somewhat overlooked. Its surrounding frequencies, microwave and infrared, as shown in the diagram of the electromagnetic spectrum (figure 1.1), have been well explored. The cause for this gap in research within the terahertz region has been largely due to a lack of coherent sources [1]. Recent advances in sources and coherent detection technology have allowed for further research into a wide range of applications within the so-called terahertz gap.

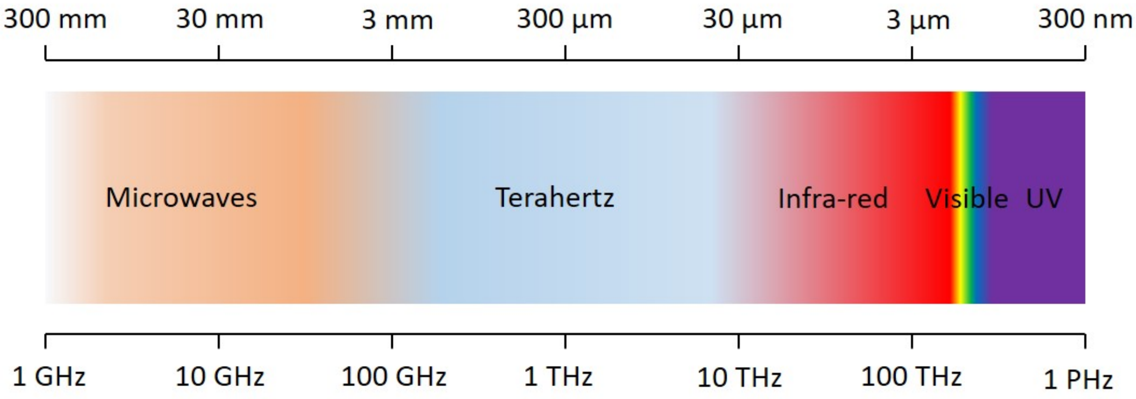

Figure 1.1: Diagram of the electromagnetic spectrum showing the frequency and wavelengths of the terahertz region and neighbouring regions.

1.2 Applications of Terahertz Radiation

Terahertz radiation has low photon energies (1 THz $\equiv$ 4.1 meV) which correspond to the thermal energy associated with a range of biological processes, allowing the terahertz region to directly probe a range of complex mechanisms such as conformal changes in protein structures [2,3]. Terahertz radiation has also been used to explore a range of intra- and inter-molecular vibrational dynamics of a variety of structures including DNA [4, 5], chiral compounds [6], saccharides [7], and protein hydration shells [8–12].

Terahertz imaging is suitable for security applications [13] for the purposes of detecting hidden objects in clothing and common packing materials along with the future possibility of using higher frequency terahertz (over 0.5 THz) for chemical identification. Low levels of terahertz radiation are capable of imaging concealed weapons and explosives along with chemical and biological agents due to most non-polar, non-metallic materials, e.g. fabric, clothing and packaging being transparent to terahertz radiation and the fact that it poses little to no risk for the use on humans [14–16]. The major problem facing security applications of terahertz technology is penetration depth in a multi-layer sample. This is low due to scattering, absorption loss by each layer and reflection losses at the interfaces.

Terahertz imaging has two main benefits as opposed to millimetre wave imaging; improved spatial resolution (from shorter wavelengths) and spectroscopic signatures. The resolution of terahertz is ten times better than that of millimetre waves due to a ten times shorter wavelength allowing for sharper imaging. Although terahertz radiation has the capability to identify compounds through a specific molecular ‘fingerprint’, to successfully implement this application, a more comprehensive terahertz spectral database needs to be established [17]. This ‘fingerprint’ is vital to identify the spectra of explosives, biological and chemical agents and illegal drugs. It is of particular importance for explosives, for example those with low vapour pressures which cause difficulty with trace vapour detection techniques [18]. Studies have also been shown to identify non-metallic weaponry along with the ability to identify the difference between common chemicals, medicines and threat materials [19]. The largest issue with terahertz technology for security applications is the stand-off distance which introduces losses due to environmental factors such as humidity, absorption and dust scattering. To overcome these attenuation losses, higher power sources need to be developed [20].

The terahertz region is of interest to historians and art experts as its non-destructive nature allows for a method of evaluating paintings without harming them; in addition, most pieces of art can be further explored to show the different layers of paint that have been built up upon these paintings [21]. In some cases, it has been possible to reveal covered sections of paintings that are not visible via optical inspection [22, 23]. These same principles and advantages have been applied to many similar mediums from historical wall paintings [24] to wooden dolls [25]. This has been expanded to alternative materials such as historic plastics in terms of their characterisation [26] and a wide range of applications for example varnish wear on historical instruments [27]. This method also allows for real time quality measurement in modern products e.g. automobile paint thickness and subsequently dryness monitoring [28, 29].

The non-ionising nature of terahertz radiation has attracted interest from industry and academia for biological applications [30]. This non-ionising property has led it to being utilised for in vivo skin measurements [31].

1.3 Refractive Index

The refractive index (RI) of a material is a measure of how it interacts with radiation. It is a characteristic inherent to a particular material for a given temperature and wavelength of incident radiation. This property can be used to identify materials and their prevalence within mixtures. As the property is not constant with varying temperatures [32] and frequencies, to use this property for material identification, a database of values for materials across different temperatures and frequencies needs to be collected.

Refractive index takes the form of a complex number. The real part of the refractive index describes its effect on radiation in terms of phase velocity while the imaginary part of the refractive index described the attenuation of radiation.

The work in this thesis focuses on real RI extraction techniques using a terahertz vector network analyser (VNA) of range 0.75-1.1 THz. The techniques explored range from novel methods using cuvettes to a metamaterial driven sensing procedure. Figure 1.2 shows an image of an example metamaterial which has been fabricated on a polyethylene naphthalate (PEN) substrate which could be used for these sensing purposes.

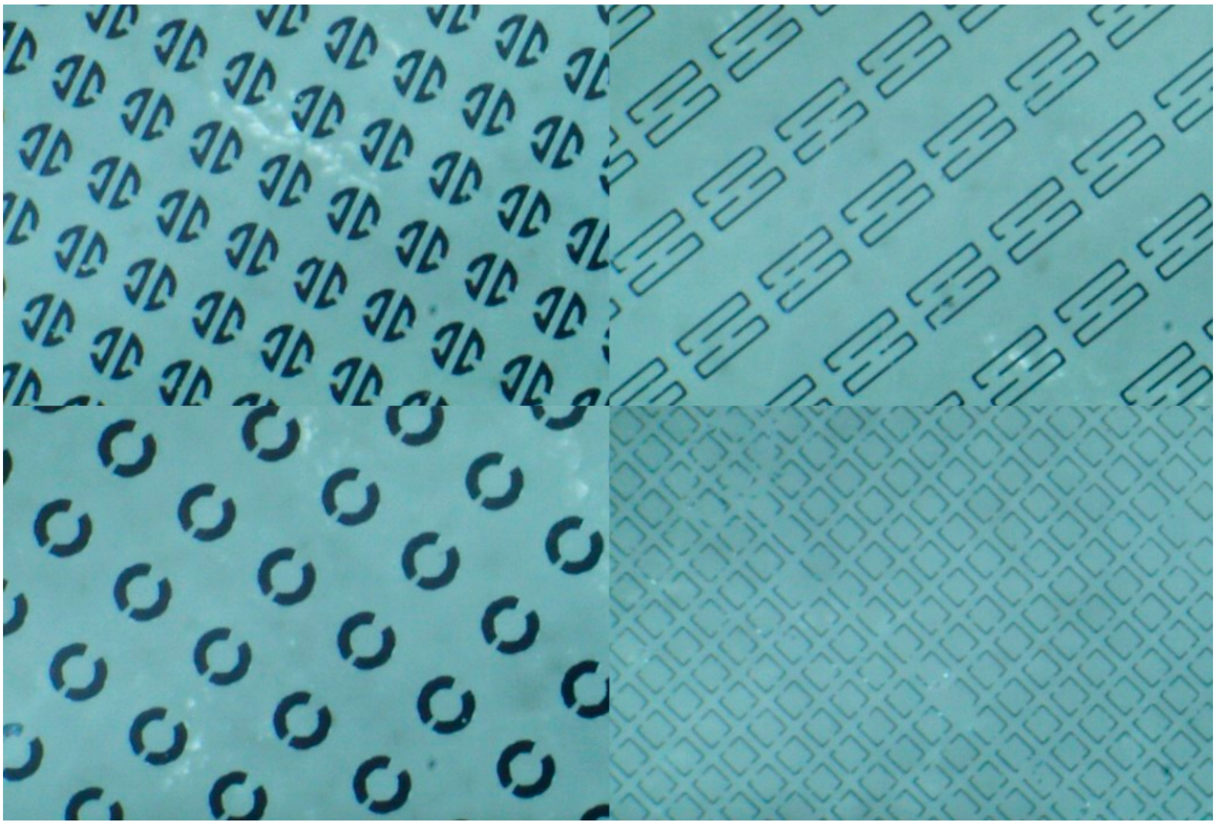

Figure 1.2: Exemplar image of metamaterial arrays which could be used for sensing purposes.

This thesis also applies the use of terahertz metamaterials for sensing of tumour markers within human serum samples. It reports on a study conducted in association with the Durham and Darlington NHS Trust which has provided surplus serum samples to use for a feasibility study to assess the possibility of testing for these markers using terahertz metamaterials. Thousands of tumour markers exist and each may be elevated in only one or many different cancer types. In addition to this, the percentage of people with elevated levels of these markers can be very low for some markers while false negatives can also be high. For example pregnancy can cause a positive result for many tumour markers regardless of the individuals cancer status. Markers alone are rarely used as a diagnostic tool, they are more commonly used to refer patients for further testing for diagnostic purposes but their most powerful use is to monitor patients progress through treatment and to check for recurrence. A small selection of the most reliable tumour markers are tested which cover the most common cancer types. The low sensitivity of tumour marker testing has been shown to increase through multi-analyte tests [33]. As this metamaterial testing method tests full serum, it may be possible to simultaneously test for multiple markers. This thesis focuses on the feasibility of the terahertz metamaterials testing method for individual markers alone which has the potential to be extended to multi-analyte tests which, with further work, could increase the reliability of tumour marker testing.

1.4 Thesis Structure

Chapter 2 presents an overview of the current state of research in terahertz technology, the development of sources, detectors and devices along with modern day applications.

Chapter 3 provides an introduction into the equipment and experimental methods used in this thesis.

Various methods of refractive index measurement using a cuvette and vector network analyser are discussed in chapter 4.

Chapter 5 considers the use of paper at terahertz frequencies. It places a particular focus on the effect of wicking liquids into paper and how that affects the properties of paper such as refractive index. It outlines a study involving paper Fresnel lenses; an application which utilises the permeability of paper at terahertz frequencies.

Chapter 6 discusses the design, simulation and characterisation of a metamaterial device. It focuses on the choice of the design from metamaterial topology to the physical arrangement and fabrication of a metamaterial device for sensing of liquids. Each of the design decisions made in this chapter are made to maximise sensitivity whilst accounting for ease of fabrication and cost.

Some of the devices in chapter 6 are explored in various sensing experiments in chapter 7. These are used to assess the performance of the metamaterials and decide on the most appropriate design for the purpose of sensing trace tumour markers in serum samples.

Chapter 8 presents the findings of the metamaterial device with respect to serum sample measurements for the purpose of tumour marker detection for a range of markers.

Chapter 9 concludes this thesis, presenting the outcomes of these findings and discussing potential for future progression of this work.

Chapter 2

Terahertz Generation, Detection and Use

The terahertz region, formerly a relatively unexplored area of the electromagnetic spectrum, has had a rapid increase in the development of technology and use over the past few decades. This chapter provides general background information for the terahertz region as a whole and gives a brief overview of its current uses. It considers the different methods of generation and detection of terahertz radiation with a particular focus on the two sets of terahertz equipment available at Durham University; a terahertz time domain spectroscopy (TDS) system and a terahertz vector network analyser (VNA). Finally, it considers the benefits and drawbacks for the two systems.

2.1 Terahertz Generation

Terahertz radiation is generated naturally through cosmic background radiation [34]. This is in one of the most basic forms of a terahertz radiation source; a thermal source. In the lab, thermal sources like this have been replicated through devices such as a mercury lamp and a globar. A mercury lamp produces light through an electrical arc travelling through a mercury vapour. This causes electrons in the mercury gas to be promoted to higher energy levels; once these naturally fall back down again, they release this energy in the form of light. The light produced has a frequency related to the energy difference between the bands the electron is travelling between, as this is the energy being released from the electron moving back down to the lower energy state. This is an intrinsic property of the material used which, in the case of mercury, produces radiation with frequency components ranging from 120 GHz-6 THz.

The lack of research within the terahertz region has been filled by the development of many novel sources [1]. The problem has been approached from a variety of angles; electrical techniques from a lower frequency perspective have led to the continued development of high-frequency transistors while an approach adapted from higher frequency technology in the optical region, has resulted in terahertz quantum cascade lasers (QCL's) [35].

QCL's exploit molecular beam epitaxy (MBE) techniques to create periodic semiconductor quantum structures, in which population inversions can be engineered between sub-bands. After undergoing a successful intersub-band transition (leading to photo emission), the electrons tunnel through to the next intersub-band, where the same process is repeated. Cryogenic temperatures are required to ensure the intersub-band transitions are not overwhelmed by interband transitions, which are readily excited at room temperatures. Peak powers now exceed 1 W at 3.4 THz [36,37] and their continuous wave (CW) power output exceeds 100 mW [38]. Current research looks to lower the output frequency down to and below 1.2 THz [39], and increase the operating temperatures [40], whilst others have sought to fabricate two colour sources [41]. As the frequency of terahertz in the case of a QCL is based on the energy spacing of intersub-band transitions this is dictated by the thickness of the semiconductor layers. Two colour sources are born from heterogeneus QCL's which combine the active regions designed to emit at different wavelengths monolithically in the same waveguide thus providing gain across several wavelengths as opposed to the intrinsically narrow gain presented by conventional QCL's. Broadband gain regions can be integrated with an external cavity to realise compact, widely tunable terahertz sources. Two colour devices have also been used for difference frequency generation [42].

Gunn [43] and Schottky [44] diodes can, in conjunction with multipliers provide terahertz sources which shift fundamentally sub-terahertz electrical oscillations into the lower end of the terahertz range. While high-frequency transistors, Gunn and Schottky diodes are commonly used electronic sources, these solid-state electronic sources are typically low power (µW). Vacuum electronic sources such as the backward-wave oscillator, extended-interaction klystrons, travelling-wave tubes, gyrotrons, free-electron lasers and synchrotrons are typically high power (W). Molecular gas (CO_2) lasers operate at the higher end of the terahertz frequency range at around 28 THz [45], while backward wave oscillators are reliable sources for the lower terahertz frequencies in the region of hundreds of GHz [46, 47].

Gunn diodes consist of three doped regions, two heavily n-doped regions on each terminal and one thin layer of lightly n-doped material in the middle. Upon the application of a voltage across the terminals the electrical gradient will be largest across the thin middle layer, however, as this is increased further, the current increases through this layer. Following the initial current increase, at even higher field values, the conductive properties of the middle layer alter, increasing resistivity and therefore causing the current to fall. Hence, Gunn diodes effectively have a negative resistance at this point in the current-voltage characteristic curve. This feature can be used as a radio frequency amplifier or, in this case, it can become unstable and be used as an oscillator. As the frequency of oscillation is partly determined by the properties of the middle layer, this can be chosen to produce electrical sources of a designed frequency. Further manipulation of the source can be achieved by external factors e.g. changing the size of the cavity the diode is set in. Schottky diodes are essentially lowered forward voltage diodes; this lowered voltage allows for faster switching speeds hence development up to terahertz frequencies.

Travelling-wave tubes are vacuum tubes used to generate microwaves. A radio wave is amplified in a travelling wave tube by it absorbing the power from a beam of electrons as it passes down the tube. Operating frequencies are typically from 1 to 200 GHz with pulsed power levels in the 0.1 to 3 MW range and CW levels in the 10 W to 20 kW range [48]. Modern fabrication techniques have extended their operating frequency to 1 THz [48]. There are two main types; helix travelling wave tubes where the radio waves travel down a wire helix surrounding the beam or a coupled cavity travelling wave tube where the radio wave interacts with the beam through a series of cavity resonators. Helix travelling wave tubes produce broadband and typically low power outputs while coupled cavity travelling wave tubes function as narrowband power amplifiers.

Backward-wave oscillators are a type of travelling wave tube where an electron gun generates a beam of electrons. Oscillations are sustained by propagating a travelling wave backwards against the beam. Backward-wave oscillators are tunable over a wide range of frequencies by varying the accelerating voltage.

A klystron is a specialised linear beam vacuum tube, it is used as an amplifier for high radio frequencies up to microwaves. The energy from an electron beam interacts with a radio wave as it passes through resonant cavities amplifying the signal. An electronic oscillator can be formed from a klystron by coupling the output signal to the input cavity. Klystrons can have large gain but tend to be narrowband. Extended-interation klystrons (EIK's) are the optimum blend between a klystron and a coupled cavity travelling wave tube. An EIK achieves enhanced power (up to 30 W dependent on frequency), bandwidth (in the region of 2 GHz) and efficiency at millimetre wavelengths through the introduction of cavities with multiple coupled gaps. The number of cavities and gaps depends on the application and required specifications. Current EIK's function up to 280 GHz [49].

Gyrotrons generate high-frequency electromagnetic radiation by stimulated cyclotron resonance of electrons moving through a strong magnetic field. It can produce high powers (up to 25 W) at millimeter wavelengths (20-527 GHz) [50]. As a fast-wave device, its dimensions can be much larger than the wavelength of radiation unlike conventional vacuum tubes e.g. klystrons. A hollow tubular beam of electrons is emitted which is accelerated by a high voltage anode which travels through a large resonant cavity with a strong axial magnetic field. This causes the electrons to move helically in tight circles along the tube. At the position of maximum magnetic field, the electrons radiate electromagnetic waves perpendicular to the axis of the tube, these are radiated through a window in the side of the tube into a waveguide.

Free-electron lasers are a form of high speed electron beam moving freely through a magnetic structure of alternating magnetic poles. The alternating magnetic field causes the electron beam to wiggle in a sinusoidal motion transversely to the direction of travel. The wavelength of the emitted radiation is adjusted by changing the magnetic-field strength of the magnets and their physical spatial period. An example of a terahertz free-electron laser is the FELIX facility in the Netherlands [51].

Synchrotrons consist of an accelerating particle beam travelling around a fixed closed path loop. A magnetic field being used to bend the beam into this closed path increases as the particle accelerates thus ‘synchronising’ to the kinetic energy of the particles.

MIRIAM at Diamond in the UK is an example of a terahertz Synchrotron [52].

Visible and near-infrared lasers can also be used as terahertz sources via optical pumping. Two continuous laser sources can be mixed resulting in a laser within the terahertz range. Laser sources used for these systems include diode lasers, dual-mode lasers, multi-mode lasers and dual-colour-vertical-external-cavity surface-emitting-laser (VECSEL) [53]. The efficiency of these systems can be improved using periodically inverted electro-optic crystals and tilted fields.

Time domain spectroscopy (TDS) systems rely on pulsed laser sources. Commonly gallium arsenide (GaAs) photoconductive antennas are used to create a terahertz pulse but alternate material photoconductive antennas and air plasma based sources are also used.

2.2 Terahertz Detection

The detection of terahertz radiation falls into two main categories incoherent or coherent; incoherent detection measures the heating effects of incident radiation while coherent detectors can measure both the magnitude and the phase of the incident terahertz electric field.

Incoherent detectors are unable to measure phase information; only a measure of the total radiation intensity can be measured. Golay cells, neon tubes, bolometers and pyroelectric detectors are typical incoherent thermal detectors.

Golay cells, invented by Marcel J. E. Golay and patented in 1947, use a strain gauge or light sensitive detector to measure the expansion of a diaphragm as the xenon gas, it contains, is heated by the incident radiation. Golay cells can detect low powers ($<$ nW) with a broad well-characterised spectral response however, they are sensitive to mechanical vibration, have slow response times ≈ 1 s, are fragile due to their thin membranes, have a transient response with room temperature, can only handle low power ($\approx$ µW), require a HDPE window and are expensive. Golay cells also have liquid and solid equivalents where thermal expansion is used to measure terahertz radiation in the form of liquid-in-glass thermometers and nano-cantilevers.

A neon tube or glow discharge detector [54] is another incoherent detector which can measure electrical or optical response. It operates at room temperature, is compact ($\approx$ 1 cm^3) and inexpensive ($\approx$ 1 USD) but it has many sources of noise. The noise decreases with current and frequency. Electrical detection gives better signal to noise ratio so increased sensitivity while optical detection has a faster response. Sensitivities are around 10-100 V W^{-1}.

Bolometers employ an electrical resistance thermometer to measure the temperature of the radiation absorber. They consist of an absorbing material of appropriate size to intercept the signal made out of a material with a low heat capacity and a large absorptivity over the frequency range of interest. This absorber is in contact via a high thermal conductance link to thermally connect the absorber to a heat sink where the temperature difference is measured using a thermocouple. Cryogenic temperatures are required for bolometers which can be physically large. Bolometers offer a simple method of obtaining a high sensitivity (10^7 V W^{-1}). Thermopiles are stacked thermocouples providing N times the amount of sensitivity where N is the number of alternating material pairs. They are each fast $\approx$ 1 ps (for nanoscale designs), inexpensive and small however can provide only small voltage outputs. Following the bolometer, work began on the pyroelectric detector which has become the most widely used ambient temperature thermal infrared detector.

The pyroelectric detector works by utilising a property of certain crystals which are naturally electrically polarised as a result of large electric fields. Pyroelectricity is the ability of these crystals to generate a temporary voltage when they are heated or cooled. Its instantaneous polarisation is a function of the rate of temperature change of the crystal. The advantage of this method is that is does not require cryogenic temperatures. However, it generally has a broad flat spectral response across most of the electromagnetic spectrum and has large internal thermal noise. Therefore, it cannot be used to distinguish between frequencies of radiation. A high power beam is required to instigate this effect, so is less commonly used in systems at terahertz frequencies as these are commonly low power [55]. A lithium tantalate ($LiTaO_3$) pyroelectric detector is sensitive (nW), has a broad flat spectral response, large operating temperature range, a slow response time ($\approx$ 0.1 s), can handle high power (50 mW), is cheap, rugged and readily available.

The mechanisms used for coherent measurements need an additional layer of detection so that the phase data can also be taken. An example of a coherent detection method is electro-optic detection which uses an electro-optic material such as zinc telluride (ZnTe). Electro-optic materials alter their refractive index at visible frequencies in the presence of a terahertz electric field. Electro-optic detection relies on the Pockel's effect which is a linear electro-optic effect, where birefringence is induced within an optical medium via the application of an external electric field. Birefringence occurs within the crystal as the change of refractive index is different for each polarisation of light, this occurs in all anisotropic crystalline materials affecting the speed at which orthogonal polarisations traverse the crystal. With incident light perpendicular to both the optical axis and the face of the crystal, orthogonal polarisations experience unequal refractive indices, causing a retardation of one polarisation with respect to the other. Each polarisation inevitably emerges at different times, incurring a phase difference, which can be calculated given the crystal thickness and wavelength of incident radiation is known. Zinc telluride (ZnTe) crystals are commonly used for terahertz detection in conjunction with a quarter wave plate, wollaston prism, photodetector diode pair and a differential amplifier. A photodetector provides high speed, narrowband detection and established fabrication but requires cooling, typically to at least 77 K, and can provide sensitivities of 1 $\mathrm{A\,W^{-1}}$. The current measured between the photodiodes is directly proportional to the instantaneous electric field of the incident terahertz pulse. The crystal is cut in the best direction for the strongest electro-optic features typically (110) and tuned for thickness which increases sensitivity, due to a greater polarisation rotation for the same terahertz signal, however this decreases bandwidth due to poorer phase matching. Electro-optic detection provides a large dynamic range, good signal to noise ratio, deep modulation and fast detection ($\approx$ fs).

Electron transition can be used for electrical detection at terahertz frequencies which provides a narrowband, quick detection method (12.5 ns for Schottky diodes) operated at room temperature.

Another example of a coherent detector is the photoconductive antenna which detects via the optical excitation of semiconductors to produce a pulse of electromagnetic radiation. Photoconductive antennas [56] consist of two metal antenna electrodes commonly in a strip line or bow-tie geometry patterned on a substrate. Electron-hole pairs are excited by an optical laser pulse of energy greater than the band gap of the semiconductor. This is known as photogeneration. Once a terahertz electric field is applied, these electron-hole pairs are subsequently accelerated between two unbiased electrodes by the incident terahertz radiation. The resultant current established between the two electrodes gives a direct measurement of the instantaneous electric field amplitude of the terahertz signal. The phase information can then be obtained by varying the time of arrival of the probe pulse relative to the terahertz pulse. An identical structure to a photoconductive antenna emitter may be used but rather than applying a bias voltage to the electrodes of the antenna, a current amplifier and an ammeter are used to measure a transient current. Photoconductive antennas provide fast, coherent, ultrahigh bandwidth detection (in excess of 20 THz) [57].

Plasmonic detectors, for example a graphene FET (which functions up to 400 GHz), are physically small ($\approx$ 0.01 mm^2), so well suited for imaging, typically operated at room temperature, require standard fabrication and have low power consumption ($\approx$ 100µW). Unfortunately, they have limited spectral range, detectivity is often limited by noise and it requires impedance matching. Examples and their sensitivities: TeraFET 2.5 $\mathrm{V\,W^{-1}}$ at 200°C, TeraFET 10^3 $\mathrm{V\,W^{-1}}$, CMOS 4.7x10^5 $\mathrm{V\,W^{-1}}$, single ring 10^3 $\mathrm{V\,W^{-1}}$, dual ring 10^2 $\mathrm{V\,W^{-1}}$, graphene FET 10^2 $\mathrm{V\,W^{-1}}$ and heterojunction bipolar transistor 10^5 $\mathrm{V\,W^{-1}}$.

2.3 Terahertz Time Domain Spectroscopy

The terahertz time domain spectroscopy (TDS) system developed by Daniel Grischkowsky and his co-workers in the 1980's has quickly become a staple tool in both chemistry and physics laboratories worldwide [58].

The TDS system has the ability to resolve a pulsed signal and its associated in-axis reflections within the time domain. Each of the terahertz pulses has the benefit of a broad spectral bandwidth as well as high power density. TDS systems use coherent detection, current systems can reach a peak dynamic range of 90dB [59], however, the beam alignment associated with the TDS system can make reliable and reproducible conditions difficult to reconstruct over an extended period of time. Laser beam drift introduces a time-dependent systematic error causing variation in peak signal and bandwidth [60].

To detect the full range of frequency components in a free space photoconductive antenna system the receiver is manually stepped using a delay stage. Since 2000, fibre coupled systems have been developed which allow movement of the antennas providing flexibility and stability [61]. The delay stage moves in discrete spatial steps (Δx) which correspond to time steps (Δt) as in equation 2.3.1.

$$\Delta t = \frac{2\Delta x}{c} \tag{2.3.1}$$

Where c is the speed of light. The electrical field strength E of the signal received can be expressed as in equation 2.3.2.

$$E(t) = n\Delta t \quad where \quad n = 1, 2, 3, ..., N \tag{2.3.2}$$

A fast Fourier transform (FFT) is used to obtain the frequency spectrum which consists of discrete values where the frequency resolution Δv is as stated in equation 2.3.3.

$$\Delta v = \frac{\Delta t}{N} \tag{2.3.3}$$

The resulting data can then be used to calculate optical frequency-dependent properties e.g. refractive index. To do this, the measured waveform needs to be compared with the free space reference to isolate the effect of the sample and its refractive index. Other properties such as reflection at each interface can be examined.

This method results in a large measurement time (30 minutes for the Durham system) and also a low spectral resolution as defined by Δv in equation 2.3.3.

As an alternative technique, a terahertz vector network analyser (VNA) relies on an electrical microwave (GHz) source which is frequency multiplied to the terahertz region. This eliminates the need for laser alignment; thus removing concerns regarding beam drift.

2.4 Terahertz Vector Network Analyser

There are two main types of network analyser; the scalar network analyser (SNA) which measures signal magnitude only and a vector network analyser (VNA) which is capable of measuring both magnitude and phase. The first VNA was developed in the 1950s. Mostly used at high frequencies, network analysers are machines which measure network parameters of electrical networks. These commonly take the form of scattering (S) parameters but can also be in the form of Y, Z or H parameters which measure admittance, impedance and hybrid parameters respectively. Nowadays, VNAs are commonly used for many frequency ranges from below the terahertz region up to around 1.1 THz although there are few researchers working at the top end of that frequency range. Technologies exist up to 1.5 THz however these have reduced dynamic range [62]. A typical dynamic range for a WM-250 (WR1.0) extender head functioning at 0.75-1.1 THz is 65 dB [62].

The S parameters measured by the VNA take the form of complex numbers. These complex parameters can be used to calculate both the magnitude and phase of the received signal. The VNA measures using a continuous wave (CW) and can take measurements at different frequencies by sweeping through a range of CW frequencies. The VNA has a fast measurement time (in the region of seconds dependent on measurement parameters) and high spectral resolution but has a narrow measurement range. Therefore, the VNA is suited to applications where a high spectral resolution is needed within a narrow band frequency spectrum for example detailed material characterisation of gasses [63]. VNA systems can also make use of the Farby-Perot response for material characterisation [64].

The terahertz radiation of a VNA setup is emitted and received via horn antennas which are mechanically coupled to waveguides. The frequency mixing process is described in detail in [65], with an achievable dynamic range of 90 dB, within a rectangular waveguide. The errors introduced by the use of antennas, mirrors and propagation through air has been shown to be negligible by the sensitivity analysis performed in [66]. Following calibration, the typical precision delivered by the measured scattering (S) parameters is +/- 1%.

The VNA at Durham University consists of an Agilent PNA Network Analyser N5224A and two VDI WR1.0-VNAX extender heads with a 0.75-1.1 THz range. As this is a two port VNA, once the extender heads have been added, it measures four S parameters (S_{11}, S_{12}, S_{21} and S_{22}) which correspond to transmission and reflection measurements from each of the two transceivers. The extender heads use Schottky diodes as triplers and subharmonic mixers upon the PNA's standard specification, (as shown in figure 2.1) to achieve the frequency range. Each of the extender heads is used with a horizontally polarised diagonal horn antenna with an 11° divergence to allow for free space manipulation of the terahertz beam.

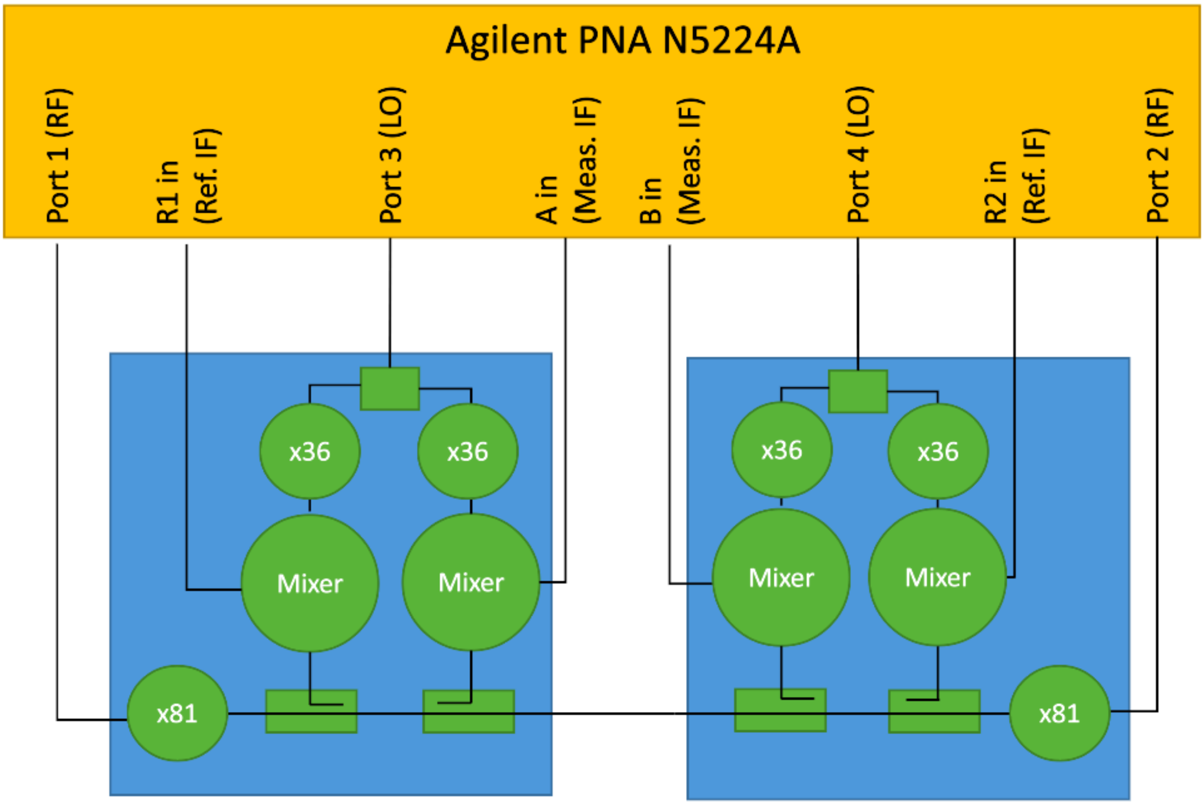

Figure 2.1: Diagram of VNA's function with respect to the 0.75-1.1 THz extender heads.

The dynamic range of the VNA is an important performance factor which can refer to the system dynamic range or the receiver dynamic range. System dynamic range is defined as the difference between the highest output power level, (P_{max}), as per the VNA's specifications, and the noise floor, also set by specifications, (P_{min}). Receiver dynamic range is defined as the typical test port compression at 0.1 dB minus the measured noise floor. Dynamic range can therefore be changed by altering the noise floor of the receiver. The noise floor is dependent on the intermediate frequency bandwidth (IFBW) set within the VNA. The scan time increases with an inverse proportionality to the increase in IFBW e.g. if a scan takes 20 seconds at an IFBW of 100 it will take $\approx$ 40 seconds for an IFBW of 50 given all other variables remain the same. Aside increasing measurement time reducing the IFBW lowers the noise floor and thus increases the dynamic range. This is is the case because the noise received by the VNA is thermal noise which is directly proportional to the IFBW. The noise power P_n is given in equation 2.4.4.

$$P_n = k_B T B \tag{2.4.4}$$

Where k_B is the Boltzmann's constant, T is the absolute temperature (K), and B is the receiver bandwidth (Hz).

Figure 2.2 shows the dynamic range of Durham's VNA in a standard transmission setup for varying values of IFBW.

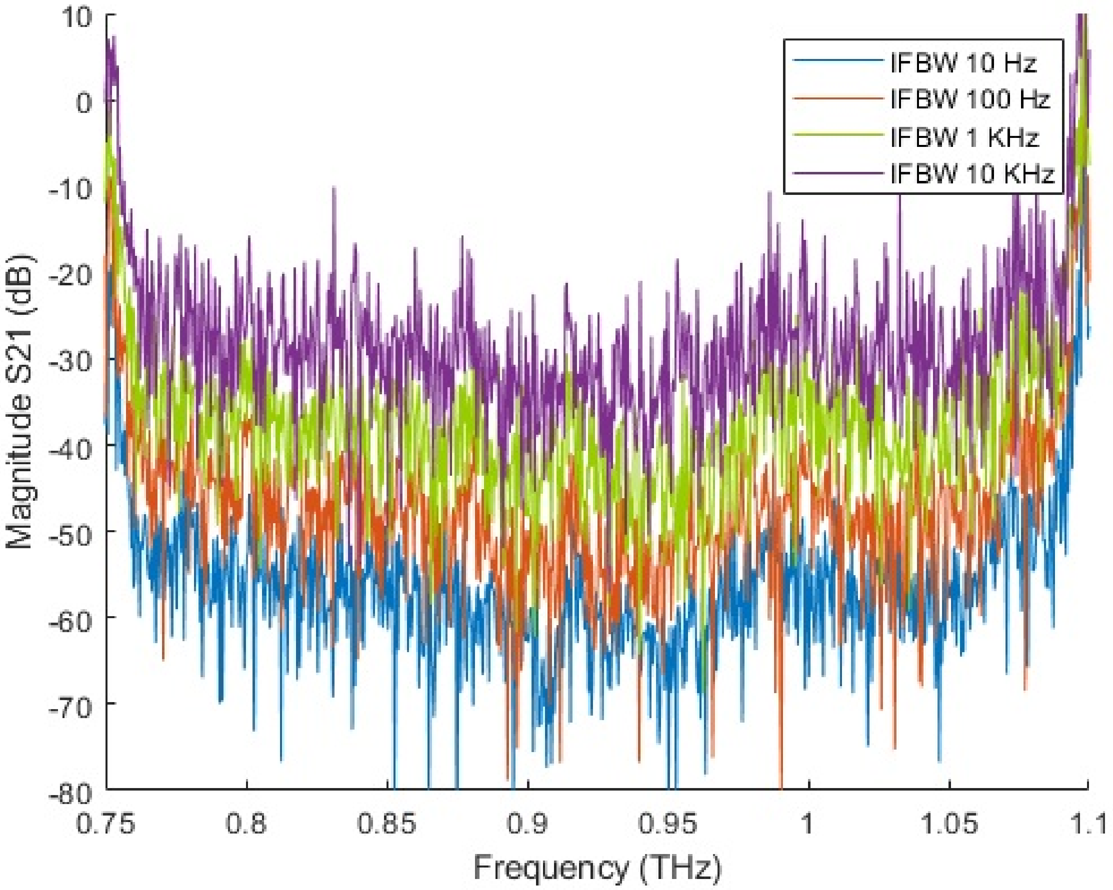

Figure 2.2: Dynamic range for the VNA with IFBW's of 10 Hz to 10 kHz.

The IFBW also affects the root mean square (RMS) noise and thus the precision of the measurements. If the IFBW is reduced, similarly with the reduced noise floor, the RMS noise will also reduce as can be seen in figure 2.3, again, this will be at the cost of scan time. An increased number of scans and averaging can also be used to reduce the RMS noise as it is white noise which has a zero mean value. Again, this increases scan time as multiple scans are taken then averaged.

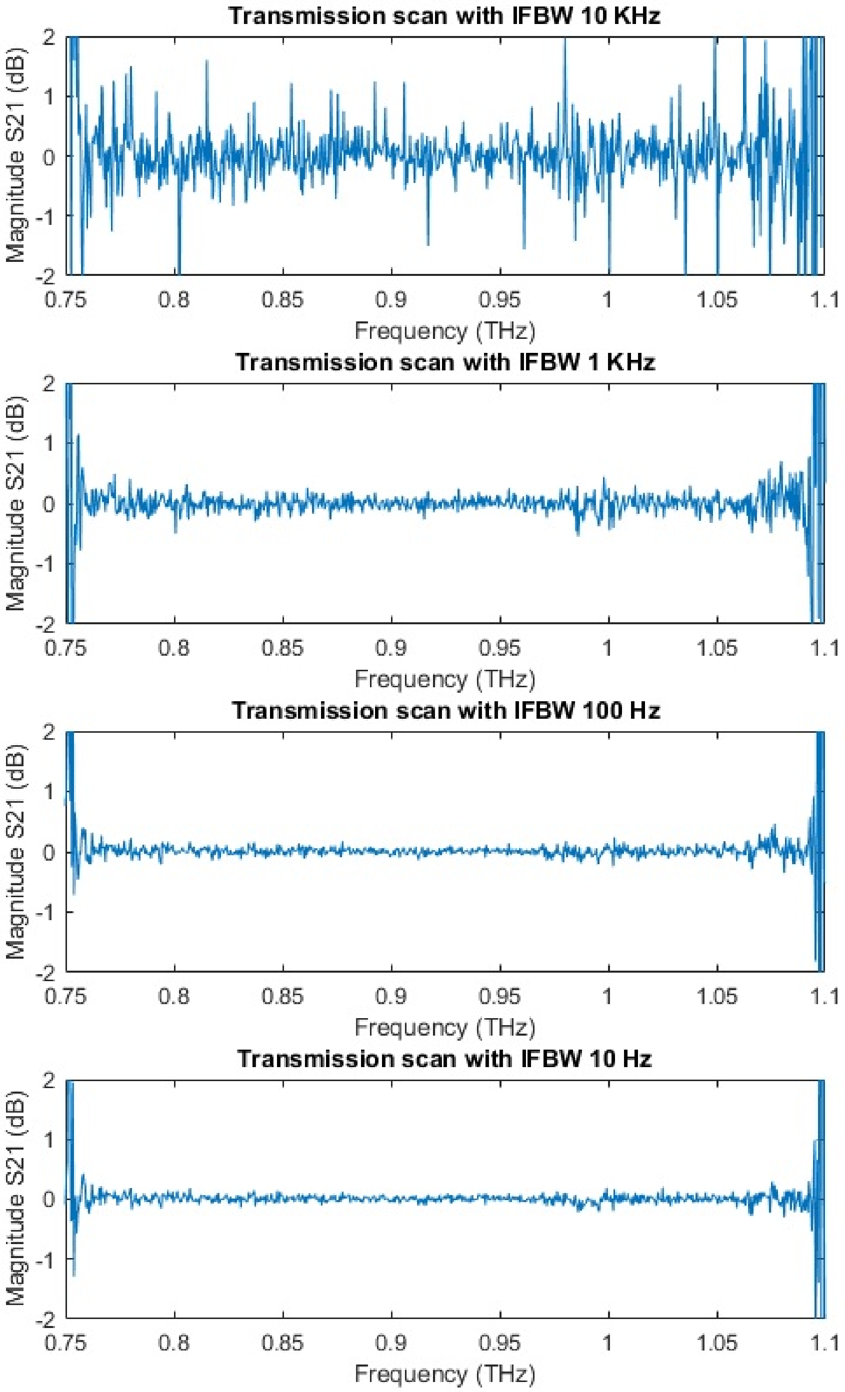
Transmission scan with IFBW 10 KHz

Transmission scan with IFBW 1 KHz

Transmission scan with IFBW 100 Hz

Transmission scan with IFBW 10 Hz

Figure 2.3: RMS noise for the VNA with IFBW's of 10 Hz to 10 kHz.

2.5 Conclusion

This chapter has outlined the methods of generation and detection for terahertz radiation with a particular focus on the TDS and VNA systems. It has discussed the advantages and disadvantages of various source and detector devices used at terahertz frequencies. The function of the TDS and VNA systems are described along with a short demonstration of the effects of certain parameters on the VNA system.

The TDS system has the benefit of broadband detection through femtosecond laser pulses which can be measured across the whole frequency range with a stepped delay. A major benefit of a terahertz VNA when compared to a TDS is that the system is significantly easier to work with in terms of alignment and can provide a significantly higher spectral resolution in a given time frame.

At this point in technology development, the sensitivity of a TDS measurement is limited by the TDS system itself and the measurement precision is highly influenced by the complicated measurement procedure and data processing [67]. Making even minor improvements in sensitivity to a TDS system costly.

As the TDS system is a laser driven terahertz source, it requires a large number of optical components which are sensitive to alignment. This reduces the flexibility of the system as alignment is difficult and time consuming. TDS measurements can also be difficult to reproduce due to drift in laser alignment over time [60]. A VNA functions in the frequency domain using an electrical source thus does not require sensitive laser alignment. The VNA can be reconfigured often due to the nature of its source, the reduced number of optical components and ease of alignment. Hence, the VNA is not subject to drift over time as the system is both realigned often and not as sensitive to alignment as its TDS counterpart.

Chapter 3

VNA Experimental Techniques and Material Characterisation

This chapter highlights the theory of material characterisation with a particular emphasis on refractive index. It describes a selection of possible VNA experimental setups and introduces the use of moving stages highlighting the flexibility of the VNA system. Its flexibility stems from the ease of alignment. The use of MATLAB to control both the VNA and moving stages is demonstrated showing each of these setups can be automated for quick and easy extraction of S parameters. Finally, examples are given demonstrating these techniques and characterising common materials.

3.1 Refractive Index

Refractive index is a fundamental property of a material which describes how the material interacts with light. The complex refractive index ($\underline{n}$) describes a complex number with two constituent parts 3.1.1 [68];

$$\underline{n} = n + i\kappa \tag{3.1.1}$$

where (n) corresponds to the real refractive index, and (κ), the extinction coefficient. These respectively describe the phase velocity and attenuation of the electromagnetic wave as it travels through a material. For any given temperature and wavelength of external stimuli, refractive index is constant for a material so is commonly used to identify substances and to measure purity or concentration within mixtures. It is used to quantify the capabilities of optical components i.e. the focusing power of lenses and the dispersive power of prisms. Refractive index information can be used to further optimise lenses via the use of anti-reflection coatings [69, 70]. Another common application is to estimate the thermophysical properties of hydrocarbons and petroleum mixtures.

As refractive index varies with frequency, each substance must be characterised for each frequency where refractive index data is required. When it comes to measuring the refractive index of materials at terahertz frequencies, the most commonly used method is a TDS. TDS systems send a short pulse of terahertz radiation through the sample and the receiver can resolve the pulse in the time domain. The associated changes in the time domain caused by the material can be related to the velocity of the pulse in the material and the ratio of this velocity as compared to the velocity through a vacuum gives the real part of the refractive index. The extinction coefficient can be calculated by considering the magnitude of the received pulse and calculating the retardation of the beam per unit of distance travelled through the material.

As refractive index measurements at terahertz frequencies can both distinguish between materials and also identify their prevalence within a mixed material, they are ideally suited for biomedical applications. Such applications range from the probing of human skin cancer and skin tissue [71] to monitoring tooth decay [72] and even as quality control for coated or gelatinous tablets [73].

3.2 Transmission Measurements

The Agilent PNA Network Analyser N5224A itself produces and measures electrical signals of 10 MHz-43.5 GHz. The two VDI WR1.0-VNAX extender heads use Schottky tripplers to multiply up to terahertz frequencies, producing a range of 0.75-1.1 THz.

Each of the extender heads is a transceiver, they can radiate and/or measure a signal so we may consider one of the extender heads as a transmitter and the other as a receiver however, they can be used interchangeably.

Standard transmission measurements are taken using the VNA setup as shown in figure 3.1. One of the extender heads acts as a transmitter directing the beam into a parabolic mirror. This transforms the divergent beam from the horn antenna into a collimated beam. Parabolic mirrors are available in a range of sizes resulting in collimated beams with differing beam widths. Each diameter mirror has a focal length which maximises the spread of the beam over the mirror area while avoiding the beam overshooting the mirrors edges and losing power. The horn antenna is a diagonal horn type which has a beam length of 9 mm and an aperture diameter of 1.6 mm resulting in a full 3 dB beamwidth angle of 11° [74].

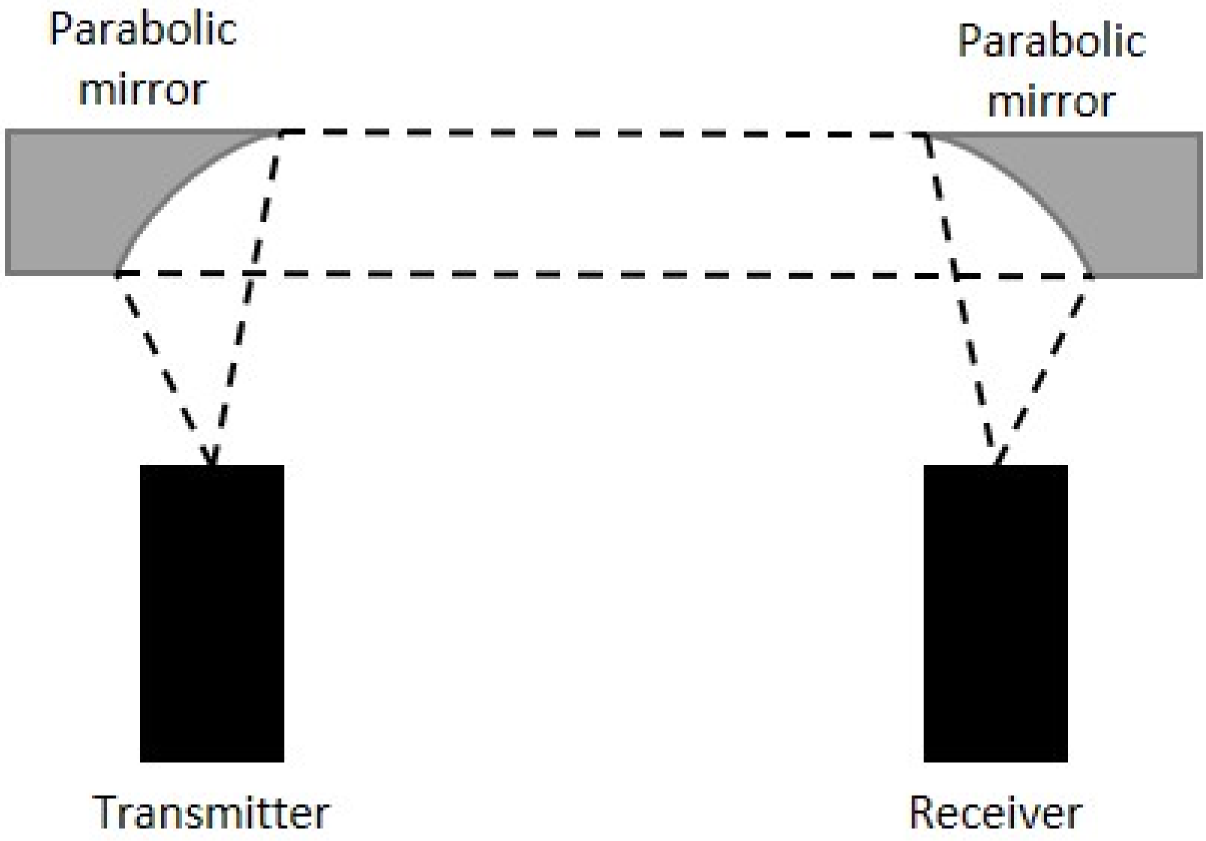

Figure 3.1: Diagram of a VNA setup for transmission measurements.

The smallest mirror size should be used to maximise the power density of the beam that will pass through the sample. In some cases, the beam width is required to be even smaller than the smallest available mirror size. In which case, an iris can be used to further reduce the beam width. An iris should only be used if absolutely necessary as, unlike mirrors, it does not translate the beam to reshape it, it physically blocks the beam, this causes loss of power. Another benefit of using an iris can be to increase the sharpness of the edges of the beam. The parallel beam produced by a parabolic mirror will have a variation in power across the beam area which will tail off at the edges similar to a Gaussian distribution. Hence, reducing beam width with an iris maintains the centre of the beam which has the highest power density and clips the lower power density edges.

Following the steering and clipping of the beam, it travels through the sample. This is the purpose of a transmission experiment; to measure the effect of the sample on the beam as it passes through the sample. Thus the dynamic range available must be larger than the power absorbed by the sample for a measurable response. To measure this response, the beam must be directed into the extender head acting as the receiver. The collimated beam is directed via another parabolic mirror which steers the beam into a converging path. The horn antenna of the extender head acting as a receiver is placed at the convergence point of the beam; maximising the received power. Again, this distance is dictated by the focal point of the mirror.

Each of the components are held into place on an optical table which is physically stable and electrically earthed. At Durham, there is an orthogonal array of 25 mm by 25 mm spaced 6 mm diameter screw holes.

Using the transmission setup, the characteristics of materials can be extracted for the range 0.75-1.1 THz. Figure 3.2 shows the S21 transmission through a selection of substrates. The thickness of the HDPE is 6.08 mm; the acetal is 1.95 mm; the nylon is 1.05 mm; the PVC is 1.43 mm and the aluminium is 1.98 mm. S21 transmission corresponds to the received power at extender head 2 from extender head 1. S12 is the transmission measured at extender head 1 from extender head 2. The various plastics are relatively transparent to the terahertz radiation whereas the aluminium inhibits the transmission to a negligible value as the S21 transmission received is around the noise floor as shown in figure 3.2. As discussed in chapter 2 of this thesis, the noise floor represents the minimum signal the VNA can measure and is equivalent to no detectable power from the transmitter reaching the receiver as the signal measured is built up entirely by the inherent noise of the environment and system.

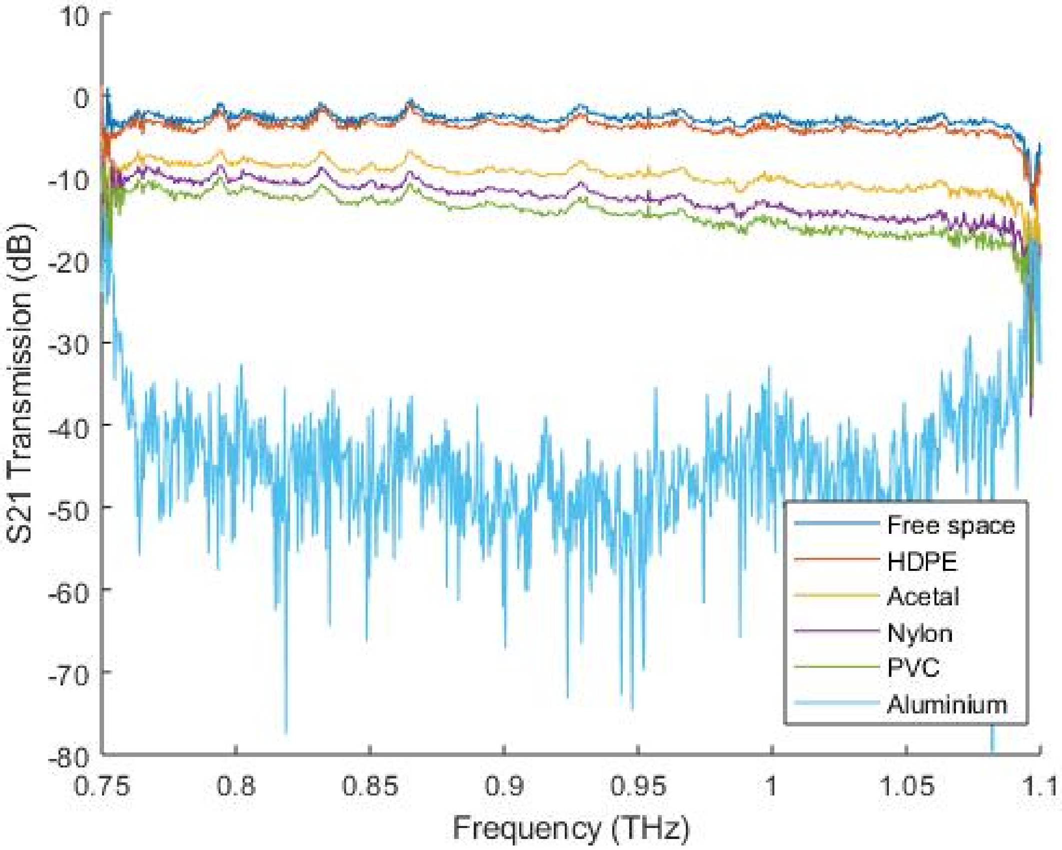

Figure 3.2: Figure showing S21 measurements of plastic and metal substrates measured using a transmission measurement setup.

Generally, terahertz systems have lower power as compared to neighbouring frequency technologies. VNA systems, in particular, are low power (µW) so it is important to maximise transmitted power and reduce unnecessary losses. Therefore, it is imperative the most appropriate sized mirror is selected, the number of optical components is minimised and, if possible, avoid the use of high power loss components such as irises. As explored in chapter 2, the VNA system has a particular dynamic range available based on the comparison between the maximum measurable power and the minimum measurable signal (noise floor). The maximum measurable power is based on the power producible by the extender head and the losses based on the system setup. The power cannot be increased for a given VNA, so to maximise the power that reaches the receiver the losses need to be minimised. The noise floor is dependent on the inherent background noise and the system measurement parameters. System measurement parameters can be improved to a certain extent by decreasing the IFBW, taking averages of measurements etc. all of which increase measurement time. However, there is a fundamental limit based on VNA's measurement capability and the inherent background noise. If too much power is lost through the system that the measured response is at the noise floor the measurement will not be valid and no useful information can be extracted from it.

For some measurements, only a small dynamic range is required, thus some losses can be tolerable however, for high absorbent materials or more complex measurements involving many components, a larger dynamic range is required. It is always best practice to maximise dynamic range as the dynamic range cannot be too large it simply increases measurement capacity.

The system itself will have some features, which could be due to anything system based such as signal leakage, signal reflections, system noise, environmental conditions and frequency response of the test system e.g wire length and orientation. These can be classified into three main types of errors; systematic errors, drift errors and random errors.

Systematic errors are removed via calibration of the VNA system. VNA systems need to be calibrated on a regular basis, to account for varying parameters for example coaxial wires used from the VNA to the extender heads can have a significant effect on the system. Calibration effectively removes systematic errors by measuring well-defined standards and mathematically comparing them to models which can then be used to correct for the character in the specific setup to produce an accurate and consistent measurement system. To do this, open, load (50 Ω impedance) and short measurements need to be taken. Different attachments can be used in place of the horn antenna on the extender heads to measure each of these configurations. To keep on top of systematic errors over time, calibration needs to be repeated whenever there is a significant change to the system e.g. a cable is changed.

Drift errors can also be somewhat accounted for via calibration, these are due to environmental errors driven primarily by temperature. Hence, maintaining a stable ambient temperature, allowing the VNA and extender heads to warm up and stabilise prior to calibration and measurements along with properly ventilating equipment can reduce these errors. Over longer periods of time, these errors are unavoidable but they can be removed via re-calibration. However, even with these precautions in place many factors can still affect the performance of a system once setup with the different orientation of test cables and addition of optical components there will be new features introduced into the system. To remove these additional features, the measurements can be normalised in the measurement setup before the sample is placed in the beam. Normalising the measurements means that the effects of the sample under test will be isolated with respect to other components. Figure 3.3 shows the same materials as in figure 3.2 with normalisation of the system without a sample. It can be seen in this figure that each trace for each of the plastics is much flatter with fewer small features across the frequency range as compared to the raw data in figure 3.2. The additional features in figure 3.2 can be drawn down to a range of system components. Firstly, optical components used in the transmission setup i.e. mirrors will add some noise and features into the system and secondly the air itself will add some features. A component of air is water vapour which has a significant effect on terahertz radiation, although over short distances and at low humidity this effect is minimal. Most of these features are removed by the normalisation in figure 3.3 however some minimal noise and features remain. Although, calibration and normalisation techniques can help reduce unwanted features it is impossible to remove all noise as can be seen in the free space trace in figure 3.3, there is still some noise particularly at the high and low ends of the VNA range. Figure 3.3 shows each of the traces slope downwards across the frequency range, this is likely to be a feature of the material as the free space scan is flat and refractive index of a material is frequency dependent.

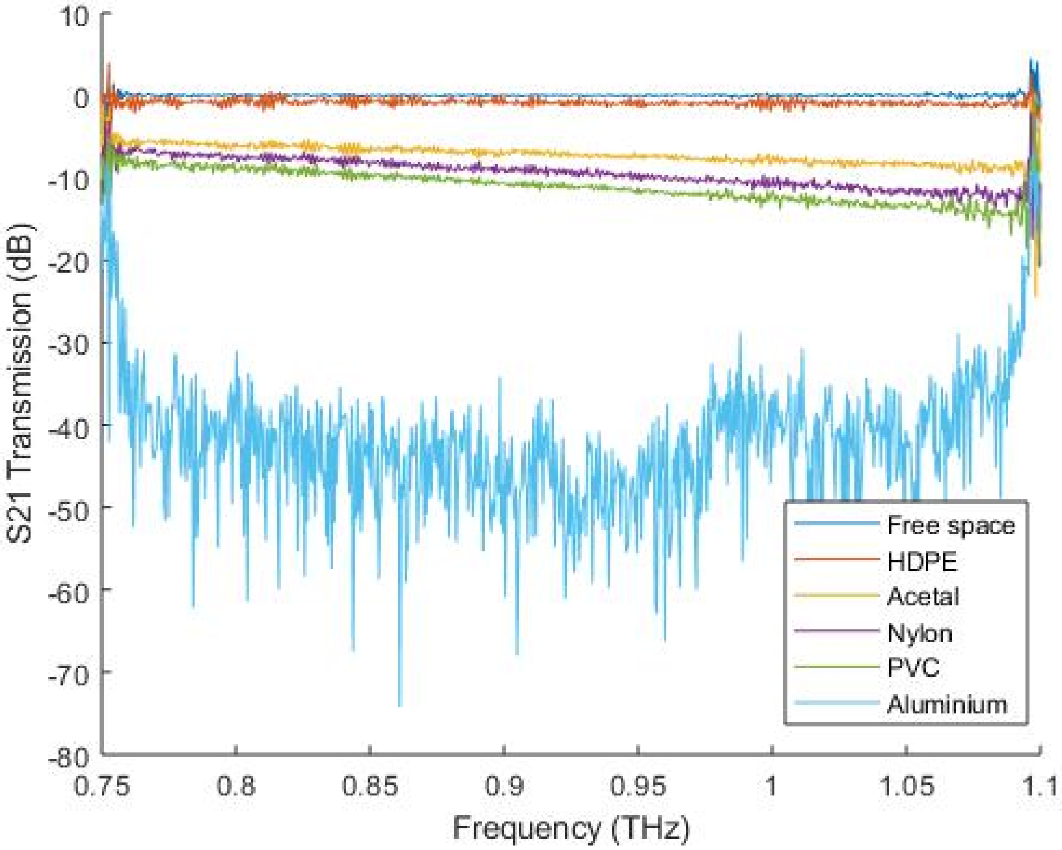

Figure 3.3: Figure showing S21 measurements of plastic and metal substrates measured using a transmission measurement setup normalised against free space measurements. Identical materials as in figure 3.2.

Finally, random errors are based on instrument noise, predominantly source phase noise, sampler noise and IF noise. These cannot be removed via calibration however, as they are generally white noise and not systematic, their effects can be reduced by decreasing IFBW and averaging over repeat measurements each of which increases measurement time.

3.3 Reflection Measurements

The setup for reflection measurements uses one half of the transmission measurement setup as in figure 3.4. In this configuration, instead of one extender head acting as a transmitter and the other a receiver, the same extender head acts as both transmitter and receiver. A sample is placed at a normal to the incoming beam to reflect as much radiation as possible back into the extender head. A parabolic mirror is used to translate the divergent beam from the horn antenna to a collimated beam. The beam is then reflected off the sample sending it back into the parabolic mirror which translates the parallel beam to a converging beam focusing at the horn antenna. S11 (or S22) measurements are taken which correspond to the scattering parameters measured at extender head 1 from extender head 1 (or measured at extender head 2 from extender head 2).

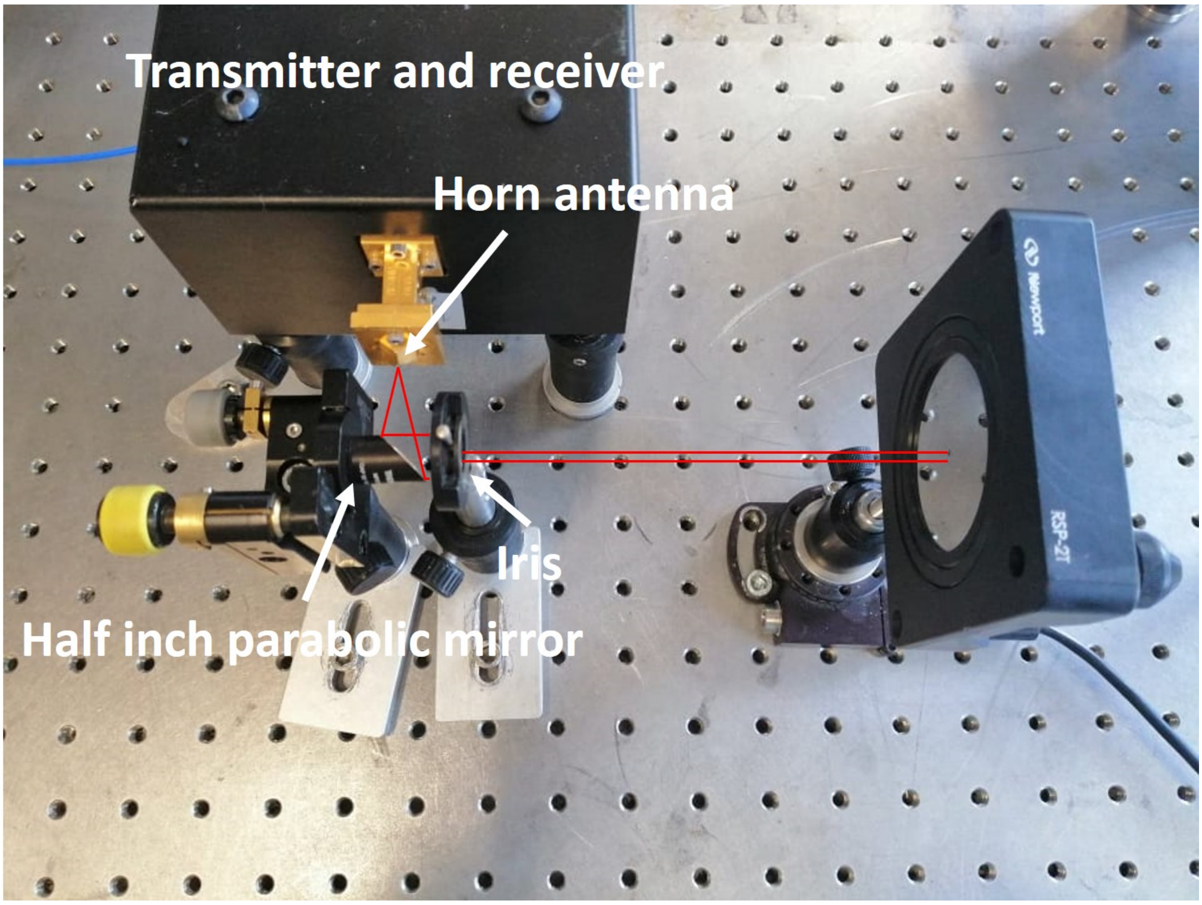

Figure 3.4: Photo of reflection setup.

Figure 3.5 shows the sample materials measured in the transmission section in a reflection configuration. As demonstrated in the figure, aluminium, which in the transmission experiments had little to no received power, has the highest received power. This is because metal is a good reflector so reflection is high and transmission is low. Conversely the plastics allow the majority of the power to pass through in the transmission measurements but they are poor reflectors. The sum of reflected and transmitted power do not add up to the original power as the beam loses power from passing through a material. The amount lost is dependent on the absorbance of the material. Even metals in reflection measurements lose power by passing though the skin depth of the material, which, for aluminium is approximately 80 nm at terahertz frequencies this has been calculated using equation 3.3.2.

$$\delta = \sqrt{\frac{\rho}{\pi f \mu_r \mu_0}} \tag{3.3.2}$$

Where the skin depth, δ, can be calculated using the resistivity, ρ, the permeability of free space, μ_0, the relative permeability of the metal, μ_r, and the signal frequency, f. For aluminium at room temperature, the resistivity is 0.265 $\mathrm{n\Omega\,m}$, while the permeability of free space is 4πx10^{-7} $\mathrm{H\,m^{-1}}$ and the relative permeability of aluminium is 1.00002 [75]. The shape of figure 3.5 shows significantly more features than the previous transmission scans the reasons for this are two fold. Firstly, the scans are not normalised (as in figure 3.2) hence some of the features shown could be due to this. It is more difficult to normalise reflection scans compared to transmission scans as the sample itself is used as part of the system to reflect radiation back into the extender head. It is possible to normalise an S11 scan with a perfectly flat, polished gold plate however this is not likely to be a perfect reference as gold is not a perfect reflector and still has a skin depth. Another factor which makes it more difficult is alignment. A transmission measurement can be easily aligned to maximise power whereas when the sample is used as a reflector if the sample is not perfectly flat or is in some way different to the reference it will cause alignment errors. It is also important to note that the aluminium plate used in this section is brushed and not polished so many reflections will go off in random directions and not reach the receiver.

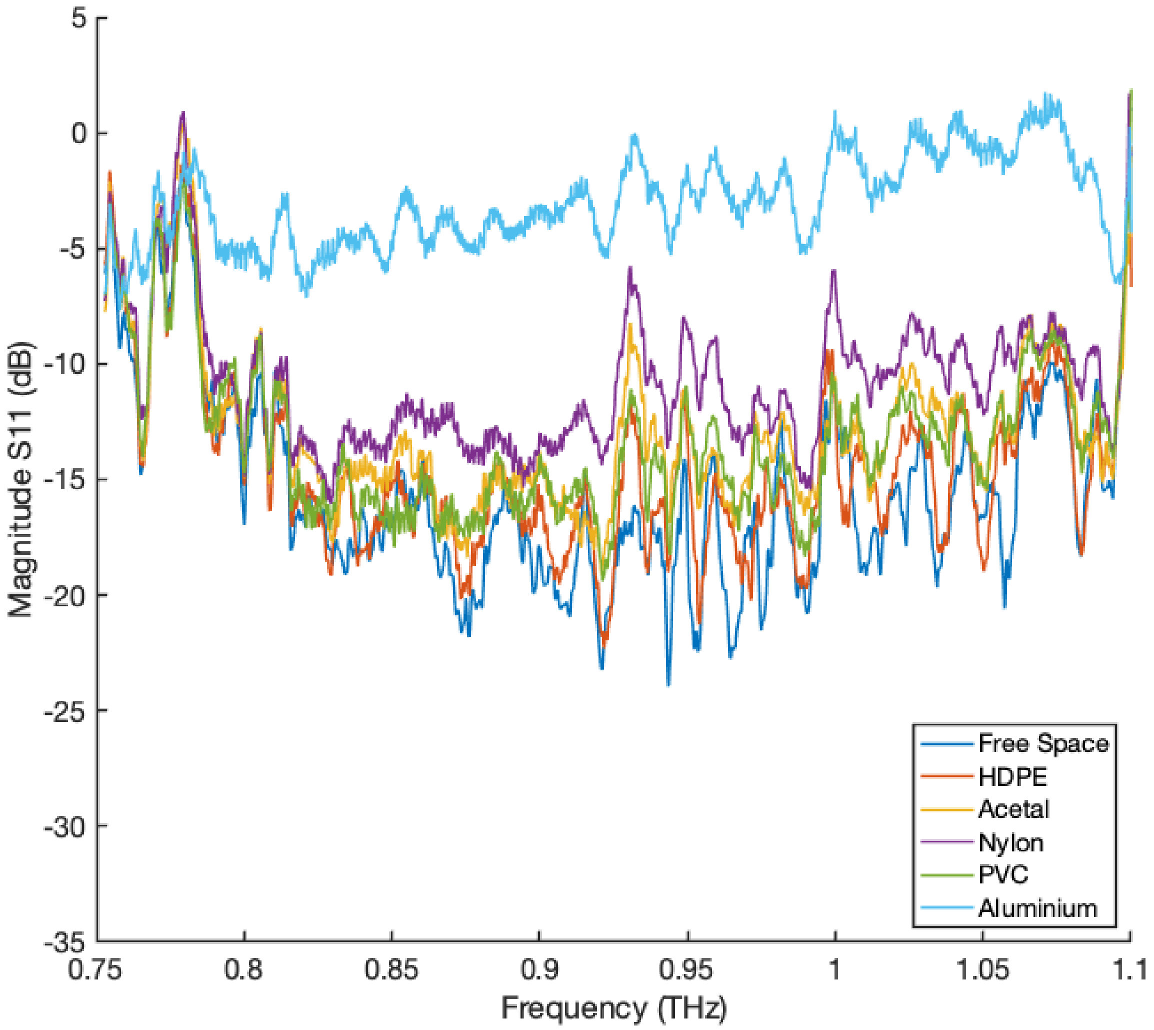

Figure 3.5: Graph showing magnitude of S11 reflection responses for a selection of materials: Aluminium, Acetal, HDPE, Nylon, PVC and Tufnol.

3.4 MATLAB Control

3.4.1 Controlling the VNA using MATLAB

MATLAB programs can be used in conjunction with the VNA to automate control. The connection between the VNA and the PC is setup via serial. SCPI commands are used to control the VNA via MATLAB. Channels are selected for the VNA to set up measurements and parameters are set for these measurements. An S21 measurement can be set up by using the `fprintf(vna, 'CALC:PAR:EXT ''ch21'',S21');` command, similarly S11, S22, and S12 measurements can be setup for the two port system. The number of points to measure can be set by `fprintf(vna, 'SENS:SWEep:POIN 101');`, the frequency can be set by using `fprintf(vna, 'SENS:FREQ:CW 1thz');` and the IFBW can be set by using `fprintf(vna, 'SENS:BWID 50');`.

Once everything has been set up, the scans can be initiated using the command `fprintf(vna, 'INITiate:IMMediate;*WAI');`. This instructs the VNA to take a full set of measurements, the commands to set up each S measurement then select it can be used in turn to get the data for each of the S parameters.

The program instructs the VNA to continuously take measurements. MATLAB `tic` and `toc` commands are used to record the time each measurement is taken. The data is saved in .csv files which can be analysed and post processed at a later date.

The data can be plotted displaying the change in transmission over a period of time. Discrete time intervals are not used, measurement time is based on the measurement parameters (number of points measured, IFBW) and the VNA is utilised to its maximum measurement capacity.

3.4.2 Controlling Moving Stages using MATLAB

Most stages used in this thesis are controlled using a MATLAB program which automates control of the stage in conjunction with VNA control. There are some exceptions where manual stages are used but, where possible, MATLAB is used to control both the stages and the VNA simultaneously. This reduces human error, allows for higher measurement throughput, improves stage movement accuracy and allows for more complex setups.

Each of the Thorlabs stages uses the APT system to control each device. Within the APT system ActiveX controls are used as an interfacing technology which allows universal commands across a range of development environments, MATLAB is used here. Thorlabs provide a graphical user interface (GUI) MATLAB script which sets up a stage with the serial number entered into the script. The GUI allows the user to see the current position of the stage and instruct the stage to move using the commands on this GUI. Figure 3.6 shows a screenshot of the GUI.

SN: 83850772: V3.0.4(2.0.8)

Driver: TDC001 DC Servo Drive
Stage: CR1-Z7
Calib File: None

Min/Max V: 0.000/4.000 °/s
Accn: 4.000 °/s/s
Jog Step Size: 1.000 °

Figure 3.6: Screenshot of APT GUI user interface for a rotational stage.

Although the GUI can be used to move the stage, for the work in this thesis, it is generally just used to setup each stage which will then be controlled using the ActiveX commands. Controlling the stage using the ActiveX commands allows for more distinct and accurate control of the stage, automation within scripts (i.e. in conjunction with the VNA) and also for feedback loops which check variables. A flow chart showing an example process for a VNA scan using a moving stage is shown in figure 3.7.

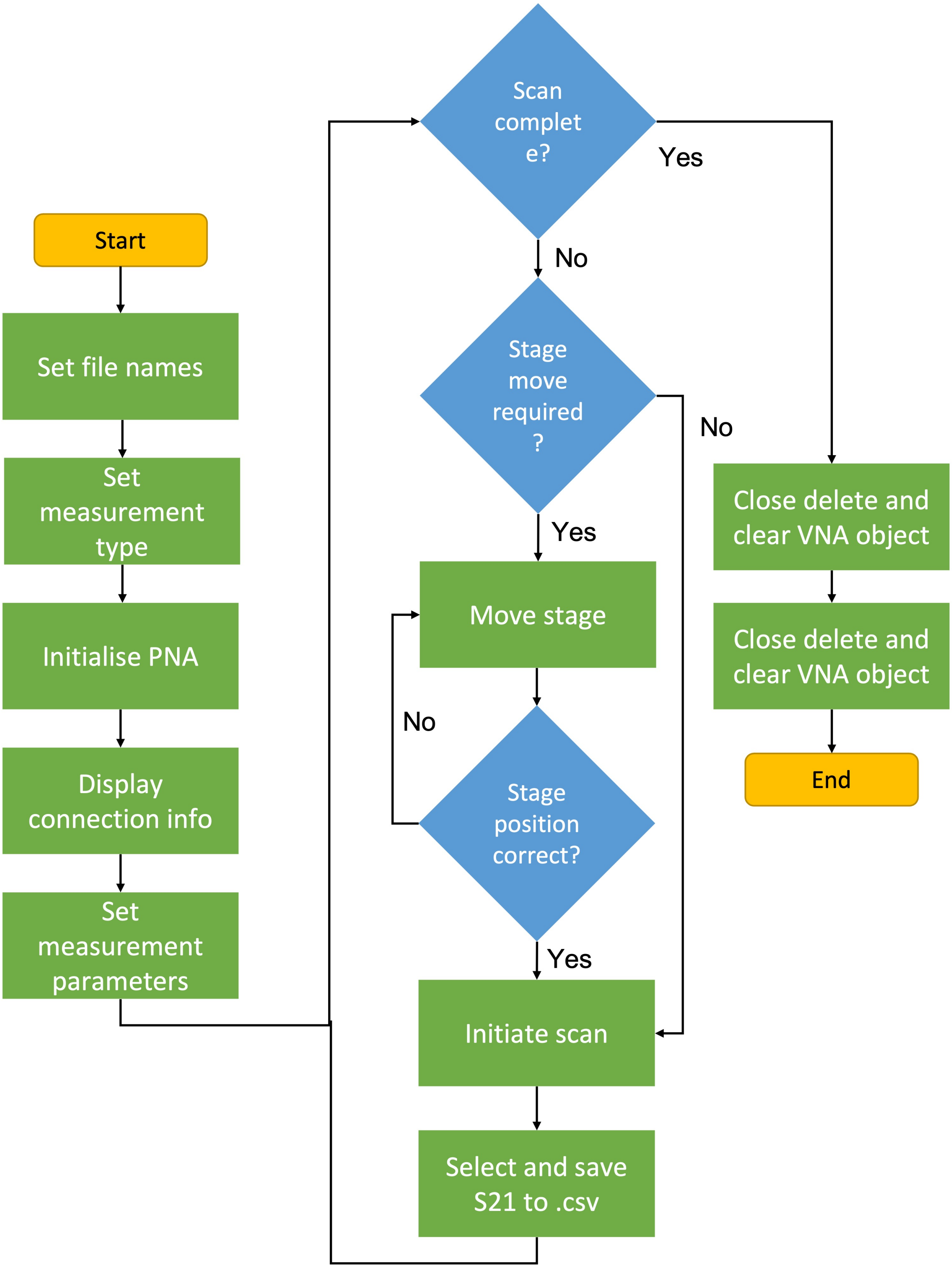

Figure 3.7: Flow chart showing the process for control of the VNA via MATLAB with or without the use of a moving stage.

3.5 Linear Stage

The Thorlabs NRT150\M stage has a 150 mm range of motion and is accurate to 2.0 µm. The linear stage can be used to move the extender heads, optical components or a sample in a linear motion. It can also be used to fine tune alignment or automate moving an object in or out of the beam. The weight limit is 2.5 kg. The stage can be used parallel with the beam to move an object closer or further away from an extender head or it could be used perpendicular to the beam to pass the object across the beam. Geometrical techniques such as diagonal motion can be used to increase precision of the instrument.

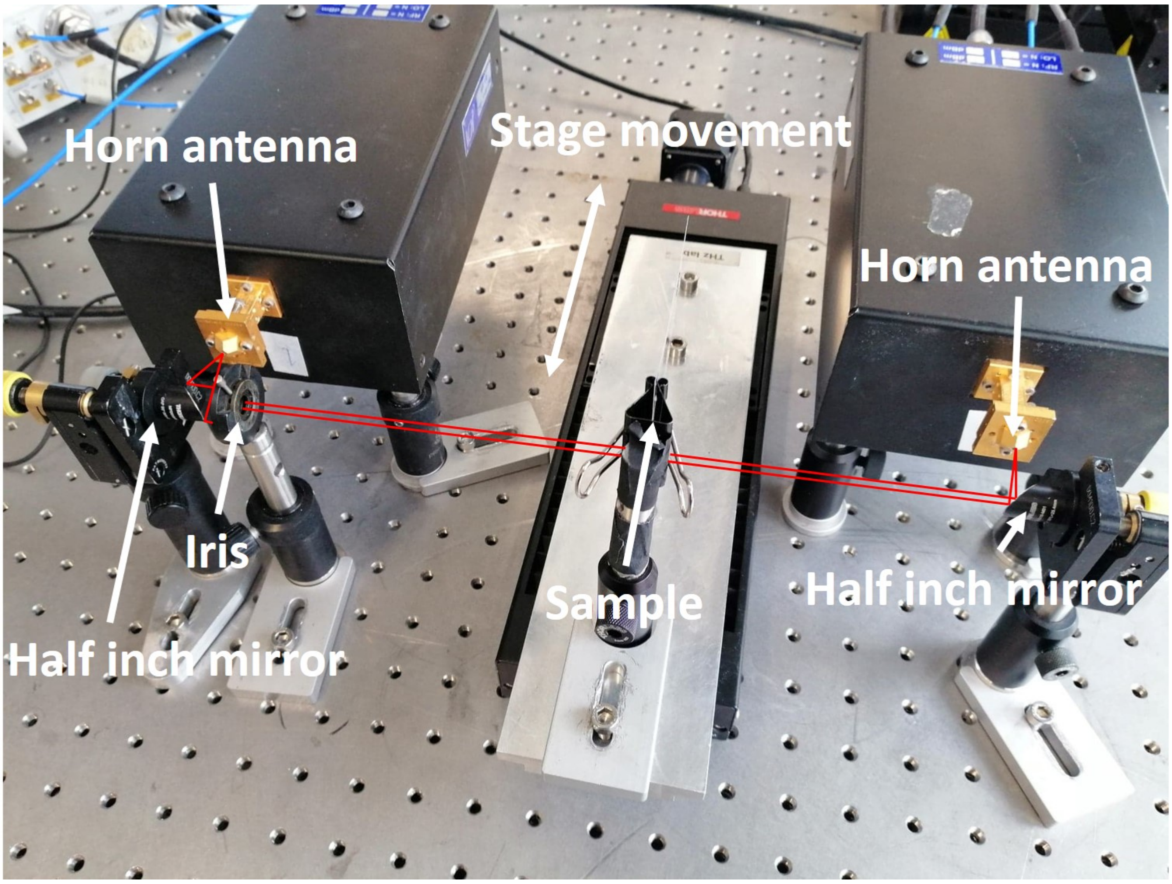

Figure 3.8: Image showing an experimental setup using a the NRT150\M linear stage.

3.6 Angular Stage

The angular stage setup uses the Thorlabs NRT150\M linear stage to drive the system. The linear stage is attached to two custom-made aluminium plates each holding one side of the transceiver and mirror setup. The two plates are connected at a pivot point which is also the position the sample needs to be placed. This is so that the sample remains on the pivot point in the beam path of both transceivers and is able to reflect the response directly into the receiving extender head while the two sides move. The angular stage is aligned at a 0° angle essentially imitating a transmission setup. This setup can be seen in figure 3.9. As can be seen in the figure, there is an additional screw used to connect the two plates along with pivot screw. This inhibits movement between the two plates and ensures they are fixed at 0° for the purposes of alignment. Each of the optical components and extender heads are attached to the plates using an M6 screw and a nut through the plate. The screw holes are countersunk so it does not hinder movement.

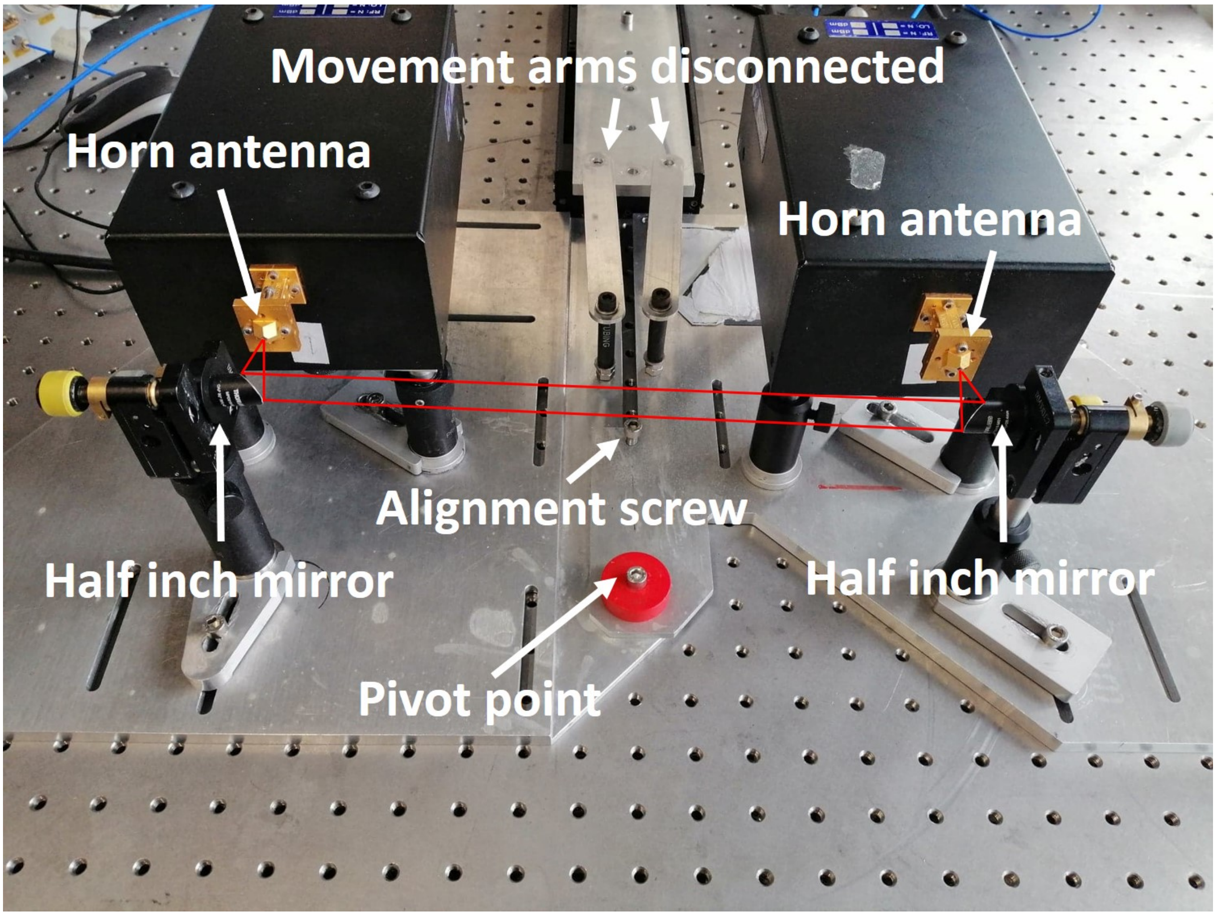

Figure 3.9: Image showing the alignment of the angular measurement setup. Pivot point is the centre of the angular system and the position where the sample will be placed (at the height of the mirrors). For alignment setup is in transmission however when the angular setup is complete it will be used in reflection.

Once aligned, the alignment screw is removed and the two movement arms are connected as shown in figure 3.10. As the linear stage moves, it pushes the two aluminium plates around the pivot point altering the incident angle of the beam by simultaneously moving both transmitter and receiver thus remaining aligned whilst the incident angle changes. The three screw holes along the plates and three on the linear stage are used for the movement arms to select different angular ranges and movement precision. The setup is shown with the movement arms in different positions in figures 3.10 and 3.11.

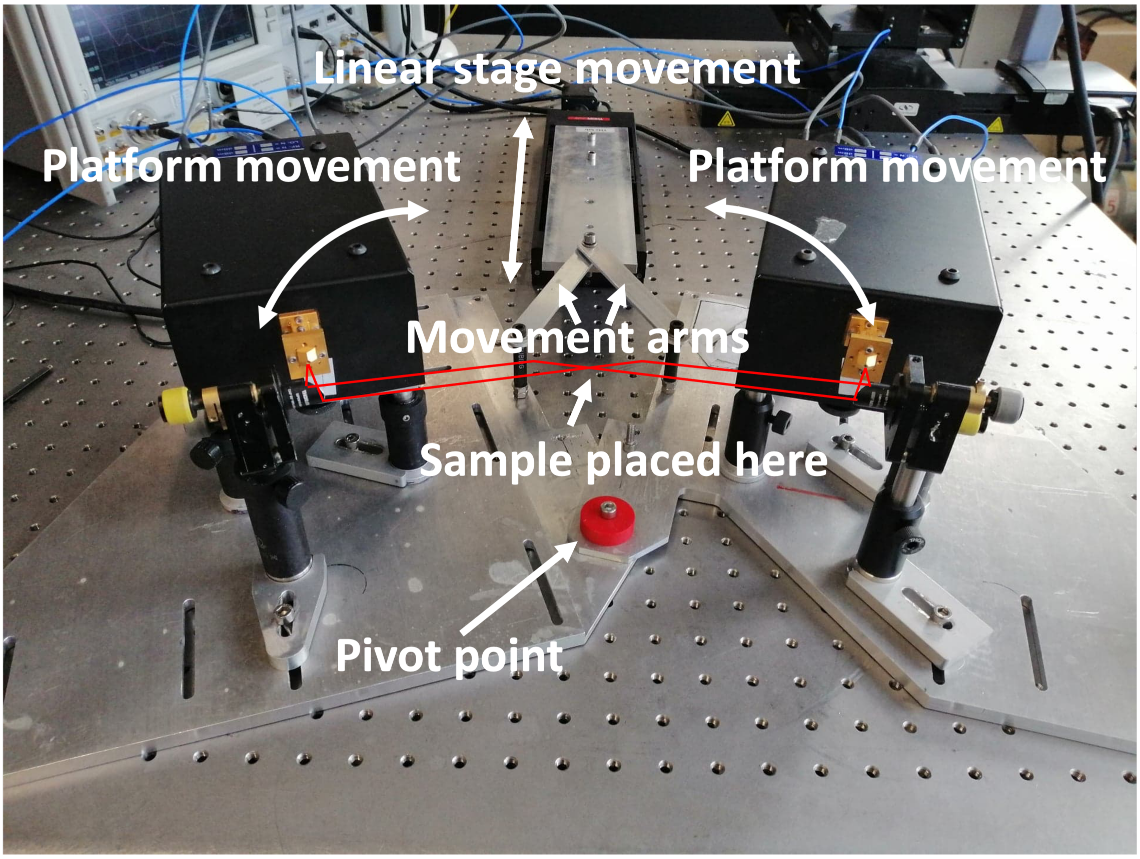

Figure 3.10: Image showing the motion for the angular measurement setup, position where the sample will be held (above the pivot point) and the red lines represent the beam which demonstrates how the angular measurement setup measures in reflection.

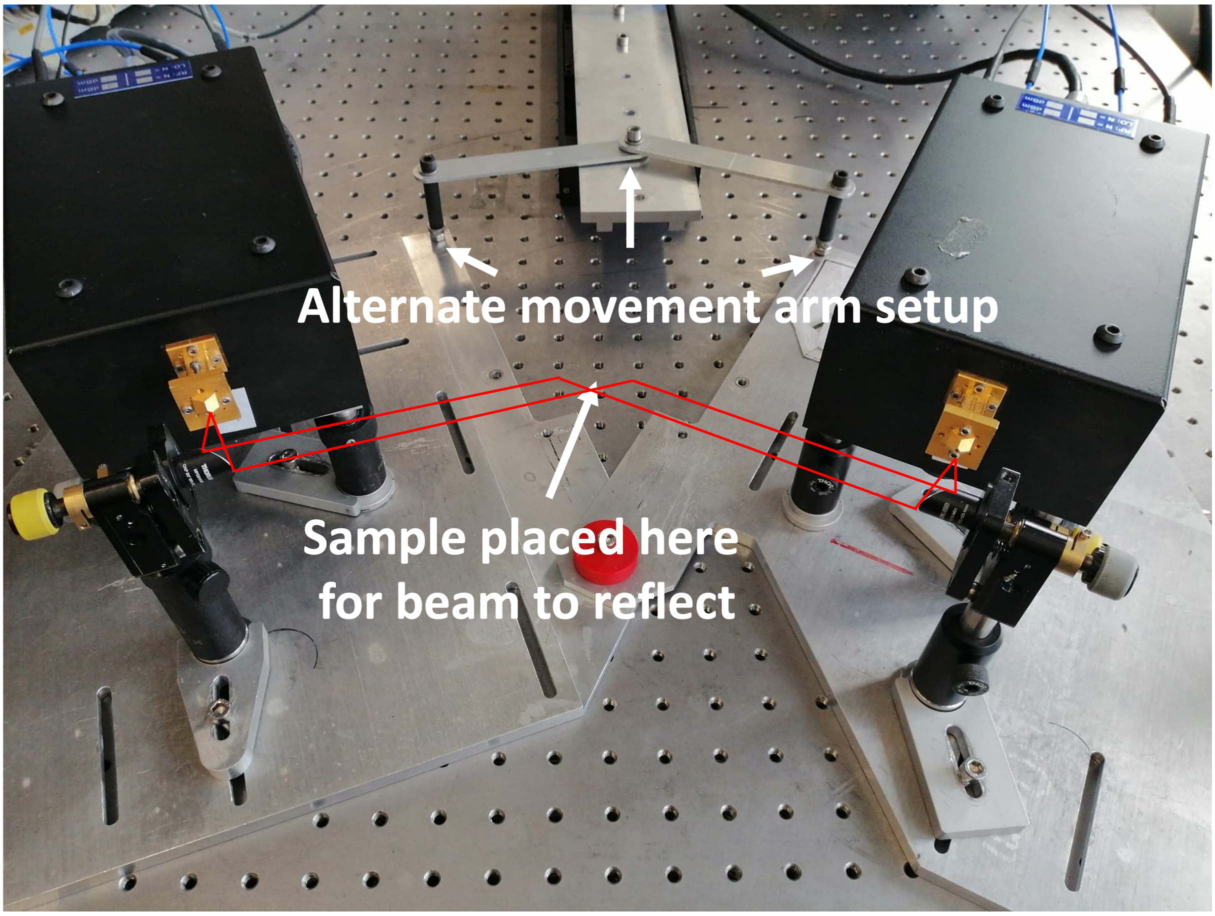

Figure 3.11: Image showing an arbitrary movement arm position for the angular measurement setup. When the sample is positioned as labelled this reflects the beam as shown by the red lines.

The corresponding range for each configuration is stored within the MATLAB program used to control the angular stage to ensure the setup is correct for the desired angular measurement sweep. The arm positions are selected within the MATLAB program. The angular range of motion for an arbitrary screw position (1.5°-25°) is shown in figure 3.12. Other screw positions allow for angular ranges of: 15.5°-34.7°, 20°-43.5°, 10°-43.5° and 4.11°-27.88°. In addition to these mechanical limits a smaller range sweep can be set electronically on the GUI.

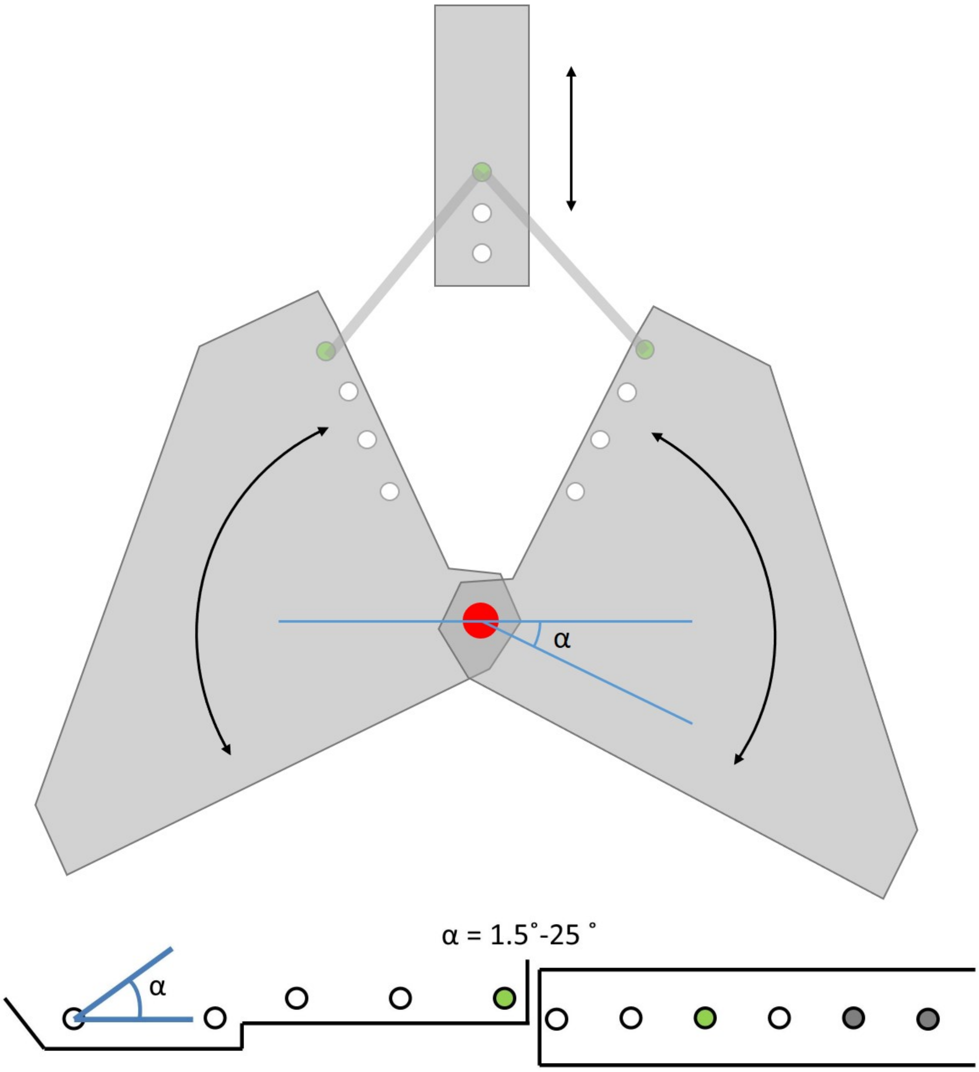

Figure 3.12: Diagram of screw positions with respective angular range. Top is a diagram of the full setup. Bottom shows specifically the screw holes and selected positions which, for the setup shown, correspond to 1.5-25° left shows the angular plate, right shows the screw holes in the linear stage.

This system is useful to assess the response of a thin dielectric with additional sensitivity. This setup of particular use in this case as it can extend and control the path length of the beam travelling through the thin surface, by altering the angle of incidence. This enables the extraction of more accurate and detailed information than would otherwise be possible through a thin material. This setup is used in section 3.9 of this thesis.

3.7 XYZ Stage

The XYZ stage consists of three linear stages which can drive a platform in a 3D Cartesian domain as displayed in figure 3.13. A vertical platform with screw holes is moved. A common mounting element used on this platform would be the 'L' plate. This is attached on the vertical platform creating a horizontal platform allowing for one of the VNA extender heads to be mounted underneath this. The XYZ stage can move in three orthogonal directions X, Y and Z, where X corresponds to a left and right motion, Y, upward and downward motion and Z, forward and backward motion.

The XYZ stage consists of three Newport motorised linear stages connected to the Newport universal motor controller driver. The stage is controlled using a MATLAB program and has a range of motion of ±100 mm in X and Z and ±25 mm in Y. Commonly and as shown in figure 3.13 the transmitting extender head remains stationary and the receiving extender head is swept stepping through all three orthogonal directions. This can map a plane in any two of these directions. For most situations, a vertical plane intersecting the beam usually gives the most useful information. Planes taken at different distances along the beam can show the behaviour as the beam travels through free space. Another use for the XYZ stage could be to locate a focal point or to align a component as the fine movements in each direction could be used to automate this easily.

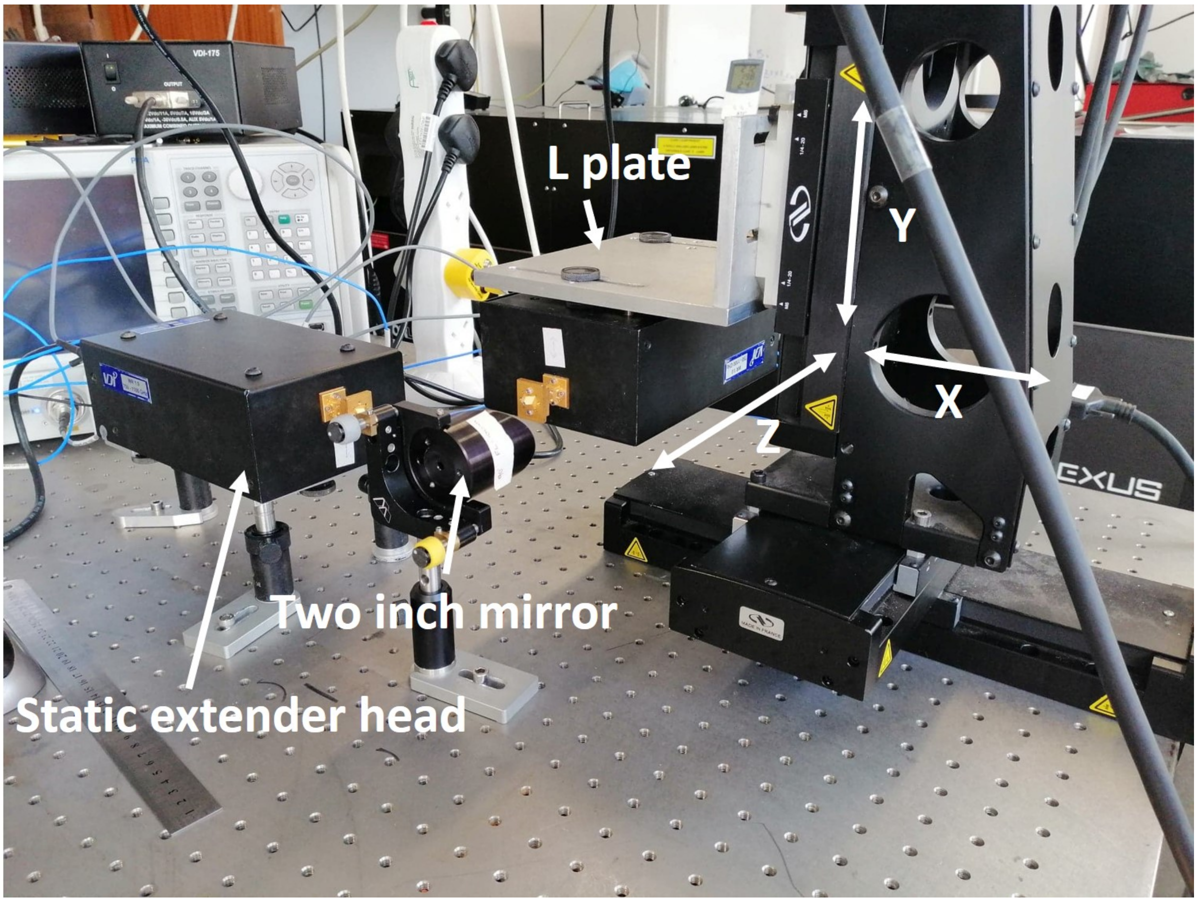

Figure 3.13: Image showing a simple experimental setup using the XYZ stage which is mapping the response from a two inch parabolic mirror. The static extender head is used as a transmitter and the other extender head (receiver) is swept across X, Y and Z directions mapping the beam profile.

3.8 Beam Characterisation

Figure 3.14 shows intersections of the terahertz beam as it travels through free space from the horn antenna. This is measured using the XYZ stage which moves one of the extender heads stepping through an array of points in three orthogonal directions whilst measuring the received power at each point. One extender head is placed stationary on the optical table, while the other is swept through 0.1 mm steps over a 10 mm by 10 mm XY plane dissecting the beam. The plane measurements are repeated every 10 mm from the horn antenna of the stationary extender head (where both horn antennas are placed as close as possible to each other while allowing movement) to a distance of 50 mm away

(Z direction). This figure shows that the beam is small upon exit of the horn antenna and diverges at larger distances from the antenna. It shows a higher power in the centre of the beam as compared to the edges for each of the measured distances. The full width half max (FWHM) of the beam at each of these distances from the horn antenna is as shown in table 3.1. Some astigmatism is shown as the FWHM values for X and Y are slightly different.

Distance from antenna (mm)	FWHM X (mm)	FWHM Y (mm)
0	1.3	1.4
10	2.9	2.9
20	5.0	4.8
30	7.0	6.7
40	9.5	8.8
50	10.1	9.7

Table 3.1: Table of FWHM values for the horn antenna at different distances from the antenna in both X and Y directions.

As most setups include the use of a parabolic mirror the beams formed by each of the mirrors commonly used at Durham are shown in figures 3.15, 3.16 and 3.17. These correspond to $\frac{1}{2}$, 1 and 2 inch mirrors which have $\frac{1}{4}$, $\frac{1}{2}$ and 1 inch focal lengths respectively. Figure 3.18 shows the beam as it travels through Z space (horizontally away from the mirror while Z is 0 mm away from the mirror the receiving horn antenna is placed as close to the mirror as possible without restricting movement so just past the farthest point of the parabolic mirror) from a $\frac{1}{2}$ inch mirror. This figure as compared with figure 3.14 clearly shows that through the Z space there is a lack of (or significantly reduced) divergence of the beam as it travels through free space. The beam is now considered to be travelling in ‘parallel’. The FWHM for the $\frac{1}{2}$ inch parabolic mirror at different distances in the X and Y directions are shown in table 3.2. These show reasonable consistency at different distances from the mirror but a slight astigmatism as shown by the difference in FWHM for X and Y directions. The FWHM values at 0 and 50 mm in X and Y for the 1 inch mirror are 6.5 mm and 5.75 mm and 6.25 mm and 5.25 mm respectively. For the 2 inch mirror, they are 47 mm and 51 mm and 51 mm and 48 mm respectively.

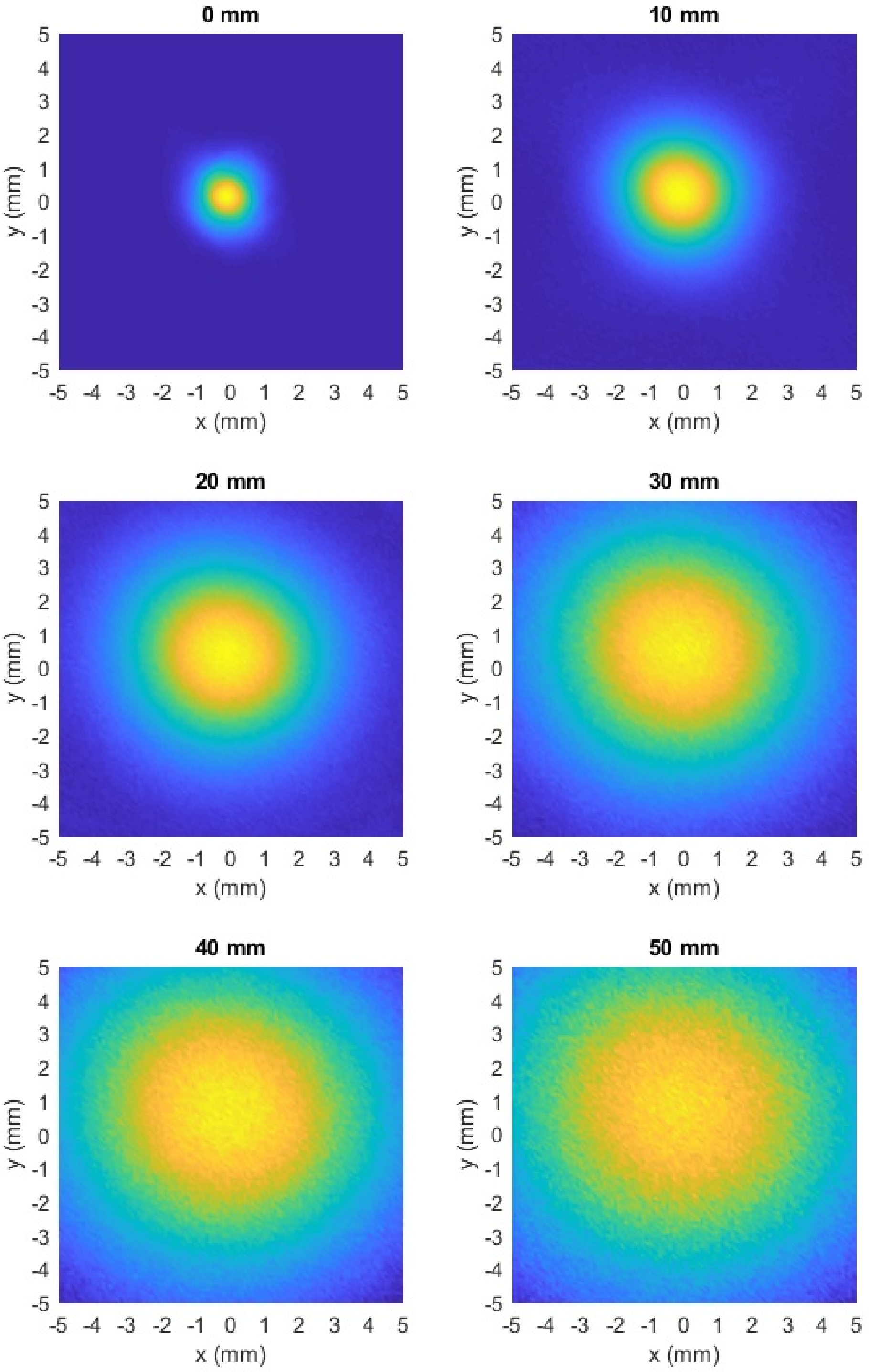

Figure 3.14: XYZ scans showing the divergence of a terahertz beam using a horn antenna. X and Y measurements taken every 0.1 mm over a 10 mm by 10 mm plane. XY plane measurements have been taken with varying (z) distance from the horn antenna every 10 mm from the horn antenna to 50 mm away through the beam.

Distance from antenna (mm)	FWHM X (mm)	FWHM Y (mm)
0	6.1	4.0
10	6.1	3.8
20	6.2	3.8
30	6.3	3.7
40	6.3	3.7

Table 3.2: Table of FWHM values for the half inch mirror at different distances from the antenna in both X and Y directions.

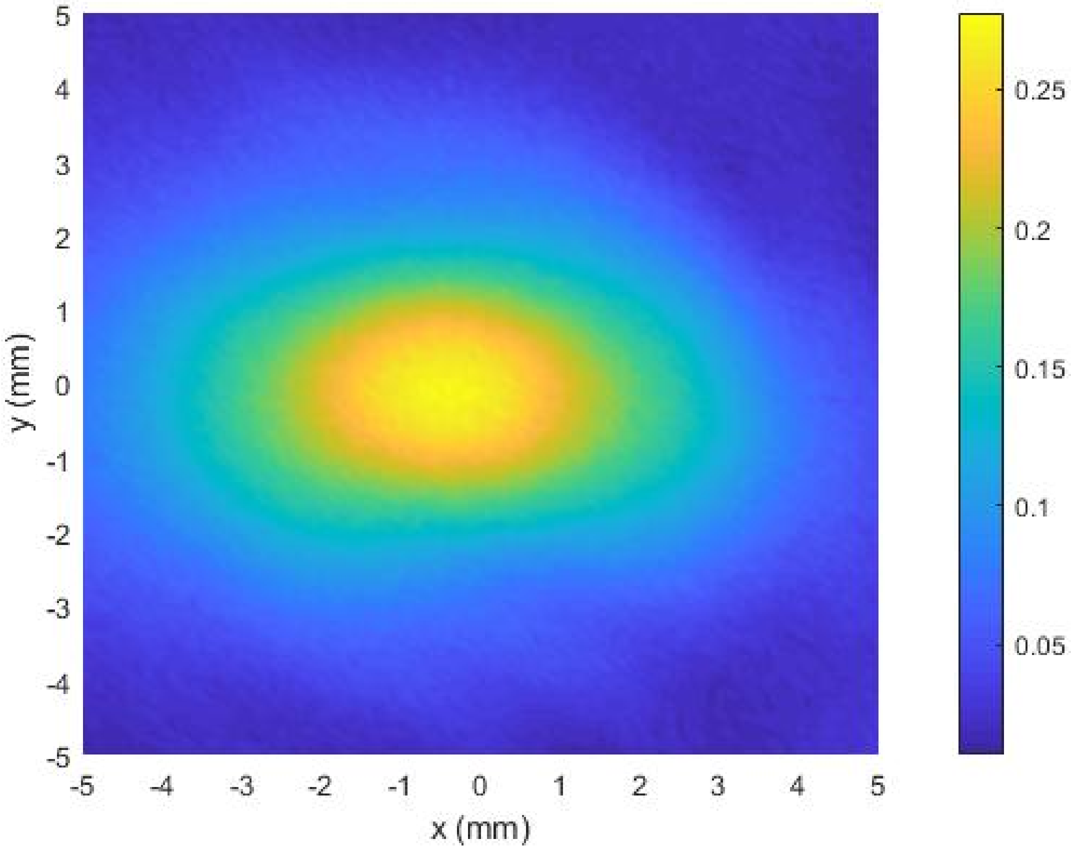

Figure 3.15: Figure showing and XY scan of the collimated beam formed by a $\frac{1}{2}$ inch parabolic mirror with measurements taken every 0.1 mm over a range of 10 mm in each X and Y.

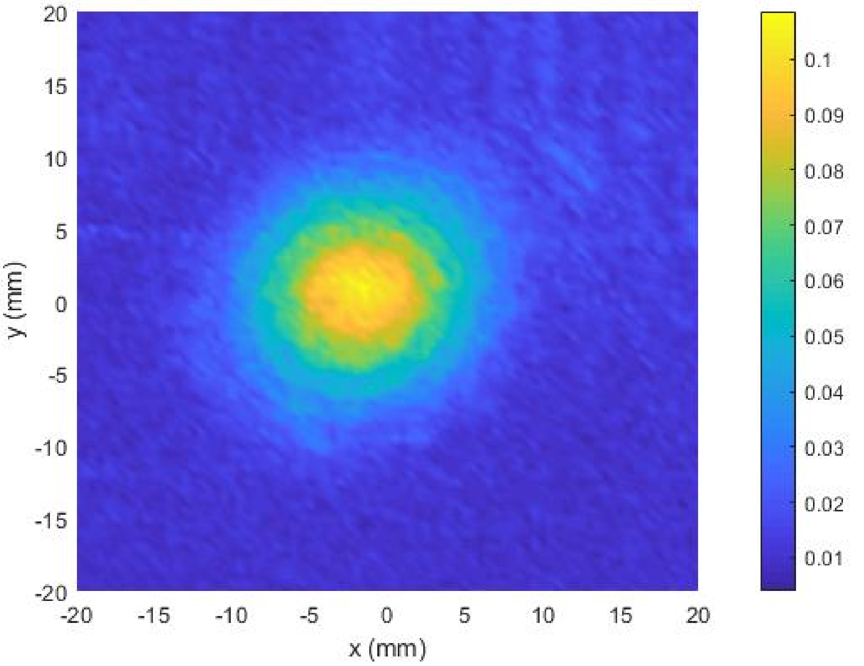

Figure 3.16: XY scan of beam formed by a 1 inch parabolic mirror with measurements every 0.5 mm for a range of 40 mm in each X and Y.

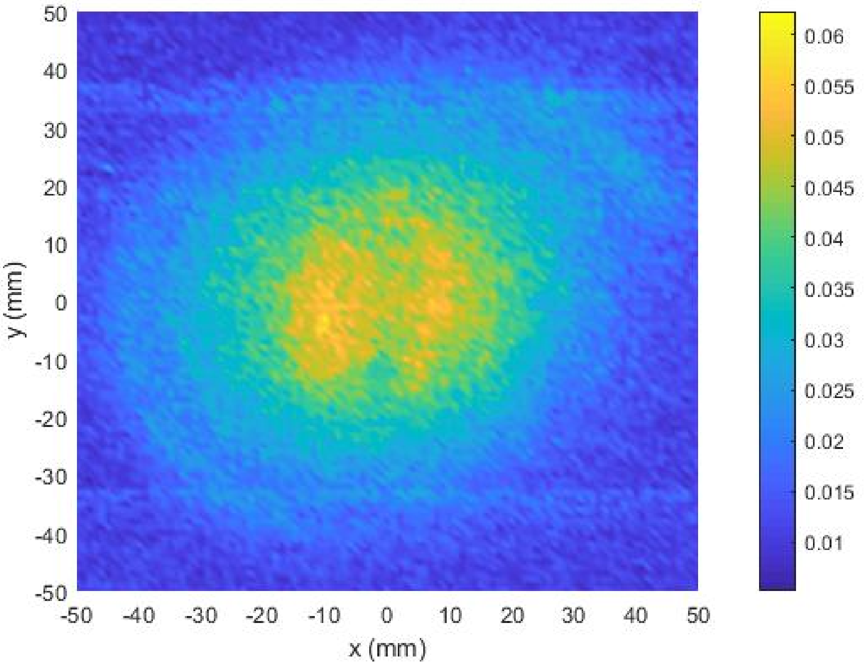

Figure 3.17: XY scan of beam formed by a 2 inch parabolic mirror with measurements every 1 mm over a range of 100 mm in each X and Y.

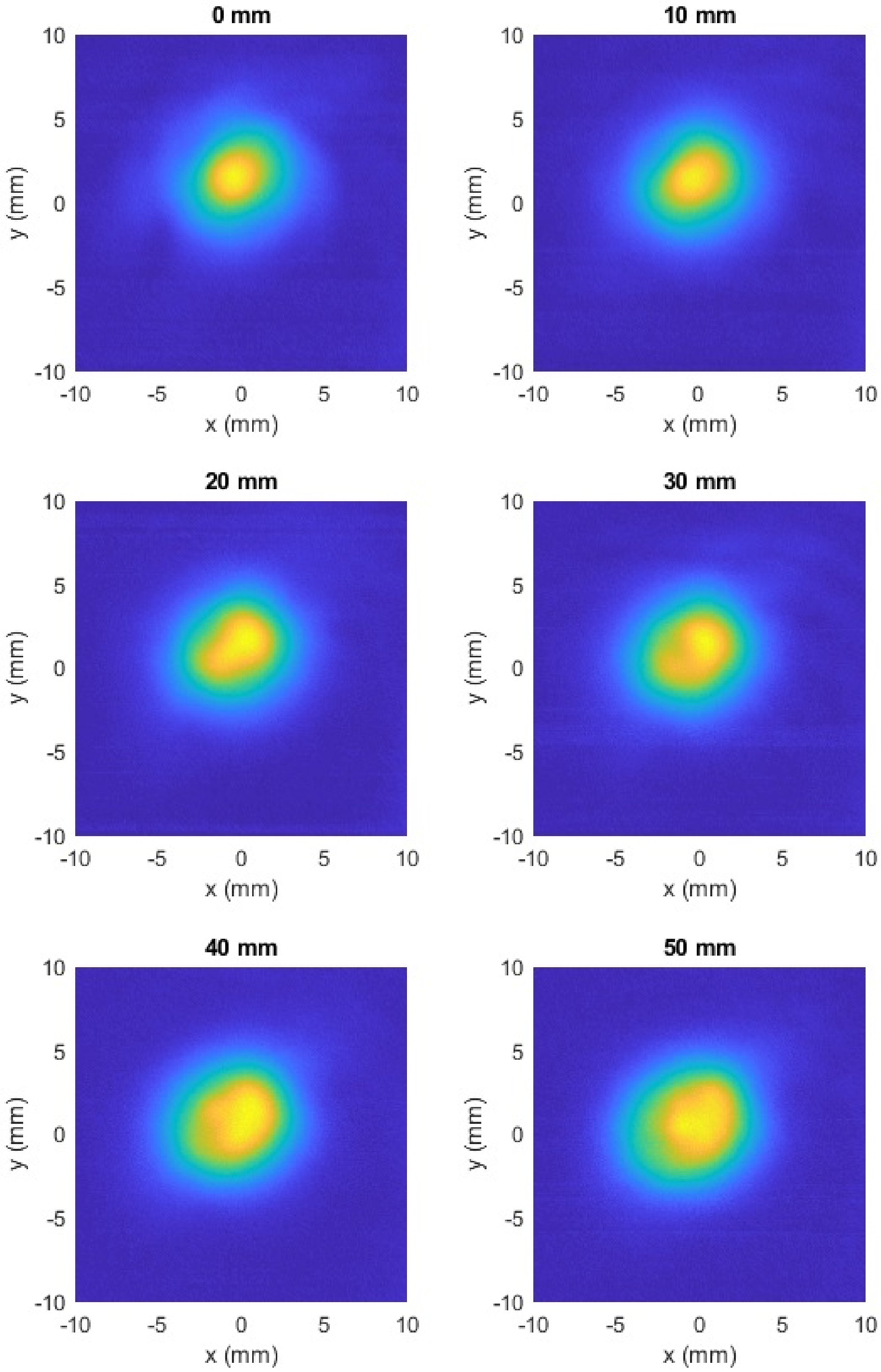

Figure 3.18: Terahertz beam following a $\frac{1}{2}$ inch parabolic mirror. X and Y measurements taken every 0.1 mm over a 20 mm by 20 mm area. XY plane measurements are taken with varying distances from the mirror (Z) at 10 mm steps from 0 mm to 50 mm.

Figures 3.16 and 3.19 show a $\frac{1}{2}$ inch mirror with and without an iris clipping the beam respectively. The contrast of the two figures shows that the beam width is reduced significantly by the iris. A further image, figure 3.20, demonstrates how the beam diverges over a distance of 50 mm further away from the iris and the mirror than in figure 3.19. The measurement taken close to the iris has a FWHM of 4.6 mm and 4.9 mm in X and Y while the measurement taken 50 mm away from the iris has a FWHM of 5.2 mm and 4.8 mm in X and Y respectively. This shows little to no astigmatism and only a slight divergence. The beam has increased in area and its peak power is reduced. This increase in spread and reduction of peak power is why it is important, even when directing a beam which is considered to be 'parallel', to reduce the beam path as much as possible. As parallel beams are rarely perfect and travelling through air reduces power, so distances between components should be kept to a minimum.

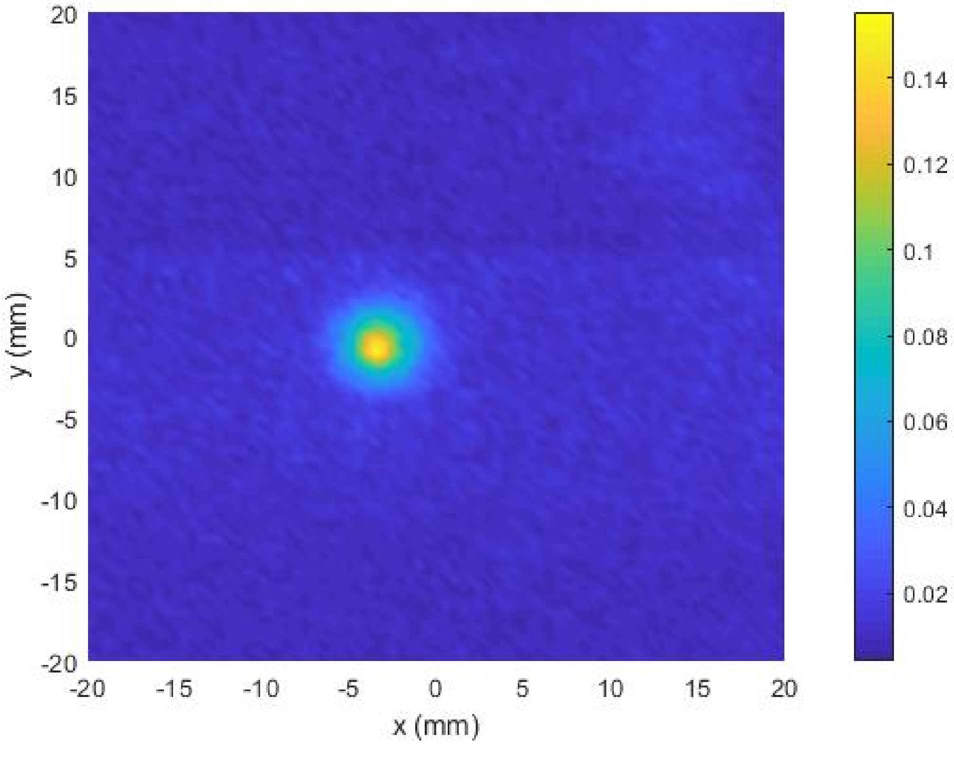

Figure 3.19: XY scan of the beam formed by a 1 inch parabolic mirror with an iris clipping the beam measurements taken every 0.5 mm over a range of 40 mm in both X and Y. The plane is taken at the exit of the iris.

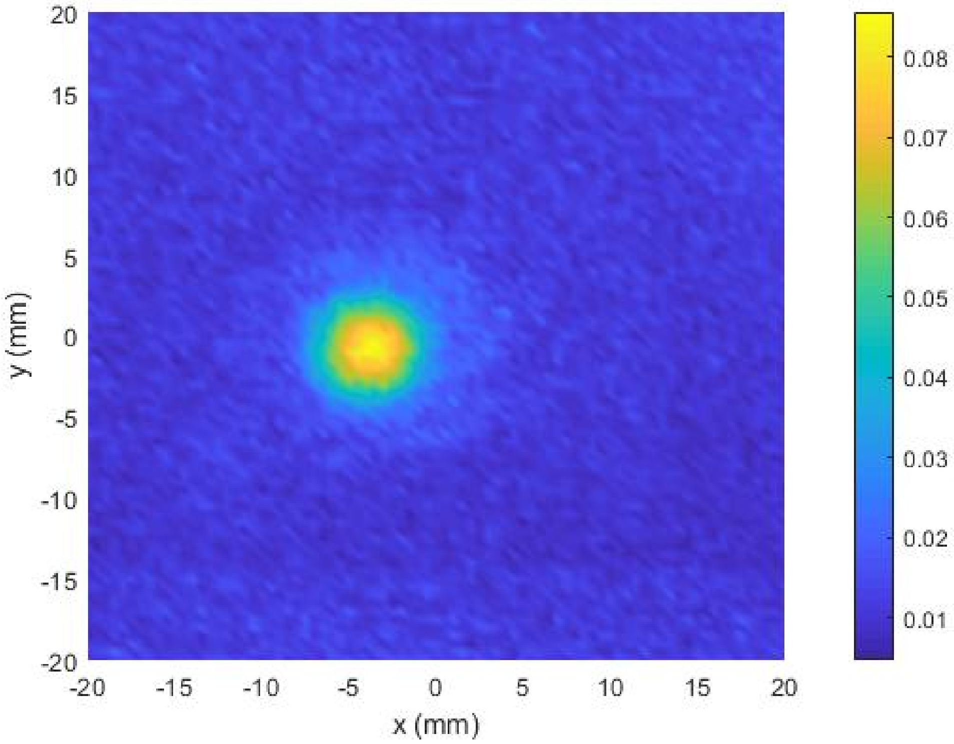

Figure 3.20: XY scan of the beam formed by a 1 inch parabolic mirror with an iris clipping the beam with measurements taken every 0.5 mm over a range of 40 mm in both X and Y. The plane is taken 50 mm away from the iris in Z.

3.9 Nail Varnish Test Case

So far, various plastic substrates have been explored, each of which are considered ‘thick’ for terahertz radiation (as the wavelength is 0.3 mm). In this section, a test case for the measurement of a ‘thin’ dielectric material, which is defined as thinner than the wavelength of incident radiation is considered. Thinner samples can be more difficult to measure, due to both the electromagnetic response and physical limitations. To consider the spectral response of a thin sample a structure to hold the thin film is required. A common household substance considered ‘thin’ at terahertz is nail varnish. The thickness of a single nail varnish layer is in the region of 5-30 µm dependent upon formulation. Painting nail varnish onto a surface and peeling it off to place in the beam is an option, but as a single layer of nail varnish is very thin it is likely to break or snap in the removal from the surface or whilst affixing it within the beam path. It is simpler to measure the effects of nail varnish directly on a surface and to normalise the effects of the additional material thus isolating the effects of the nail varnish.

Nail varnish primarily consists of a plastic (nitrocellulose) in a solvent solution with other ingredients which dictate the aesthetic look or performance of the nail varnish. Pigments are used to give the colour, additives generically referred to as 'pearls' add glitter, shimmer or other effects while resins can increase the flexibility and longevity of the lacquer.

A transmission setup using two $\frac{1}{2}$ inch mirrors and a HDPE disc to hold the sample is shown in figure 3.21. Normalisation is used to remove the effects of the HDPE disc. $\frac{1}{2}$ inch mirrors have been chosen because the nail varnish is painted on to the 2 inch HDPE disc using the standard applicator which is designed to quickly paint a nail within a couple of strokes. As the average nail length is 12.8 mm and width is 12.3 mm [76], a half inch mirror (12.7 mm) is appropriate. A larger mirror is not chosen as it would take much longer to paint the area causing uneven drying. This could also result in an uneven thickness as the self-levelling feature of nail varnish is only effective whilst wet. HDPE is suitable as it is transparent in the VNA range (see figure 3.3) therefore minimises loss of dynamic range through normalisation.

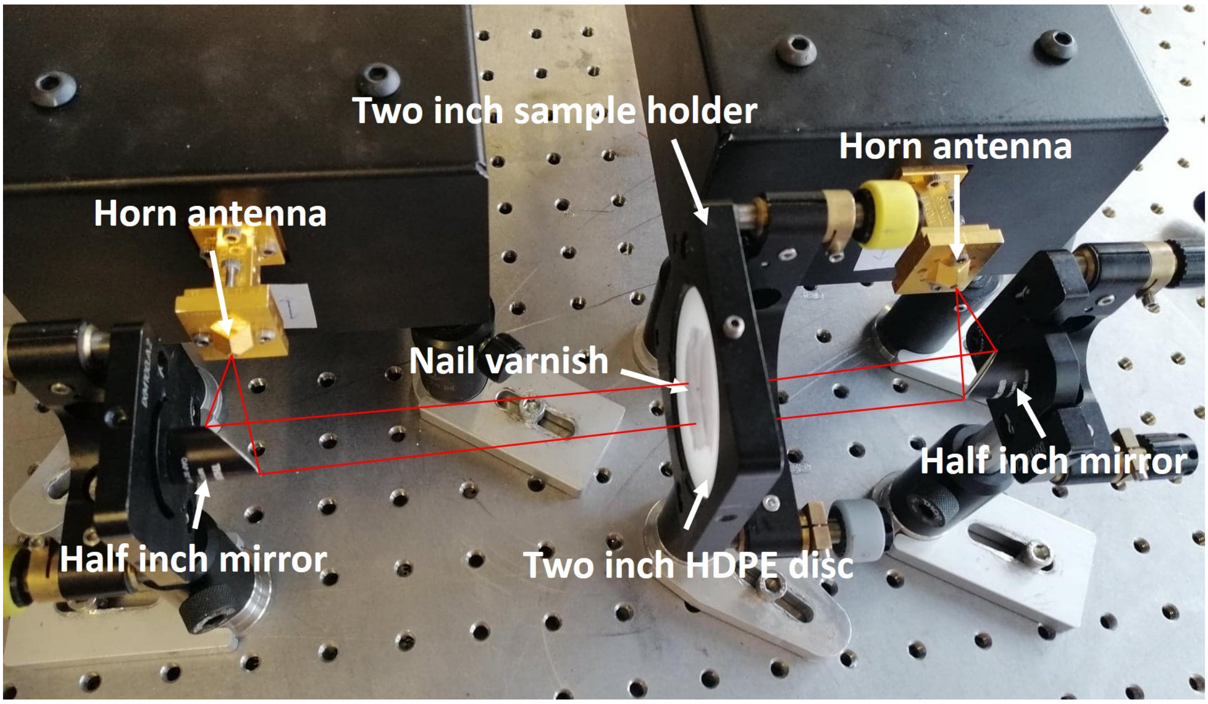

Figure 3.21: Photo of experimental setup used to measure nail varnish drying in a transmission setup.

Figure 3.22 and figure 3.23 shows the raw and smoothed transmission measurement data for three different Maybelline nail varnishes. The two figures demonstrate how the use of smoothing can make data inspection clearer without losing the features of the data. Both figures demonstrate that each of the tested nail varnishes are featureless with a periodic response across the VNA range. It is thought that this periodic response is due to Fabry Pérot reflections in the nail varnish layer which would explain why the response is sometimes above 0 dB given the overall low absorption of the samples. The outer edges of the image have been removed as these are known to have an increased level of noise within the system. The absorption due to the nail varnish is consistently less than 1 dB. It can be noted that the clear version of the nail varnish (Crystal Clear) has a lower absorption whereas the coloured nail varnishes (Mauve On and Carbon Grey) exhibit more absorption with Carbon Grey showing the most absorption. Mauve On has a creme finish whereas Carbon Grey contains shimmering particles, these could be the cause of the increased absorption.

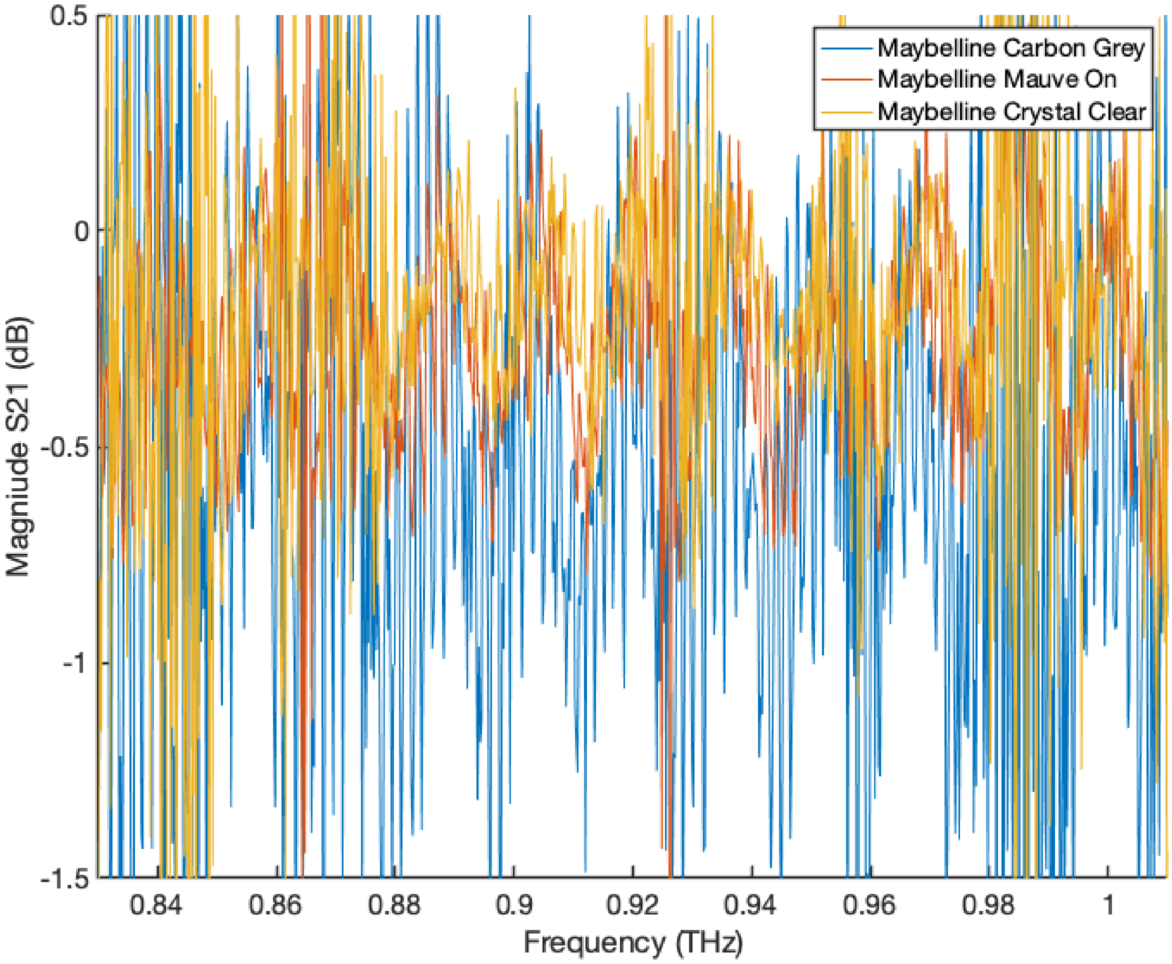

Figure 3.22: Figure of spectra through a single layer of nail varnish measured on a HDPE disc which has been removed from the data via normalisation. No smoothing has been applied to a 1601 point scan.

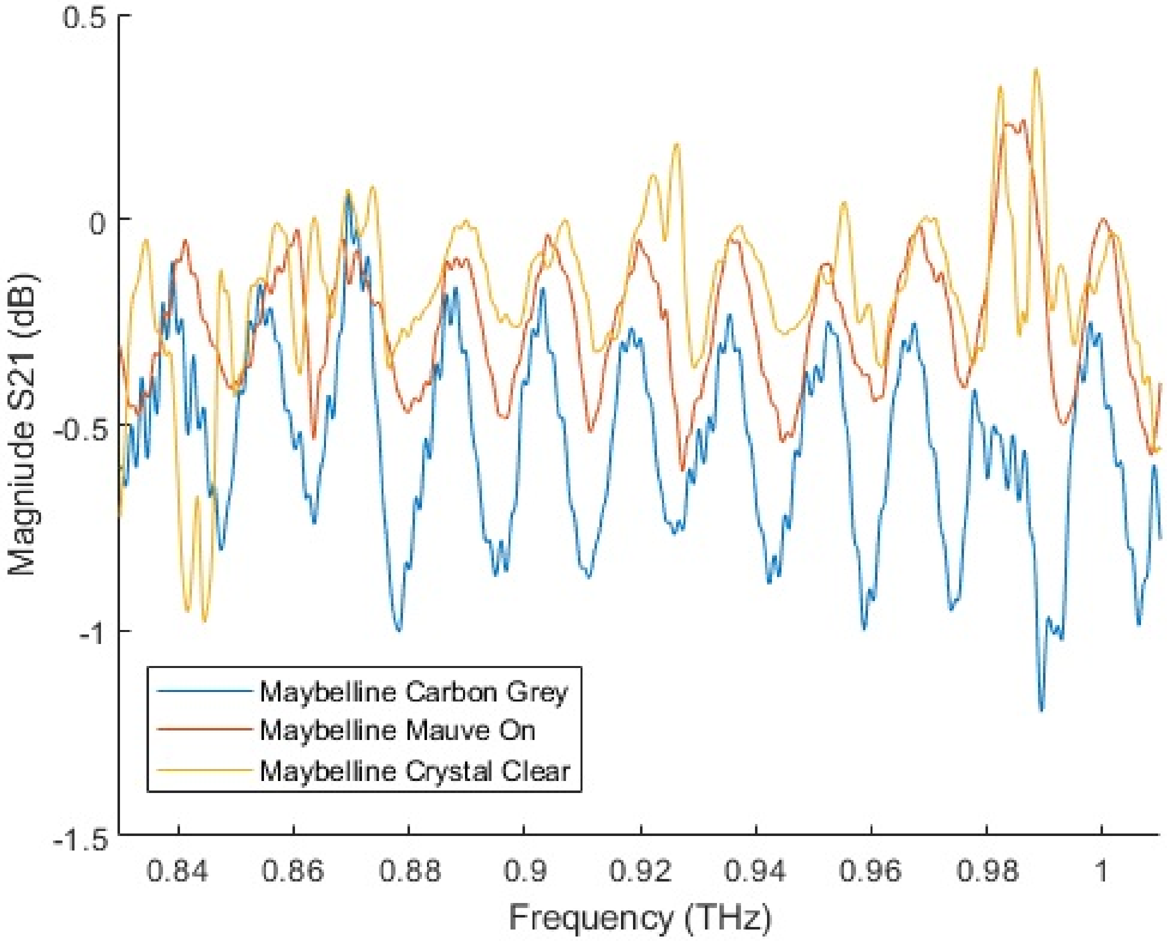

Figure 3.23: Figure of spectra through a single layer of nail varnish measured on a HDPE disc which has been removed from the data via normalisation. 20 point smoothing has been applied to 1601 point scan.

Besides colour and finish, there are a number of properties which a consumer is concerned about regarding the aesthetic appearance and physical performance of the nail varnish. An example of this is nail varnish chipping; this is not aesthetically pleasing as it looks messy and damaged, it also reduces the structural benefits of the nail varnish. As nail varnish can be used to protect the natural nail, chipping would nullify this purpose. Hence, the importance of the resin component, which increases flexibility preventing the nail varnish from being brittle and reducing the likelihood of it breaking. The thickness of a layer can also effect the longevity and wear of a nail varnish.

Another key concern of the consumer with respect to nail varnish performance is the speed at which a nail varnish dries. Not only does this affect the speed of application time but it also increases the period of time where the lacquer can be smudged. The longer a nail varnish remains wet, the more likely the user is to smudge it. Similar to chipping, smudging negates the positive aesthetic properties of the product. Therefore, it is beneficial for a nail varnish to dry as quickly as possible to leave the user with a perfect finish.

To apply the nail varnish the aesthetic components, nitrocellulose and solvents are painted on the nail. The solvents evaporate leaving a mainly nitrocellulose film on the nail. Various methods are currently used to test the speed with which a nail varnish dries. However, most current methods are based on touch. This is for measuring softness, as a probe enters the lacquer, or adhesion as a probe is removed from the lacquer. In either case, there are issues with this touch based method as the outer surface of the varnish dries faster than the main body so the nail varnish appears drier than it is. The concern is that the nail varnish can appear dry to touch but it is still soft underneath which subsequently risks the nail varnish being smudged. This is because when a higher pressure is applied, the thin dry outer layer is cracked and the soft still wet under layer is disturbed. This problem is more prevalent with the application of multiple layers.

The time in which a nail varnish dries is dependent on the chosen solvents and their composition within the nail varnish mixture. Most nail varnish solvents are polar such as ethyl acetate and isopropyl alcohol. Polar solvents generally have a strong absorbance within the terahertz region [77] whereas the absorbance due to the nitrocellulose in the varnish (a plastic) is low (see figure 3.23). During the nail varnish drying process, the solvent concentration reduces and the radiation absorbed by the film is reduced as a nitrocellulose rich structure remains. With the use of terahertz radiation, the loss of solvents over time can be measured and drying parameters can be extracted.

Figure 3.24 shows measurements of the S21 transmission through various nail varnishes as they dry. The figure shows that the transmission is initially low. The nail varnish is freshly applied at the start of the measurements so it has the highest concentration of solvents thus the lowest transmission. Over time the transmission through the nail varnish increases as the solvents evaporate leaving mainly the low absorbance nitrocellulose.

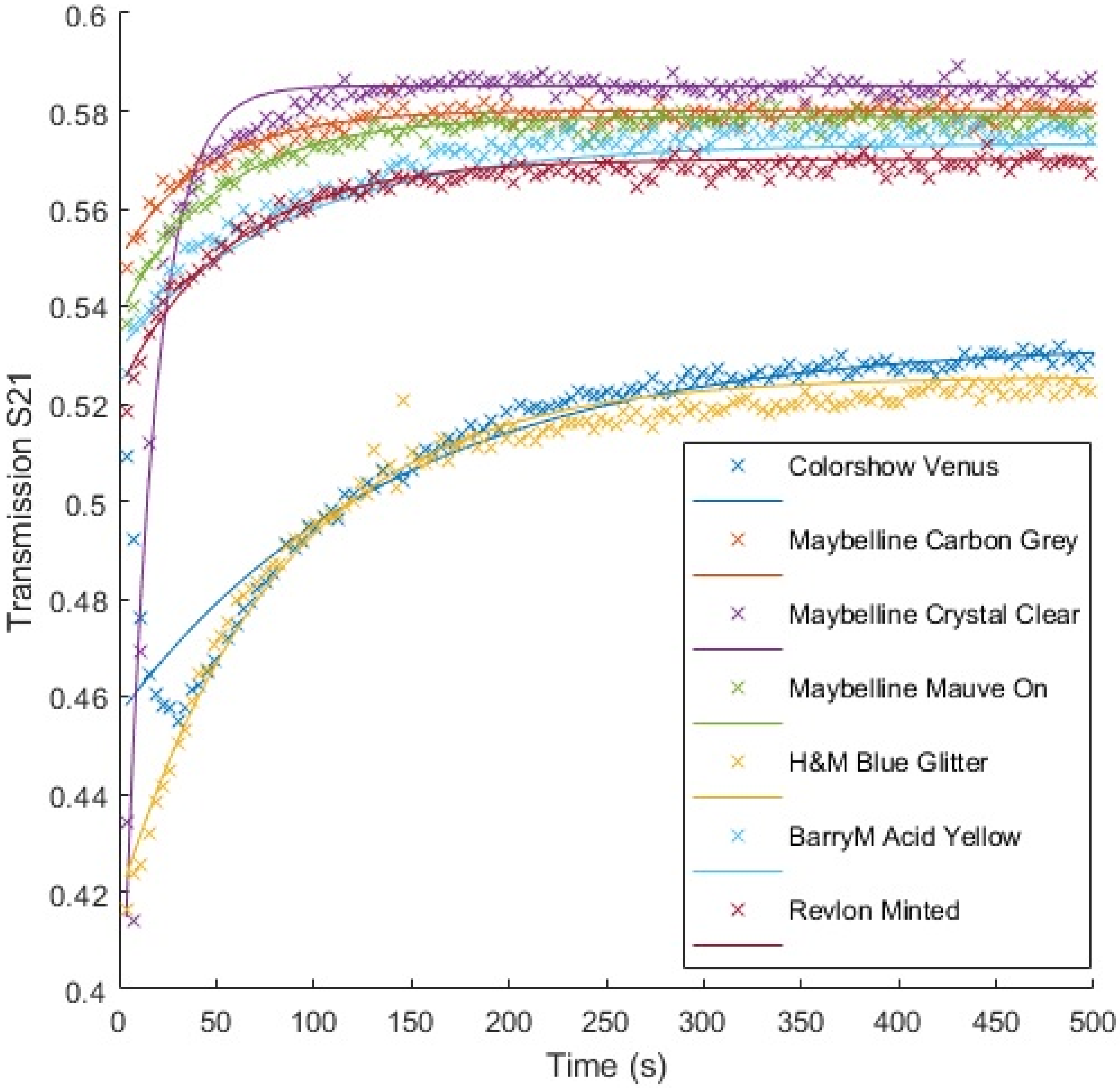

Figure 3.24: Graph showing the raw data and fitted models for each of the nail varnishes normalised through the HDPE disc measured at 1 THz. Data given in transmission raw data not dB to exaggerate the curves as they are the focus of this data set.

The relationship between the transmission through the substrate over time for this system is an exponential transient as in equation 3.9.3. The noise within this system is mainly white noise, as can be seen with the comparison between the raw data and the model, it appears to be random and has a neutral average. The noise is particularly high in this case as lots of measurements need to be taken in a short period of time so the IFBW is high and no repeats to average can be taken.

$$a - be^{-ct} \tag{3.9.3}$$

Where a is a constant which correlates to the S21 transmission through the nail varnish at the measurement end time which would correspond to the received power of the HDPE disc and the completely dry nail varnish layer. b is a constant denoting the magnitude of absorbance caused by the solvents and c is a constant describing the rate of the nail varnish drying. The time is noted by t.

The constants a, b and c are found by fitting to the measured data using a least squares fit. This can be seen for the exemplar data set in figure 3.24.

This technique has been used on a selection of nail varnishes demonstrating the difference between nail varnish compositions. Different nail varnish brands have been tested along with nail varnishes from the same brand with varying colours and finishes. Figure 3.24 shows the fitted models for each of the nail varnishes. Table 3.3 shows the extracted time constants for each sample.

Sample Name	Time Constant (s^{-1})
Colourshow Venus	37.55
Maybelline Carbon Grey	11.93
Maybelline Mauve On	13.64
Maybelline Crystal Clear	4.11
H&M Blue Glitter	22.24
BarryM Acid Yellow	23.08
Revlon Minted	15.52

Table 3.3: Table of time constants for the measured nail varnishes calculated by fitting the results to the exponential transient equation (3.9.3).

To investigate nail varnish further, an angular measurement arrangement is used. As the angular setup works in reflection an aluminium plate is used to hold the sample as it will reflect the beam better than a HDPE disc. A HDPE disc would not be suitable here as it is a poor reflector (see figure 3.5). In this previous figure normalisation was difficult due to the reflection setup, here although measurements are still being taken in reflection the angular measurement system uses both extender heads so normalisation can be carried out as in a standard transmission measurement (see figure 3.3). The figure also shows that an aluminium plate that is thicker than the skin depth (≈ 80 nm) has a better reflection performance. The nail varnish sample is applied to the aluminium plate and allowed to dry. Once dry, angular scans are taken. The theory is that with the use of angular scans the path length travelled through the thin dielectric material is greater and therefore more detailed material properties can be extracted from these measurements. The angular movement also enables small controllable changes in path length. Figure 3.25 shows how the angular setup can control the path length of the beam through a thin dielectric. This produces a set of measurement data across a range of thicknesses with a well defined geometric distribution. Allowing for isolation of the change in response due to the thickness from the spectral response of the material. Which, as with any spectral response, will remain constant throughout the angular scans while the refractive index will affect change as a function of the path length travelled through the dielectric material.

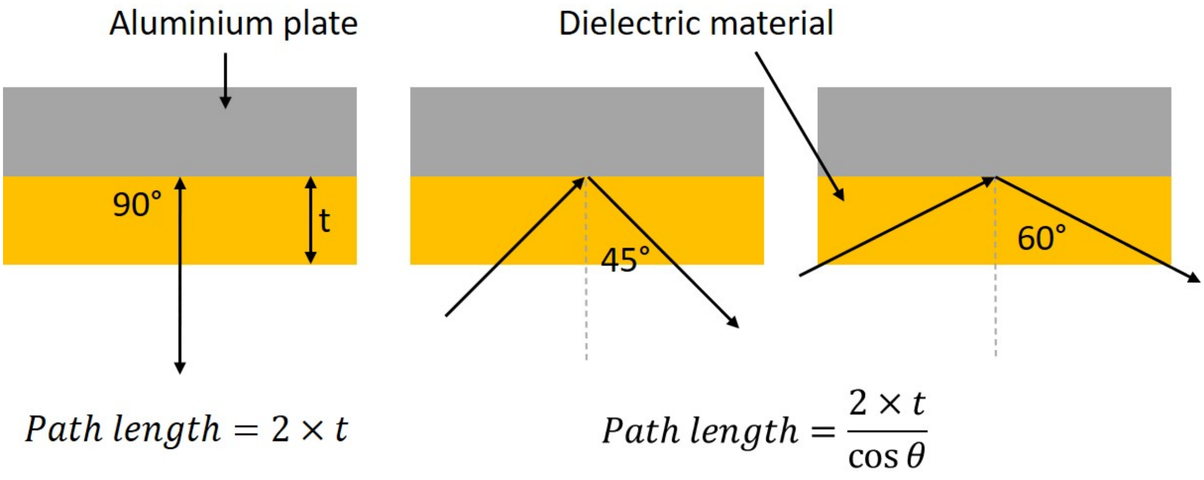

Figure 3.25: Diagram showing how the angular measurement setup can be used to increase and control the path length of the beam through a thin dielectric material.

A strong area of absorption was found for this single dielectric layer that was both frequency and angular dependent as displayed in figure 3.26.

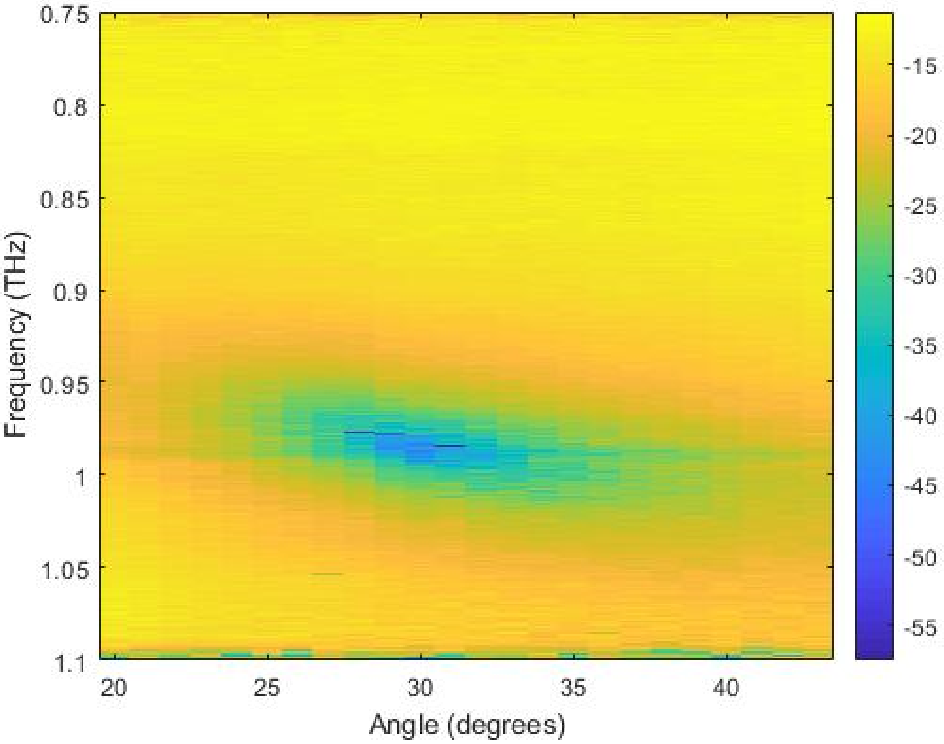

Figure 3.26: Image showing angular S21 reflection measurements with nail varnish on an aluminium plate.

This absorption peak was found to be repeatable where a slight variation in nail varnish thickness gives a different angular and frequency position. To investigate this further the experiment was repeated replacing the nail varnish with a dielectric material that has been well characterised at terahertz frequencies in literature.

Repeat tests use gold coated wafers, instead of the aluminium plate, for improved reflective properties. SU-8 photoresist [78] was used to produce varying thickness layers of the dielectric. A hard bake process ensures the stability of the SU-8 layer. Again, the sharp frequency and angular dependent feature was found (see figure 3.27) however, no consistent trend with thickness for either angle or frequency was found. Thickness was noted both theoretically and experimentally; the nominal thicknesses are calculated from the spin speed by using the SU-8 data sheet. The full set of results are shown in table 3.4.

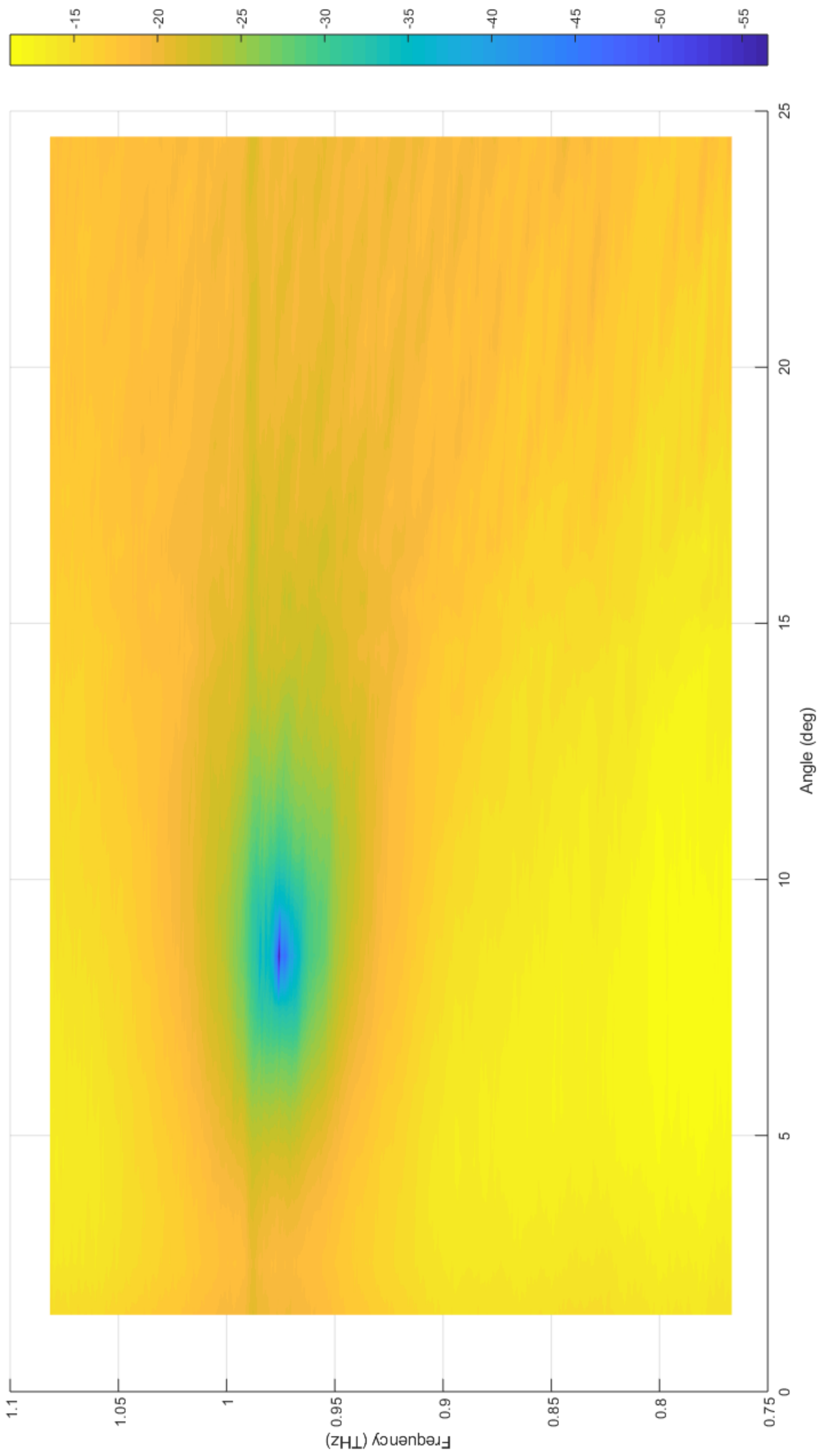

Figure 3.27: Image showing scan of S21 reflection measurements with SU-8 on a gold coated silicon wafer.

Spin speed (rpm)	Nominal thickness (µm)	Angle (degrees)	Frequency (THz)
1290	51.475	12.4	0.7570
1350	51.125	11.8	0.8091
1400	49.000	15.7	0.7999
1420	48.550	15.2	0.8121
1440	48.100	15.8	0.8147
1450	47.875	10.8	1.0838
1460	47.650	13.1	0.8340
1480	47.200	13.4	0.8598
1490	46.975	13.0	0.8961
1510	46.525	13.6	0.8353
1530	46.075	16.6	0.8266
1550	45.625	15.9	0.9145
1580	44.950	14.2	0.8108
1610	44.275	13.7	1.0068
1630	43.825	10.3	0.8983

Table 3.4: Table of spin speeds and corresponding feature angle and frequency positions.

Repeat measurements are taken to prove repeatability, four samples each at 1400, 1500 and 1600 rpm spin speeds. No feature was found for the SU-8 layers spun at 1400 rpm. Two features were found from each of the sets of four samples spun at 1500 and 1600 rpm as shown in figure 3.28. These features were found to be at the positions as described in table 3.5. Although the strong absorption peak was repeatable, there were occasions it was not present, it was assumed due to the narrow region of the VNA these were not in range.

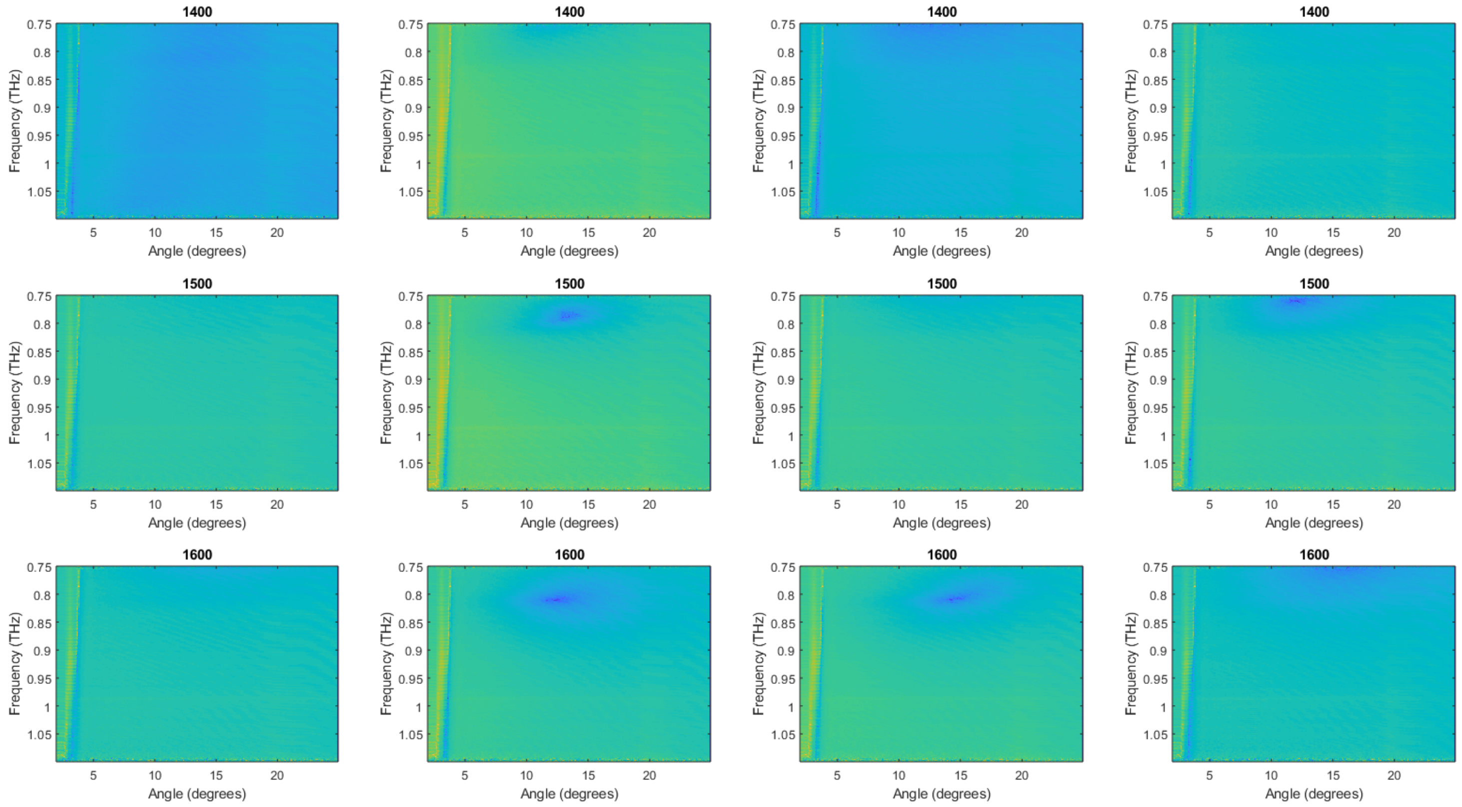

Figure 3.28: Figure of repeat experiments for SU-8 layers spun on gold coated silicon wafers at 1400, 1500 and 1600 rpm and their corresponding feature positions or lack thereof.

Spin speed	Repeat Number	Angle (degrees)	Frequency (THz)
1500	2	13.4	0.7819
	4	12.2	0.7588
1600	2	12.6	0.8108
	3	14.7	0.8073

Table 3.5: Table of spin speeds with repeat experiments and their corresponding feature positions.

Figure 3.29 shows the angular response of an SU-8 layer spun at 1630 rpm. The figure shows a strong absorption peak at a 10° incident angle and 0.9 THz. Figure 3.30, shows the same scan but one of the arms of the angular measurement system is held at the angle where the feature was found (10°) while the other arm is swept as normal. This scan shows that the absorption peak is spread across frequencies and angles. The feature appears to be present between 0.85 THz to 0.92 THz for angles of 8° to 12°. This shows that the feature appears at different frequencies for slight variations in angle and consequently path length, hence the method is extremely sensitive to thickness.

An additional test identical to the previous but spun at 1580 rpm is shown. Figure 3.31 and 3.32 show the two arm and one arm responses respectively. It is possible that the path of the feature not taking a straight line and curving back on itself is due to a defect in the material further backing the idea that these measurements are extremely sensitive to dielectric thickness.

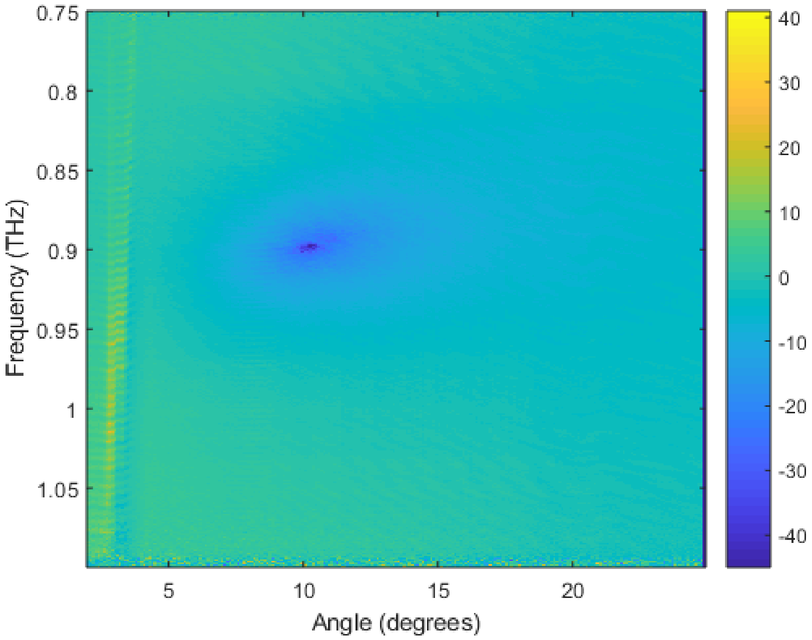

Figure 3.29: Figure of SU-8 spun on a gold coated silicon wafer at 1630 rpm showing frequency and angular dependent absorption response.

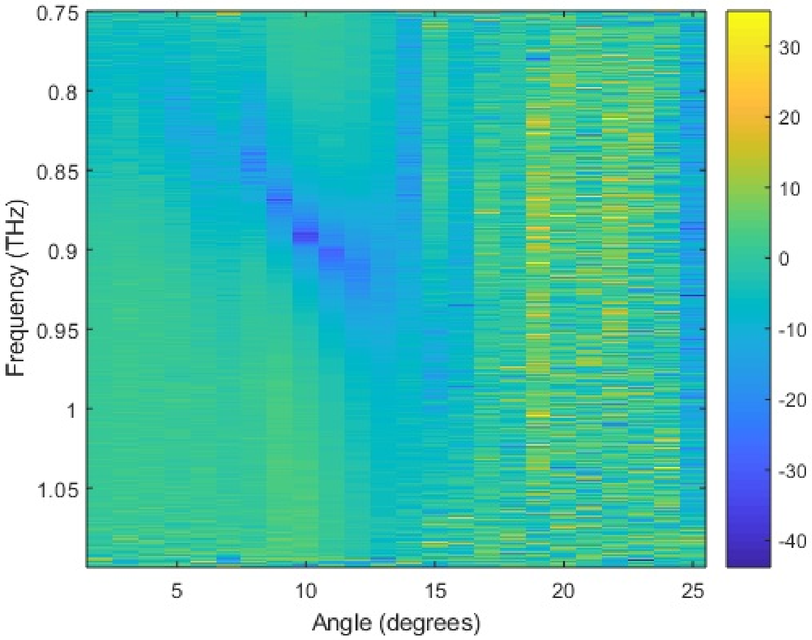

Figure 3.30: Figure of SU-8 spun on a gold coated silicon wafer at 1630 rpm showing frequency and angular dependent absorption response with one arms from the angular measurement system moving and the other stationary at the angle of the absorption (10°).

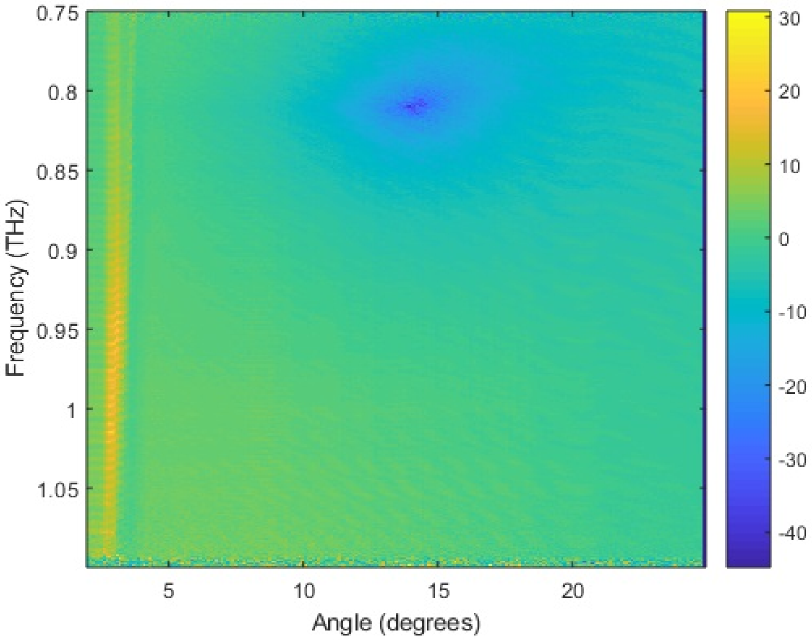

Figure 3.31: Figure of SU-8 spun on a gold coated silicon wafer at 1580 rpm showing frequency and angular dependent absorption response.

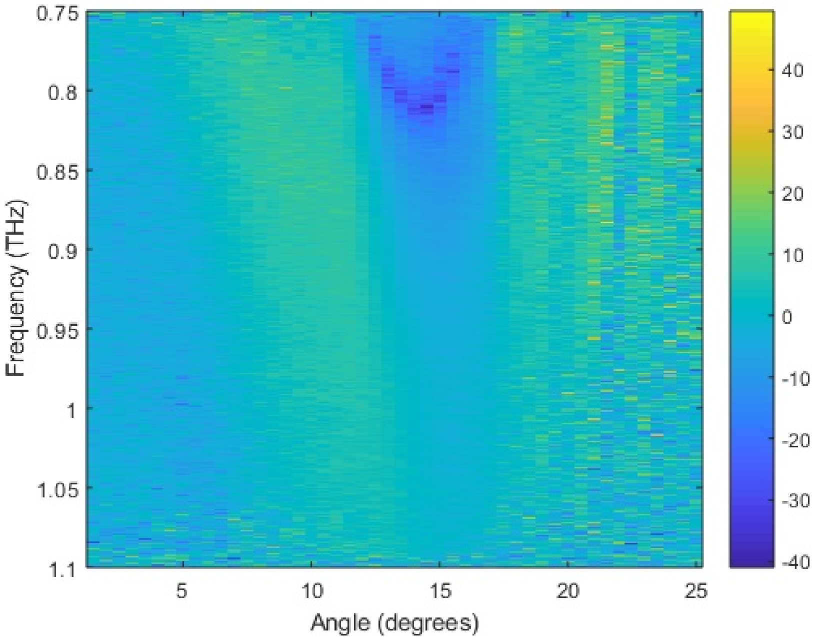

Figure 3.32: Figure of SU-8 spun on a gold coated silicon wafer at 1580 rpm showing frequency and angular dependent absorption response. One arm is kept stationary at the angle of the absorption in figure 3.31).

A scan with and without SU-8 is shown in figure 3.33. Both measurements are taken with one arm sweeping and the other positioned stationary at the edge of the sample. A significant increase in radiation is found at the edge of the sample with SU-8 as compared to the metal only sample, indicating radiation is travelling through the SU-8 layer as it exits at the edge. It is inferred that the absorption is caused by trapping of radiation within the SU-8 layer. The previous measurements show the peak is sensitive to both frequency and angle. Once inside the SU-8, the radiation appears to become reduced in power and broad across frequency and angle. This could be due to scattering either within the SU-8 layer of off the edge of the substrate.

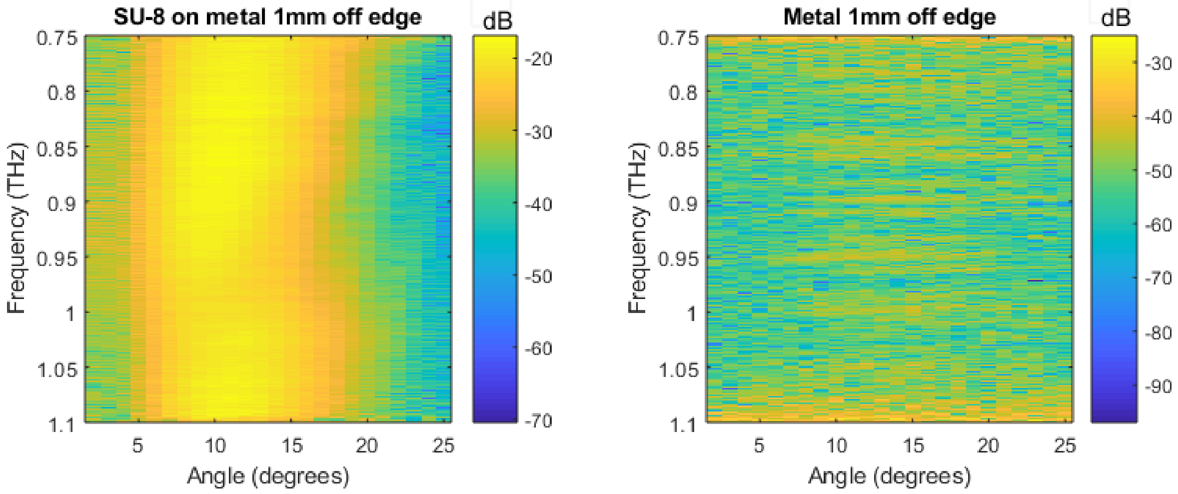

Figure 3.33: Figure showing comparison between aluminium and SU-8 coated aluminium of off edge measurements indicating that the radiation which did not reach the receiver in previous experiments has travelled through the dielectric and not been reflected away or scattered. Scans taken from one arm moving in the angular arrangement with the second extender head stationary 1 mm from the edge of the sample.

3.10 Conclusion

This chapter has highlighted the requirement for characterisation of materials at terahertz frequencies. Some experimental setups have been described using the VNA along with methods of controlling both the VNA and moving stages via MATLAB.

The XYZ stage is used to characterise beams formed by horn antennas and common components including parabolic mirrors.

Finally, a test case using nail varnish is given displaying exemplar uses of a variety of experimental setups.

Chapter 4

Cuvette Refractive Index Measurements using a Vector Network Analyser

4.1 Introduction

Refractive index measurements are vital for a wide range of applications. As refractive index values change with frequency and the terahertz region is becoming a more commonly used frequency range, the need to characterise materials in this range is rising.

A standard method of measuring refractive indices of liquids involves a cuvette. A cuvette is a vessel used to contain liquids with a standardised length cavity. This path length can then be used to calculate the velocity through the liquid from a measured time delay as compared to the empty vessel. The sides of a cuvette must be flat and polished. The cuvette is ideally made with a low absorption, low refractive index material to reduce its impact on the incoming radiation. Commonly, reference scans will be taken to effectively isolate the liquid response by removing the effect of the container, mirrors and air. This only takes into account radiation that manages to reach the receiver so reflections etc. can still cause error. This is important if the cuvette is not positioned perfectly square to the beam. Also if a container has a large absorption this reduces the available dynamic range.

At terahertz frequencies, polar liquids generally exhibit high absorbance [77] while non-polar liquids tend to have a lower level of absorbance [79]. Hence, it is relatively simple to extract the properties of non-polar liquids as in [79] using a cuvette with a TDS setup. However, this is not the case for polar liquids. In the case of polar liquids alterations need to be made to overcome the strong absorption, for example reducing the path length of the cuvette to 200 µm [80] or using a variable path length from 50-100 µm [81]. Vessels other than cuvettes can be utilised; for example [82] uses standard plastic bottles to measure inflammable liquids in a reflection setup. Alternative methods are starting to emerge such as measuring the dielectric properties of mixtures of polar and non-polar materials thus reducing the absorption for a given path length [83] or taking measurements in reflection [84]. These methods can be used in applications where transmission measurements would not be possible as the absorption of the polar liquid is too high such as measuring aqueous alcohol concentration in reflection measurements through the container [85].

In this chapter the use of a VNA to measure refractive index is considered. A set of measurements have been taken to distinguish between materials with slight variations in refractive index. Alkanes are used to demonstrate this as for terahertz frequencies their refractive indices increase with chain length [32]. The issue with using a VNA in this application is that the VNA functions in the frequency domain and therefore a direct time delay cannot be measured. Refractive index can be measured using a VNA by considering the phase component of the complex scattering (S) parameters measured at the receiver. However, this leads us to an issue, as the phase data contains an unknown number of full phase rotations e.g. a 30° response could represent a true 30° phase rotation or it could mean that there is any number of full rotations with a 30° offset (30°+n×360°) hence measuring the absolute refractive index is difficult.

As TDS measurements are limited by the precision of the system itself research has expanded into alternate methods of increasing sensitivity whilst using similar standard measurement equipment as increasing the sensitivity of the TDS system is costly. For example, a microfluidic sensor using a parallel-plate waveguide resonant cavity can increase sensitivity of measurements whilst still using a commercial TDS system [86]. Another option to increase measurement sensitivity is utilising metamaterial devices from split ring resonators [87] to photonic column arrays [88].

Other sources of error affecting the repeatability of TDS cuvette measurements have been assessed in [89] where system stability, cuvette positioning, cuvette cleaning and cuvette assembly are taken into account, system stability and cuvette assembly were found to be the largest contributing factors to the lack of repeatability in these measurements. Thus the only large source of error that is not removed by switching to VNA measurements is the cuvette assembly.

In addition to TDS and VNA measurements, although not as popular in use at this moment in time, backward-wave oscillators (BWOs) can be used in similar setups (transmission and reflection) to extract material properties at low and sub terahertz frequencies [90]. BWO measurements are similar to VNA measurements in that they require only simple setups with few components however their frequency range is limited to lower than that of VNA and TDS systems alike whilst generally offering lower dynamic range. Therefore, they can only be used to measure low absorption materials or short path lengths.

To use a VNA's phase data to calculate absolute RI an alternative method with a built-in reference system is described. The system has a VNA and fast Schottky diode-based frequency converters to measure the scattering parameters of liquid samples. This system also employs the use of a cuvette, in conjunction with a simple physical system which allows for sensitive refractive index testing of liquid refractive indices. The number of optical components required is significantly smaller than that of a TDS system. As the VNA system does not require a laser, the alignment is much easier and there is minimal drift in the system due to the shorter optical path lengths.

An example application for these measurements is the petrochemical industry. The petrochemical industry has many aspects of the product to test for each intended use may that be via chemical or physical testing. Chemical testing commonly includes elemental analysers such as combustion analysers, sulphite analysers and mass spectrometers while physical testing uses equipment from viscometers, rheometers to flash point testers. To meet certain standards a petrochemical company must adhere to an organisation e.g. American Society for Testing and Materials (ASTM) or International Organisation for Standardization (ISO). Varying methods exist to test for each of these standards from chromatography to elemental miroanalysis. Ethanol and gasoline mixtures were measured using a TDS setup and a 2 mm path length cuvette [91]. More recently, novel techniques are being explored in the academic community to reduce test time, cost and number of tests required. An example of this is a capillary sensor which measures multiple parameters based on the fuel's response to partial heating in the capillary tube [92]. Recent works probing the sample to measure refractive index include a surface plasmon resonance based fiber optic sensor [93]. The main aim of this paper was to differentiate between the percentages of kerosene combined with petrol or diesel via extracting refractive index values.

4.2 Rotational Stages

Another type of stage in addition to the ones as described in chapter 3 are rotational stages. Commonly used types include a horizontal axis rotational stage and a vertical axis rotational stage.

A horizontal axis rotational stage can be extremely useful in VNA setups as it can be used in conjunction with a polariser to measure both S and P polarisations automatically. Figures 4.1 and 4.2 show setups measuring each of these polarisations.

A Thorlabs NR360S/M is used as a horizontal axis stage in conjunction with a Thorlabs BSC102 two-channel stepper motor controller. This stage can take 1.8° steps, it is not particularly accurate and sensitive, however, it allows an on-axis load capacity of up to 50 kg.

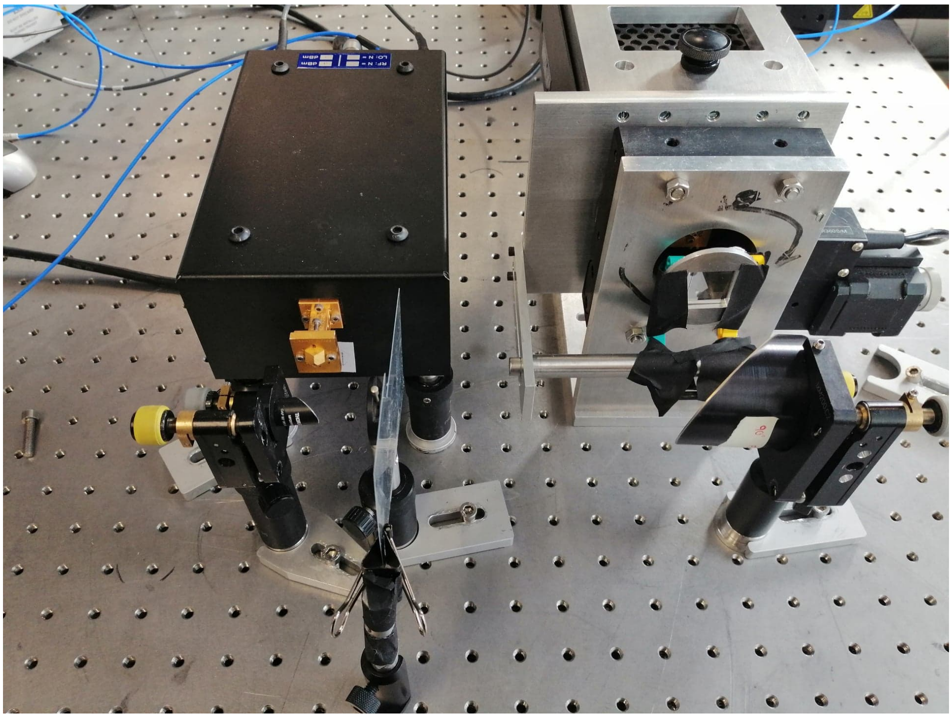

Figure 4.1: Image of a transmission setup using a horizontal axis rotational stage to measure both S and P polarisations automatically. S polarisation shown.

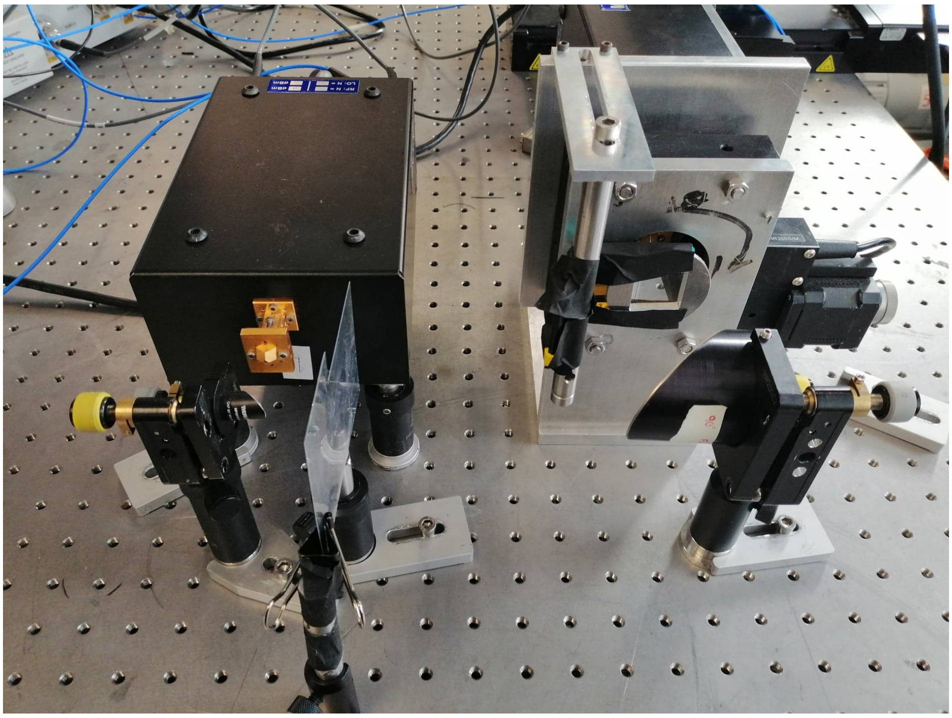

Figure 4.2: Image of a transmission setup using a horizontal axis rotational stage to measure both S and P polarisations automatically. P polarisation shown.

Figure 4.3 shows a vertical axis rotational stage. The vertical axis rotational stage can be used to rotate a sample through the beam, as in figure 4.3, or to rotate optical components though the beam. The stage is a Thorlabs CR1/M-Z7 which is controlled using a Thorlabs TDC001 controller. This stage allows for continuous circular motion, its minimum step size is 2.19 arcsec (0.0006°). A MATLAB program is used to control the device during measurements so the VNA and stage can be controlled simultaneously.

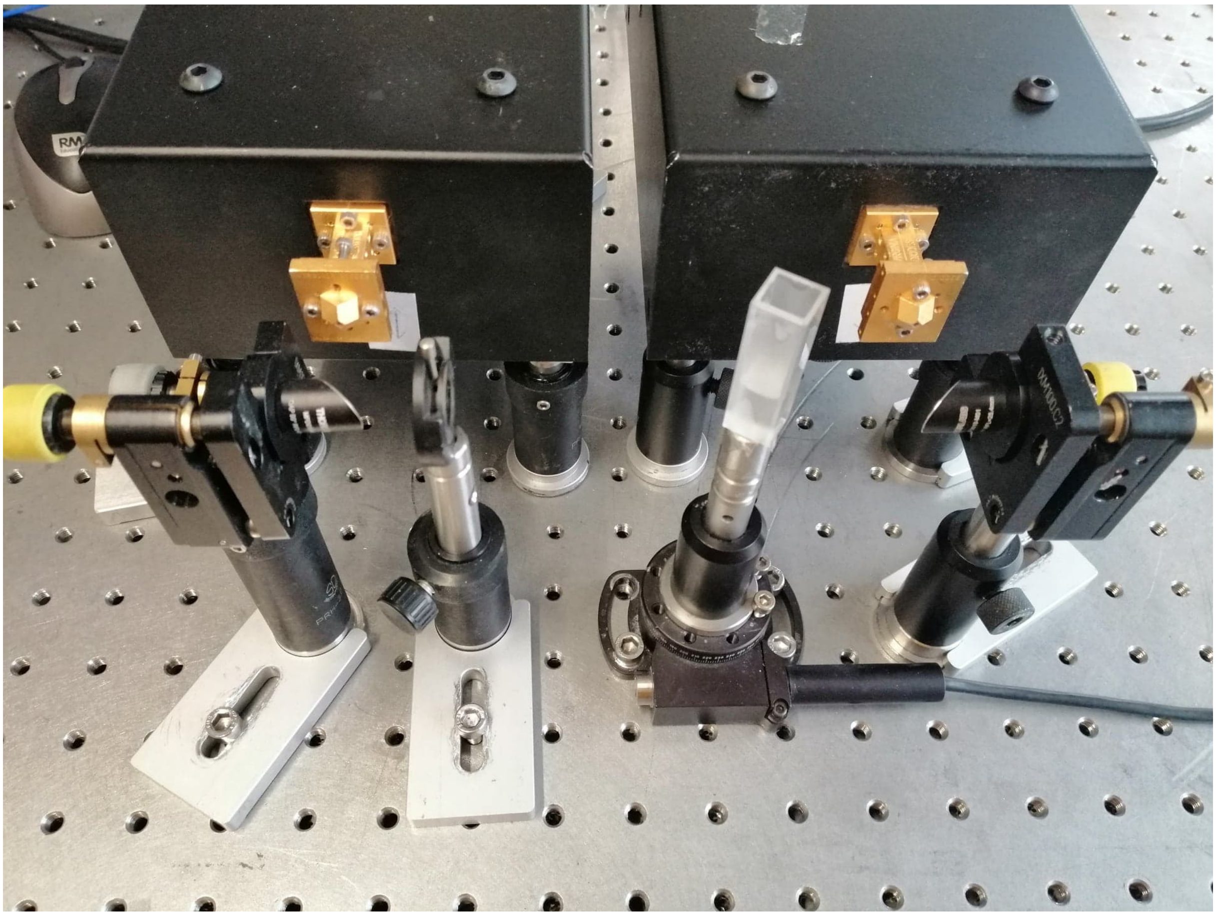

Figure 4.3: Image showing an experimental setup using a vertical axis linear stage where the sample is rotated within the beam path.

4.3 Rotational Cuvette

As the VNA measures complex scattering (S) parameters, the received phase of the electromagnetic wave is directly available from the phase of the complex number measured. The RI of a liquid through a finite path length is directly proportional to the change in phase. However, without measuring the absolute phase (an unwrapped value), it is not possible to measure the RI of a liquid through a single measurement of a cuvette. Examining smaller distances, less than one full phase rotation, the absolute RI can be calculated. One method of doing so is to use a small path length cuvette. This can problematic as this path length would need to be roughly tuned to the RI of the material under test to ensure less than a full phase rotation. An alternative is to use a finite rotation of the cuvette introducing a small change in path length. The issue with this method is that a small error in calibration to the normal can cause a large error in the path length calculation. For example, the path length difference between a cuvette at 0-1° is significantly smaller than that between 7-8°. This discrepancy would greatly affect the refractive index calculations so it is important that the normal position to the cuvette is accurately known. A series of measurements can find the normal position of the cuvette by sweeping the cuvette through a large rotation and isolating the position based on the received data. The peak phase at the receiver will be when the cuvette is at a normal to the incident beam, as this is the shortest path length through the liquid under test.

4.3.1 Experimental Setup

The setup for the rotational cuvette measurement technique is shown in figure 4.4. It a transmission measurement using $\frac{1}{2}$ inch mirrors. The sample is placed in a 10 mm path length cuvette. The cuvette used is a commercially purchased 10 mm path length cuvette made of polystyrene, a quartz cuvette has also been used the results were similar however they were marginally preferable using the polystyrene cuvette as this has a slightly lower absorbance and fewer resonances so a cleaner response. The cuvette is mounted on a vertical axis rotational stage so that the sample can be rotated through the beam. The parallel beam formed between the two parabolic mirrors is passed through an iris to reduce the beam waist so it is significantly smaller than the cuvette. The ideal setup has an infinitesimally small beam width so its response angle upon exit of the cuvette can be isolated exactly. In reality, reducing the beam width reduces the power so a compromise is made which has a 5 mm beam so that it always remains within the cuvette and does not pass through any of the side walls at any of the swept angles but maintains as much power as possible.

A Thorlabs CR1/M-Z7 rotational stage and a Thorlabs TDC001 controller are used to rotate the cuvette during measurements. The stage is controlled using a MATLAB program which automates its movement with VNA control. Hence, the program can loop through taking measurements, moving the cuvette and recording the complex S parameters.

The stage is moved to the first measurement position using an absolute move command `h.MoveAbsoluteRot(0,i,i,3,0);` where, `i` denotes the angle of the stage. Following this, before a measurement is taken, the position is checked using the command `pos = h.GetPosition_Position(0);` this relays the position of the stage to the variable `pos` which can then be used to ensure the stage is within tolerable limits and instruct the stage to readjust if not. The tolerable limits are set to ±half an increment, so in the case of 0.1° steps this would be 0.05°.

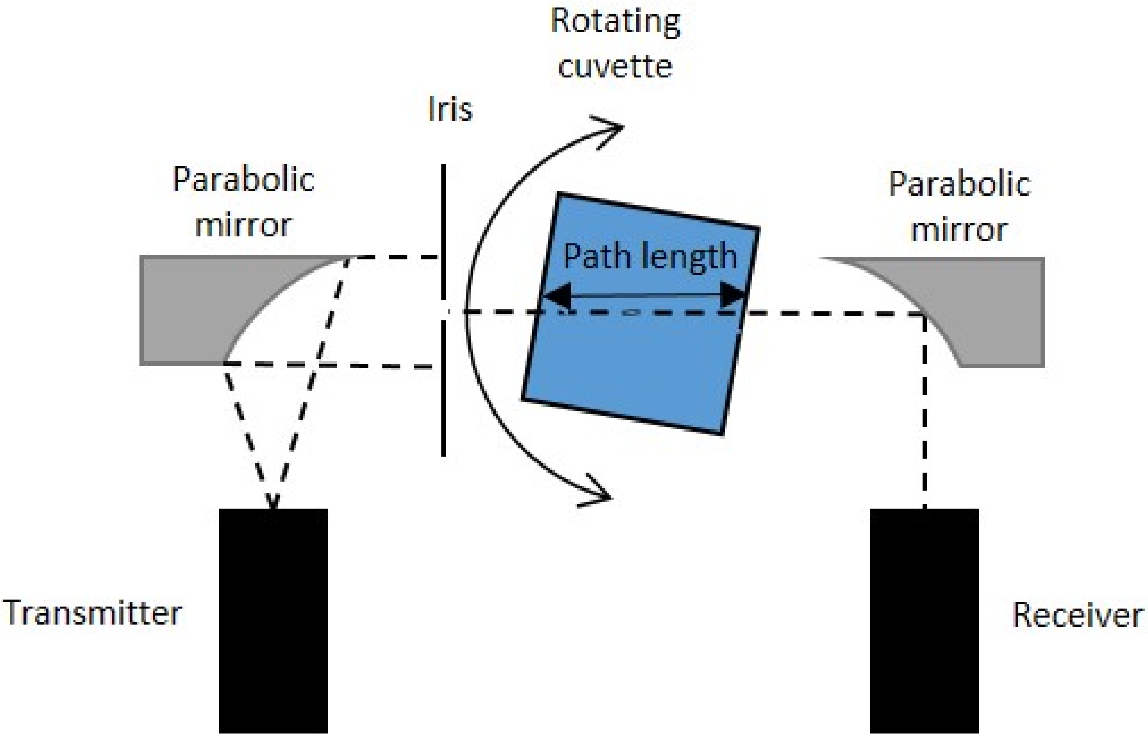

Figure 4.4: Diagram of VNA setup for the rotational cuvette experiments.

4.3.2 Theory

Geometrical optics are used for the calculations [94]. The cuvette containing the liquid is rotated through 60°. This rotation allows for accurate calibration of the normal whilst also providing data which can be used to extract the refractive index. Equation 4.3.1 shows the change in path length (ΔL) through the liquid in the cuvette as a result of its rotation through angle θ. The relative phase change ($\Delta\phi$) as measured by the VNA and the relative refractive index change (Δn) have the relationship shown in equation 4.3.2 as a consequence of the change in path length (ΔL) through the liquid under test.

$$\Delta L = \frac{L_0}{cos(\theta)} - L_0 \tag{4.3.1}$$

$$\Delta n = \frac{\lambda \Delta\phi}{2\pi \Delta L} \tag{4.3.2}$$

Where L_0 is the path length of the cuvette when placed at a normal to the beam and λ is the wavelength of incoming radiation. As ΔL is small, the change in phase received gives an absolute phase change as there are no full phase rotations.

A cosine function is fitted to the data for each frequency, figure 4.5 shows both the raw data and model whose parameters are calculated via MATLAB. The program then calculates the location of the maximum phase, which is the position where the cuvette is at a normal to the incident beam. The difference between the phase at this point, and when the cuvette is rotated through an angle θ is calculated. This measured phase difference $\Delta\phi$ is used in equation 4.3.3 to calculate the refractive index (n).

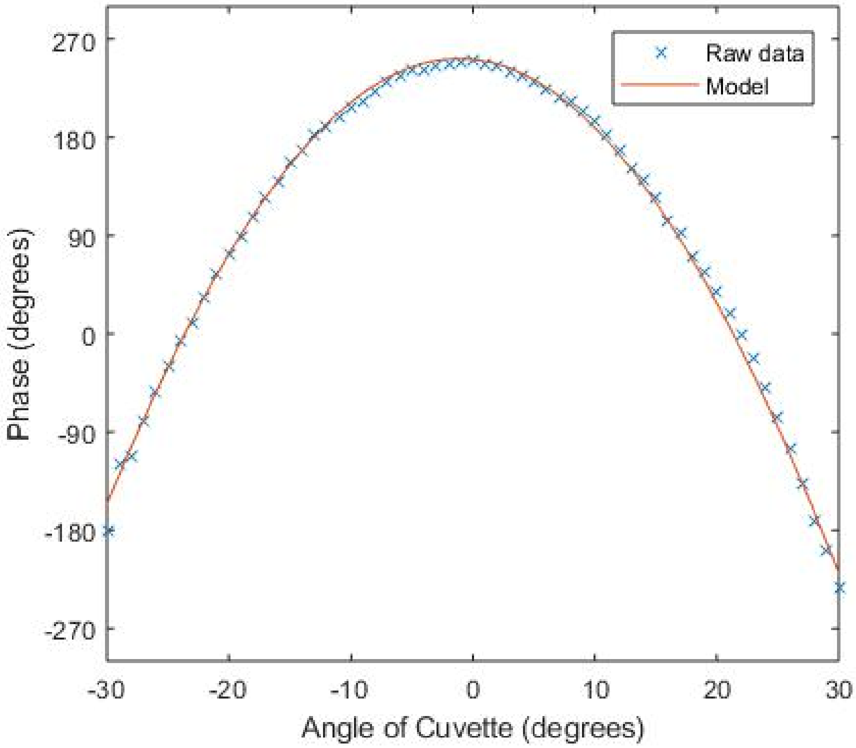

Figure 4.5: Plot of rotational cuvette raw data and modelled curve for the measured phase at the receiver through -30° to 30° swept angles measured every 0.1° for hexane.

$$n = \frac{\lambda \Delta \phi}{2\pi(\frac{L_0}{cos(\theta)} - L_0)} \tag{4.3.3}$$

This is a simplification of the path length change, a more refined version will take into account the cuvette walls. Equation 4.3.4 shows the full version considering the whole cuvette including the walls.

$$\Delta L = \frac{2l_c}{\cos\left(\arcsin\left(\frac{\sin\theta_0}{n_c}\right)\right)} + \frac{l_s}{\cos\left(\arcsin\left(\frac{\sin\theta_0}{n_s}\right)\right)} - 2l_c - l_s \tag{4.3.4}$$

Where l_c is the length at the normal through a single cuvette wall, l_s is the path length at the normal through the sample, n_c is the refractive index of the cuvette walls, n_s is the sample refractive index and θ_0 is the incident angle of beam with respect to the cuvette. This extended calculation for ΔL can be used in the same phase equation as in 4.3.2 but as n_s is also required in the calculation of ΔL it is iterative.

4.3.3 Results and Computation

Model Curve Fitting Method

Measurements using the model fitting method resulted in refractive index values as follows. Figure 4.6 shows the calculated refractive index values for each of the measured alkanes (hexane, heptane, octane, nonane, decane, undecane, dodecane, tridecane, tetradecane, pentadecane and hexadecane) at 0.9 and 1 THz.

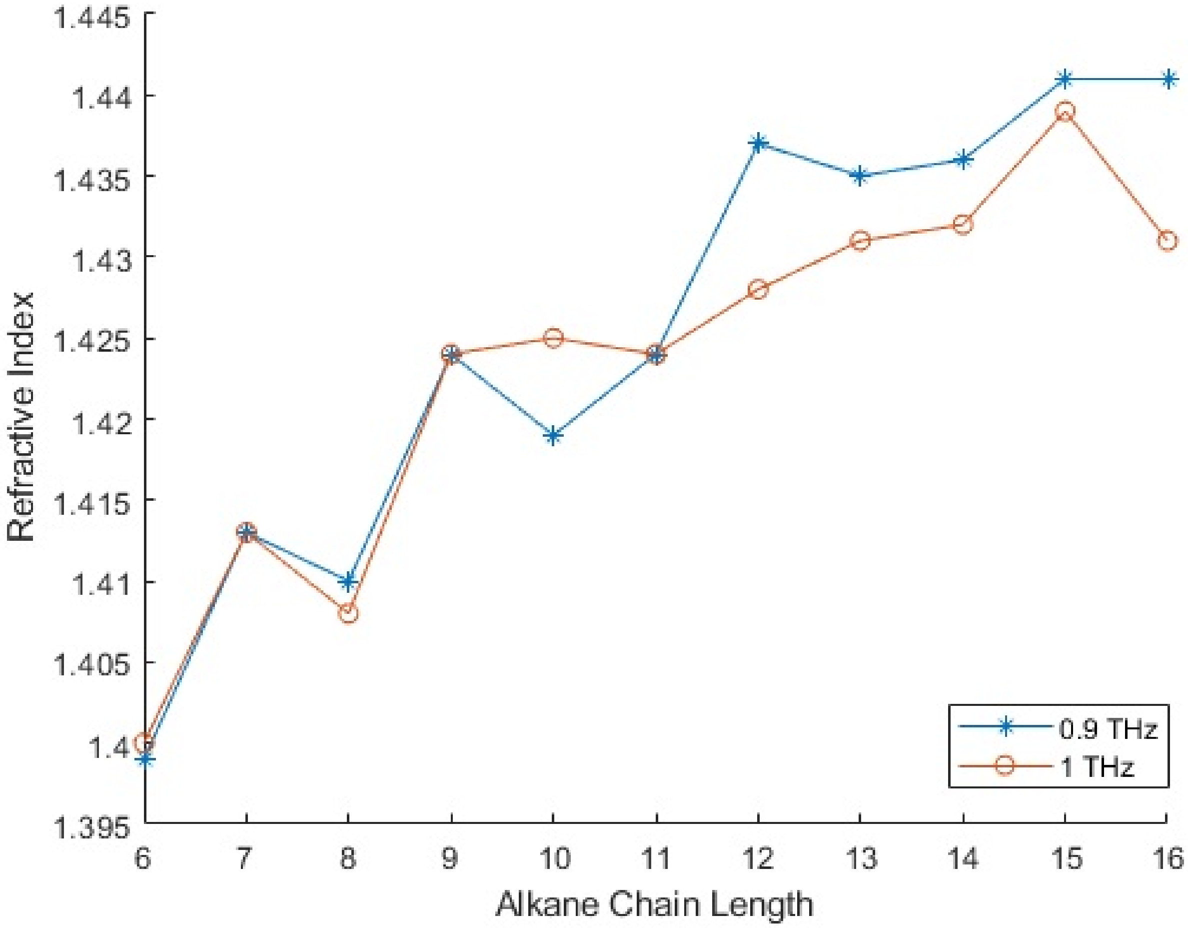

Figure 4.6: Plot of refractive index values measured at 0.9 and 1 THz using the modelled curve fitting method with the rotational cuvette for alkanes from hexane to hexadecane inclusive. Connecting lines are included to guide the eye.

This figure shows that the rotational cuvette method does not provide a level of accuracy which can distinguish between individual alkanes through refractive index alone. However, there is a distinct difference between the high and low refractive index alkanes such as hexane and hexadecane. If the work of [32] is taken as the true values for each of the measured alkanes (in reality this is likely false as these measurements were taken using a TDS system while the rotational cuvette uses a VNA) the rotational cuvette method is consistently calculating higher than expected refractive index values. The range of refractive index values is not as wide as expected as the maximum range measured by the rotational cuvette method is 0.041 refractive index units while the reference values range by 0.059 refractive index units from hexane to hexadecane. The standard deviations for the rotational cuvette at 0.9 and 1 THz are 0.0643 and 0.0609 respectively. The somewhat periodic nature for the lower chain length alkanes is thought to be due to multiple reflections within the cuvette causing errors within the system.

4.4 Split Cuvette

Instead of considering the refractive index directly by the change in speed of terahertz radiation we can consider it in how it affects radiation in other ways. In this section, a split cuvette which can determine the refractive index of a material through its effect on refraction is explored. Refraction changes the path that the light travels, as can be seen in an optical prism the different wavelengths of light appear at different physical positions out of the prism. Using the laws of refraction, spatial positioning can be used to measure the refractive index of a material at a single frequency. This set of experiments is designed to exploit the change in path of a terahertz beam through two liquids. The resultant spatial position allows direct extraction of the relationship between the two liquids' refractive indices.

4.4.1 Experimental Setup

The split cuvette setup is shown in figure 4.7. The beam from the horn antenna of the extender head acting as the transmitter is directed onto a $\frac{1}{2}$ inch parabolic mirror which translates the divergent beam into a parallel beam. This beam is clipped using an iris. This is so that the entirety of the beam will exit through the opposing side of the cuvette from entry. The cuvette is placed on a custom built stand which ensures it is held in the same position within the beam for each measurement. Upon exit of the cuvette, the beam is reflected using a flat mirror on a Thorlabs CR1/M-Z7 rotational stage. The stage uses a Thorlabs TDC001 controller. Once reflected off this mirror, the beam is directed into another parabolic mirror which directs the beam into the extender head acting as a receiver. To find the angle at which the beam exits the split cuvette, the mirror is swept through a range of angles with the peak magnitude denoting the angle of interest. This mirror angle producing peak power is geometrically related to the exit angle of the beam.

The stage used for the split cuvette is the same stage used for the rotational cuvette thus has identical commands are used to instruct movement. The split cuvette MATLAB code also uses the check-back on the position and adjusts accordingly should it not be where was instructed to be. Once in position, the code instructs the VNA to take the measurement.

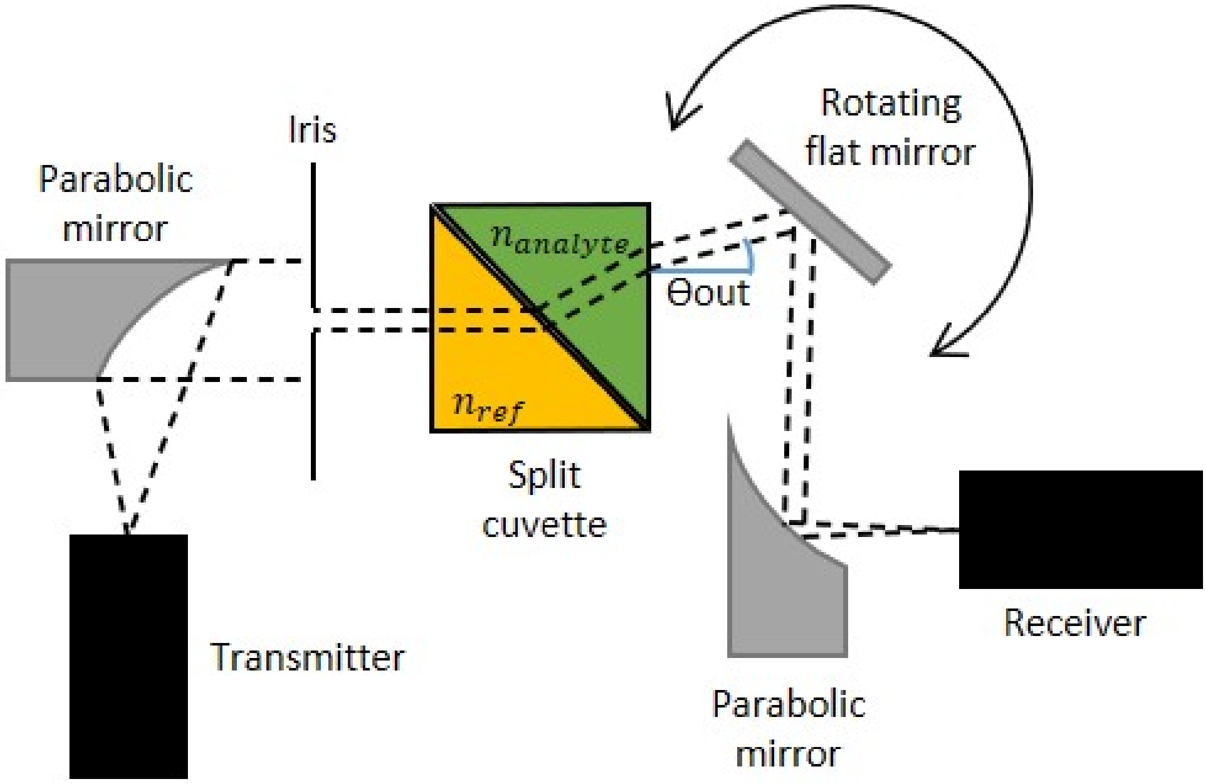

Figure 4.7: Diagram of VNA setup for the split cuvette experiments.

4.4.2 Cuvette Fabrication

Similarly to the rotational cuvette both a polystyrene and quartz version has been fabricated. Both designs use a commercial 10 mm path length cuvette which has been modified. Both designs use the same respective material for the split as the base cuvette. Each split is 0.1 mm thick and glued in by hand. Similarly to the rotational cuvette the polystyrene version was found to be preferable to the quartz cuvette due to a slightly lower absorption and fewer resonances resulting in a cleaner signal. In addition to this, for the split cuvette only, fabrication was found to be much easier with the polystyrene version and PVA glue was found to be preferable following a number of trials using a variety of glues and epoxy resins. As PVA is water based this may not be suitable for all analytes. Similarly, polystyrene is less chemically stable than quartz so, dependent on application, this may need to be considered.

4.4.3 Theory

The split cuvette uses the basic principle of Snell's law. Equations 4.4.5 and 4.4.6 form from considering two refractive index boundaries shown in figure 4.8.

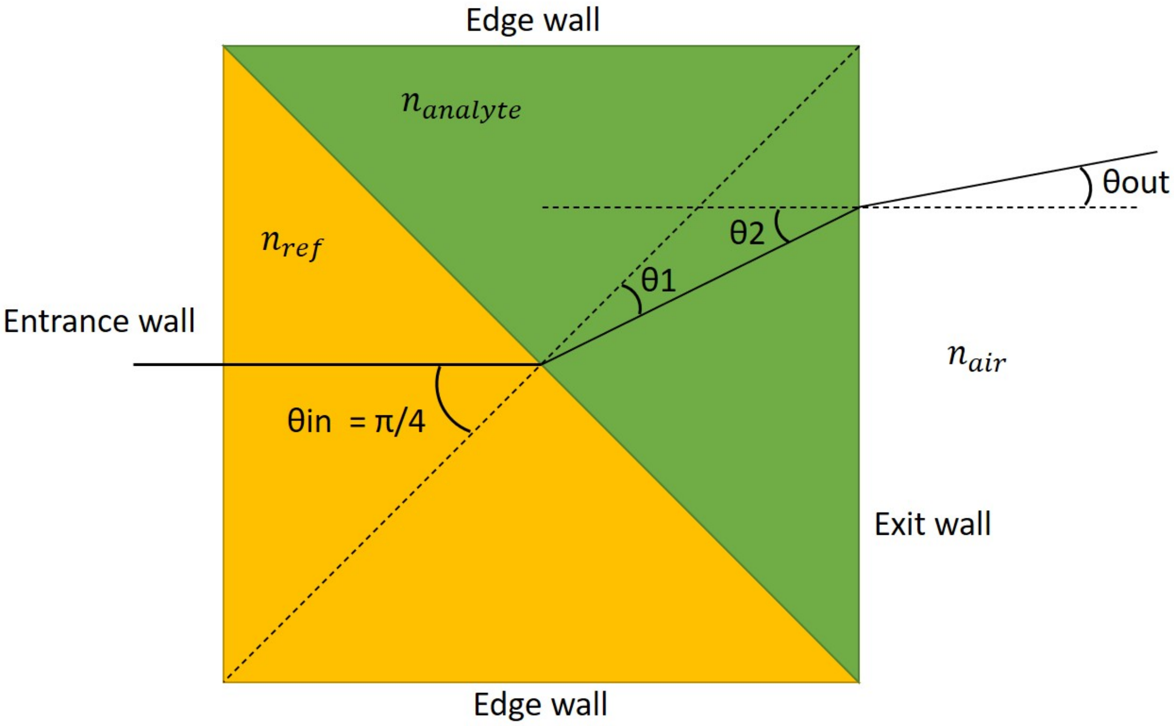

Figure 4.8: Diagram of the beam path through the split cuvette arrangement.

$$n_1 \sin \frac{\pi}{4} = n_2 \sin \theta_1 \tag{4.4.5}$$

$$n_2 \sin\theta_2 = \sin\theta_{out} \tag{4.4.6}$$

Simple geometry can show that:

$$\theta_2 = \frac{\pi}{4} - \theta_1 \tag{4.4.7}$$

From this, we can rearrange $\sin\theta_2$ to:

$$\sin\theta_2 = \frac{\cos\theta_1}{\sqrt{2}} - \frac{\sin\theta_1}{\sqrt{2}} \tag{4.4.8}$$

Substituting this into equation 4.4.6 and combining it with 4.4.5 gives:

$$\frac{n_2\cos\theta_1}{\sqrt{2}} - \frac{n_2\sin\theta_1}{\sqrt{2}} = \sin\theta_{out} \tag{4.4.9}$$

Equation 4.4.9 can then be simplified to:

$$\sqrt{2\delta^2 + 4\delta + 1} - 1 = \frac{2\sin\theta_{out}}{n_1} \tag{4.4.10}$$

Where δ is:

$$\delta = \frac{n_2}{n_1} - 1 \tag{4.4.11}$$

As δ is small it is assumed $\delta^2 << \delta$. Using the Taylor expansion of $\sqrt{1+4\delta}$ to simplify 4.4.10 further gives:

$$\delta = \frac{\theta_{out}}{n_1} \tag{4.4.12}$$

Therefore:

$$n_2 = n_1 + \theta_{out} \tag{4.4.13}$$

For systems where the split of the cuvette is not at an angle of 45°. A split angle of θ_s gives:

$$n_2 = n_1 + \frac{\theta_{out}}{\tan\theta_s} \tag{4.4.14}$$

This equation shows that a higher sensitivity can be obtained from altering the angle of the split to be larger than 45°. However, increasing this angle will also increase the thickness of the liquid the beam must travel through, increasing absorption and reducing power. Although an infinitely long cuvette will theoretically give a more sensitive measurement from deflecting the beam more it will also increase the absorption so attenuation coefficient of the liquid under test needs to be taken into account. Additionally, the width of the cuvette is reduced the beam is more likely to exit through the side of the cuvette which would mean no exit angle is measurable.

4.4.4 Results

Split Cuvette for Measuring Refractive Index

For this set of experiments, alkanes from hexane to hexadecane are measured and hexane is used as the reference liquid. This has been chosen as it is a cheap and readily available non-polar solvent. A higher chain alkane would have a refractive index central to the full range being tested thus being closer to all of the analytes combined however, the lower cost and lower absorption of hexane outweighs this benefit.

The power at mirror angles, from ±3° in steps of 0.01° is measured for each of the test alkanes. The mirror angle can be translated by simple geometry to give the exit angle of the beam from the cuvette as described in equation 4.4.15. Figure 4.9 shows the measured power for each of the exit angles showing a peak. The exit angle of the beam is calculated at the peak magnitude.

$$\theta_{exit} = 2\theta_{mirror} \tag{4.4.15}$$

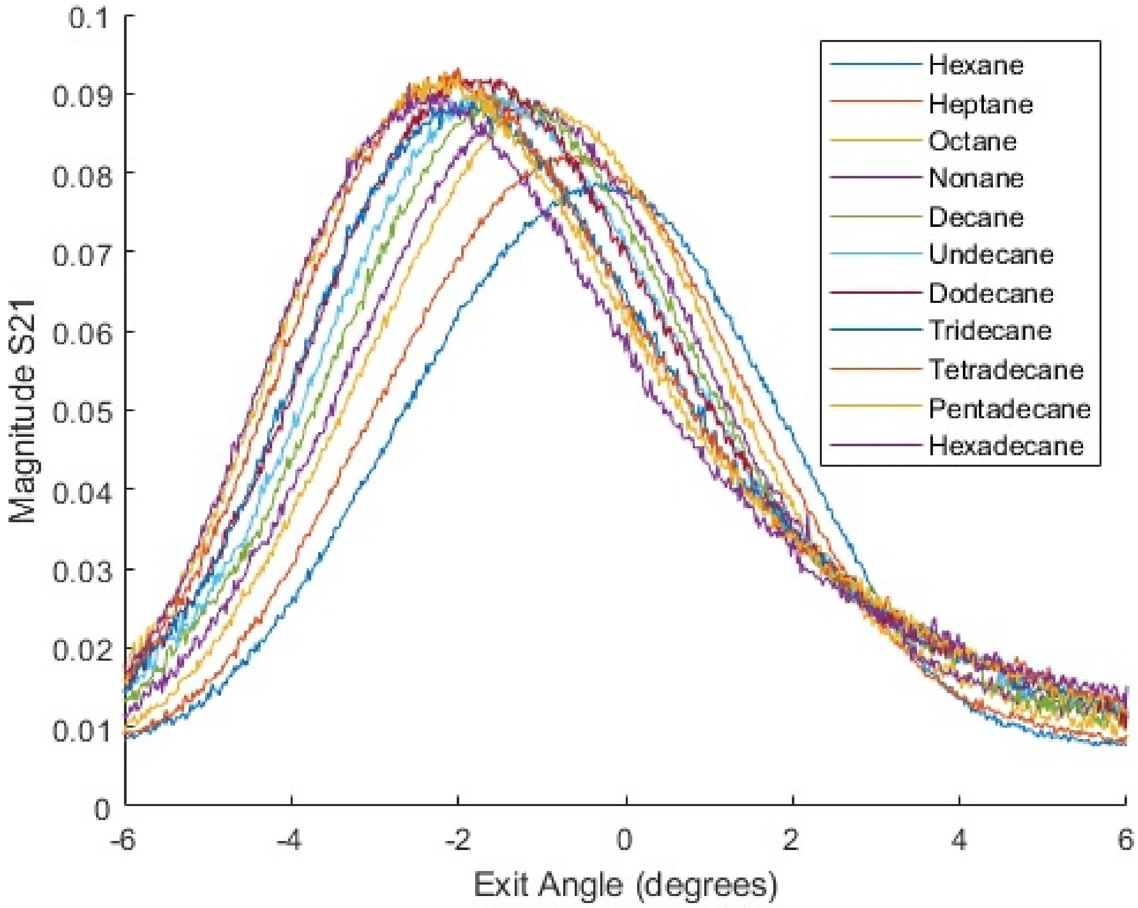

Figure 4.9: Plot of measured split cuvette transmission with beam exit angle. Measurements taken at 1 THz.

The exit angle can be used to calculate the refractive index of each of the analyte liquids given a refractive index for the reference liquid. A reference refractive index of 1.4 is used as measured for hexane in the rotational cuvette measurements at 1 THz.

Figure 4.10 shows the computed refractive index values for each of the measured alkanes from hexane to hexadecane inclusive. These values are taken from average values of three full scans through each of the alkanes. Error bars have been included for each analyte showing the standard deviation of the three scans. Effort has been taken to ensure the measurement conditions are different in each of these scans confirming the robustness of the method. A zero error is shown for hexane as in each set it is used as the reference and therefore forced to the same value (1.4).

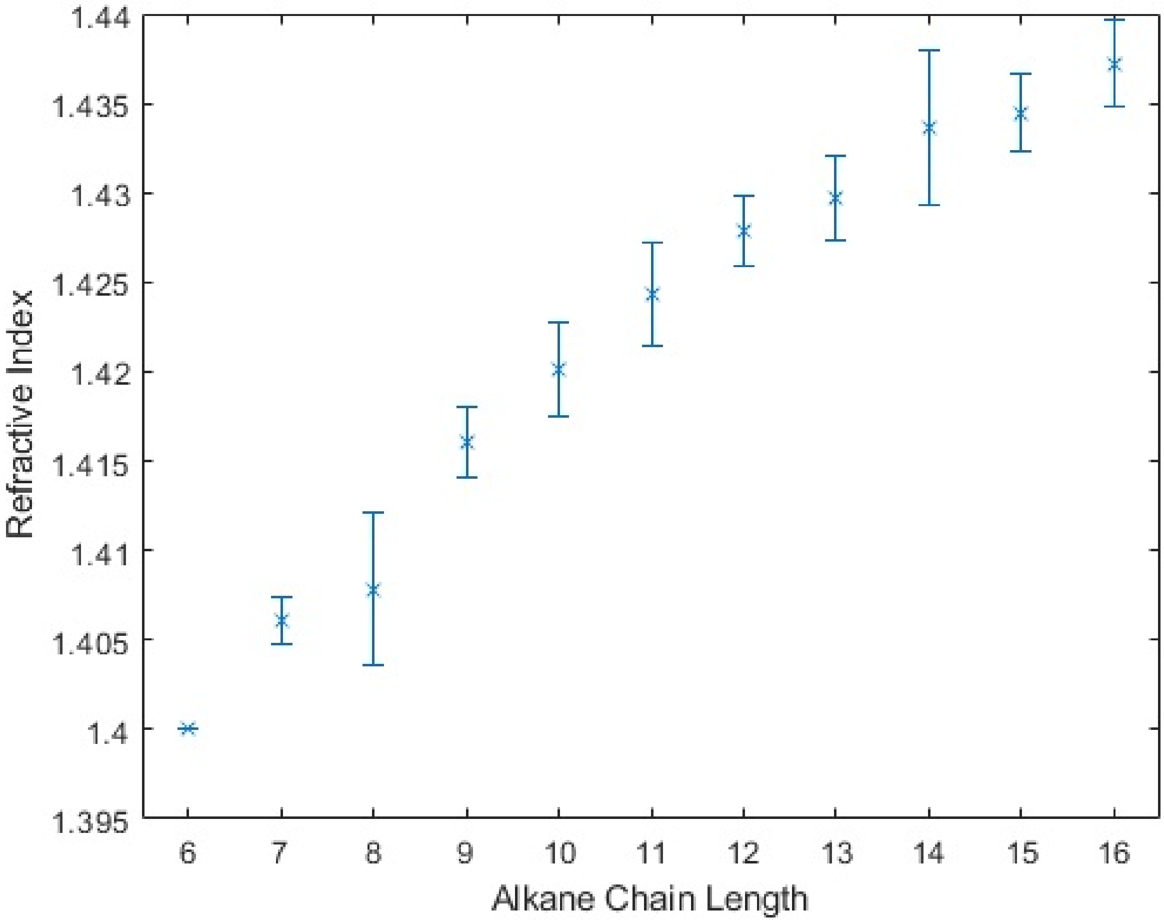

Figure 4.10: Graph of measured alkane refractive indices by chain length as measured by the split cuvette method using hexane as a reference assuming hexane refractive index is 1.40 as measured by the rotational cuvette method at 0.9 and 1 THz. Error bars showing standard deviation are included.

Calibration to Single-Angle Measurements for In-Flow Testing

To use the split cuvette in industrial applications, for example in the petrochemical industry for quality testing, the swept mirror measurements do not need to be taken. Once initial tests have been carried out to calibrate the system for both wanted and unwanted products, measurements can be isolated to a single mirror angle enabling fast, continuous measurements. Consequently, these tests could be used on flowing tubes for quality testing.

To maximise the sensitivity of these measurements the most sensitive angle must be selected. This is dependent on the reference material and the possible test analytes. To find this angle, prior tests investigating the full sweep of angles for each expected analyte is required. The angle of maximum sensitivity is at the angle where the measurements for the two analytes have the largest difference. Figure 4.11 shows the difference between the hexane and tetradecane scans. These are posing as the desired product and an undesired product. It can be seen here that -2.58° has the maximum contrast in magnitude between the hexane and tetradecane scans so this angle is chosen.

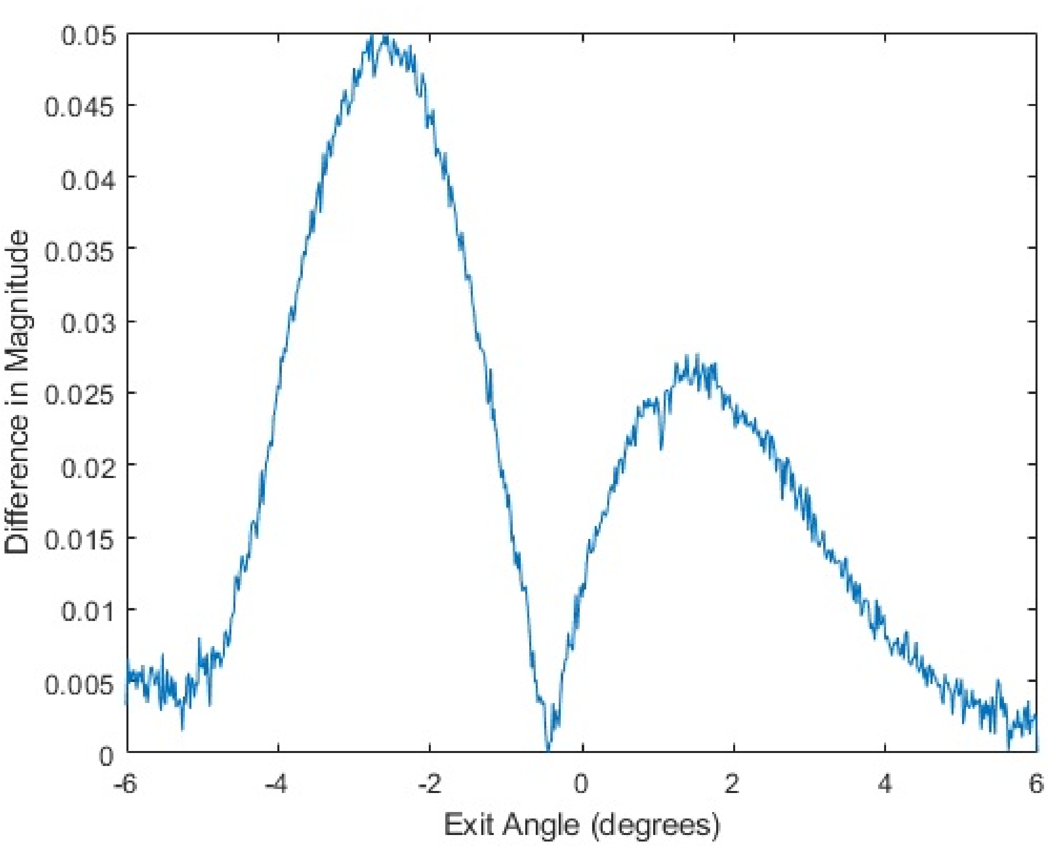

Figure 4.11: Calibration scan showing the difference between scans with hexane and tetradecane as the test analyte; both using hexane as the reference liquid.

To demonstrate a single angle scan figure 4.12 shows how small changes in refractive index can be detected in continuous measurements. The demonstrated example has a sensitivity of 0.0061 RIU/dB, the sensitivity of this method is dependent on the specific analytes and the contrast between them so would need to be calculated for each application. The mirror is set to the angle of -2.58°. Drift can be accounted for by regular re-calibration. As in all experiments, the reference hexane cell is continually refilled as to not drop below the beam and invalidate the experiment. The S21 magnitude in the hexane and tetradecane scans remains constant with only slight variations which could be due to noise, temperature etc. The other scan which drip feeds tetradecane over time into hexane shows an increase in S21 magnitude moving from a similar result of the hexane scan to that of the tetradecane scan. Note that hexane evaporates somewhat at room temperature so this will also have an effect on the concentration of the two analytes within the mixture. This demonstrates single angle scans can detect small changes in refractive index. An average of 1000 data points at 1 THz have been taken. No smoothing has been applied to the data.

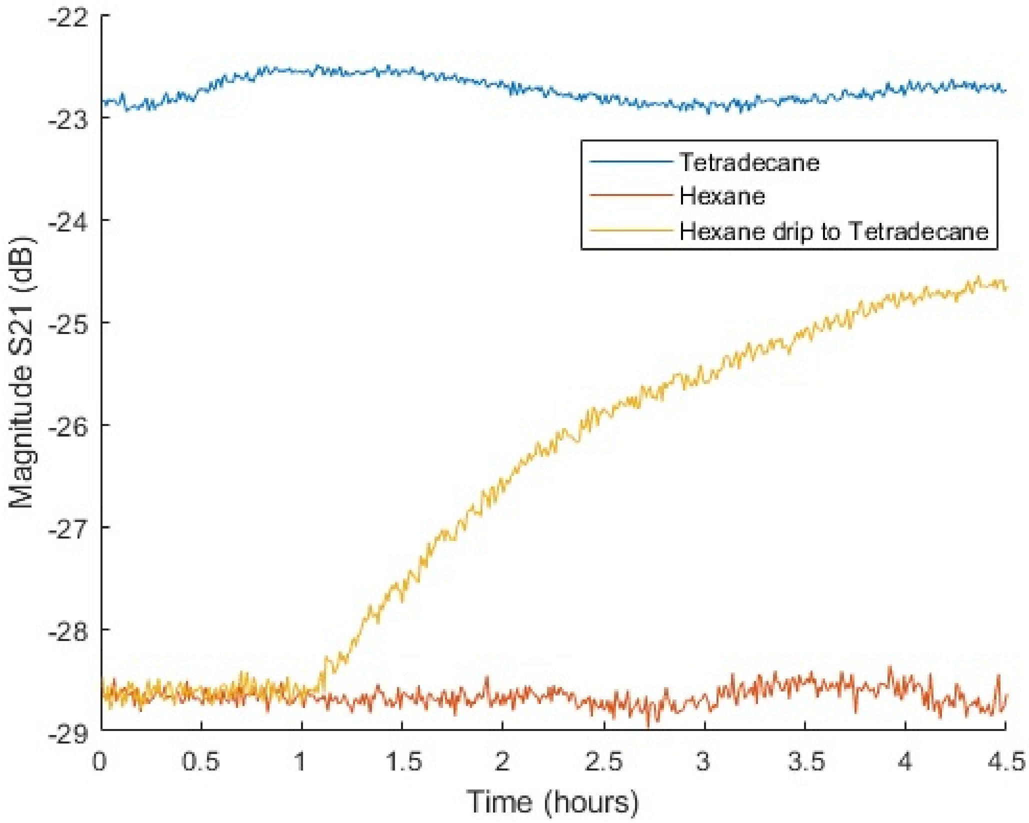

Figure 4.12: Single angle scan (at -2.58°) showing three scans each with hexane in the reference cell. One with hexane in the analyte cell, one with tetradecane in the analyte cell and one which initially has hexane in the analyte cell and tetradecane is drip fed on top, gradually increasing the tetradecane concentration and reducing the hexane concentration within the mixture.

Phase Boundary Measurements

The split cuvette uses an iris to reduce the beam width to ensure there is no leakage or reflections through the sides of the cuvette. Although the iris is used to minimise the beam width as much as possible, an infinitesimally small beam is not possible, as this will leave no power. The relatively large wavelength of terahertz radiation (0.3 mm) also restricts the minimum beam width possible.

As the beam remains large compared to the cuvette ($\approx$ 5 mm as compared to the cuvette of $\approx$ 10 mm), experiments were undertaken to explore how the split cuvette method performs if the beam is only partially covered by the reference or test material. This not only gives an indication of the result if the beam passes through a phase boundary (e.g. hexane evaporates below the beam) but it also gives an indication of how the split cuvette behaves with regions of different refractive index materials given a horizontal boundary.

The split cuvette VNA setup is used and the reference chamber is filled with hexane. This is filled to above the beam height and is refilled during the experiment. The analyte chamber is initially empty. An electronic micropump is used to inject hexane into the analyte chamber causing the level of hexane to rise through the entirety of the beam. Scans are taken sweeping the mirror to locate the exit angle of the beam, this is repeated as the analyte cell is filled.

The results are compared to single analyte tests of hexane and air. The hexane scan has a peak at 0° as in this case the reference and analyte have the same refractive index so there is no alteration in beam path. The scan taken with air in the analyte cell had a consistent result at the noise floor. This indicates that the exit angle of the beam with air as the analyte is too large to be picked up by the mirror as it likely exits at a severe angle so misses the mirror completely. This is due to the large difference in refractive index between air and hexane of ≈ 1 and ≈ 1.4 respectively. This highlights the benefit and limitations of the split cuvette method as it is a useful tool for detection of small refractive index discrepancies but cannot be used to detect large differences in refractive index. The needle from the micropump is in contact with the central wall of the cuvette so hexane is expected to flow down the central split into the cuvette. Hexane is injected at 0.5 mL per hour. 25 measurements are taken at a single frequency of 1 THz and the mirror is moved in 0.1° steps for mirror angles from -10° to 10°. The mean average of these 25 measurements is taken giving a single trace across the swept angles. This process is repeated through time building up the image shown in figure 4.13. No smoothing has been applied to the data. The time is recorded electronically within the program and saved to a separate .csv file which is used to plot the data. At the start of the experiment, no peak is found as expected from the initial tests using air as the analyte. At 40 minutes, a faint peak at 0° starts to form getting stronger and more pronounced until at about 75 minutes. It is assumed that this is the effect of the hexane/air boundary crossing through the beam until the beam is fully covered so additional hexane does not affect the result further.

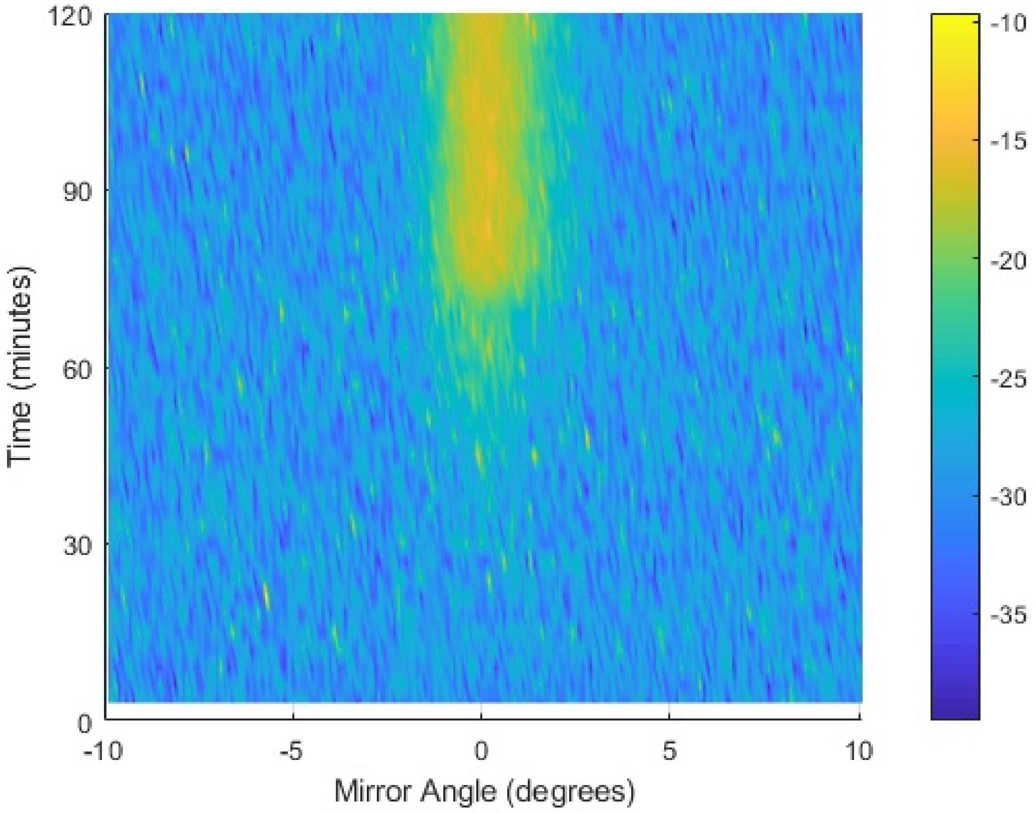

Figure 4.13: Figure of measured S21 response (dB) from dynamic measurement through time of split cuvette swept angles from hexane in the reference cell and air in the analyte cell to showing the analyte cell filling up with hexane over time. Averages of 25 measurements were taken at 1 THz for each point and no smoothing has been applied.

These results show that when the beam through the split cuvette encompasses a boundary between two differing refractive index materials, the scan slowly transitions from the expected response from one material to the expected response of the other material. This means that the split cuvette can distinguish two distinct refractive index areas and does not treat them as a bulk material with a combined refractive index. In addition, as the analyte travelled down the centre split for the duration of the experiment we can say that, at least for an analyte with as low viscosity as hexane, the thin layer of material has no effect on the split cuvette result. This is likely due to the wavelength of terahertz (0.3 mm) being significantly larger than the thickness of this layer and that is spreads sufficiently across the split so that it is flat.

Vertical Measurements to Explore Mixing of Alkanes

The measurements of the air and hexane boundary layers show that the split cuvette method can distinguish between multiple analytes across a boundary layer. This knowledge is used to assess the interaction between two alkanes in a mixture that has been left to settle. Hexane and tetradecane will be assessed using the terahertz split cuvette method to see how they interact whether they will mix or form a boundary layer.

In the air and hexane measurements, the hexane will clearly fall to the bottom of the cuvette and this can be confirmed visually. However, the two alkanes have similar densities so could mix instead of forming a boundary. As they are both clear colourless liquids it is not visually obvious how they interact. Any disruption or turbulence within the mixture should be reduced as this could affect the boundary layer (if there is one). Instead of drip feeding the hexane, as in the air-hexane experiments, both materials will already be present in the cuvette and the cuvette will be moved vertically through the beam. This method reduces the movement of the liquids in the cuvette but the beam should still pass through the boundary layer if there is one present. A manual vertical stage is used to move the cuvette, this ensures all movement is smooth and controlled with accurate fine precision.

The reference cell is filled with hexane and remains totally filled over the full beam width for the duration of the experiment. The analyte cell is first filled with tetradecane, the level of tetradecane will be filled so that at the top of the vertical stage the tetradecane fully covers the beam. When the vertical stage is at its lowest position the beam fully passes above the tetradecane. The remainder of the analyte cell is filled with hexane and left to settle. The cuvette is left for 10 minutes to settle. It cannot be left to settle for too long as the hexane is evaporating.

The measurements are taken from the lowest vertical stage position to the highest, this measures from the top of the cuvette down. Ensuring the hexane does not evaporate past the beam. The vertical stage has a movement of 25 mm along the micrometer scale which corresponds to 12.5 mm vertical movement. Once each measurement is taken across the desired range of angles as in a standard split cuvette measurement the micrometer is moved manually and another measurement can be taken until the full range of vertical height has been measured.

Figure 4.14 shows the measurements taken across mirror angles of -10° to 10° with an angular step size of 0.025°. 25 measurements are taken at 1 THz and the mean is taken for each point. Vertical measurements are taken every 1.25 mm. As can be seen in the figure both the magnitude of the peak and the position deviates from 8 mm to 10 mm vertical cuvette height. This is the result expected for a distinct boundary layer as within a 2 mm space there is a clear difference between the standard hexane response towards that of a standard tetradecane response. The expected exit angle for pure tetradecane in the analyte cell with hexane in the reference cell is $\approx 1°$ and as tetradecane has a higher absorbance than hexane the magnitude of the peak should reduce as it does. The positioning of the hexane and tetradecane within the cuvette for their respective densities is also as expected because the highest position for the cuvette corresponds to the lowest position for the beam within the cuvette as the beam remains stationary. It would be expected that the tetradecane would be at the bottom of the cuvette and therefore at a higher cuvette height.

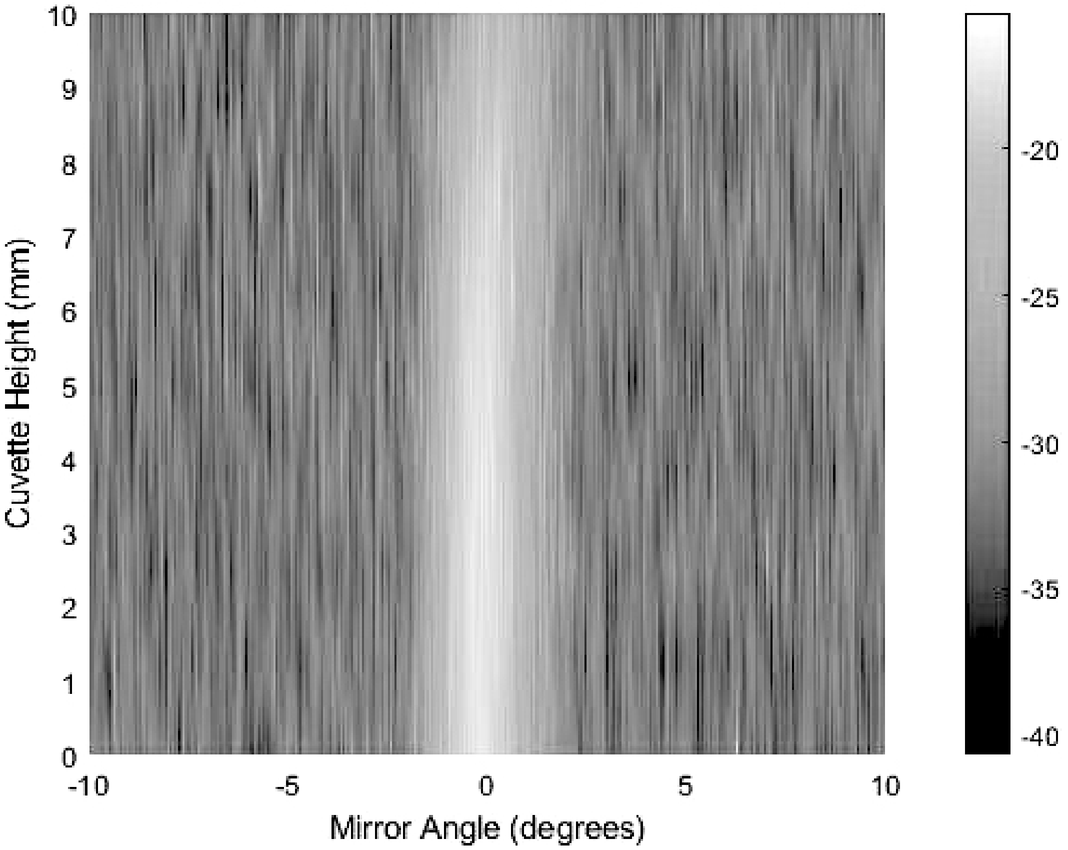

Figure 4.14: Figure of measured S21 magnitude response from dynamic measurement through vertical space of the split cuvette with hexane and tetradecane mixture left to settle, for 10 minutes, in the analyte cell with hexane in the reference cell.

A further experiment with vertical measurements taken every 0.5 mm and a range of 28.5 mm is shown. To speed up the experiments the angular range of the mirror is reduced to -5° to 5° and the step size is 0.05°. Again, an average of 25 single frequency measurements are taken at 1 THz. The following figures 4.15 and 4.16 each are measured using the described parameters with different concentrations of hexane and tetradecane at 75%:25% and 50%:50% respectively.

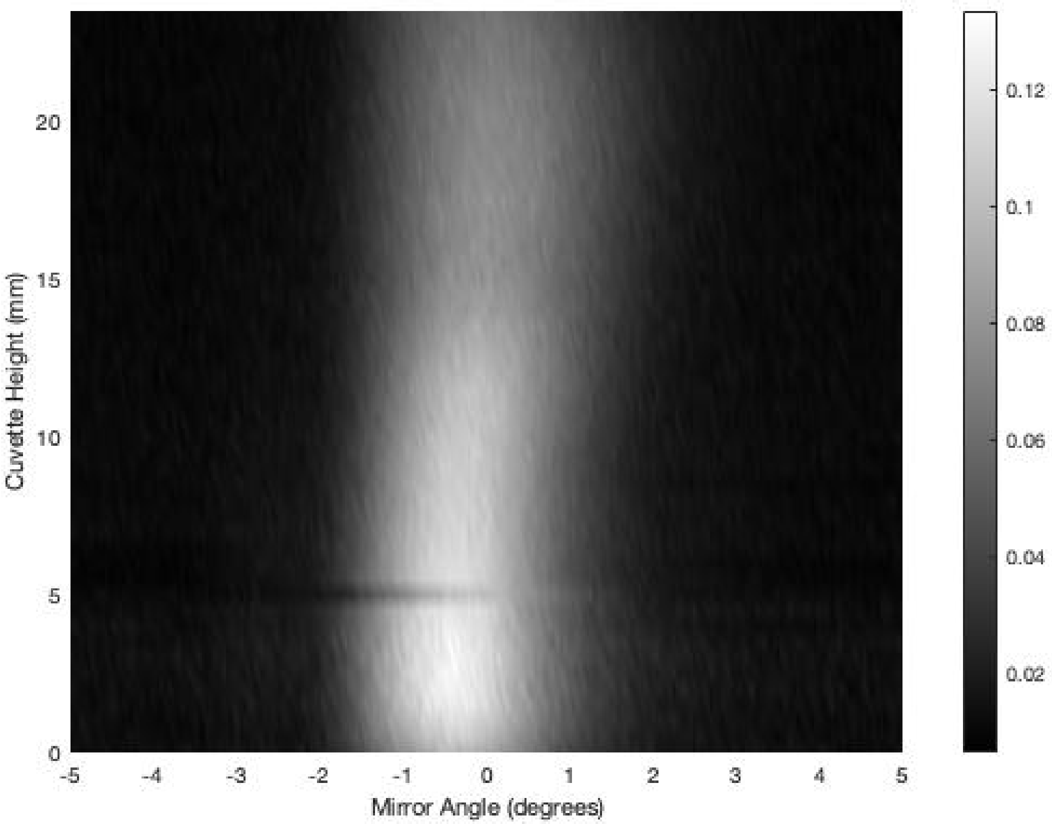

Figure 4.15: Figure of measured S21 magnitude response from dynamic measurement through vertical space of the split cuvette with hexane (50%) and tetradecane (50%) mixture left to settle, for 10 minutes, in the analyte cell with hexane in the reference cell.

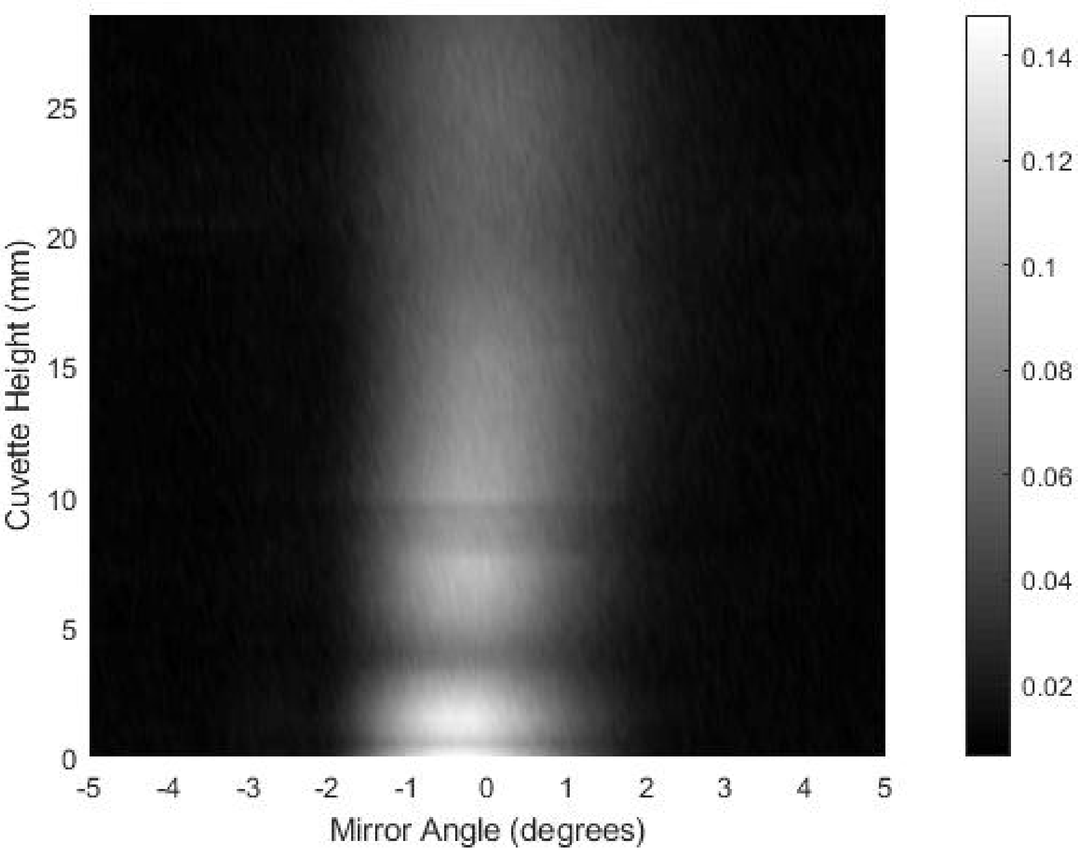

Figure 4.16: Figure of measured S21 magnitude response from dynamic measurement through vertical space of the split cuvette with hexane (25%) and tetradecane (75%) mixture left to settle, for 10 minutes, in the analyte cell with hexane in the reference cell.

Further examination of the data shows trends in the dispersion of the two liquids throughout the vertical space of the cuvette at different proportions. Figures 4.17 and 4.18 show the trends of the peak mirror angle across each of the mixtures.

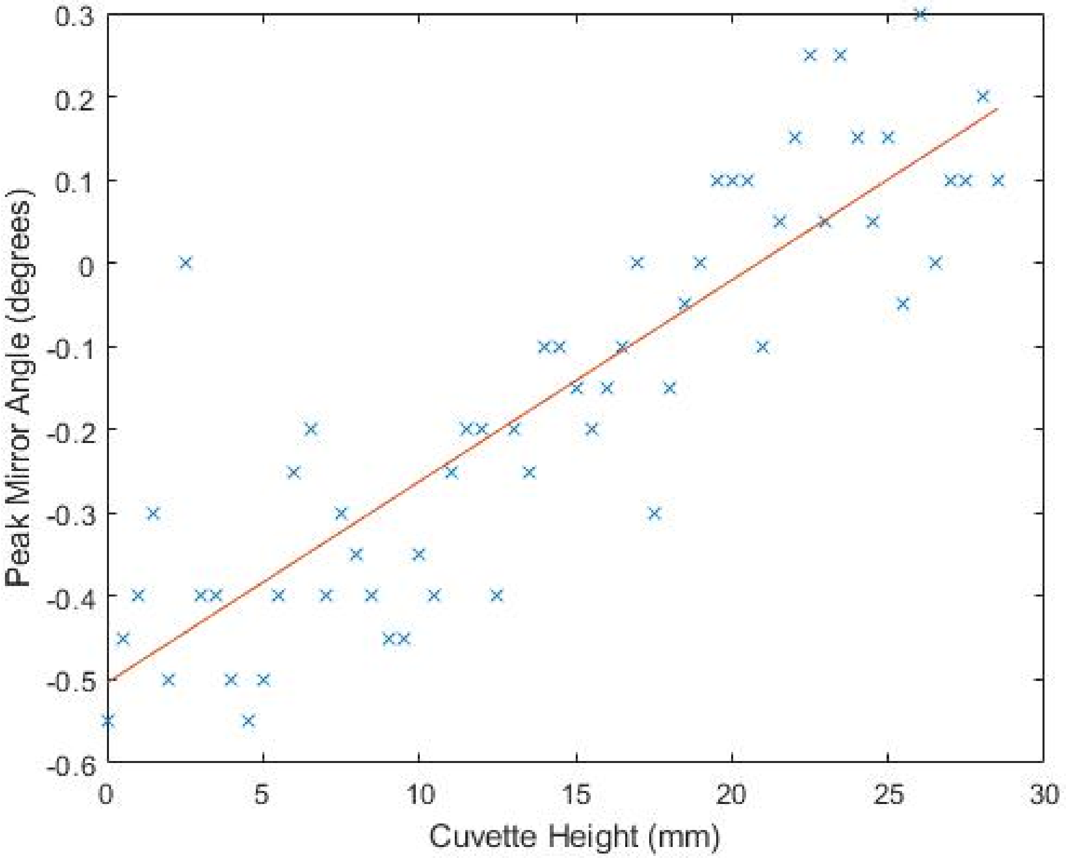

Figure 4.17: Figure of peak mirror angles from dynamic measurement through vertical space of the split cuvette with hexane (50%) and tetradecane (50%) mixture left to settle, for 10 minutes, in the analyte cell with hexane in the reference cell.

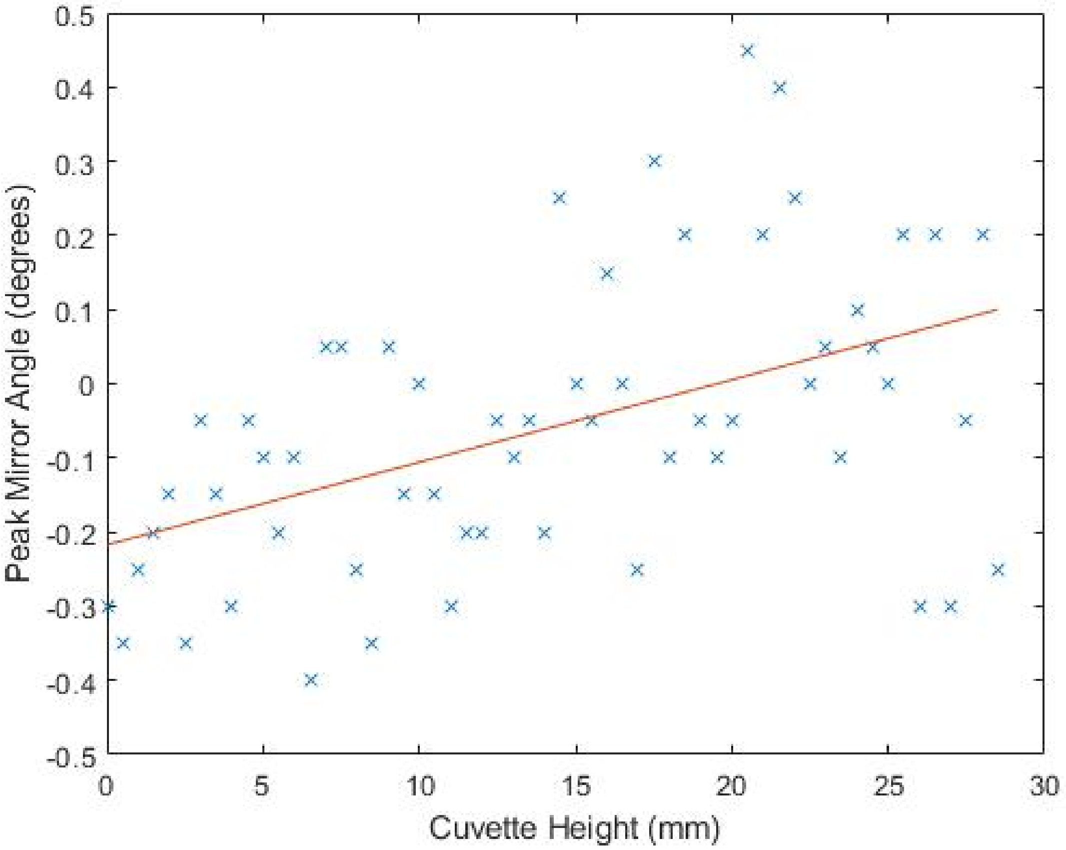

Figure 4.18: Figure of peak mirror angles from dynamic measurement through vertical space of the split cuvette with hexane (25%) and tetradecane (75%) mixture left to settle, for 10 minutes, in the analyte cell with hexane in the reference cell.

A shift of 0.7° is seen with the use of 50% tetradecane to 50% hexane in figure 4.17. The shift expected from pure hexane to pure tetradecane is 1° so 0.7° is still not the full range expected if it is pure tetradecane at the bottom of the boundary and pure hexane at the top of the boundary. So although the solution is somewhat mixed there is a higher proportion of tetradecane at the bottom of the cuvette where the hexane is dominant higher up in the vessel. With the 75% to 25% solution a 0.2° shift is shown. It is assumed this is because the dominant substance is present across the full cuvette in higher concentrations which enables better solubility or mixing of the trace substance.

4.5 Conclusion

A range of techniques for measurements of refractive index using a cuvette in conjunction with a VNA have been demonstrated.

The rotational cuvette, while providing a quick and easy method of extracting the refractive index of a material using a VNA, does not provide a sufficent level of accuracy to distinguish between individual alkanes but a mean error of 0.017 refractive index units is suitable for some other applications. The measured refractive indices do however sometimes provide extremely small standard deviations as shown in figure 4.19 which plots the average of the 0.9 and 1 THz rotational cuvette measurements and their standard deviations. As some of the points have extremely small standard deviations the inaccuracy of the results could be attributed to a systematic error however as some of the points e.g. dodecane have large standard deviations it is more likely a coincidence but this is interesting to note as there are multiple alkanes with very small ranges in results across the measurements. One issue regarding the rotational cuvette method is the long path length, with 10 mm of liquid it is possible that a test liquid would have too high absorption to be measurable. This could be reduced by using a smaller cuvette but this is limited by beam width (it cannot leave the side of the cuvette). A rectangular based cuvette could provide a short path length whilst keeping the width to ensure no beam leakage.

The split cuvette is able to distinguish between small differences in refractive index. Although for some values the standard deviation in measurements is greater than that of the rotational cuvette, it is much more consistent across all alkanes measured and the values are more coherent in the sense that each of the refractive indices measured are in order for the chain length of alkane which is to be expected. The split cuvette method can distinguish between individual alkanes. It can also detect multiple substances and mixtures either to a reduced extent if the boundary layer is positioned across the beam or to a more detailed extent if multiple scans are taken vertically through the sample. This means that if the split cuvette were to be used in industry for dynamic testing of a flowing sample it could easily distinguish even small quantities of unwanted substances which cause a change in refractive index. The split cuvette can be modified to change path length if required and half of the path length will be filled with a reference liquid which can be chosen to have a low absorption thus reducing absorption issues.

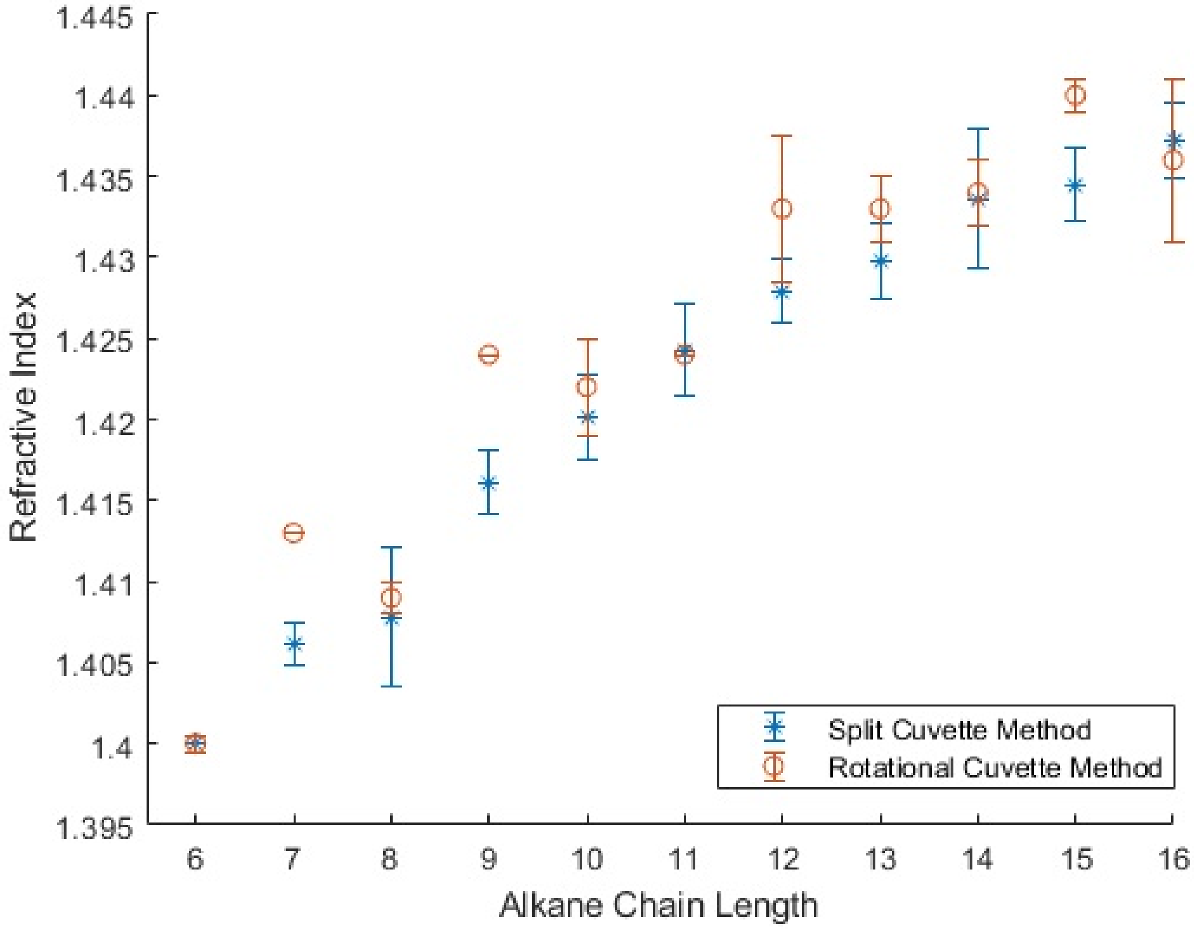

Figure 4.19: Figure of refractive index values and their standard deviations from the repeat tests of the rotational and split cuvette methods.

Figure 4.19, which collates data from figures 4.6 and 4.10, shows that the two methods agree in the spread of refractive index across the full range of alkanes tested and although the rotational cuvette method is not able to distinguish between individual alkanes well it does show an overall trend across all the samples which are extremely close in refractive index as the full range from hexane to hexadecane is ≈ 0.04 refractive index units. The split cuvette shows a very promising method of comparative refractive index testing and allows for further extension into dynamic testing.

Chapter 5

Paper Fresnel Lenses

5.1 Introduction

Paper has typically low loss in the terahertz region [95], is cost effective, readily available, absorbent, sustainable and recyclable. Lower-cost materials which can be used either for rapid prototyping, disposable applications or even as the final system components are worth investigating as currently terahertz components are costly.

Invented over 2000 years ago in China as other writing materials were either too heavy or expensive [96], paper is one of the most versatile products ever created; it is inexpensive, lightweight, mechanically flexible, permeable, flammable and easily recyclable. These properties make its appearance in everyday life common place for instance it is used for packaging, books, newspapers, magazines, bags, artwork etc. Therefore, it is expected that various areas of engineering will investigate the use of paper and how it can be a valuable asset to their respective applications.

Wood [97] and paper [98] has been well characterised and its properties explored at terahertz frequencies; the findings show that the attenuation coefficient is relatively low and the refractive index of 1.48 at 1 THz. This, along with the fact that commonly paper is supplied in thin sheets, which can be easily cut using a laser cutter, makes it a cheap and convenient option for terahertz optical devices [95]. The literature shows it has been used for many common devices such as Fresnel lenses [101–103] or wave plates [104].

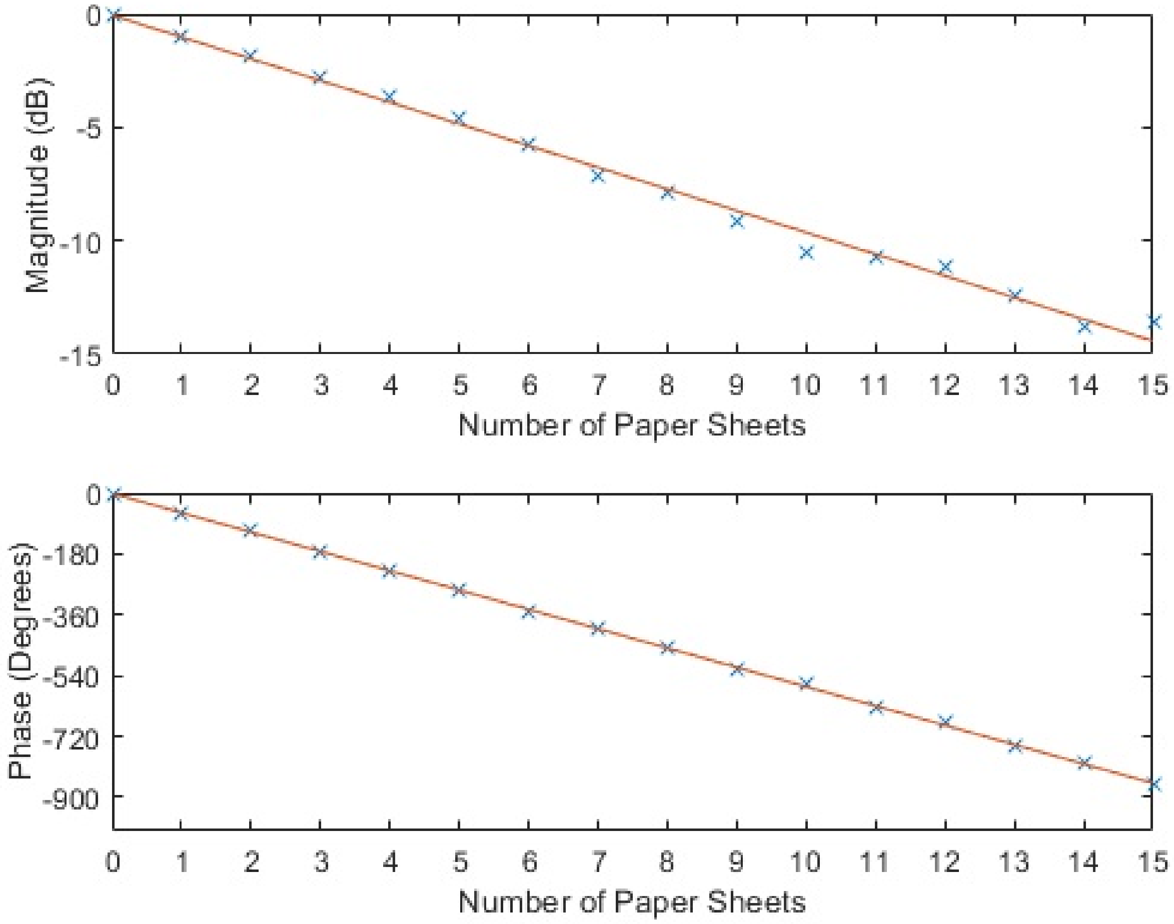

Figure 5.1: Graph of phase delay and transmission at 1 THz as a function of the number of paper sheets.

This chapter aims to introduce the use of paper at terahertz via a study into paper Fresnel lenses. It then introduces the idea of soaking paper in liquids which will be used in later chapters of this thesis.

5.2 Paper Characterisation

All the paper used in this chapter is 80 gsm, 100 µm thick, standard bright white copy paper. Figure 5.1 shows the phase retardation of paper, where on average, each sheet causes 57° phase retardation. Figure 5.1 also shows the magnitude loss through each sheet of paper which, on average, is 0.96 dB per sheet. The refractive index of paper at 1 THz is 1.48 [98].

In addition to the cellulose fibres which make up the large bulk of paper, additive ingredients can perform a range of functions from bleaching the paper, giving it a bright white appearance, to increasing the strength and mechanical performance of the product [99]. A common additive is calcium carbonate or china clay which when applied to one or both sides of the sheet can improve its characteristics for printing or writing [100].

5.3 Paper Fresnel Lenses

Fresnel lenses are approximations of convex lenses. Many versions of these approximations exist, the simplest of which is a binary diffractive Fresnel lens. The progression of these approximations is shown in figure 5.2. A measure of how well a lens works in terms of the ratio of power incident on the lens which is converted into the useful power produced at the focal point is lens efficiency. Lens efficiency decreases as the design is approximated further. For example, a curved Fresnel lens is more efficient than a linear approximation which is more efficient than a discrete approximation which is more efficient than a binary approximation. The maximum theoretical efficiency of a binary device is 40%, this limit can be increased by utilising a design with a better approximation of the standard convex lens for example a discrete Fresnel lens

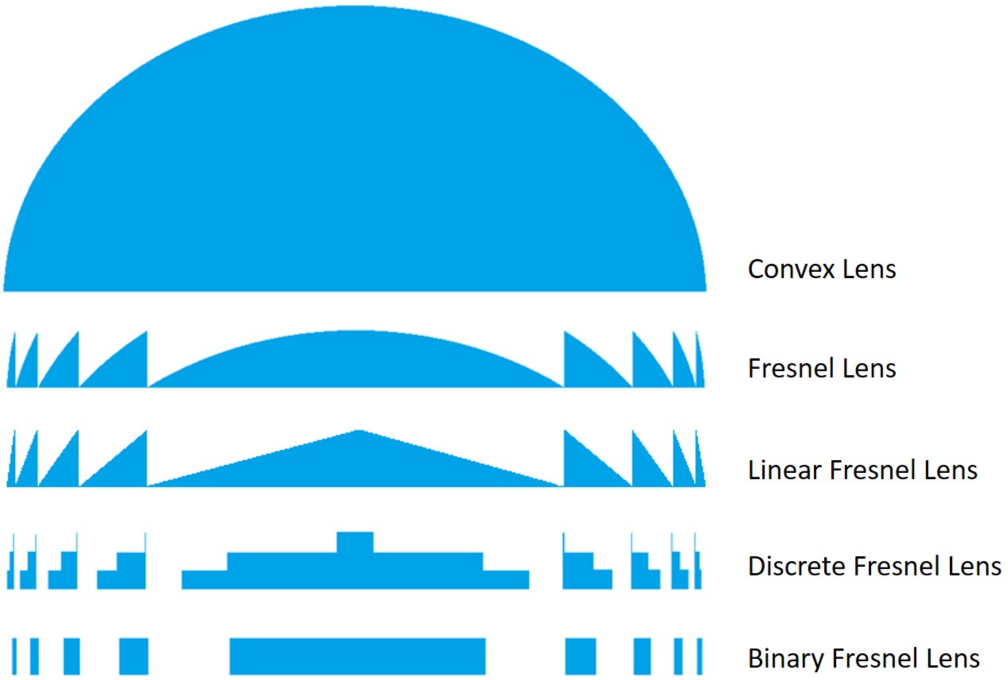

Figure 5.2: Diagram displaying the cross section of progressive Fresnel lens approximations of a convex lens.

A binary Fresnel lens consists of alternating rings of differing dielectric constant materials. In this case, the materials are paper and air. The desired focal length is used to design the size and spacing of the rings which are calculated using equation 5.3.1.

$$r_p = \sqrt{fp\lambda} \tag{5.3.1}$$

Where p is the ring number, r_p denotes the radius of the p^{th} ring, f is the desired focal length and λ is the wavelength of incident illumination. These transition points, for a binary paper lens, denote where a hole is cut and then where the paper starts again as demonstrated in figure 5.3. A HCP Laserscript 6840 was used to define the diffractive Fresnel structures, as in figure 5.3. The minimum resolution of the machine was found to be different depending whether the laser was cutting in a straight or curved trajectory yielding 150 µm and 200 µm resolution respectively. As a standard binary diffractive paper lens consists of concentric circular patterns the curved resolution is taken into account when producing designs.

The refractive index of the material only affects the phase retardation of the waves travelling through the material, therefore, it only affects the efficiency not the focal length. The efficiency of these devices is at its maximum when the phase shift between the two materials is 180°. As one material here is air, the paper thickness should be selected to produce the desired 180° phase shift.

A diffractive paper lens for use at 0.26 THz is demonstrated in [101]. Two different types of paper were used and both paraxial and non-paraxial designs were explored. Recent work has been undertaken exploring classical lens shapes such as elliptical and hyperbolic [102]. The setup in [101] uses the terahertz time-domain-spectroscopy method, here, the same techniques are explored using a vector network analyser (VNA).

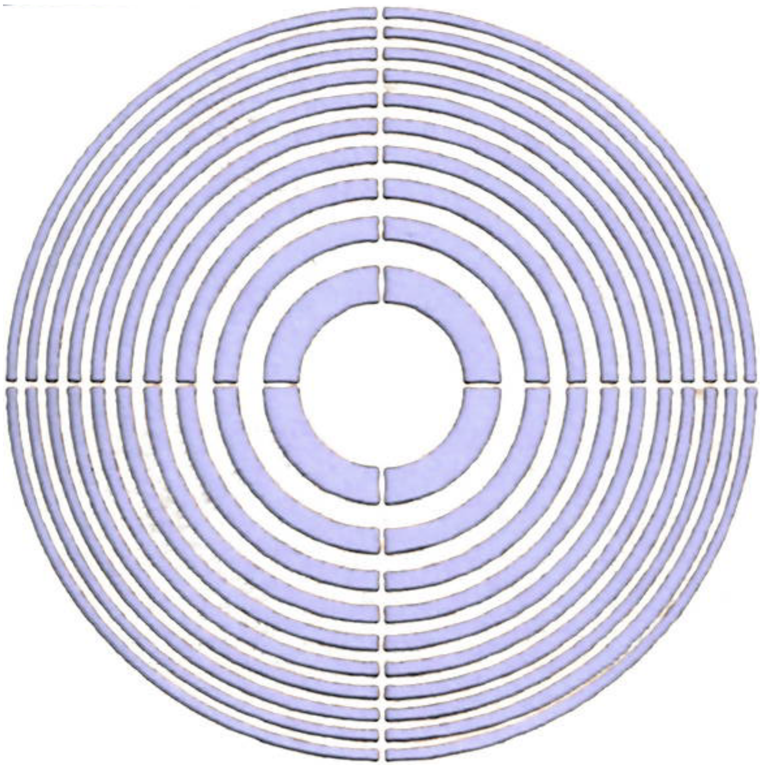

Figure 5.3: A 100 mm focal length binary Fresnel lens (49 mm physical size).

5.3.1 Design and Fabrication

A MATLAB program has been written which computes the radii for a range of focal lengths and maximum p values to identify optimal designs for the physical constraints. These physical constraints are due to the resolution of the laser cutting machine, the minimum thickness the paper can be cut to maintain its structural integrity and the maximum diameter of a beam in the terahertz setup. The maximum beam width is dictated by the largest parabolic mirror size (2 inches). As the resolution of the laser cutter is comparable to that of the feature sizes, the laser width needs to be accounted for when instructing where the laser cutter should make its cuts.

50, 100, 150 and 200 mm focal length designs were chosen. These are drawn up as a 2D sketch in Solidworks and exported as a .dxf file. This file can be imported into the laser cutter software where speeds and powers are allocated to each of the lines to be cut.

5.3.2 Experimental Setup

The experimental setup consists of one of the extender heads followed by a 90° off axis 2 inch parabolic mirror transforming the divergent beam from the horn antenna into a collimated beam. This beam passes through the lens which is held in the beam path by a 2 inch frame. At a distance of the expected focal length behind the beam the other extender head is placed as depicted in figure 5.4. This extender head is mounted on an XYZ stage.

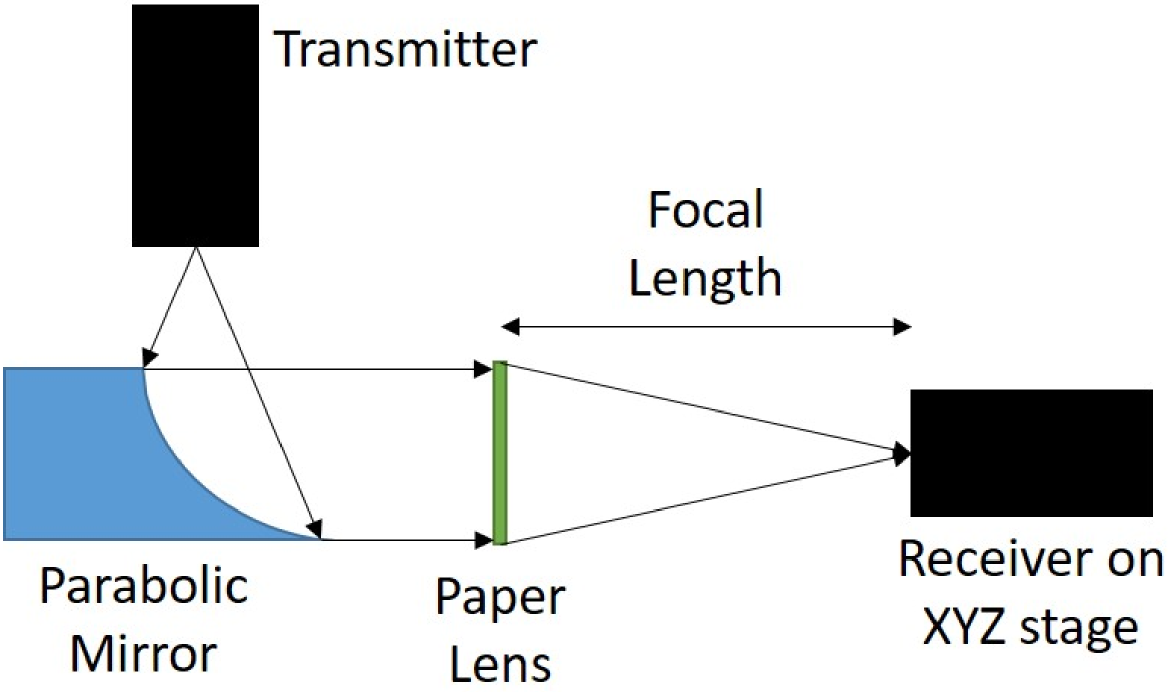

Figure 5.4: Diagram of experimental setup for testing the paper lenses.

5.3.3 Beam Profile of Lenses

Planar (XY) scans were undertaken for each of the lenses using a single sheet at the distance of the focal points (50 mm, 100 mm, 150 mm and 200 mm for their respective lenses). Figure 5.5 shows the response of each lens normalised with a scan taken without the lens. As can be seen, there is consistently an ≈ 6 dB increase in electric field intensity received at the focal point for each lens.

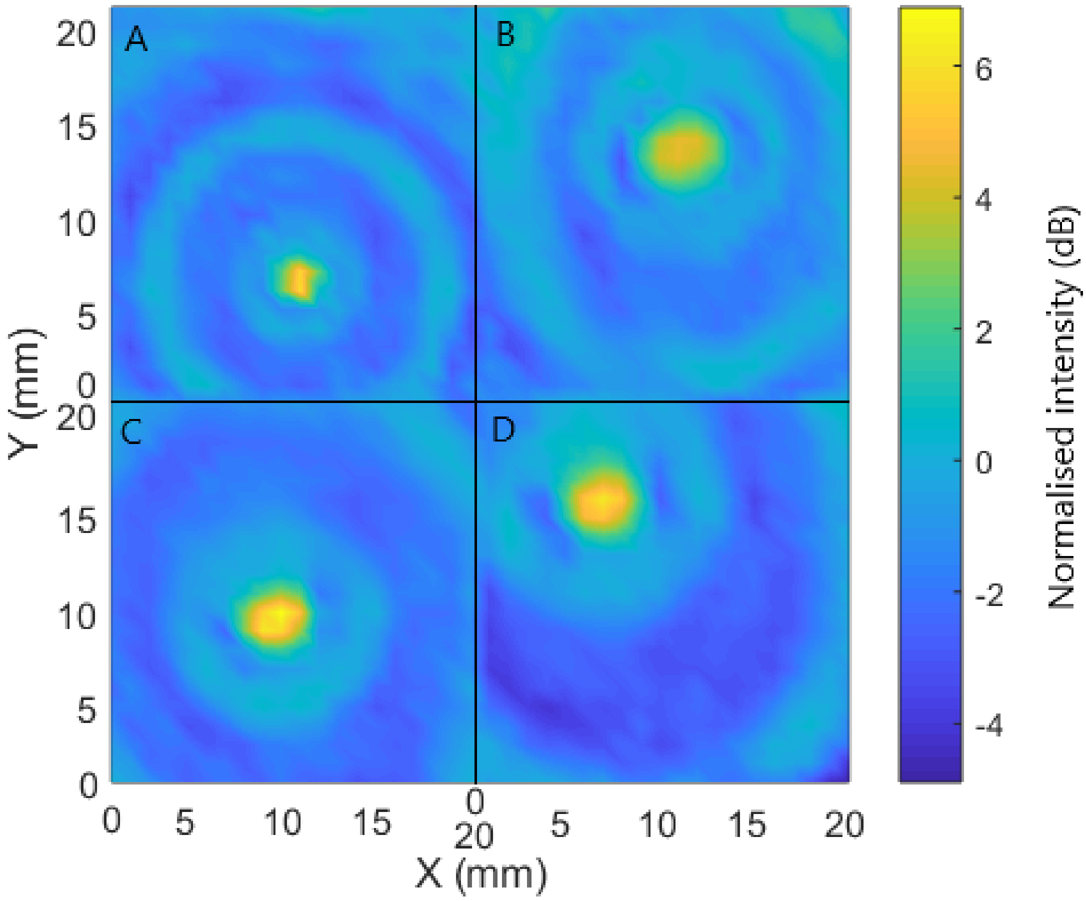

Figure 5.5: Normalised response for four designed lenses A: 50 mm focal length. B: 100 mm focal length. C: 150 mm focal length. D: 200 mm focal length.

The Fresnel lens designs are optimised for a paper thickness which gives a phase retardation of 180°. Figure 5.1 displays the phase delay measurements taken at 1 THz for various numbers of stacked paper sheets. It shows that the phase retardation introduced by three sheets of paper is the closest to the desired 180° phase shift. This is consistent with the measured electric field intensity for the lenses with different numbers of paper sheets as shown in figure 5.6, where the maximum power focal spot is observed for three sheets of paper. The optimisation increases the electric field intensity at the focal spot, by a further 4 dB, to 10 dB.

Additional sheets of paper increase absorption proportionally with the number of sheets. The additional absorption from passing through three sheets of paper, as compared to one, is small compared to the increase in peak power due to the increased efficiency of the lens by correcting the phase retardation to nearer 180°. Hence, the overall power has increased from one to three sheets. However it is useful to note that further additions of paper e.g. six sheets would result in a lower power at the focal point due to this additional absorption.

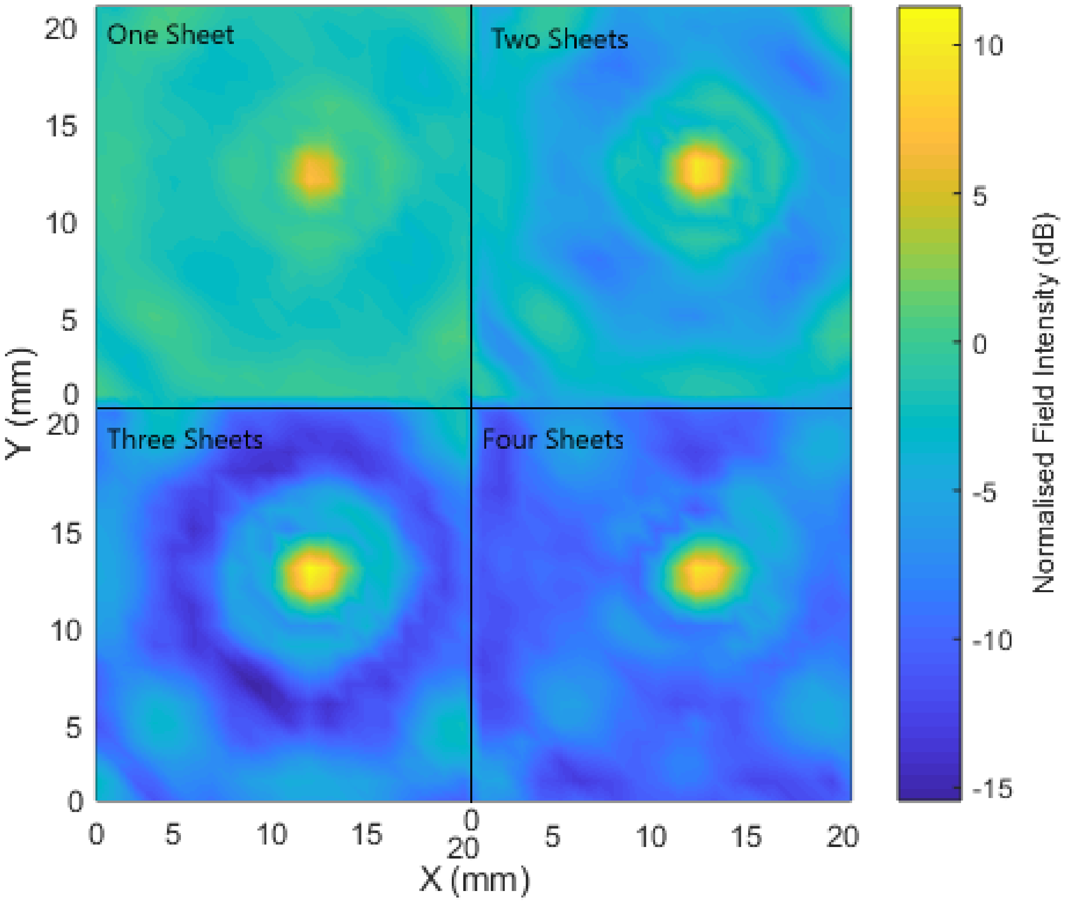

Figure 5.6: Normalised electric field intensity measured at the focal plane for identical 100 mm focal length lenses. Top left: A single sheet of paper thick. Top right: Two sheets of paper thick. Bottom left: Three sheets of paper thick. Bottom right: Four sheets of paper thick.

Shaped lenses tend to produce a distorted focal spot echoing the shape of the lens i.e. the triangular lens produced triangular shaped focal spot. The figure of eight lens (figure 5.7) shows that the overlap between the two circular designs has negligible effect on peak power as compared normal single sheet binary Fresnel lenses ($\approx$ 6 dB increase at the focal point).

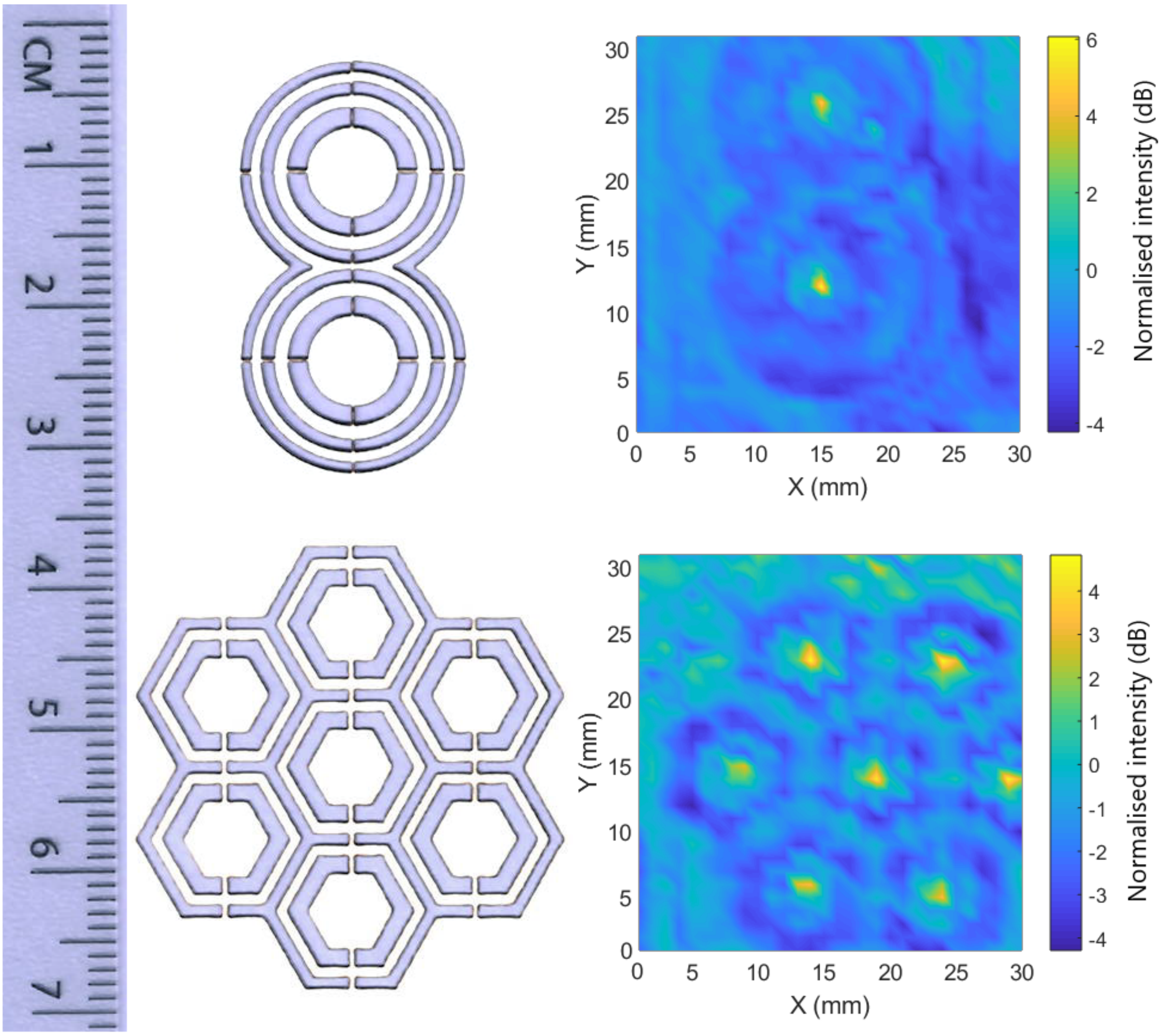

Figure 5.7: Top left: An image of the multifocal figure-of-eight paper binary Fresnel lens with 35 mm focal length. Top right: XY scan of the normalised electric field intensity for the figure-of-eight lens at the focal plane. Bottom left: An image of the multifocal hexagonally close packed (HCP) array of hexagonal lenses with 25 mm focal length. Bottom right: XY scan of the normalised electric field intensity for the HCP array of hexagonal lenses at the focal plane.

The approximation of the hexagonal lens in figure 5.7 is reasonable, yielding ≈ 5 dB which is particularly good considering the size of each lens is significantly smaller meaning there are fewer rings (max p is lower). The benefit of using shaped lenses such as hexagon or square is that they can achieve 100% packing density thus maximising the number of lenses in an array of a given area.

As previously stated, the maximum theoretical efficiency of a binary device is 40% which can be increased by better fitting the lens shape to a standard convex lens. A discrete Fresnel lens is a multi-tiered version of the binary Fresnel lens this design can increase the maximum theoretical efficiency limit as it is a better approximation of a curved lens. Each tier approximates a Fresnel lens across its respective thickness. A four tier device has a maximum efficiency of 81%. As paper comes in thin sheets it can easily form multi-level designs by stacking sheets. These sheets are held together using an acrylic frame with nuts and bolts on the corners to slot the sheets into. The lenses are cut with a paper frame and holes to slot through the bolts. Tests investigating this increase in efficiency from the introduction of multi-tiered devices show that this effect is not significant for standard copy paper. The highest increase in magnitude found at the focal point of a lens arrangement is 14.7 dB for a six tier design using six sheets of paper. Table 5.1 shows the resultant peak values for each of the measured thickness vs. number of tiers.

	Number of Tiers			
Number of Sheets	**1**	**3**	**6**	**9**
3	12.69	12.66	-	-
6	5.96	13.36	14.68	-
9	7.31	6.58	-	13.74
12	7.23	6.68	-6.744	-

Table 5.1: Table of peak focal point responses (dB) for different numbers of sheets and discrete tiers.

For any given number of sheets, it was beneficial to increase the number of tiers instead of stacking identical Fresnel lenses. However, it was found that for this type of paper increasing the thickness was not beneficial. This is for two reasons; firstly, as the thickness of the paper increases the absorption increases and therefore more power is removed from the system and secondly as each paper sheet gives 57° phase retardation three sheets is 9° away from the desired 180° required for maximum efficiency. Therefore, increasing in sets of three to six, nine or twelve sheets means moving further away from the desired 180° reducing efficiency while also increasing absorption. To maximise the utilisation of this technique it should be considered with thinner paper sheets or paper with a lower absorption coefficient. Filter paper may be one option for this as it firstly has fewer additives which can effect the absorption and it is generally made in thinner sheets than standard copy paper. A single sheet of Loikaw qualitative filter paper has a thickness of 12.5 µm, it exhibits a phase retardation of 46.7°. This produces a 4 sheet phase retardation of 186.8°. To ensure an exact 180° phase retardation either test a large range papers until one with a desirable phase retardation is found or preferably custom design paper sheets to the required phase retardation.

5.4 Liquid Wicking in Paper Lenses

V. Vassilev [105] demonstrates a terahertz moisture sensor with a resolution of 0.1% for moisture contents higher than 15%, the paper absorbs the moisture in the air and responds as a function of humidity. The fact that the moisture in the air can alter the refractive index of a lens causes an issue with using paper lenses for optical components as their refractive index is constantly changing with the variation in humidity. An option could be to keep the paper lenses in a humidity controlled environment but this can be costly and tends to negate the benefit of using cheap paper lenses in the first place. Unless a large number of varying lens designs are required, it is not the cheapest option for high quality consistent lenses. However, liquid absorption can be used to avoid this, for example, if the lens is soaked in oil then water from the air cannot displace it and absorb into the paper, producing a more stable lens design.

Water, known to be strongly absorbing in the terahertz region, results in the normalised intensity at the focal point being reduced. The dry lens (figure 5.8, left) measures 4.80 dB whilst the water soaked lens (figure 5.8, right) measures 4.51 dB. The overall reduction in the measured normalised intensity at the focal point is due to the absorbance of water being greater than the increased lens efficiency.

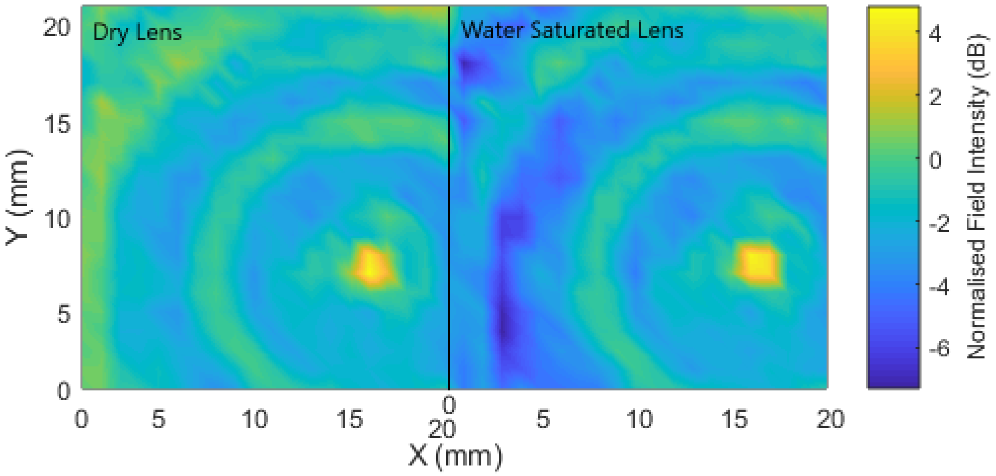

Figure 5.8: Left: XY scan of the normalised electric field intensity at the focal plane from a dry lens. Right: XY scan of the electric field intensity at the focal plane from a lens soaked with water.

The electric field intensity scans at the focal plane for oil soaked lenses are shown in figure 5.9. The normalised intensity of the focal point is increased from 6.23 dB (dry lens figure 5.9, left) to 8.36 dB (oil soaked lens figure 5.9, right). This is due to the refractive index of the lens increasing by the introduction of the oil. The phase retardation of the oil soaked lens is closer to the optimum 180° than the dry paper. The measured phase retardation for a single sheet of oil soaked paper is 82° at 1 THz as shown in figure 5.10. The increased intensity shows that the additional absorbance introduced by the oil has a lesser effect than the increased power at the focal point from a more efficient lens.

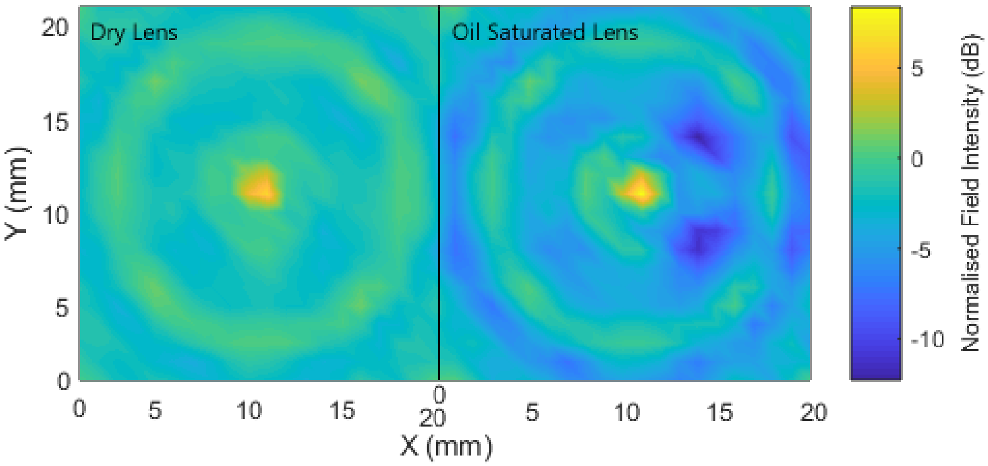

Figure 5.9: Left: XY scan of the normalised electric field intensity at the focal plane from a dry lens. Right: XY scan of the normalised electric field intensity at the focal plane from a lens soaked with sunflower oil.

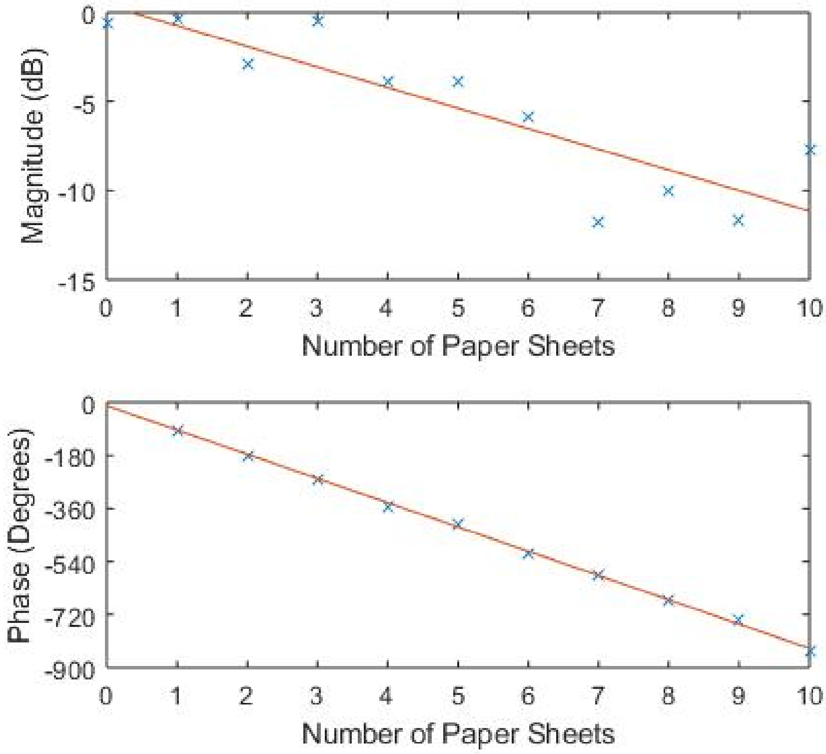

Figure 5.10: Figure of phase retardation and absorption of an increasing number of paper layers soaked in sunflower oil at 1 THz.

5.5 Conclusion

Paper is a readily available, versatile material which can be transformed cheaply and easily into 2D and stacked 3D designs. The use of a laser cutter in conjunction with the paper sheets allows for easily automated, consistent and accurate forming of an unlimited number of topologies. Its transparency to terahertz radiation can be of great use, especially with respect to its wicking capabilities. These properties lend the material well to liquid sensing applications soaking the liquid into paper. Preliminary testing of utilising the sinusoidal relationship between phase retardation and lens efficiency to calculate the refractive index of a liquid wicked into the lens found that for standard copy paper the absorption is too high to collect sufficient data to accurately map the sin wave. It may be possible, with further research, to utilise this technique using thinner paper sheets; filter paper for example.

Filling the cavities present in paper with oil prevents water from the environment being absorbed thus stabilising the lens geometry under different humidity conditions. The use of oil soaked lenses opens the possibility of tuning and tailoring the performance of paper lenses.

Chapter 6

Metamaterial Design and Fabrication

6.1 Introduction

This thesis has so far considered bulk sensing methods and introduced the use of paper as a terahertz lens. This chapter aims to move from bulk sensing to surface sensing integrating the use of paper to hold liquid analytes.

Metamaterials are engineered materials which exhibit designed properties. Two or more dissimilar materials are combined to produce a new material with different properties.

In this chapter, a dielectric and metal metamaterial is designed to produce a device with a sharp feature in the frequency range of the Durham VNA. This combination of materials is useful as the contrast between these two base materials can enable a wide range of design outputs. Metamaterials can introduce different bulk properties via artificial media structured on a scale smaller than the wavelength of the external stimuli. These shapes are periodic across the entire area and produce a bulk effect which is dependent on the pattern.

The scale of the metamaterial pattern is smaller than the wavelength of radiation; hence, at terahertz frequencies patterns are expected to be in the region of micrometres. Therefore a suitable fabrication method is photolithography.

The metamaterial shape and size can be designed to produce the desired frequency response. Often, initial designs are chosen using simulations [106]. Research is often carried out which performs in depth simulations but does not produce experimental results. Simulations often model perfect versions of the design and do not take into account many real world considerations. These cause inconsistencies with the simulated and experimental results. This chapter shows both simulated and experimental results. The differences between the simulated and experimental responses are drawn from the simulations working from 'perfect' versions of the design. For example a perfect electrical conductor is used as the metal in these simulations this can be improved by using specific metals however this is only possible if the characterisations for the metal used is available. Another strong contributor to the contrast between simulation and experimental response is fabrication defects; particularly in the case of metamaterials once the periodicity is broken this alters the metamaterial response significantly. These can be taken into account using more sophisticated simulations but the focus on this thesis is the experimental work and the simulations are just used here as a design aid.

Metamaterials can introduce a strong localisation and enhancement of fields to improve sensor selectivity enabling detection of trace substances in analytes [107]. Microfluidic sensors [108] utilise the most sensitive area of the metamaterial surface to strategically place fluid resulting in a high sensitivity per unit volume. This also keeps the layer of fluid thin which is essential for low power systems analysing high absorption liquids. Microfluidic sensors have been rising in popularity in recent years and although the sensitivity per unit volume is high for these devices it has been shown that the overall sensitivity is higher when the fluid is in contact with full metamaterial surface [109]. Therefore, in applications where the fluid is available in volumes larger than microlitres, such as serum samples, it is beneficial to cover the whole substrate with the fluid.

Paper is explored as a liquid analyte holder which offers permeability so the liquid under test can be wicked directly into the paper. Paper has been used as a substrate to measure the concentrations of substances which could be found in bodily fluids such as glucose and urea [110]. Many novel methods have been used to fabricate the metamaterial directly onto paper such as inkjet printing [111] and wax printing [112]. The metamaterial presented in this thesis is fabricated onto plastic and paper is used to hold the analyte in contact with the metamaterial surface. This improves the metamaterial pattern, due to the smoothness and non-permeability of plastic, compared to paper, allowing for superior fabrication whilst still taking advantage of the wicking properties of paper.

6.2 Photolithography

Photolithography is the general term for the use of photosensitive materials to create small structures. This is achieved by utilising the properties of a photosensitive material to enable access to certain sections of the substrate whilst protecting other sections thus allowing for the deposition or chemical etching of material to fabricate the desired structures in the desired materials. There are two types of photosensitive material; positive photoresist and negative photoresist. A positive photoresist is a cross linked material for which exposure to ultraviolet (UV) radiation causes these strong cross links to break. Post exposure, the now un-crosslinked sections of resist can be removed using a developer. Patterns within the resist can be formed by blocking sections of the resist from UV exposure. A mask is used for this. A mask can be anything which blocks light in the desired pattern from acetate with black ink to glass coated with metal tracks. Negative photoresist works on the same principle, however, the crosslinking works inversely to positive photoresist. The material starts off un-crosslinked and forms strong crosslinks with UV exposure. Where positive resist will have resist remaining on the ‘blocked out’ or unexposed areas of the substrate, negative resist will remain in the exposed areas and be removed by developer in the areas which have not been protected from UV. This thesis utilises positive lithography for the fabrication of the metamaterial designs.

6.2.1 Positive Photolithography

Positive photoresists generally consist of the same active material blended with various types and quantities of solvents to alter the viscosity of the photoresist. For example commonly used photoresists Microposit^{TM} S1813^{TM} and Megaposit^{TM} SPR^{TM} 220-7.0 both use Diazo Photoactive Compound as their photoactive ingredient. To pattern a photoresist, it needs to be in a uniform film on top of a substrate. Classically, silicon is used as a substrate in micro-fabrication [113] but many other materials are common nowadays including plastic [114]. A controlled thickness film is deposited onto the substrate via the use of a spinner. Spinners utilise centripetal force to spread the photoresist across the surface forming a uniform layer. The viscosity of the photoresist, the temperature and the spin process dictate the thickness of the layer formed. A common photoresist used throughout the work in this thesis is S1813. S1813 produces a 1.3 µm thick layer when spun at 3700 rpm at 25°C. For alternate thicknesses different viscosity photoresists can be found commercially. Alternatively, a viscous fluid can be thinned down using a solvent such as ethylene carbonate (EC) solvent. EC solvent can be used for most positive photoresists, however it is preferable to purchase a commercially available resist to ensure consistency. If fine tuning of the thickness is required, it is simpler and more common to alter the spin speed. Using the same formula, a thinner layer is produced by spinning at a faster speed and a thicker layer is produced for slower speeds. Spin coating is a reliable and consistent method of producing a uniform film and is used as the industry standard.

A photolithography process using positive resist is shown in figure 6.1. It shows the spin coating of a photoresist onto a substrate, a patterning process using a mask with UV exposure and development in a chemical developer. This results in a patterned layer of resist which is easily designed and translated onto the substrate in sizes which are significantly smaller than could be manufactured manually.

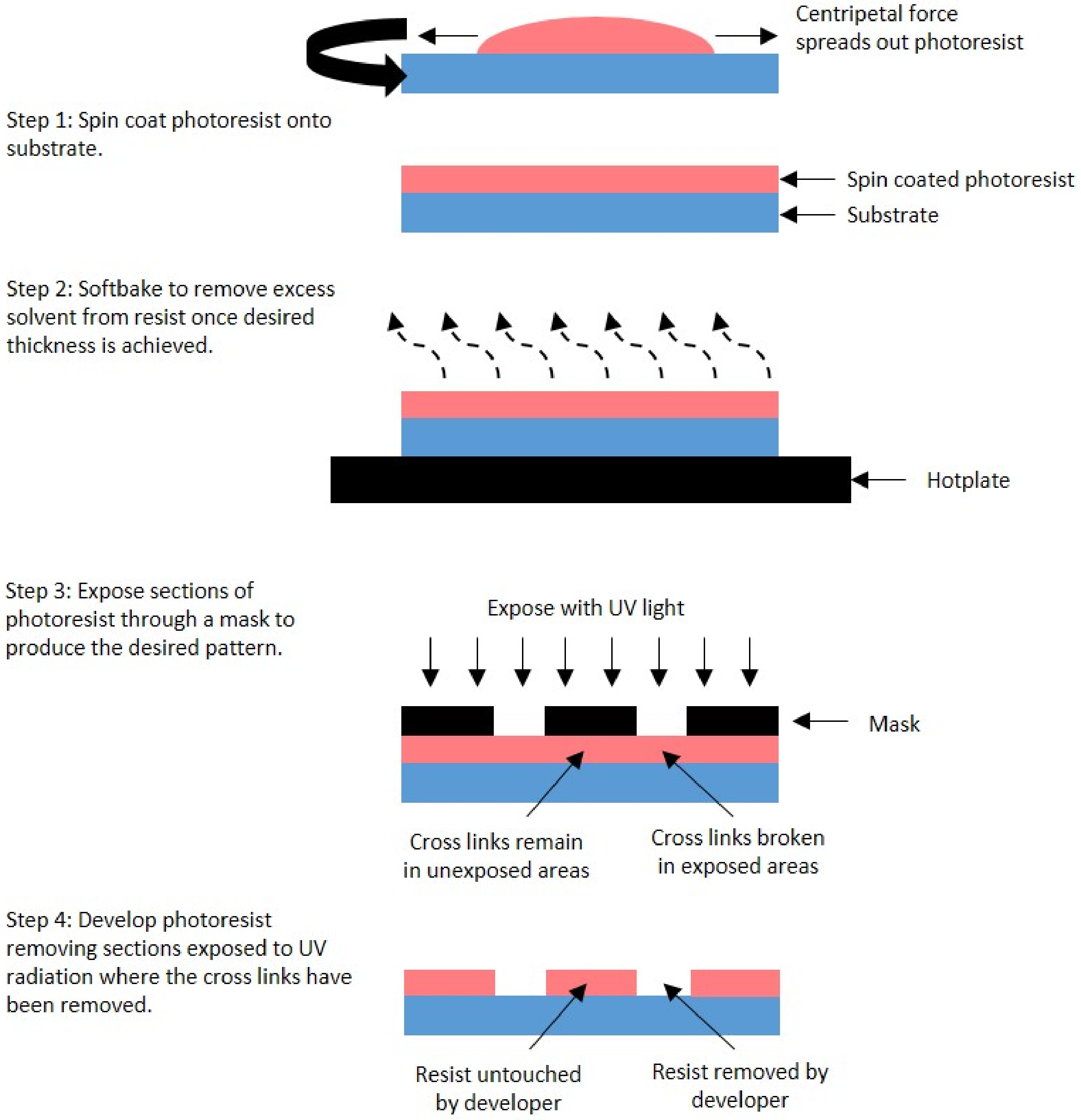

Figure 6.1: Diagram showing a lithography process using positive photoresist.

A nominal recipe for positive photolithography is as follows:

1. Clean and dry the substrate. Acetone is used to remove impurities but this is known to leave a residue so isopropyl alcohol is used following the acetone wash to remove this residue.

2. Place substrate onto spinner, hold in place using the vacuum. Deposit resist in the centre of the substrate ensuring no bubbles. Spin S1813 at 700 rpm for 30 seconds to spread the photoresist over the substrate. Spin for 2 minutes at 3700 rpm to produce an even layer of 1.3 µm in thickness.

3. Softbake on a hotplate at 115°C for 60 seconds. This removes the remaining solvent within the photoresist.

4. Expose 75 $\mathrm{mJ\,cm^{-2}}$ using desired mask to block areas of the photoresist from exposure.

5. Develop in Microposit 351 developer for 40 seconds.

6. Rinse substrate in de-ionised water to wash away developer and dry using a nitrogen gun.

6.3 Microfabrication

The patterned resist is commonly used as an aid to fabricate a metallic pattern e.g. copper tracks of a circuit. There are two methods of translating this photoresist pattern to the desired metal pattern. For lift-off metal is deposited onto the sample post lithography. This results in some of the metal laying directly on the substrate and some laying on the patterned photoresist. The photoresist that remains and thus the gold on top of these sections of resist can then be removed by a lift-off procedure. A remover is used to etch and lift-off the remaining layer of resist and metal leaving only the metal that was deposited directly onto the substrate. The other method, and the one which is used for the fabrication within this thesis, is etching.

6.3.1 Etching

Etching requires the substrate to be coated with the desired metal prior to the lithography process. The photolithography process otherwise remains the same. Once patterned, the uncovered sections of metal are wet etched to remove the metal while the covered sections are protected by the remaining resist as shown in figure 6.2. The remaining resist is removed with acetone and IPA. This thesis uses aluminium which can be removed using the etchant as follows from [115]:

- 73% orthophosphoric acid (H_3PO_4)
- 3.1% nitric acid (HNO_3)
- 3.3% acetic acid (CH_3COOH)
- 20.6% water (H_2O)

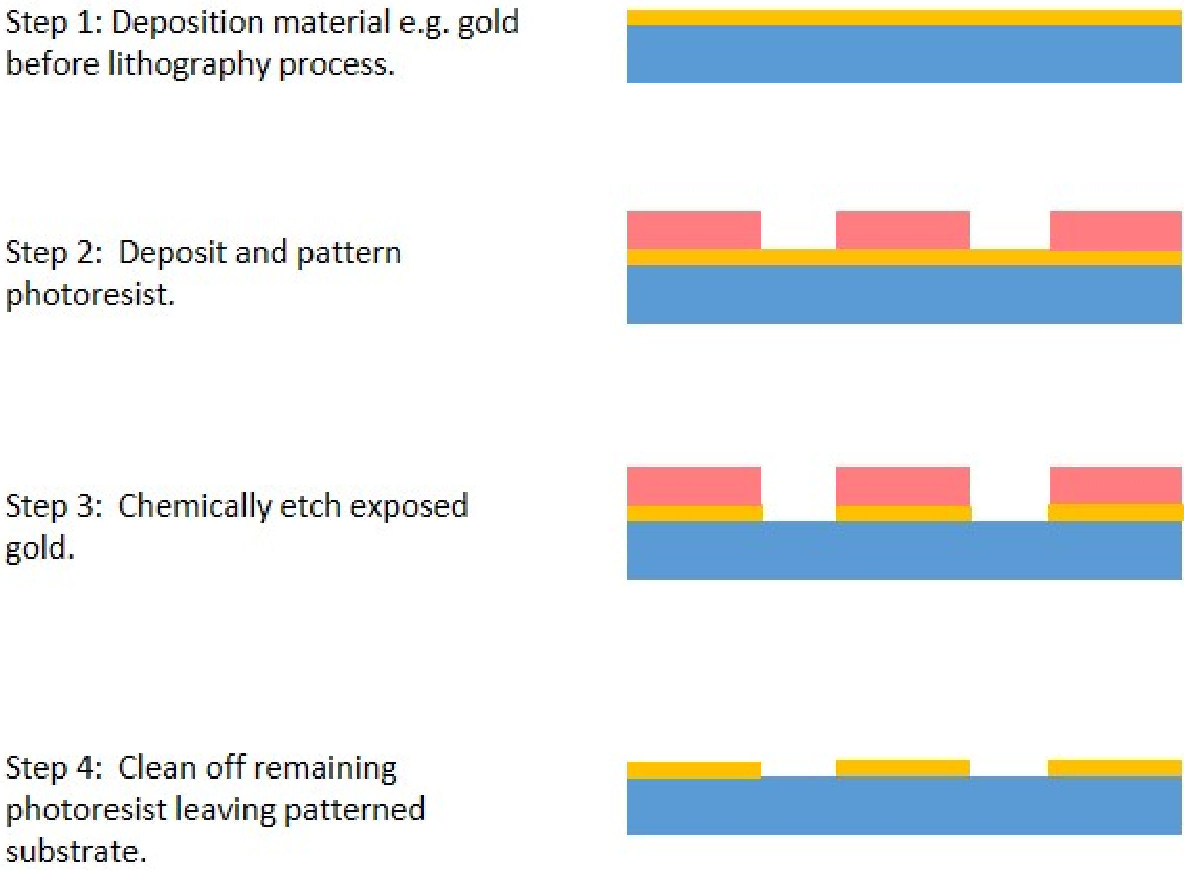

Figure 6.2: Diagram showing the etching process for patterning.

6.3.2 Processing Constraints

Processing constraints such as exposure dispersion, shadowing of photoresist in metal deposition and anisotropic or isotropic etching can cause disparities between the mask design and the design produced on the substrate.

Exposure dispersion happens with both lift-off and etching as it occurs during the exposure stage of the process. The light travelling through the photoresist disperses through the thickness of the resist. This is usually negligible however, it can produce a retrograde side wall that is overetched at the base thus producing a wider gap at the interface of the substrate than the surface of the photoresist. This can be reduced by reducing the thickness of the photoresist. A photoresist thickness of 1.3 μm is used in this thesis to reduce this issue.

Shadowing of photoresist relies on the fact that light travels in straight lines and that the light source comes from a finite position in space. Hence, for sections of the photoresist not directly in line with the light source the thickness of the mask will cast a shadow upon the photoresist. The effect is minimised in this thesis by reducing the thickness of the mask. It consist of thin metal patterns on the bottom side of a glass plate so the pattern can be placed directly in contact with the surface of the photoresisist and is approximately 200 nm thick.

Isotropic etching is where the etchant removes material in the y plane, as desired, at the same rate as it etches in the x plane. This can cause sloped side walls and undercutting. It always results in an etch where the base of the substrate has a smaller gap than the surface in contact with the photoresist. Hence, thin photoresist and metals are desired to reduce the vertical path the etchant has to travel thus reducing the horizontal etching. A 100 nm metal layer is used in this thesis to minimise issues with regards to this.

6.4 Fabrication of Metamaterials on a PEN Substrate

The plastic is as thin as possible so the loss of power is minimal. In addition, the specific plastic has been chosen to be not only chemically stable and suitable for lithographic patterning but also has low absorption.

The plastic used for fabrication is Polyethylene Naphthalate (PEN). The thickness of the PEN used is 12.5 µm. The absorbance is relatively low and could be tolerated for any of the thicknesses investigated. It was found that smaller thicknesses e.g. 4.5 µm were challenging to handle. Thicker sections of PEN (15 µm +) were stiffer and had a natural curl which caused fabrication difficulties.

The metamaterial is formed using aluminium, at a thickness above the skin depth which was chosen for ease of deposition, etching and low cost.

6.5 Metamaterial Simulation and Design

6.5.1 Lumerical Simulations

Lumerical, a 3D Maxwell solver, has been used to determine appropriate designs for the desired features at frequencies within the VNA range (0.75 to 1.1 THz). All designs were modelled on a plastic substrate, polyethylene naphthalate (PEN), using a 'perfect conductor' as the metal.

The metamaterial features for this project need to have a high-Q-factor. The reasons for this are twofold; firstly the operating window of the VNA is reasonably small therefore the primary feature of the metamaterial needs to be sufficiently narrowband to be sharp within this region, secondly higher Q-factor designs can offer higher sensitivity for sensing applications. As sensing small changes in refractive index is the sole use for these metamaterials increasing sensitivity is imperative.

Initially, well known and characterised metamaterial designs were manipulated via simulation to fall within the VNA range. A 3D model of the metamaterial design is drawn up within the Lumerical software which is simulated to inspect the results. Figure 6.3 shows how the 3D model of a standard split ring is modelled within Lumerical.

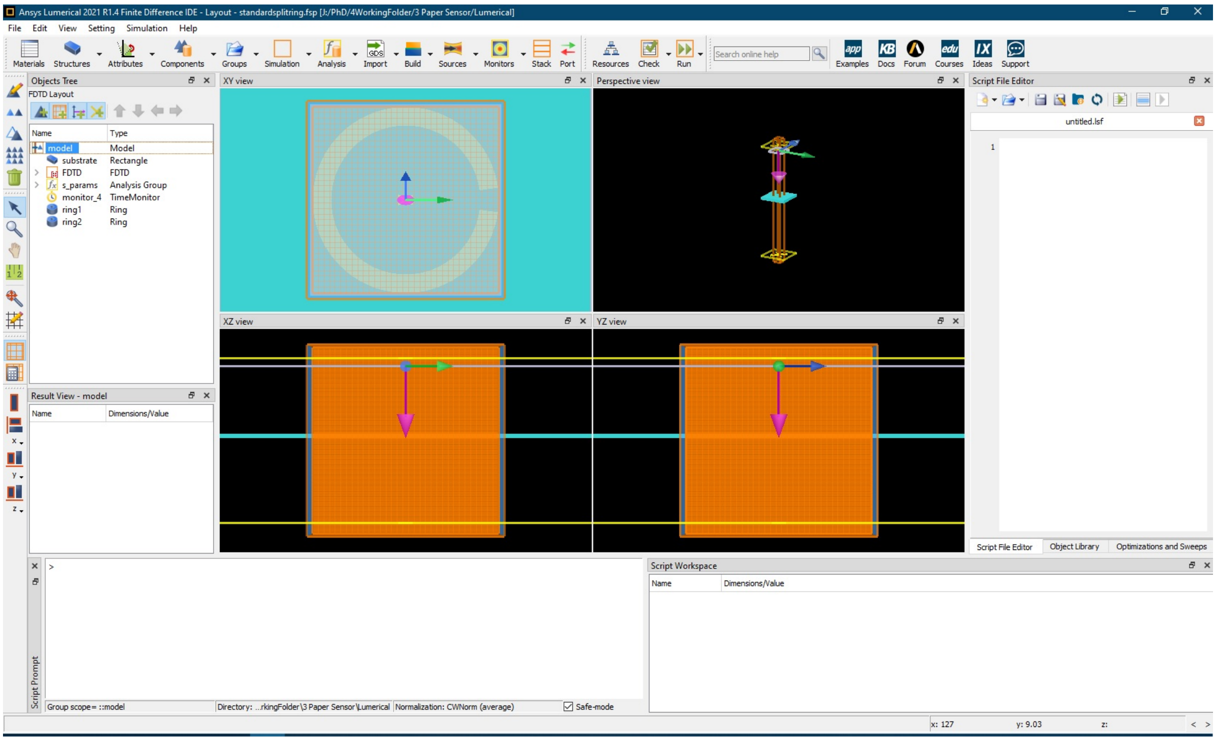

Name	Type
model	Model
substrate	Rectangle
FDTD	FDTD
s_params	Analysis Group
monitor_4	TimeMonitor
ring1	Ring
ring2	Ring

Group scope= ::model
Directory: ...rkingFolder\3 Paper Sensor\Lumerical
Normalization: CWNorm (average)
☑ Safe-mode
x: 127
y: 9.03
z:

Figure 6.3: Screenshot showing the 3D model of a standard split ring design modelled in Lumerical.

The dimensions of the metamaterial object can be altered using a geometrical code which automates the creation of different sized shapes. Figure 6.4 shows the code used to model a standard split ring. Each of the variables can be altered in the tab as displayed in figure 6.5, enabling quick and easy automated generation of a new metamaterial design. These can then be simulated and their results inspected which enables the fine tuning of the metamaterial dimensions to produce the desired feature.

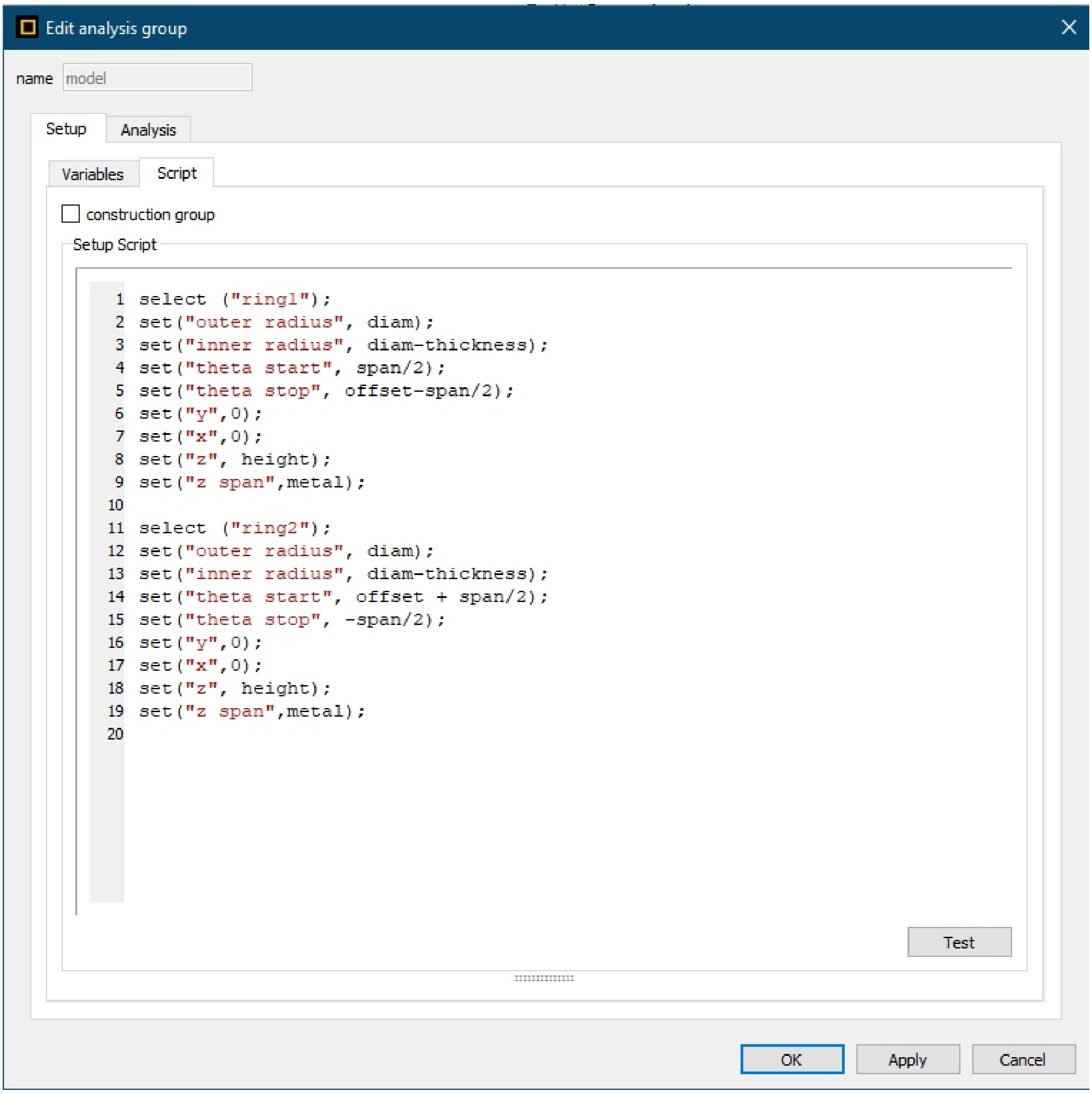

name model

☐ construction group

```
select ("ring1");
set("outer radius", diam);
set("inner radius", diam-thickness);
set("theta start", span/2);
set("theta stop", offset-span/2);
set("y",0);
set("x",0);
set("z", height);
set("z span",metal);

select ("ring2");
set("outer radius", diam);
set("inner radius", diam-thickness);
set("theta start", offset + span/2);
set("theta stop", -span/2);
set("y",0);
set("x",0);
set("z", height);
set("z span",metal);
```

Figure 6.4: Screenshot of code used to geometrically model standard split ring designs enabling automated change of model dimensions.

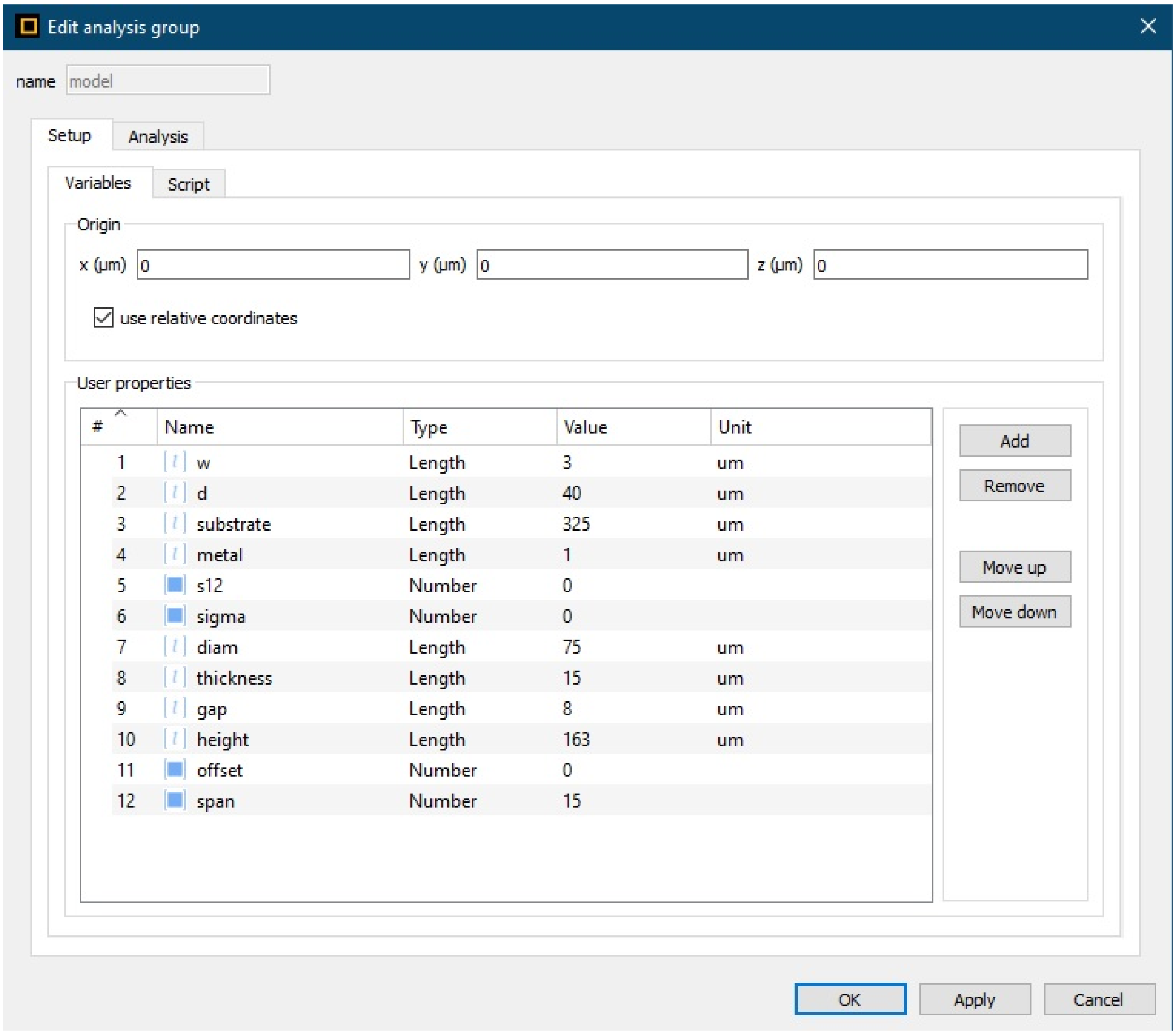

name: model

x (µm): 0
y (µm): 0
z (µm): 0

☑ use relative coordinates

#	Name	Type	Value	Unit
1	w	Length	3	um
2	d	Length	40	um
3	substrate	Length	325	um
4	metal	Length	1	um
5	s12	Number	0	
6	sigma	Number	0	
7	diam	Length	75	um
8	thickness	Length	15	um
9	gap	Length	8	um
10	height	Length	163	um
11	offset	Number	0	
12	span	Number	15	

Figure 6.5: Screenshot of Lumerical variables used to change the geometrical model for the standard split ring designs enabling automated change of model dimensions.

Boundary conditions are set as periodic for each of the X and Y dimensions. This creates the repeated square array of features which would be present on a fabricated device. The FDTD X and Y dimensions dictate the domain which is repeated using the periodic boundary conditions. In the Z direction perfectly matched layers (PML) are created to artificially absorb all incident radiation to each of these surfaces.

The simulation time is chosen so that the pulse is significantly reduced in amplitude by the end of the simulation but not excessively so that the pulse is not visible on the trace. The aim for this is to ensure the simulation has sufficient time to converge whilst also minimising simulation time as much as possible. Figure 6.6 shows the time plot of the electric field (E) for the full simulation time; 70,000 fs. This time was used for all simulations as it provided sufficient time for the simulations to converge whilst keeping memory requirements within the ability of the available resources.

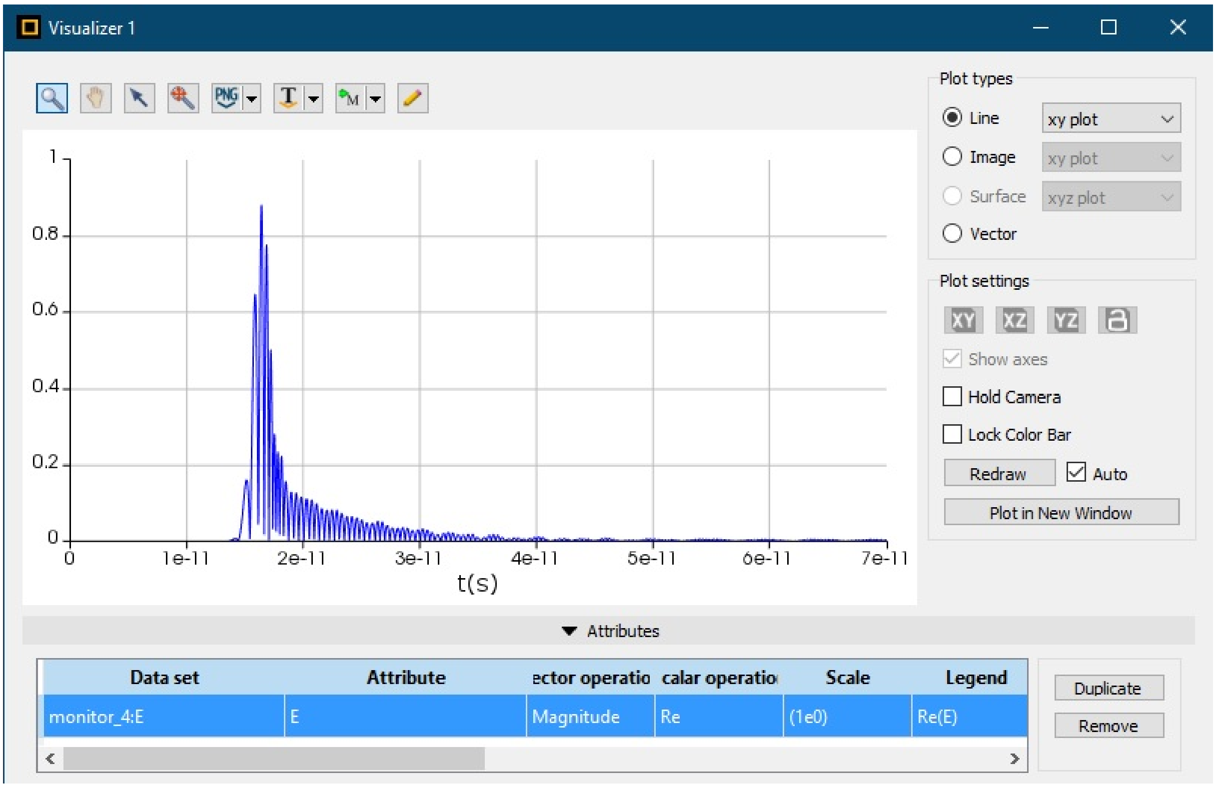

● Line xy plot
○ Image xy plot
○ Surface xyz plot
○ Vector

☑ Show axes
☐ Hold Camera
☐ Lock Color Bar
☑ Auto

Data set	Attribute	ector operatio	calar operatio	Scale	Legend
monitor_4:E	E	Magnitude	Re	(1e0)	Re(E)

Figure 6.6: Screenshot of Lumerical plot showing the electric field (E) over the full simulation time (70 ps).

An analysis group is created in Lumerical using a standard S-parameter extraction code which calculates S-parameters from T (transmission) and R (reflection) values. The analysis group has dimensions extending past the FDTD simulation window and is setup with start and stop frequencies, propagation directions and polarisation angles. For these simulations various start and stop frequencies are used depending on the specific design. However, all encompass the VNA range between 0.75 THz and 1.1 THz. Most of the final simulations span quite a bit higher than 1.1 THz up to 2 THz or more and go down to 0.5 THz which ensures a full picture of the response is received. The simulations are extended further from the VNA window in the higher frequency direction as, from preliminary simulation and experimental tests, it was found that the experimental response was generally shifted down in frequency as compared to the simulation. In addition, the higher stop frequency also affects the minimum wavelength and therefore the mesh for the simulations.

Lumerical automatically assigns a standard mesh size based on the frequency range of the simulations. This mesh can be increased in accuracy on a sliding scale from 1-8 where 1 provides low accuracy and high speed simulations and 8 provides the most accurate measurements using this feature. For the majority of the experiments an accuracy of 6 is used which provides sufficient accuracy for these designs, where the simulation response converges. However, in some cases, the designs are too small and therefore require a very small mesh. Increasing the accuracy is sometimes sufficient to fix this problem otherwise this poses a simulation memory issue. Where the metamaterial pattern is small, a mesh is created over the specific metallic features which has a significantly smaller step size. This captures sufficient information for the FDTD simulations to step through the mesh and give an accurate result. Once the mesh size is reduced around the design the remainder of the simulation can have a larger mesh reducing overall memory use whilst still providing the accuracy required using a small mesh size around the metallic features.

6.5.2 Cross and Cross Variation Designs

Simulations were carried out to explore a range of simple shapes and evaluate their effectiveness as a high Q-factor metamaterial. A few designs were found to be strong candidates and were fabricated to experimentally test their performance.

Figure 6.7 shows the design of a basic cross devised from a modification of a square mesh design as shown in [116]. This design was further manipulated to produce a variation on this design which consists of a cross design with a cross removed from the centre creating four ‘L’ shaped sections as in figure 6.8. Their simulated responses are shown in figure 6.9 and their experimental responses from a standard transmission measurement (described in Section 3.2) shown in figure 6.10.

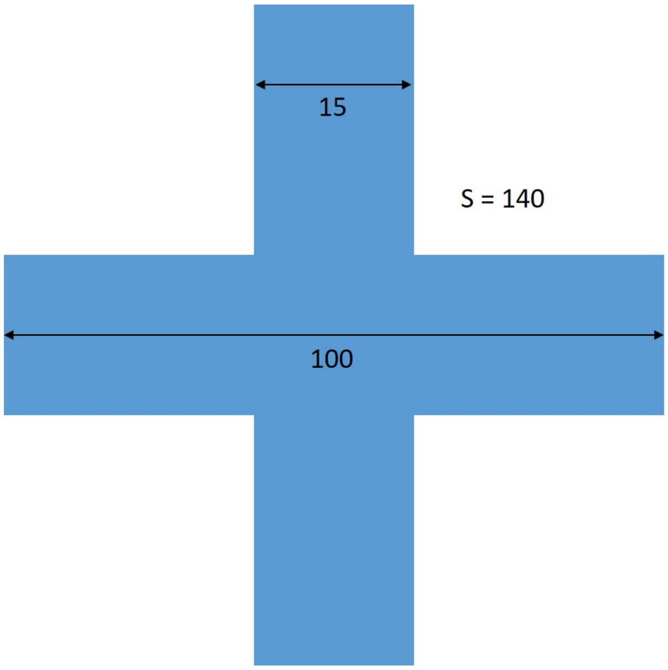

Figure 6.7: Diagram of cross design in the 0° orientation. Dimensions in micrometers (µm).

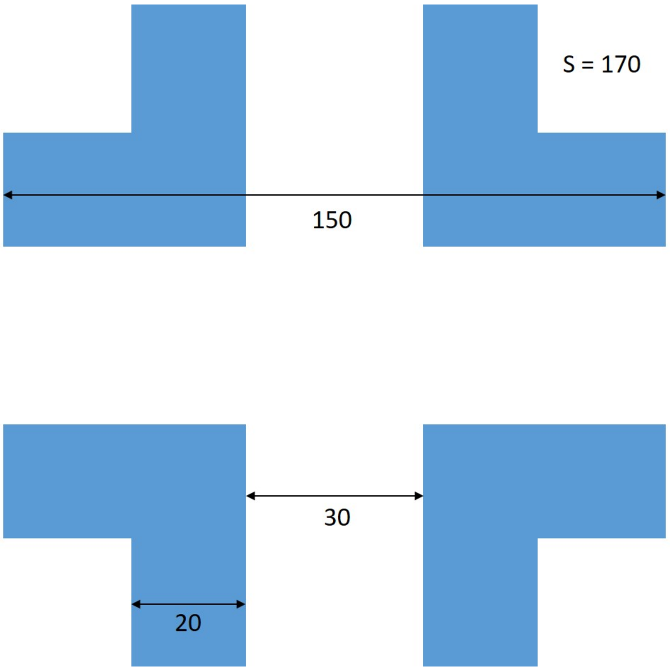

Figure 6.8: Diagram of cross variation designs in the 0° orientation. Dimensions in micrometers (µm).

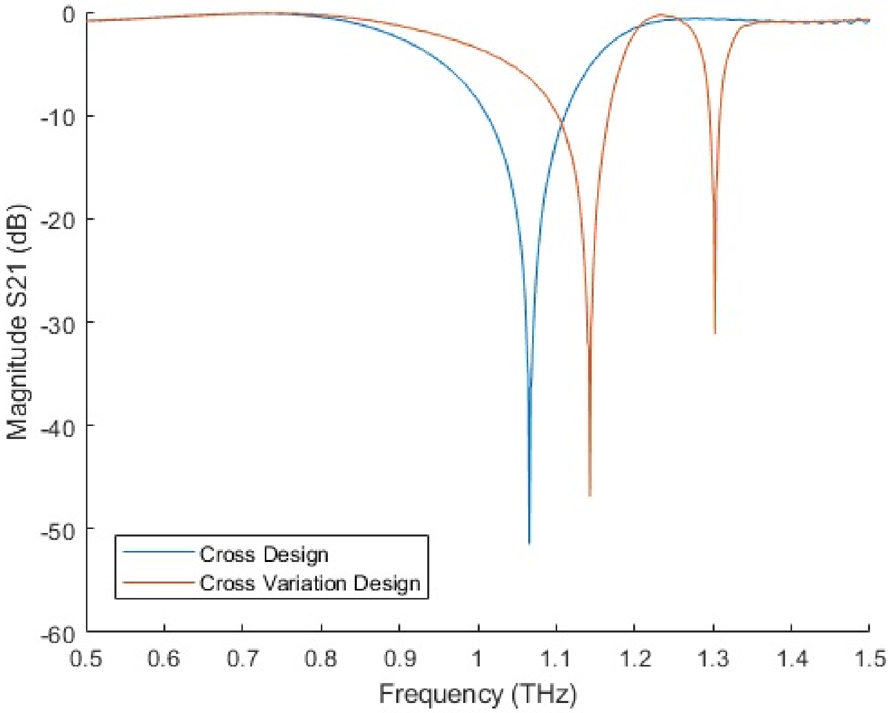

Figure 6.9: Graph of simulated responses for the cross and cross variation designs .

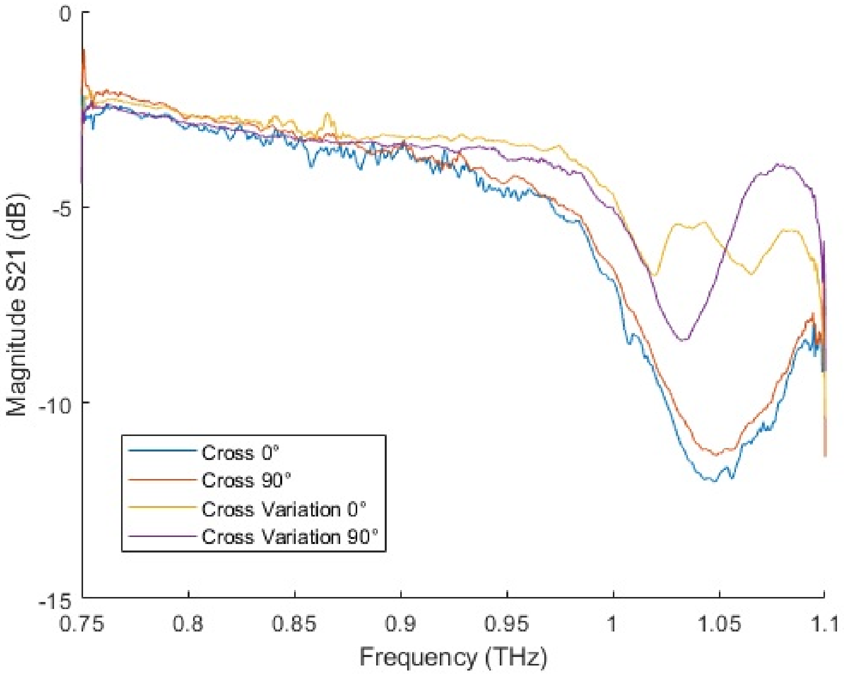

Figure 6.10: Graph of experimental response for the cross and cross variation designs each at a 0° (as shown in figures 6.7 and 6.8) and 90° angle through the beam. Data has been normalised using a free space scan no smoothing or manipulation has been carried out on this data besides finding the magnitude of S21.

As seen in figure 6.10 the cross design was found to produce a -8 dB peak within the VNA range at 1.05 THz for both the 0° and 90° orientations. The cross variation produced a smaller single absorption peak in a similar position for the 90° orientation at ≈ -5 dB. The 0° orientation showed a pair of absorption peaks as expected from the simulations however, in the experimental results the magnitude is small (≈ -3 dB). Theoretically both the 0° and 90° designs in this case should be identical as the cross and cross variation designs are geometrically identical when rotated through 90°. Hence, the significant difference between the two cross variation responses is thought to be due to either a fabrication defect or further damage to the metamaterial design due to the flexible substrate. Besides feature position and magnitude, the shape of the response is wider for the experimental results as compared to the simulated response. This is thought to be due to fabrication defects and/or damage to the metamaterial pattern from substrate movement breaking the periodicity of the metamaterial causing a broadening of the feature shape.

6.5.3 Split Ring Designs

Now that some designs have been simulated to produce features within the VNA region and the relationship between the simulation and experimental responses is better known, further designs are explored to find a higher Q-factor design. Five designs have been selected to investigate. Each of these designs has been fabricated for a range of frequencies so the optimal design can be chosen based on experimental performance. A standard transmission measurement is used as described in Section 3.2 of this thesis. This is because the experimental results are commonly different to the simulations and in this case the features need to be within the region of the VNA which is relatively narrow so this may mean that the simulated response is set outside the frequency range. Designed frequencies are generally at the higher end of the VNA range (1.1 THz) and above to ensure features are captured within the VNA range during the experimental tests as this was found to shift down. The feature will shift to lower frequencies with increased refractive index materials placed in contact with the substrate surface so features at the top end of the range are preferred.

The S dimension for each of these designs is the spacing between repetitions in a regular square array i.e. from the centre of each design there will be four other designs with their centres at a distance of S directly left, right, up and down from the designs shown and from the centres of their designs and so on.

Double ‘D’ (DD) Design

Reference [117] describes an asymmetric split ring design modified to two semicircular outlines. The two back to back resonators resemble a capital ‘D’ with a split. Therefore, this design will be referred to as the double ‘D’ design abbreviated to DD. The splits are centred at 15° off the perpendicular from the spine of the ‘D’ shape with a swept angle of 14° as displayed in figure 6.11. Radius, lattice constant, line width and central gap size were kept at the same ratio as in [117]. The design shown in [117] describes a metamaterial centred with a primary feature at 0.3 THz. The topology of the design has been modified to multiple designs with features at 1.1, 1.23, 1.42, 1.69, 1.85 and 1.99 THz.

These start at the top of the VNA range, 1.1 THz, and increase at regular intervals to identify the design that is best suited for the application experimentally. Each of the chosen values for the labelled dimensions in figure 6.11 are recorded in table 6.1. Figure 6.12 shows the simulated responses for the DD designs.

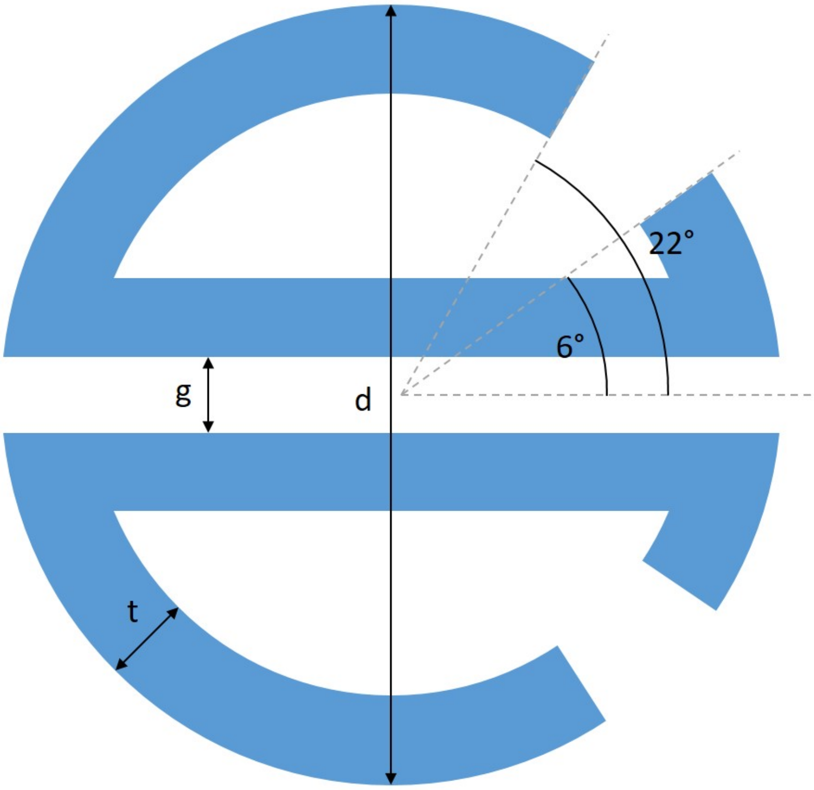

Figure 6.11: Diagram of double 'D' design in the 0° orientation.

Name	Thickness (µm)	Gap (µm)	Diameter (µm)	Spacing (µm)	Frequency (THz)
DD1	12	8	30	100	1.10
DD2	10	7	28	95	1.23
DD3	10	7	25	90	1.42
DD4	8	6	20	70	1.69
DD5	6	4	18	60	1.85
DD6	5	3	15	50	1.99

Table 6.1: Dimensions of double 'D' (DD) designs 1-6 and their simulated feature frequencies. Thickness (t), Gap (g), Diameter (d) and Spacing (s).

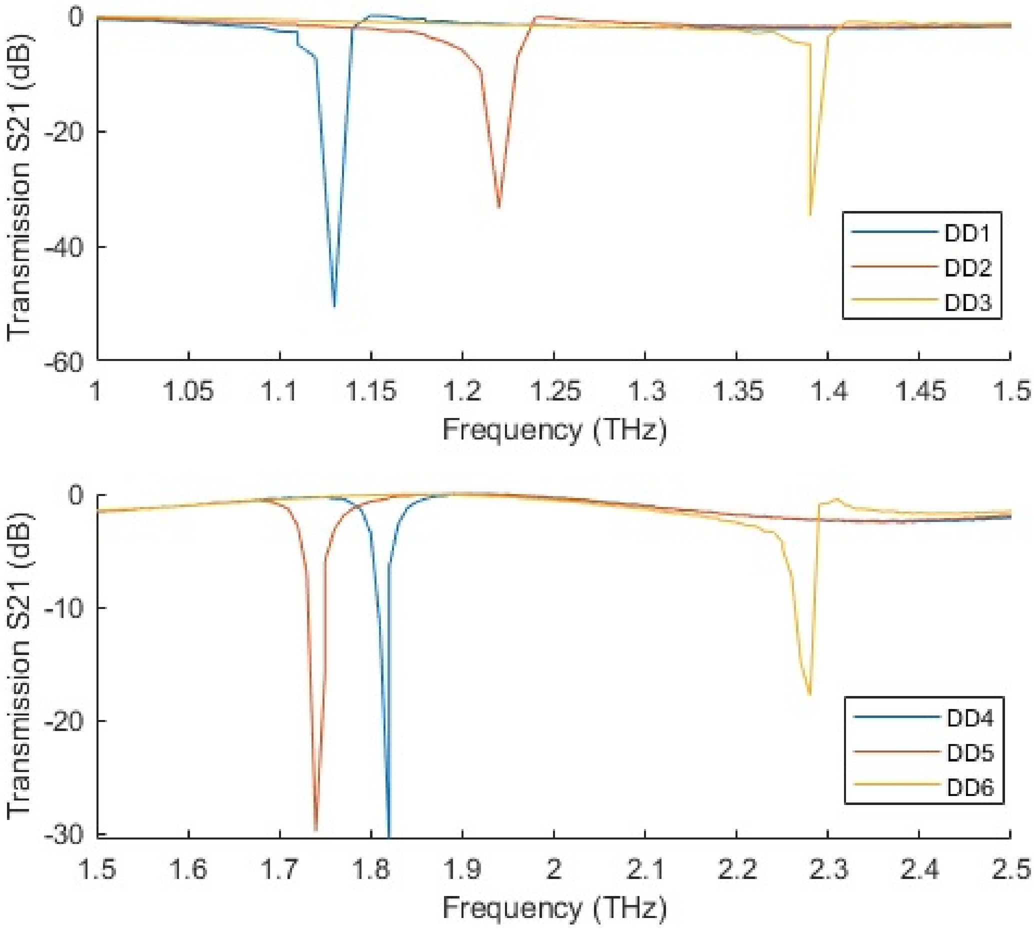

Figure 6.12: Simulations of S21 parameters with respect to the back to back 'D' designs 1-6 (DD1, DD2, DD3, DD4, DD5, DD6).

Four Asymmetric Square Split Ring (4SQ) Design

A second high-Q-factor design is described in [118] it is a square asymmetric split ring resonator in a mirrored quadrant array as shown in figure 6.13. Reference [118] shows that the mirrored quadrant arrangement has a significantly improved performance as opposed to the standard asymmetric square ring design. The example shown in [118] has a primary feature centred at 0.7 THz, this topology has been redesigned to have primary features centred at (0.98, 1.13, 1.44, 1.71 and 1.96 THz). The dimensions for each design is shown in table 6.2. Spacing for this design still refers to the spacing between the centre points of the entire design including all four squares. The spacing of each of the individual squares is $\frac{S}{4}$ from the centre of the full design to the centre of each of each of the individual squares in both orthogonal directions. Figure 6.14 shows the responses for each of the 4SQ designs.

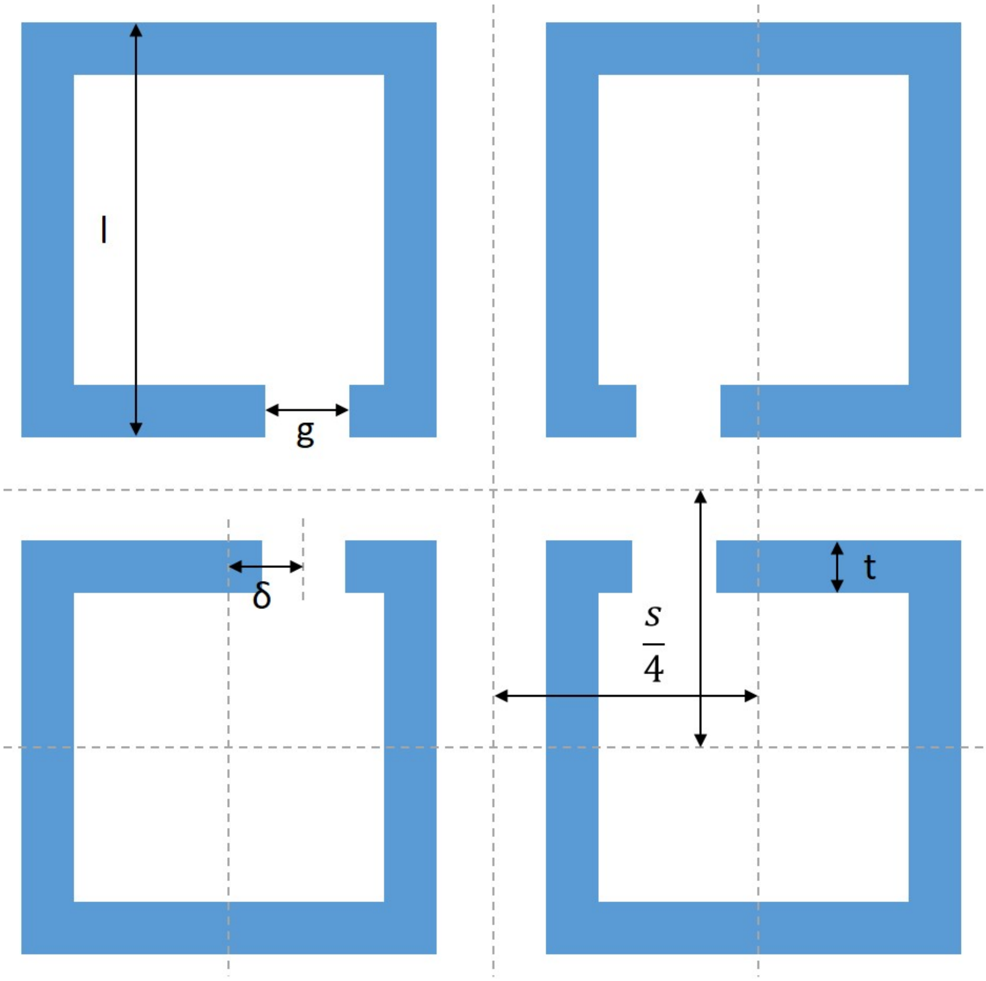

Figure 6.13: Diagram of mirrored quadrant asymmetric square split ring design in the 0° orientation.

Name	**Length** (µm)	**Thickness** (µm)	**Gap** (µm)	**Delta** (µm)	**Spacing** (µm)	**Frequency** (THz)
4SQ1	18	2	2	3	75	1.96
4SQ2	20	2.5	2.5	4	82	1.71
4SQ3	25	3	2	5	100	1.44
4SQ4	30	4	3	6	110	1.13
4SQ5	35	5	4	7	125	0.98

Table 6.2: Dimensions of four square (4SQ) designs 1-5 and their simulated feature frequencies. Length (l), Thickness (t), Gap (g), Delta (δ), Spacing (s).

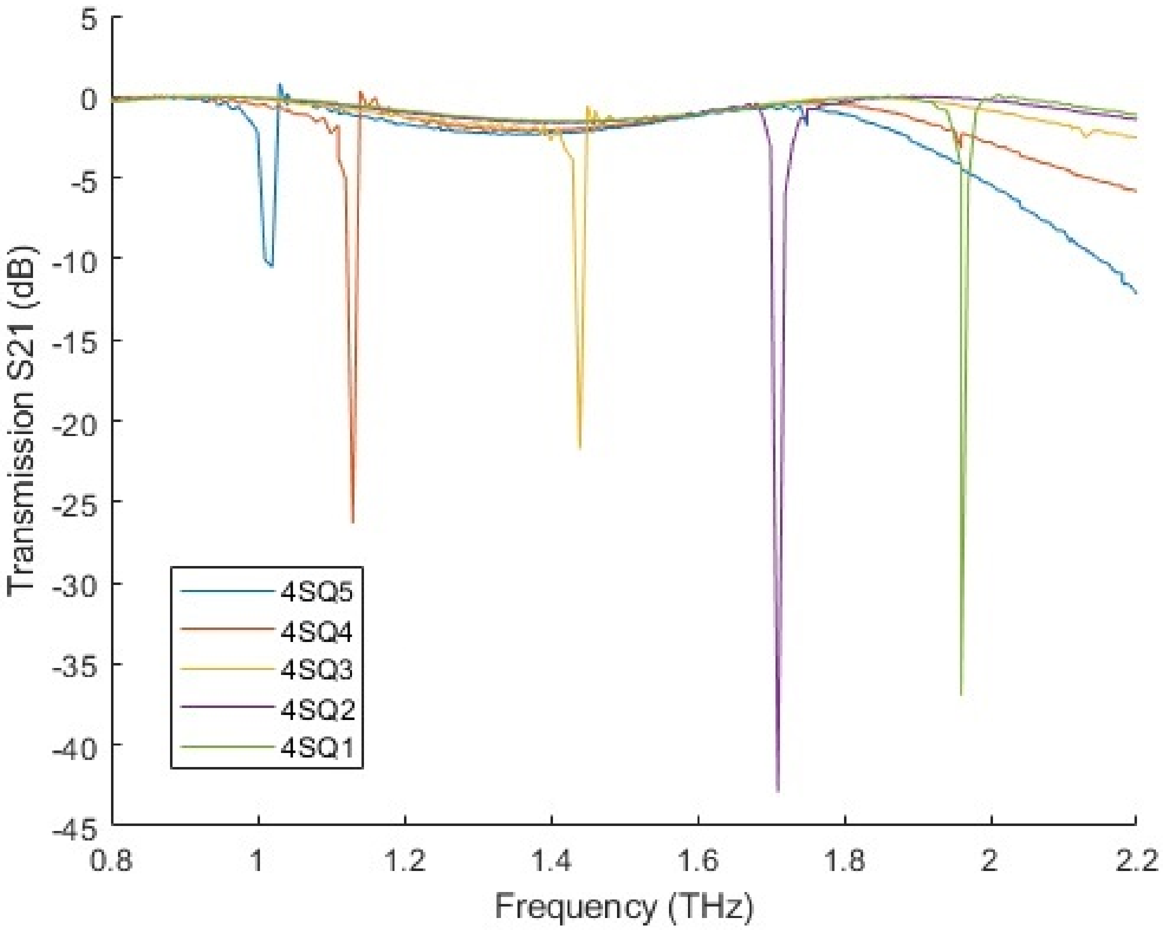

Figure 6.14: Simulations of S21 parameters with respect to the quadruplet square asymmetric split ring designs 1-5 (4SQ1, 4SQ2, 4SQ3, 4SQ4, 4SQ5).

Asymmetric Double Split Ring (SR) Design

In this next design the desired feature is the secondary feature of the response it is referred to in [119] as a 'trapped mode' resonance which is on the edge of the primary feature. This is the desired feature in this case as it produces a higher Q-factor feature. The design consists of a double split ring with asymmetric swept openings of 10° and 30° at opposite sides of the ring as shown in figure 6.15. The designs in [119] are centred at 6 GHz therefore have been significantly altered in dimensions to produce features at 0.96, 1.07, 1.24, 1.49 and 1.77 THz, however the base design remains the same. Figure 6.15 shows the dimension labels corresponding to the dimensions of the chosen designs as in table 6.3. Figure 6.16 shows the simulated responses for each of the SR designs.

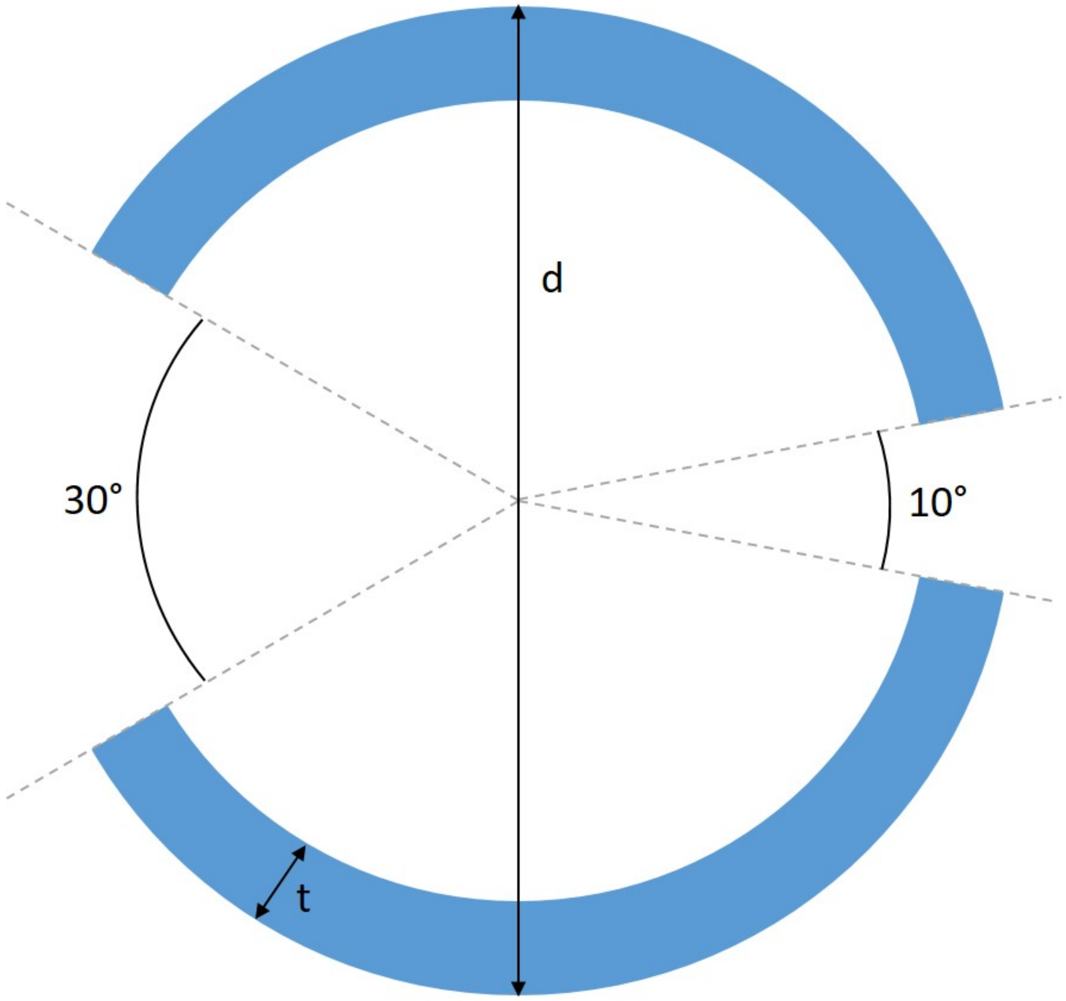

Figure 6.15: Diagram of asymmetric double split ring in the 0° orientation.

Name	**Thickness (µm)**	**Diameter (µm)**	**Spacing (µm)**	**Frequency (THz)**
SR1	15	20	100	1.96
SR2	15	25	100	1.71
SR3	15	30	115	1.44
SR4	20	35	135	1.13
SR5	20	40	135	0.98

Table 6.3: Dimensions of double split ring (SR) designs 1-5 and their simulated feature frequencies. Thickness (t), Diameter (d) and Spacing (s).

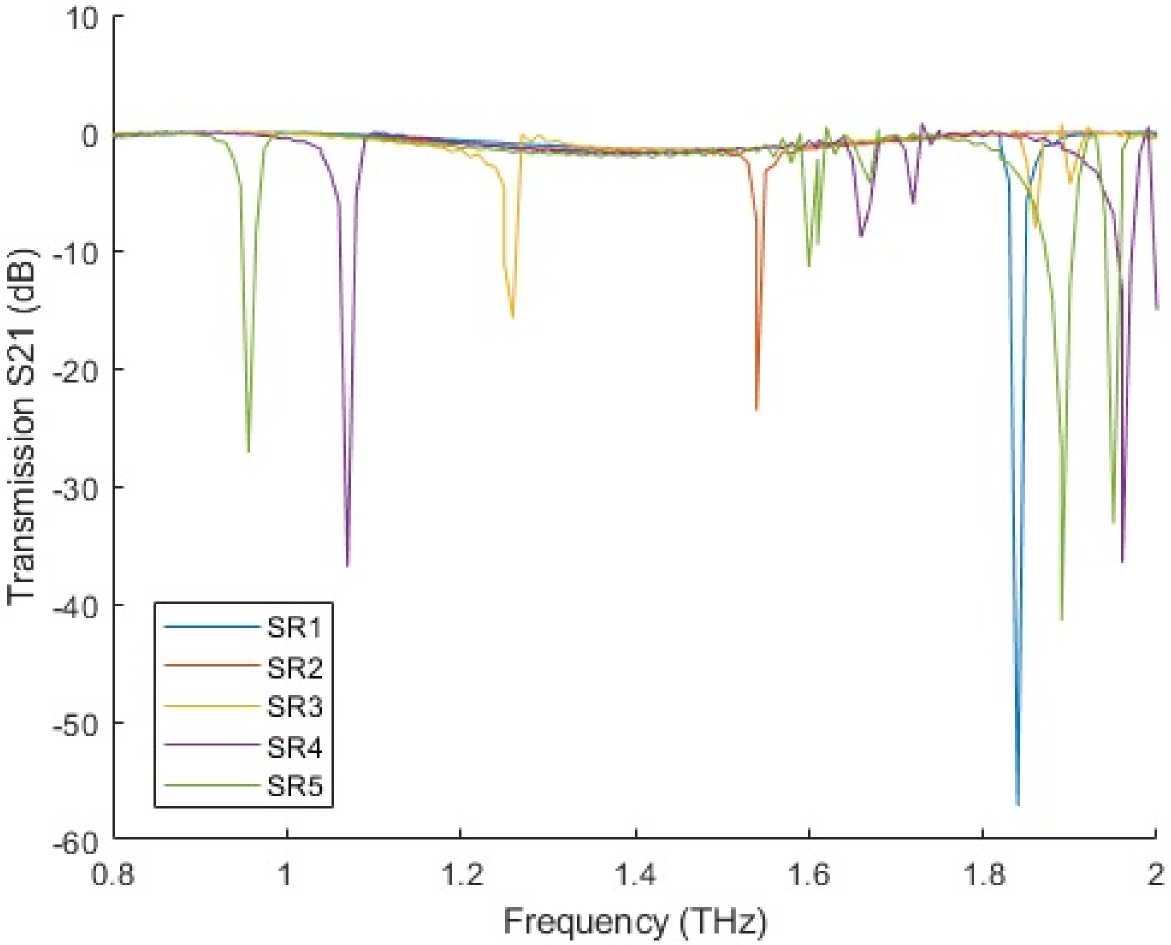

Figure 6.16: Simulations of S21 parameters with respect to the split ring design with two asymmetric splits 1-5 (SR1, SR2, SR3, SR4, SR5).

Asymmetric Double Split Square Ring (DSSQ) Design

The features considered so far have all taken the shape of sharp troughs, however the feature in the next design is a sharp peak and trough. This can be beneficial as it could potentially offer more information in terms of sensing. Reference [120] describes a double split square resonator with asymmetric split placement centred at 1.1 THz. The square ring has two splits; one placed centrally and the other positioned with an offset along opposing edges of the square as shown in figure 6.17. This topology has been designed to shift the desired feature to 1.22, 1.46, 1.72 and 2.02 THz. Figure 6.18 shows the simulated responses for the DSSQ designs while table 6.4 describes each of the designs specific dimensions.

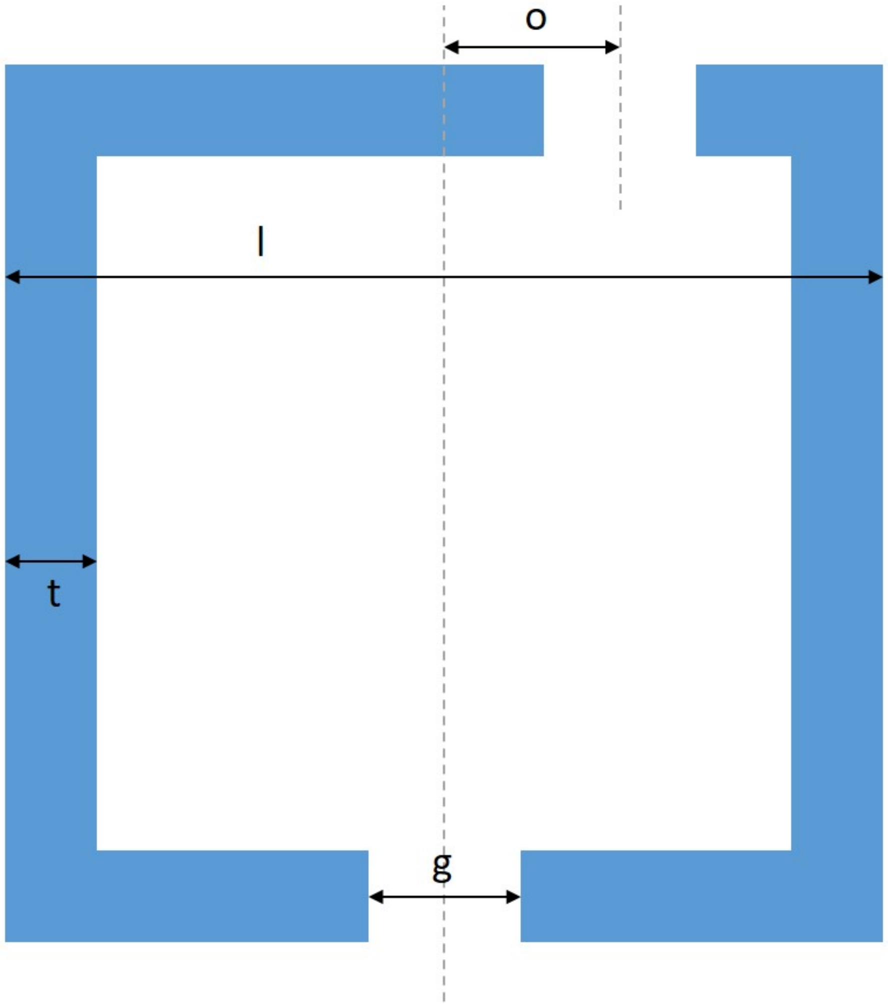

Figure 6.17: Diagram of asymmetric double split square ring in the 0° orientation.

Name	**Length** (µm)	**Thickness** (µm)	**Gap** (µm)	**Offset** (µm)	**Spacing** (µm)	**Frequency** **(THz)**
DSSQ1	54	8	4	5	70	1.22
DSSQ2	42	5	2	5	52	1.46
DSSQ3	37	6	3	5	45	1.72
DSSQ4	30	5	2	4	40	2.02

Table 6.4: Dimensions of double square split ring (DSSQ) designs 1-4 and their simulated feature frequencies. Length (l), Thickness (t), Gap (g), Offset (o) and Spacing (s).

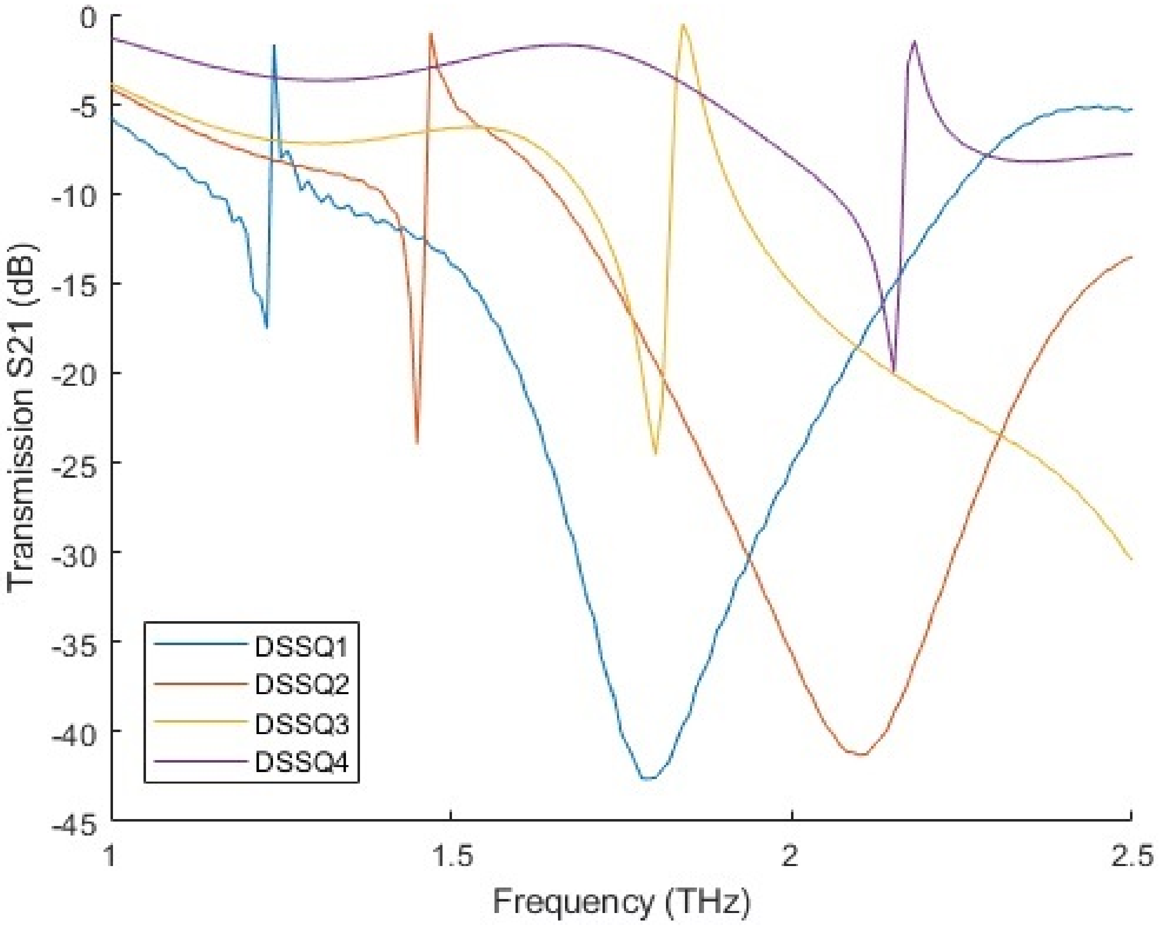

Figure 6.18: Simulations of S21 parameters with respect to the double square split ring designs 1-4 (DSSQ1, DSSQ2, DSSQ3, DSSQ4).

Double ‘C’ (CC) Design

Finally, [67] and [121] show variations of the last design to be explored. They both show two square split ring resonators one with a central split and the other with an off-centre split both splits facing each other. These designs have been simulated for centre frequencies at 0.99, 1.23, 1.42, 1.66 and 1.90 THz with dimensions as described in table 6.5. These dimensions correspond to the dimensions labelled in figure 6.19. Figures 6.20, 6.21, and 6.22 show the simulated responses for each of the CC designs whose dimensions are recorded in table 6.5.

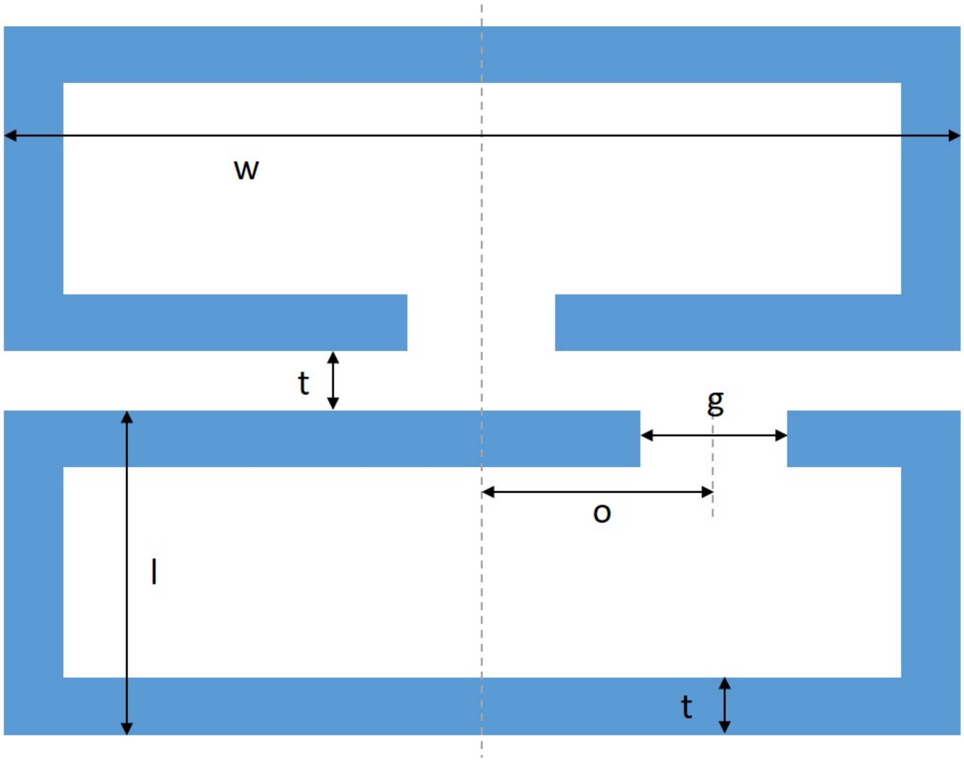

Figure 6.19: Diagram of double ‘C’ design in the 0° orientation.

Name	**Width** (µm)	**Length** (µm)	**Thickness** (µm)	**Gap** (µm)	**Offset** (µm)	**Spacing** (µm)	**Frequency** **(THz)**
CC1	90	20	7	10	25	105	1.90
CC2	100	25	8	10	30	120	1.66
CC3	120	30	10	10	35	140	1.42
CC4	130	35	10	15	35	150	1.23
CC5	160	50	10	20	50	190	0.99

Table 6.5: Dimensions of double 'C' (CC) designs 1-5 and their simulated feature frequencies. Width (w), Length (l), Thickness (t), Gap (g), Offset (o) and Spacing (s).

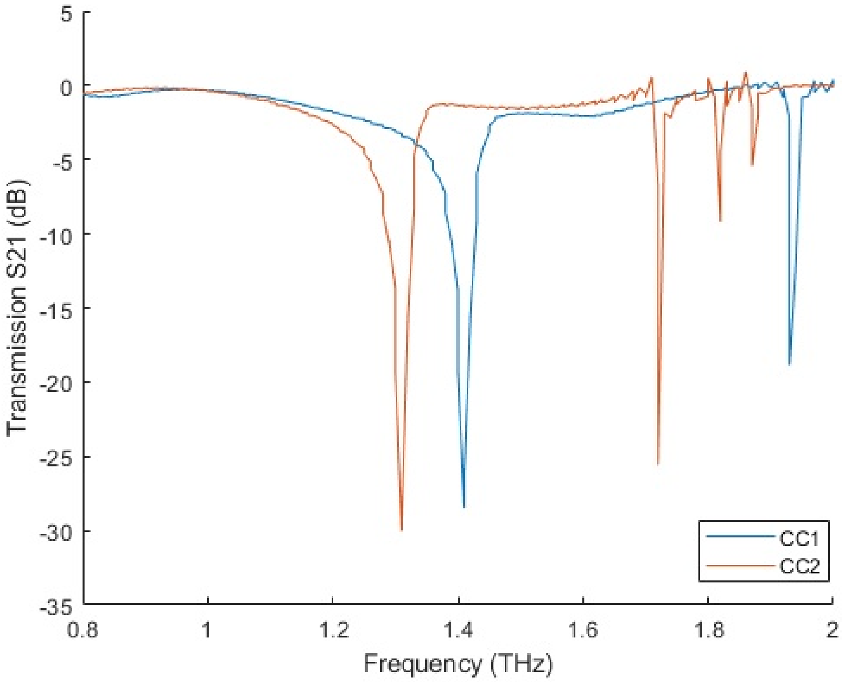

Figure 6.20: Simulation of S21 parameters with respect to the double 'C' design 1 and 2 (CC1 and CC2).

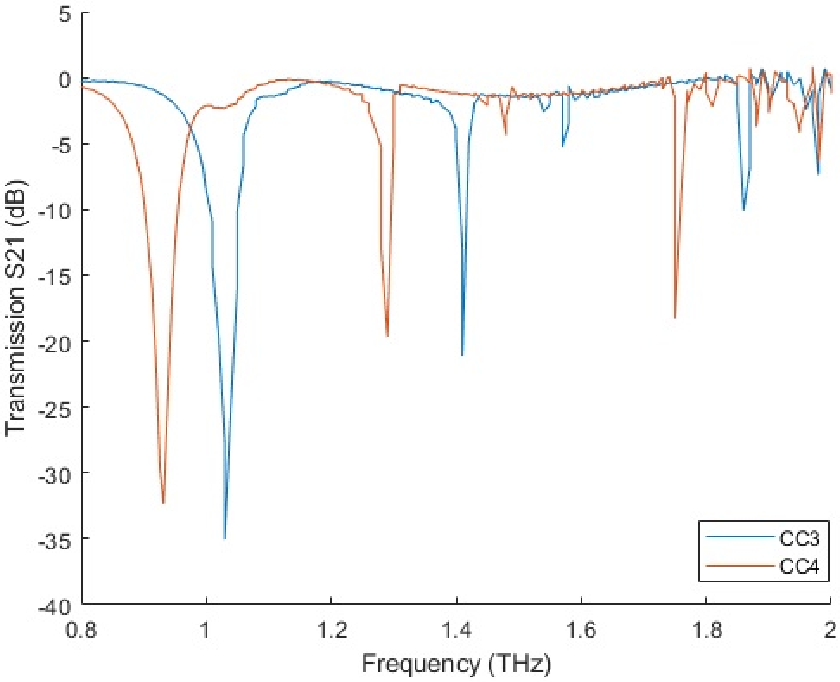

Figure 6.21: Simulation of S21 parameters with respect to the double ‘C’ design 3 and 4 (CC3 and CC4).

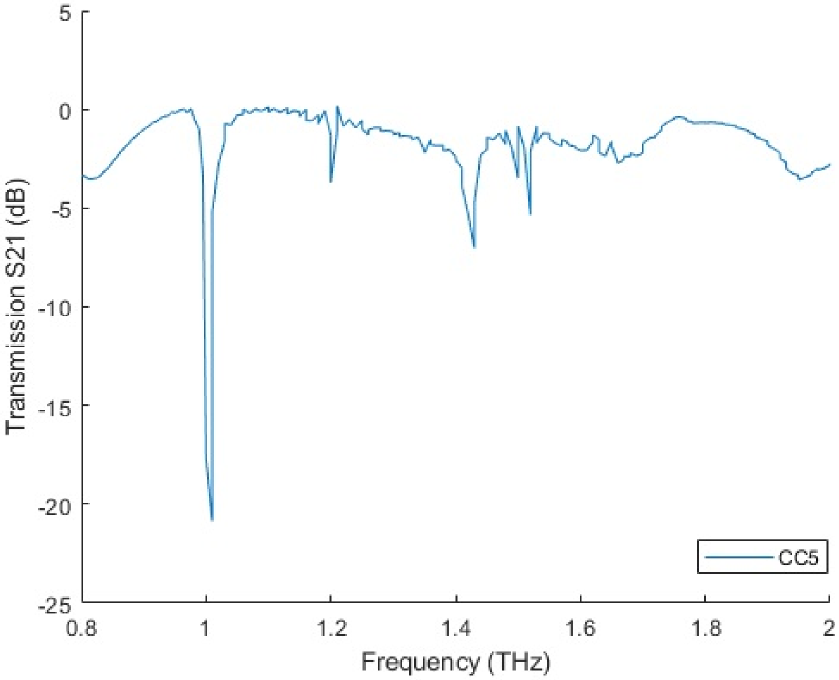

Figure 6.22: Simulation of S21 parameters with respect to the double ‘C’ design 5 (CC5).

6.6 Fabrication Consistency Testing

Figure 6.23 shows the fabrication of each of the CC designs and shows that all of the designs have minor defects in them. CC2 and CC5 appear overetched. This is not at the limit of the process as the smallest design, CC1, appears to be well fabricated, however this cannot be confirmed with a metamaterial response as no features were found across the spectrum of the VNA.

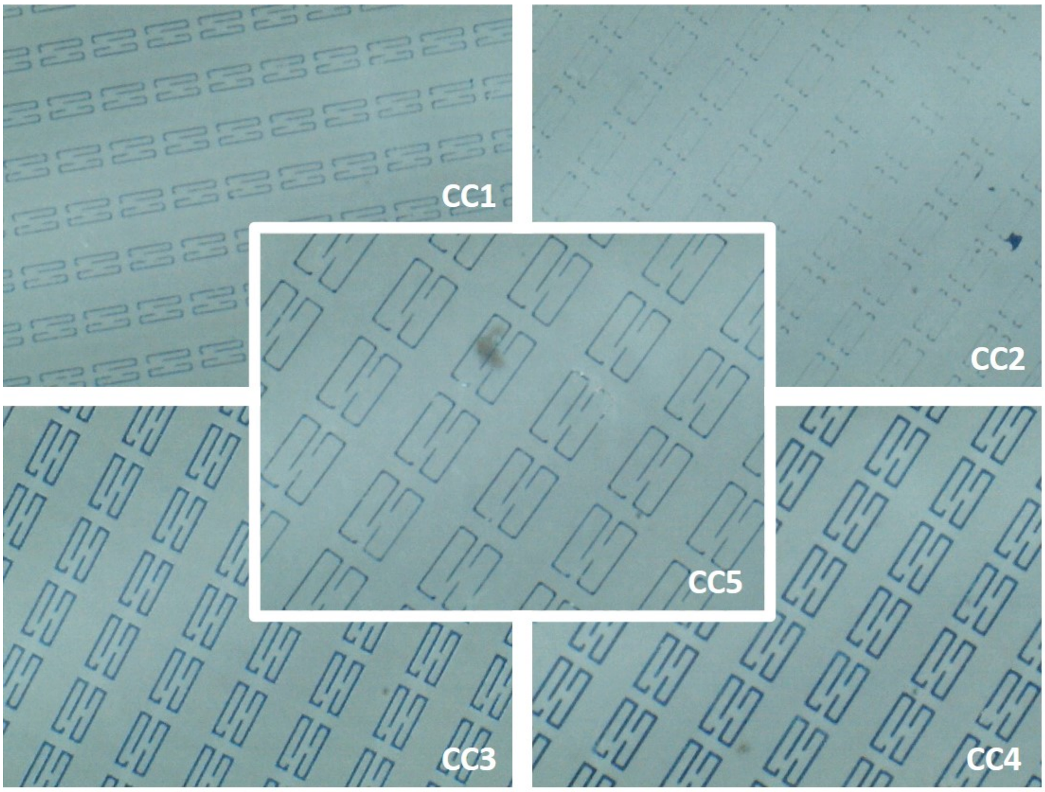

Figure 6.23: Photos showing fabrication of the CC designs.

Figures 6.24, 6.25 and 6.26 show each of the CC designs in multiple fabrications. CC3 has a clean, single absorption peak at 0.92 THz for each of the fabricated metamaterials. Similarly CC4 has consistent absorption peaks at both 0.85 and 1.1 THz across each of the figures. Figure 6.24 has a very clean response where the normalisation against an empty transmission scan has removed almost all small periodic responses, whereas figures 6.25 and 6.26 have much more disturbed responses as the normalisation has not worked as well in this case or there are fabrication errors which have affected the response. The CC5 metamaterial has a large disparity in response across the figures this is assumed to be due to fabrication issues.

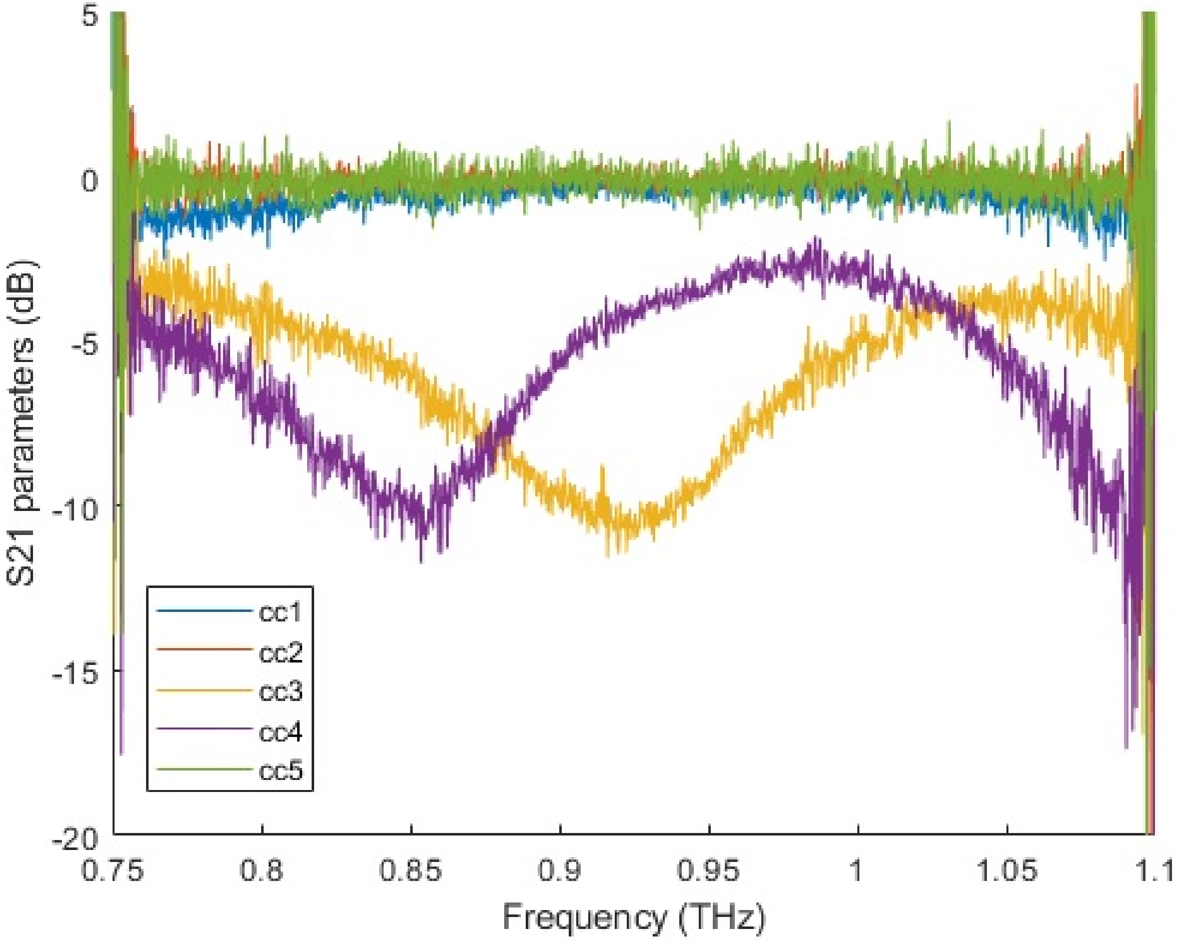

Figure 6.24: Metamaterial consistency testing metamaterial 1. Data has been normalised using a free space scan no smoothing or manipulation has been carried out on this data besides finding the magnitude of S21.

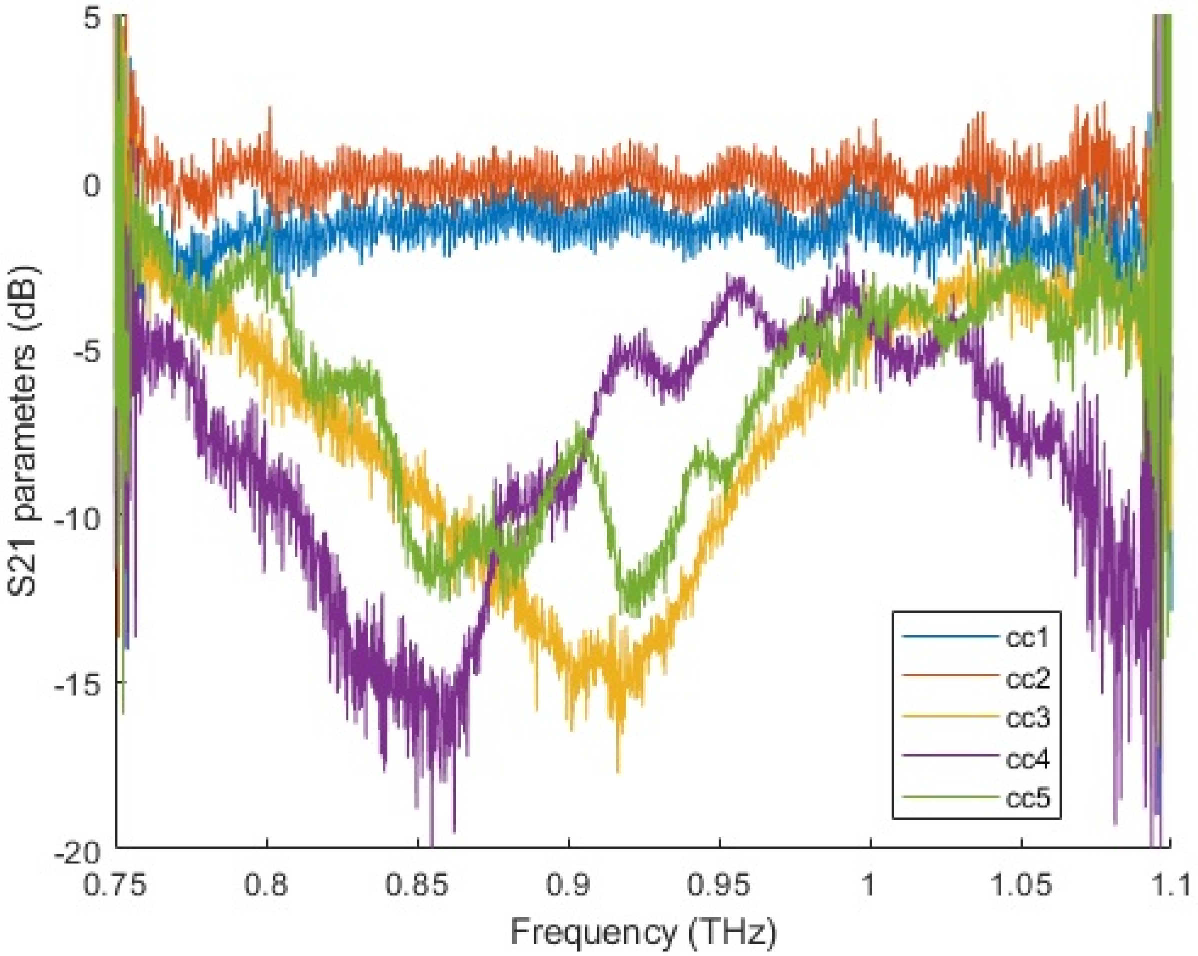

Figure 6.25: Metamaterial consistency testing metamaterial 2. Data has been normalised using a free space scan no smoothing or manipulation has been carried out on this data besides finding the magnitude of S21.

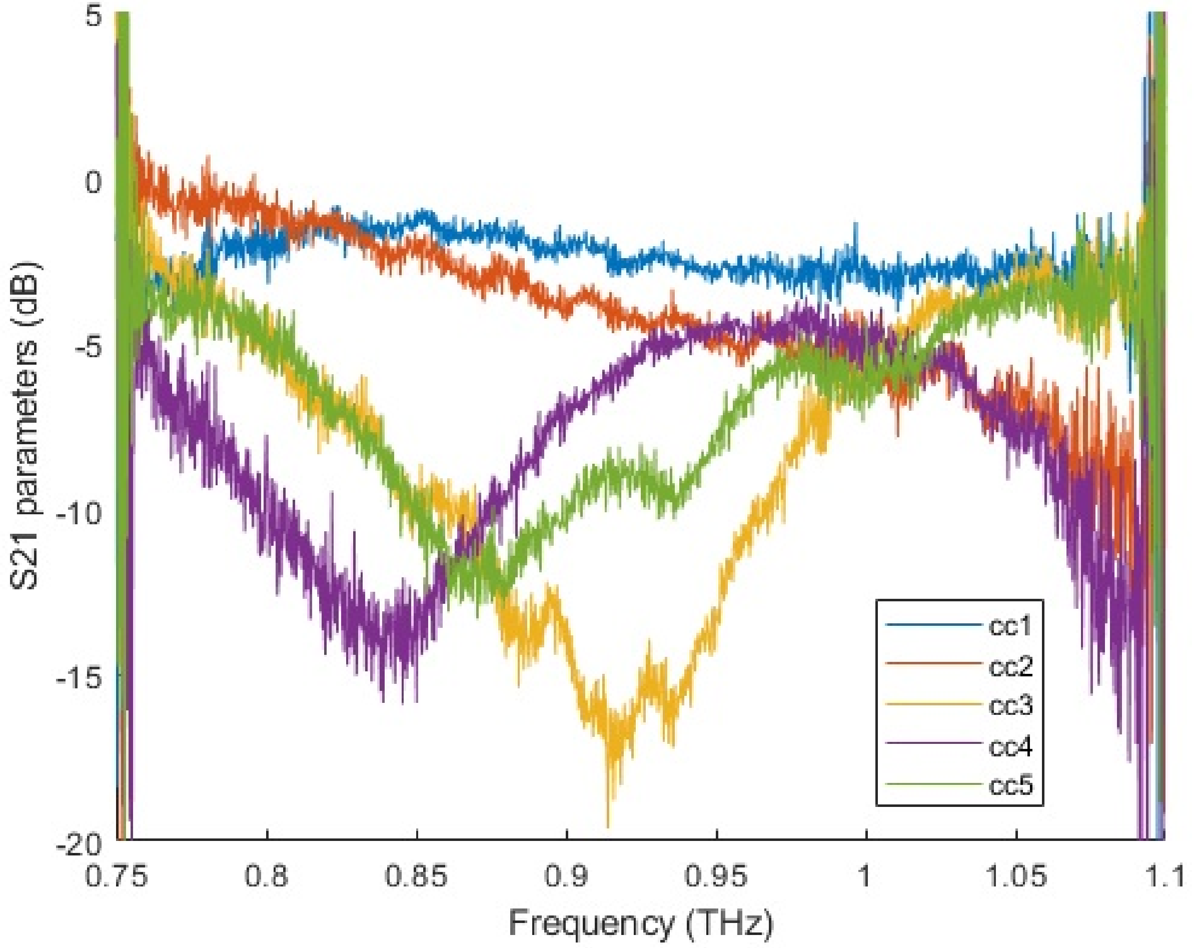

Figure 6.26: Metamaterial consistency testing metamaterial 3. Data has been normalised using a free space scan no smoothing or manipulation has been carried out on this data besides finding the magnitude of S21.

6.7 Orientation, Direction and Measurements

This section explores the experimental conditions which enable the best metamaterial response with respect to a sensing application.

6.7.1 Orientation and Angular Dependence

For designs which exhibit a feature in the VNA range a difference in response due to metamaterial angle can be seen. Dependent on the application, this can be useful or detrimental. Therefore, it is important to consider the orientation of the metamaterial prior to making a design decision. For the purpose of this thesis, it is possible to have the chosen metamaterial be sensitive to orientation as this can be controlled in lab conditions.

To explore the effect of orientation on the final designs, each has been scanned at both 0° (the orientation as shown in their respective diagrams throughout section 6.5) and 90° rotations using the beam as the axis of rotation. Figure 6.27 shows the 4SQ5, CC3 and CC4 metamaterial designs in both of these orientations. As can be seen in the figure, each of the 90° scans are shifted slightly down in frequency and have a significantly larger magnitude to the absorption peak as compared to the 0° scans.

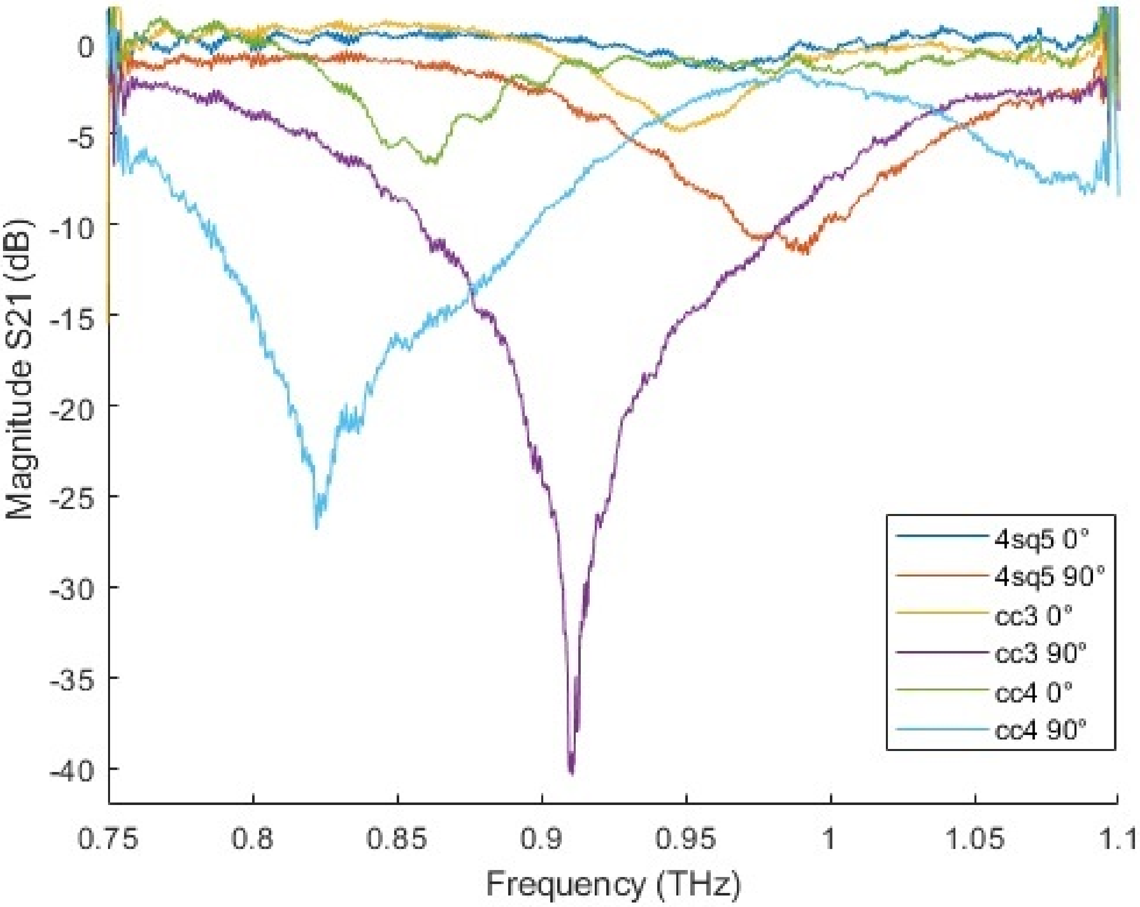

]

Figure 6.27: Figure of 4SQ5, CC3 and CC4 metamaterial designs at 0° and 90° orientations. Data has been normalised using a free space scan no smoothing or manipulation has been carried out on this data besides finding the magnitude of S21.

Figure 6.28 shows the CC4 metamaterial at 0°, 45° and 90° angles along the rotational axis of the beam. There is a significant difference in each of the scans. Demonstrating the metamaterial performance is sensitive to the angle.

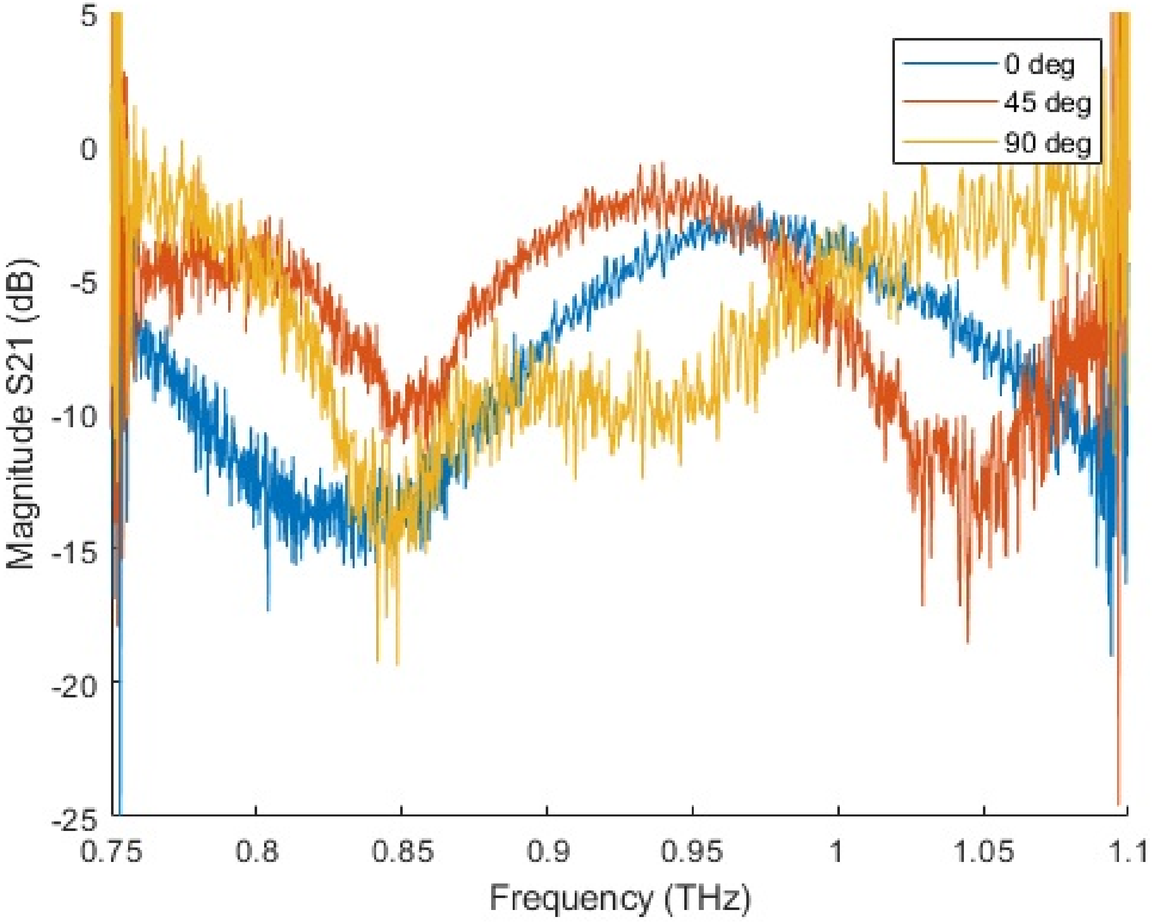

Figure 6.28: Figure of CC4 metamaterial at 0°, 45° and 90° incident angles with the beam as the axis of rotation. Data has been normalised using a free space scan no smoothing or manipulation has been carried out on this data besides finding the magnitude of S21.

6.8 Sensitivity Simulations

Sensitivity to real refractive index is calculated using Lumerical simulations as described previously. However, the refractive index values of the material in contact with the metamaterial surface is set to that expected of the sample, as it most closely represents the actual sensitivity of the metamaterial for the liquids that will be tested. The sensitivity is likely to be reduced for these higher refractive index values than lower refractive index values due to an exponential relationship between the refractive index and shift.

The metamaterial layer in contact with a test material is modelled in Lumerical, a refractive index is assigned to the test material which affects the simulation result. To simulate for the most accurate refractive index range an adjusted refractive index value for water soaked filter paper has been calculated from measurements. Figure 6.29 shows the phase response of increasing number of dry and water soaked filter paper sheets which can be used to calculate the adjusted refractive index of the water in combination with the paper fibres. Equation 6.8.1, as used in chapter 4, can be applied here.

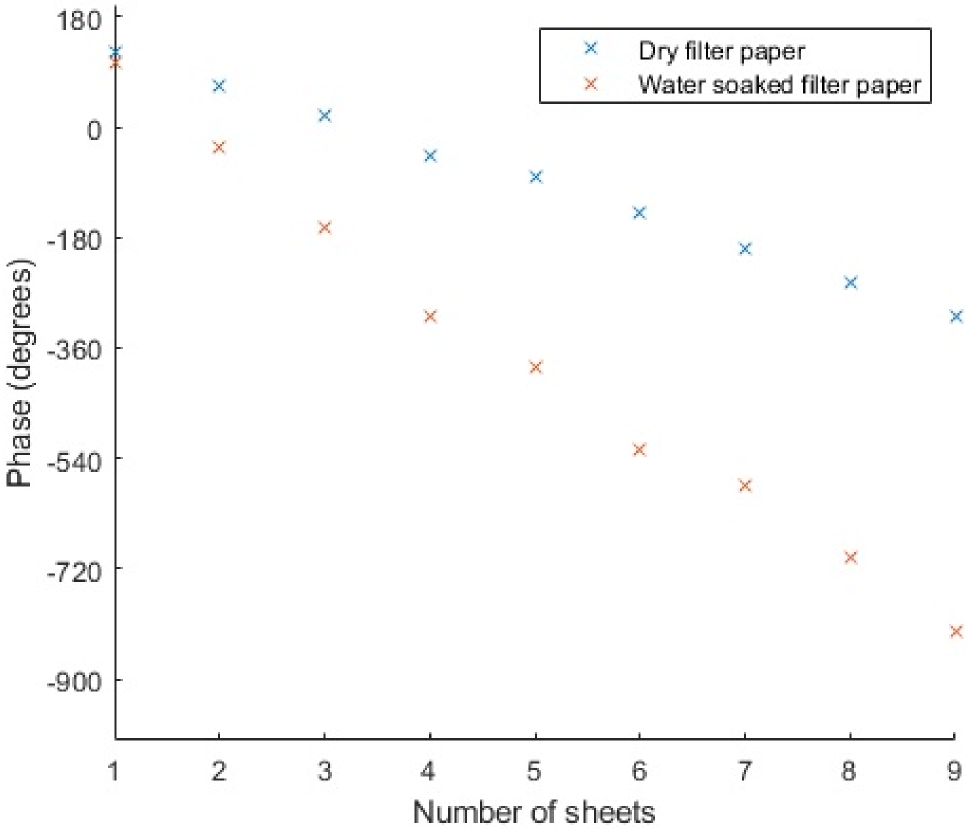

Figure 6.29: Water soaked filter paper refractive index measurements phase is relative to previous sheets hence reduction from the initial value. Absolute phase is irrelevant as the slope of the line is the important metric.

$$\Delta n = \frac{\lambda \Delta \phi}{2\pi \Delta S} \tag{6.8.1}$$

Where λ is the wavelength of incident radiation, $\Delta\phi$ is the phase difference and ΔS denotes the thickness of a single sheet of filter paper (12.5 µm).

The refractive index of dry filter paper has been measured as 1.35 and the refractive index of the wet filter paper has been measured to be 1.76. It can be determined, using the refractive index of water as 2.13 [122] that the porous volume of the filter paper and thus its capacity to hold liquid is 52.6%.

Lumerical sensitivity simulations using refractive index values between 1.5 and 2 show the theoretical sensitivities for each of the final designs are 743 GHz/RUI for the 4SQ5 design and 426 GHz/RIU and 526 GHz/RIU for the CC3, and CC4 designs respectively. So, theoretically the 4SQ5 design has the best sensitivity. This does not consider that the experimental responses may not match the simulations along with possible issues with fabrication consistency, feature position and resistance to noise.

6.9 Conclusion

This chapter has given a background to microfabrication procedures which can be used to produce micro-scale patterns. This lithography technique was used to fabricate and test a number of metamaterial patterns which were designed using an FDTD solver called Lumerical.

Metamaterial performances were discussed along with the simulated and experimental responses. Methods for sensitivity simulations were discussed showing the resultant simulated sensitivities for selected designs.

Chapter 7

Metamaterial Testing and Device Development

7.1 Introduction

The previous chapter outlined some promising designs and explored the effects of orientation on these designs. The aim in this chapter is to provide background experimental results exploring how the metamaterials function when used for sensing. All measurements are taken using a standard transmission measurement as described in Section 3.2 of this thesis. Various metamaterials for sensing techniques are explored. These explorations are setting up experiments with the future intention of use for terahertz bio-sensing of serum samples searching for blood borne tumour markers. This is explored in chapter 8.

Initially, known-refractive index samples are tested using metamaterials. Following this, work with respect to sensing of liquids using filter paper to wick and hold the liquid in contact with a metamaterial surface is undertaken. Since serum samples have a large water content, water is used as an analyte for experimental testing. Finally, milk is tested as a serum substitute due to similar levels of proteins [123, 124].

There were many issues with regards to the performance of the VNA in the data presented in the following chapters. The issues in the data in chapter 8 are discussed in chapter 8. However, it should be noted for this chapter, some of the excessive noise experienced is not a classic characteristic of the VNA or the specific test being carried out but a function of these issues with the equipment.

7.2 Metamaterial Measurement Techniques

7.2.1 Directional Dependence

Theoretically, the direction that the beam passes through the substrate should not make a difference to the metamaterial response for this setup. To confirm this experimentally, scans have been taken with the metamaterial facing each way through the beam in both S21 (figure 7.1) and S12 (figure 7.2) each of these scans are taken at the same time i.e. the dry msf narrow scan in S21 (figure 7.1) is measured at the exact same time using the VNA as the dry msf narrow scan in S12 (figure 7.2) and so on and so forth. These tests are conducted on the 4SQ5 metamaterial design as described and characterised in chapter 6. There are, however, additional sections of noise found in figure 7.2. Disregarding these areas of increased noise, the general traces are identical for S21 and S12. These figures show there is no clear feature for the metamaterial side first (msf) scan of one sheet while the plastic side first (psf) scan shows a stronger feature. As this is identical for both the S21 and S12 scans it is not due to the direction of the scan. It is thought that in this case the lack of feature is due to poor adhesion with the metamaterial surface. These figures show with confidence that the direction the beam passes through the substrate does not affect results.

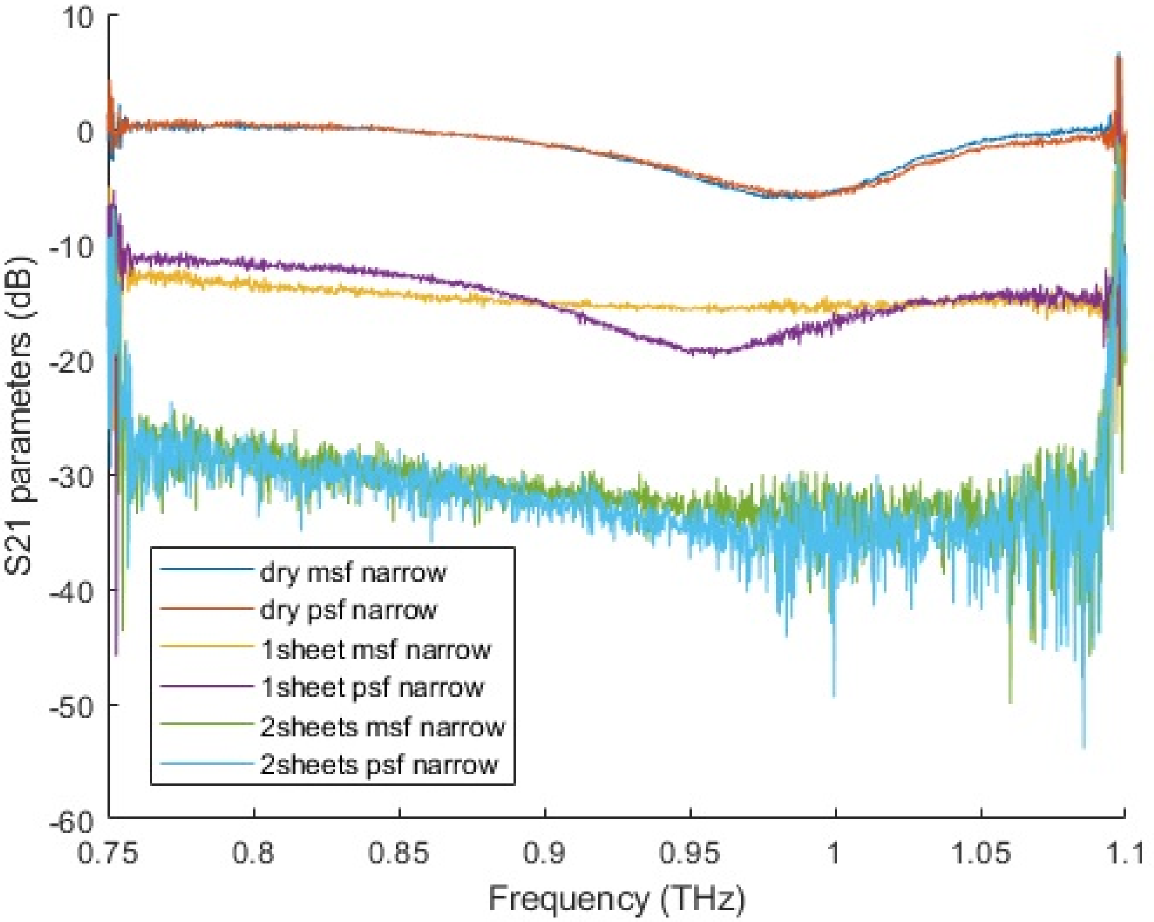

Figure 7.1: Figure of 4SQ5 metamaterial both dry and with one and two sheets of water soaked filter paper in contact with the metamaterial surface. All scans are with a ‘narrow’ aperture on the iris (5 mm). Data has been normalised using a free space scan no smoothing or manipulation has been carried out on this data besides finding the magnitude of S21.

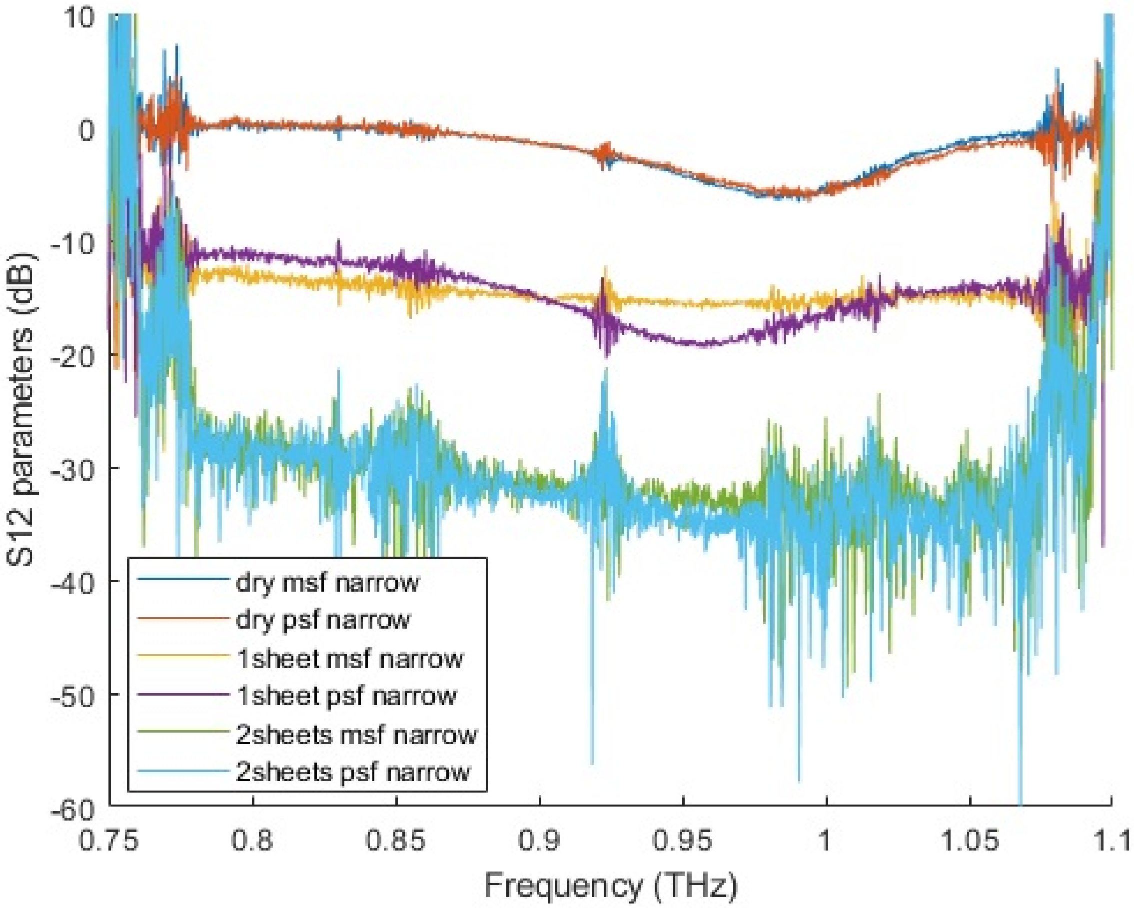

Figure 7.2: Figure of 4SQ5 metamaterial both dry and with one and two sheets of water soaked filter paper in contact with the metamaterial surface. All scans are with a 'narrow' aperture on the iris (5 mm). Data has been normalised using a free space scan no smoothing or manipulation has been carried out on this data besides finding the magnitude of S21.

7.2.2 Effect of Beam Width on Measurements

Figure 7.3 shows the 4SQ5 metamaterial and the effect of beam width on the measurements. The figure shows that the responses are more apparent the wider the aperture of the iris. This can be best seen in the one sheet measurements where the wide aperture (10 mm approximately 100 design repetitions across the circular diameter) scan shows a clear absorption peak. The narrow aperture (5 mm approximately 50 design repetitions across the circular diameter) scan also of one sheet shows a much flatter line with no clear features. These measurements show that there is an effect based on the beam width of the measurements and to extract the most information from the samples an area as large as possible should be used for measurement.

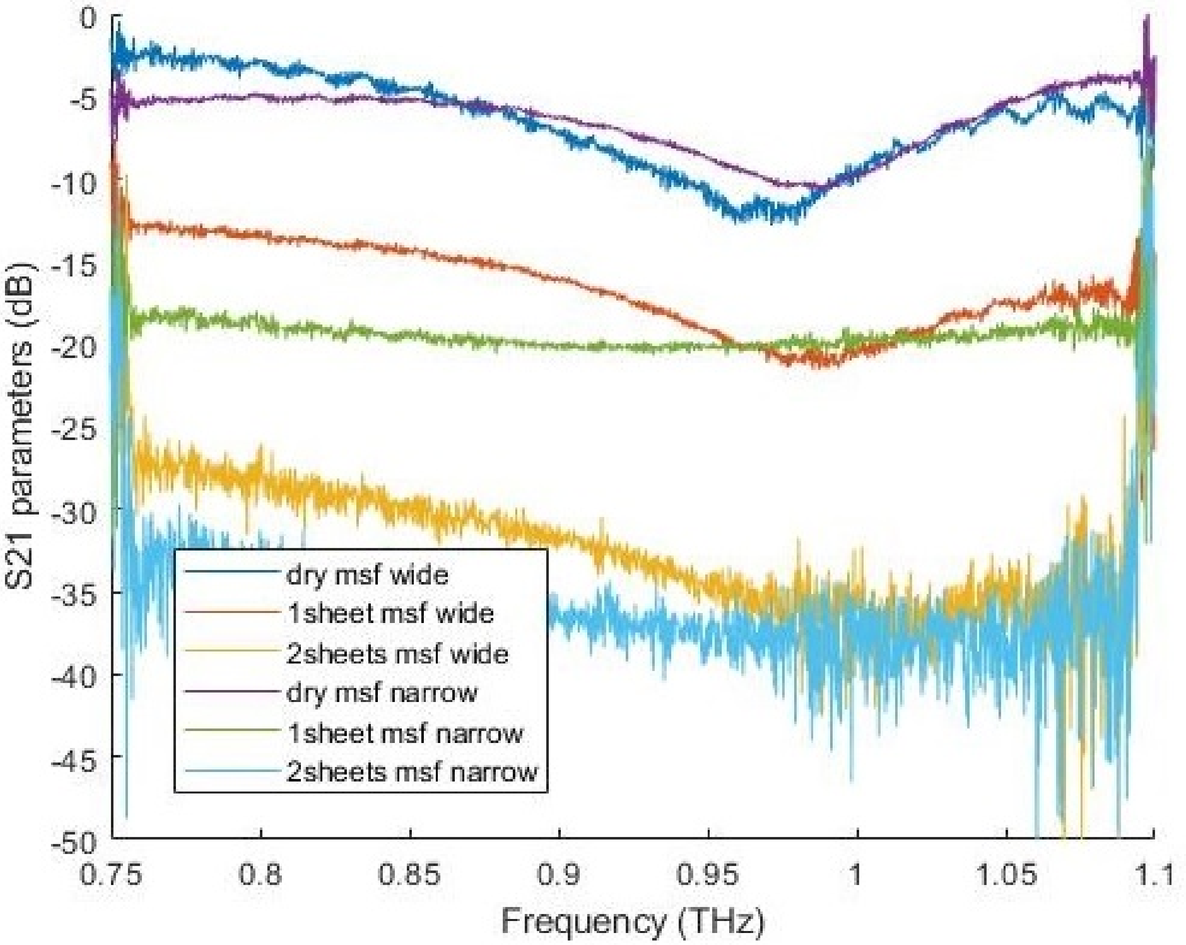

Figure 7.3: Figure of 4SQ5 metamaterial both dry and with one and two sheets of water soaked filter paper in contact with the metamaterial surface, all scans taken S21 measurements with the metamaterial side first (msf). The ‘narrow’ and ‘wide’ scans are taken with different iris apertures of 5 mm and 10 mm respectively. Data has been normalised using a free space scan no smoothing or manipulation has been carried out on this data besides finding the magnitude of S21.

7.3 Analyte Holding Methods

7.3.1 Cross Design Filter Paper

The preliminary tests for the cross design are shown in figure 7.4 which compares the response of the bare metamaterial, the metamaterial in contact with dry filter paper and the metamaterial in contact with sunflower oil soaked filter paper. The tests show that the addition of sunflower oil in the paper raises the refractive index on the metamaterial surface as the absorption peak is shifted down in frequency. The addition of the dry filter paper shifts the peak down slightly but the shift is not significant as compared to the sunflower oil test. This is thought to be due to poor adhesion as they have similar refractive indices and the sunflower oil shift is significantly larger than that of the dry paper. The oil soaked paper is able to conform to the surface and provide good contact with the metamaterial.

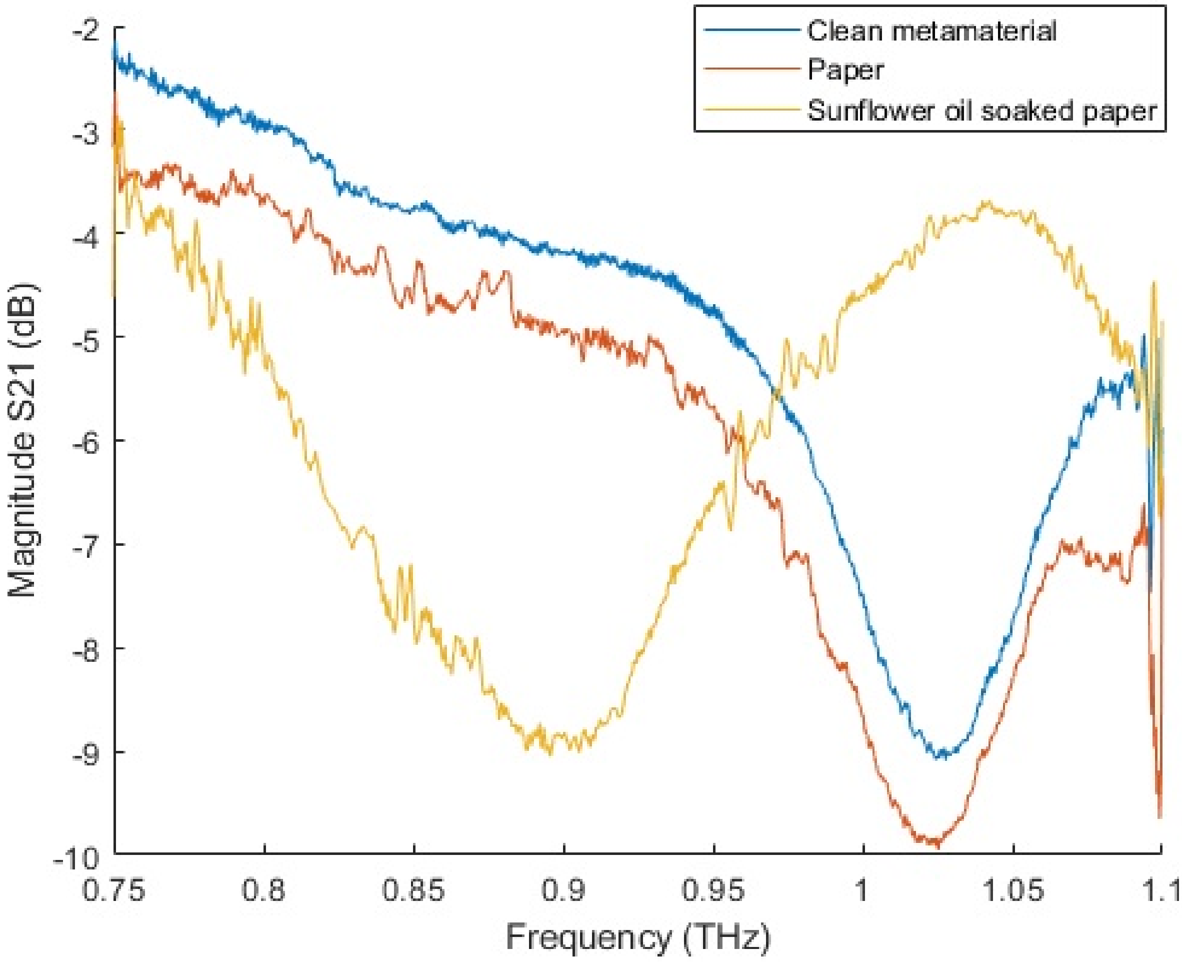

Figure 7.4: Initial experimental results of the cross design bare, in contact with dry filter paper and in contact with sunflower oil soaked filter paper. Data has been normalised using a free space scan no smoothing or manipulation has been carried out on this data besides finding the magnitude of S21.

7.3.2 Cross Design Paper Sticker

To guarantee contact between the liquid sample and the metamaterial surface an alternative option could be to use a paper sticker. The sticker can be placed directly onto the metamaterial surface and holds itself in place using the glue on the sticker. The paper surface of the sticker can then be used to collect and hold the analyte liquid. Figure 7.5 shows that both the dry sticker and sunflower soaked sticker results are similar. This would indicate that the sunflower oil is not in sufficient contact with the metamaterial as it is being blocked by the glue. Due to the similar level of electromagnetic absorption it can be assumed that a negligible amount of sunflower oil has been absorbed into the sticker.

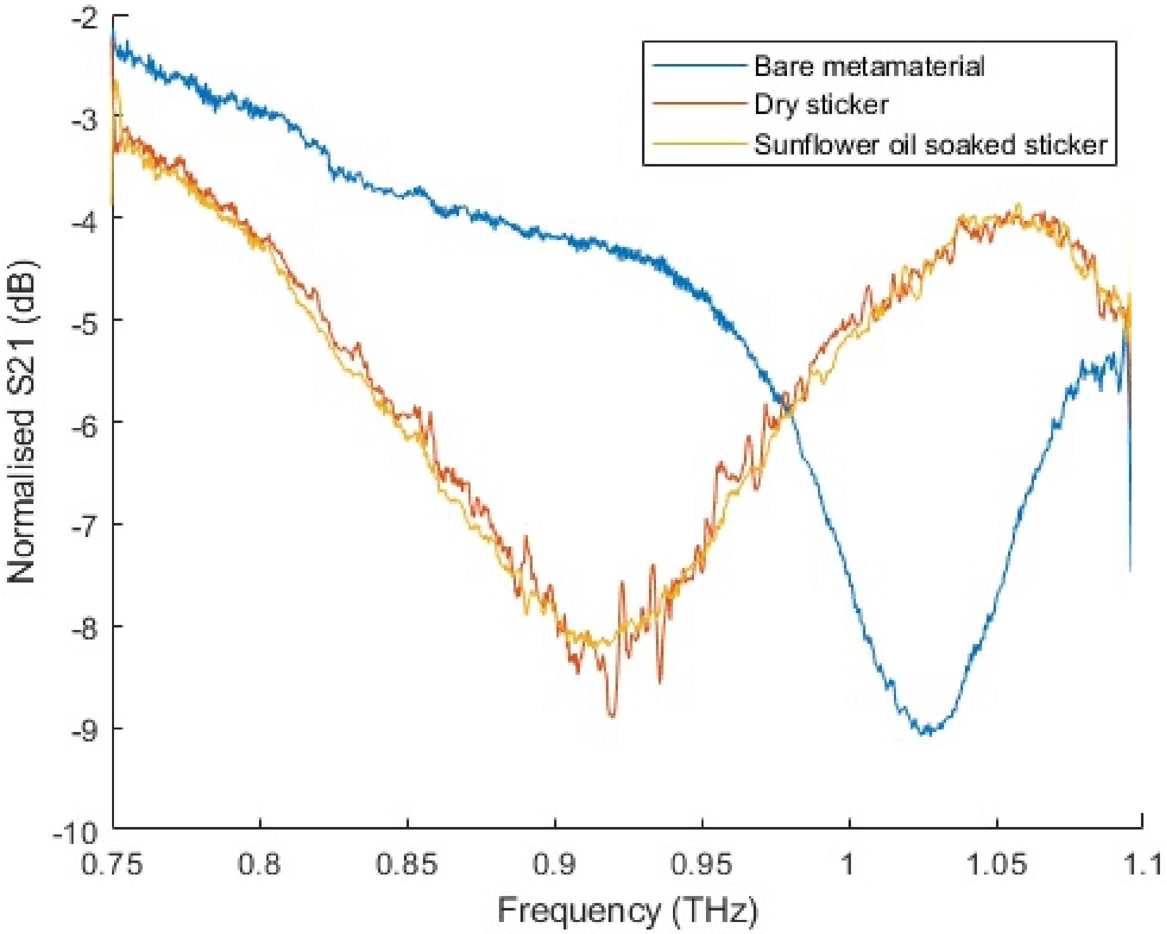

Figure 7.5: Figure of experimental response for the cross design with a paper sticker used as the sample holder. Data has been normalised using a free space scan no smoothing or manipulation has been carried out on this data besides finding the magnitude of S21.

7.3.3 Nitrocellulose Experiments

Nitrocellulose was also investigated as a method of holding the analyte. Nitrocellulose on its own is hydrophobic and requires chemical processing to make it hydrophilic [125]. From observations the applied nitrocellulose film appeared strongly hydrophobic. Nitrocellulose is a beneficial membrane to use for protein sensing as it has a protein binding capacity of 80 to 100 µg cm^{-2} however this is binding mechanism is formed through hydrophobic interactions [126] which are not compliant with a water based protein solution. To utilise the hydrophobic binding property of nitrocellulose the proteins are initially separated from the serum samples before transferring into the membrane via a methanol based buffer solution [127]. It was decided that paper provided a simpler solution which does not require significant chemical processing as the nitrocellulose method does. Presented are initial nitrocellulose experiments. The nitrocellulose is spin coated onto the surface of the metamaterial to investigate the response. Figure 7.6 shows the shift in feature frequency from the responses at varying concentrations of nitrocellulose to solvent. A consistent trend is seen that the higher concentration of nitrocellulose, the greater frequency shift of the metamaterial feature. This could be attributed to the solvent mixed with the nitrocellulose evaporating after spin coating therefore increasing the spacing between the nitrocellulose fibres. Hence, an increase in the concentration of solvent increases the proportion of air in contact with the metamaterial and thus reduces the effective refractive index of the nitrocellulose layer.

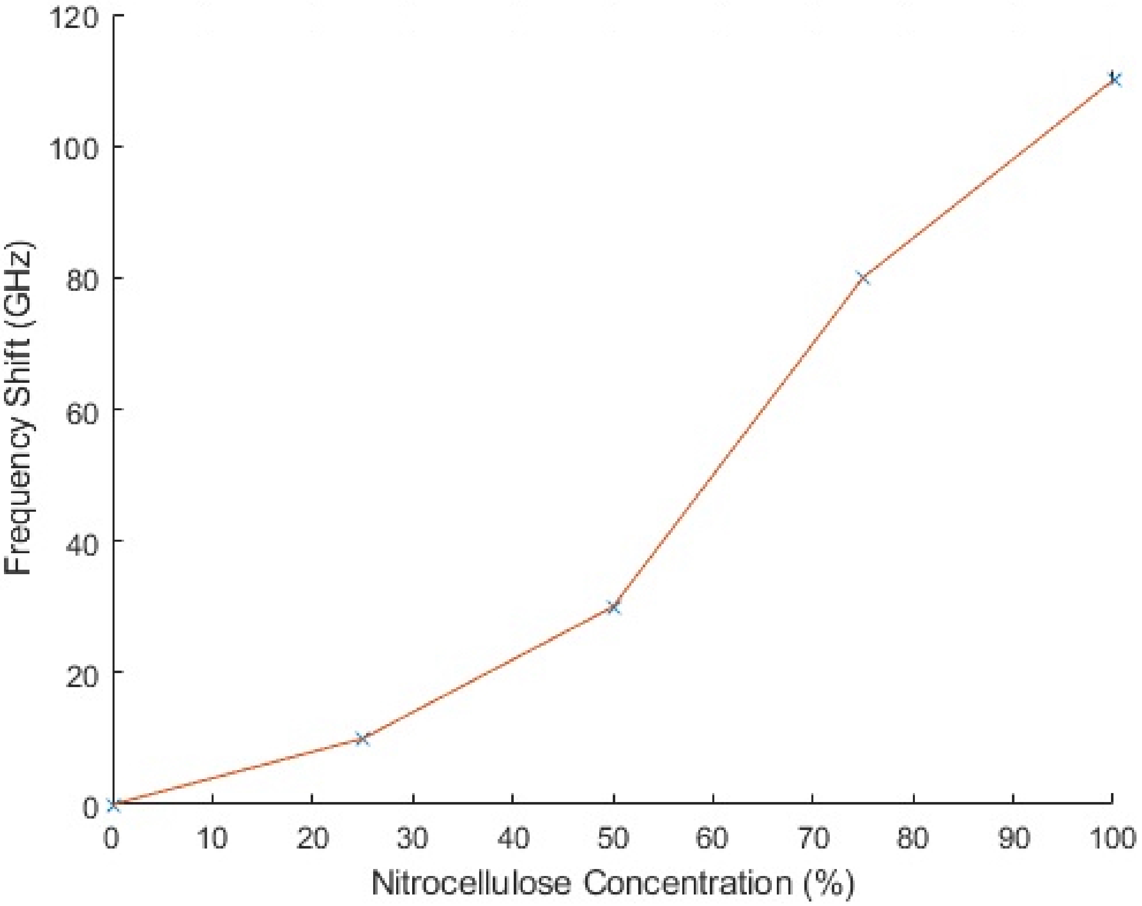

Figure 7.6: Figure showing trend of metamaterial feature frequency shift as compared to dry metamaterials for nitrocellulose concentrations of 0, 25, 50, 75 and 100% spin coated onto the surface of the metamaterial.

7.4 Analyte Experiments

7.4.1 Single Reference Material Tests

Petroleum jelly (Vaseline) is well characterised in the terahertz region so is used as a control test to characterise the metamaterial response with respect to a known refractive index material. Vaseline was tested as it self-adheres to the metamaterial. The Vaseline is applied in a manner similar to a screen printing process where a stencil is positioned over the metamaterial, the Vaseline is deposited and then the excess is scraped off. The stencil is 100 µm thick which leads to a nominal 100 µm thick layer of Vaseline. This should be sufficient as [128] shows that the frequency shift saturates and remains stable for a dielectric analyte of 1.6 refractive index at a thickness of 15µm. Figure 7.7 shows the Vaseline response of the CC3 metamaterial as compared to the dry metamaterial response. The figure shows the peak has shifted from 0.92 THz down to 0.8 THz. Vaseline is measured to have a refractive index of 1.465 using a TDS system [129]. Here, we have used a value of 1.483 measured using the VNA system following the method as in [66]. Using 1.483 as the refractive index gives a sensitivity of 248 GHz/RIU. Similarly for the CC4 metamaterial (figure 7.8) the peak has shifted down from slightly out of the range (above 1.1 THz) to 1 THz. The other peak is also shifted out of range from 0.83 THz to below 0.75 THz. As both peaks are out of range on either the dry or Vaseline coated sample the sensitivity is not calculable here.

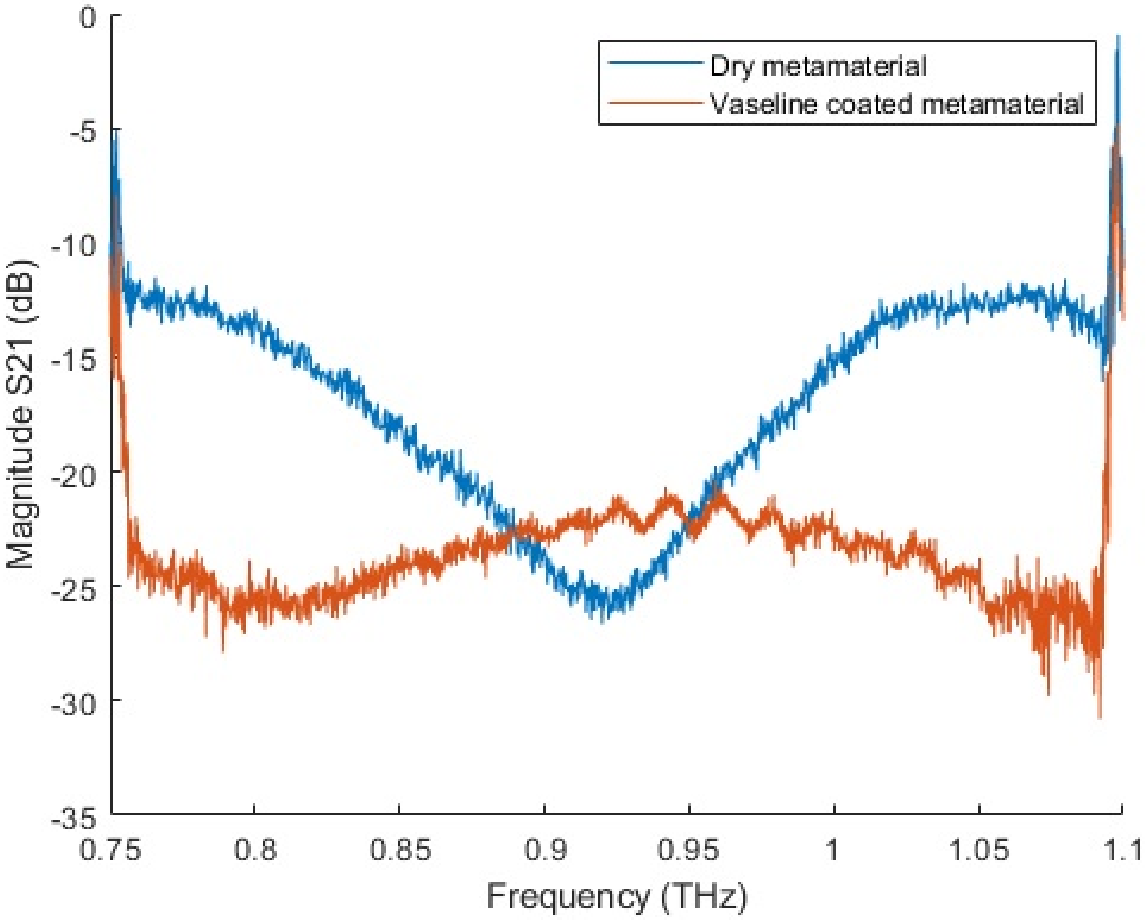

Figure 7.7: Figure showing the CC3 metamaterial responses both dry and in contact with Vaseline. The nominal thickness of the Vaseline is 100 µm. Data has been normalised using a free space scan no smoothing or manipulation has been carried out on this data besides finding the magnitude of S21.

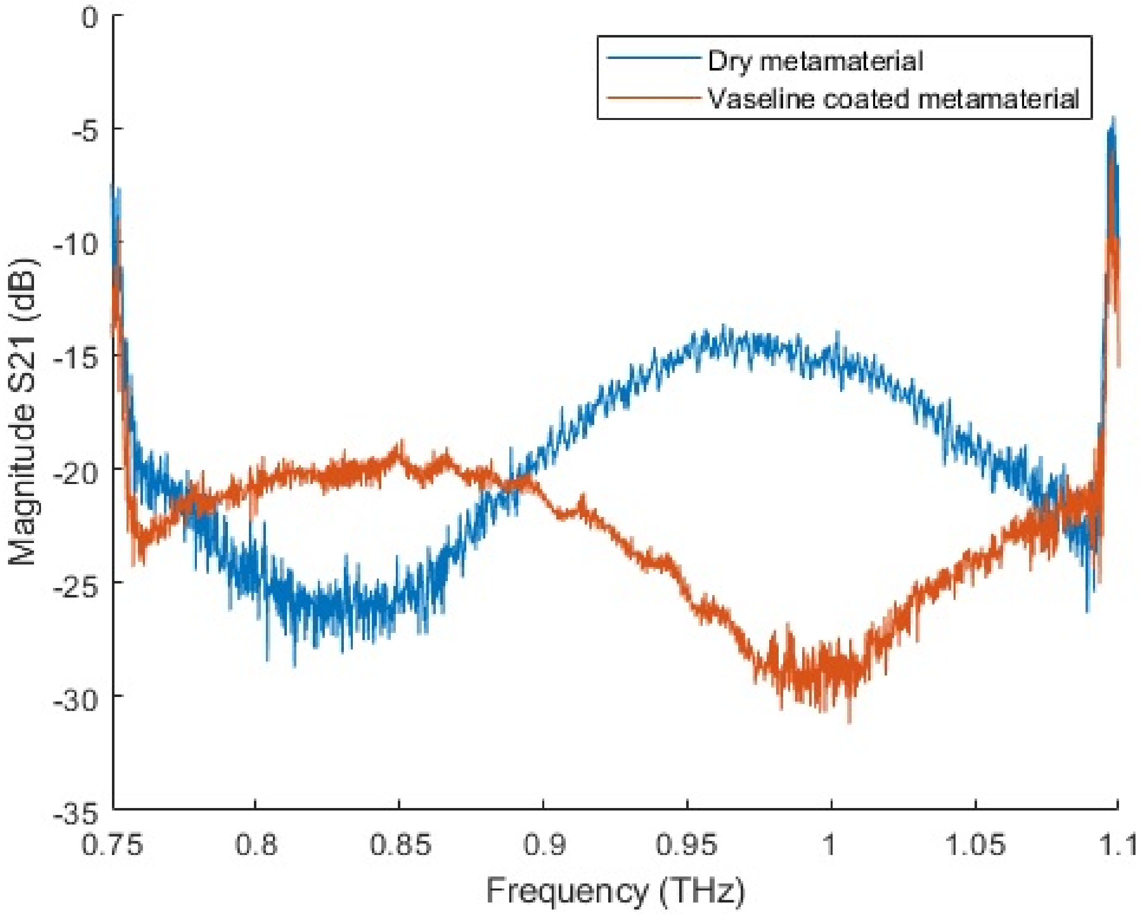

Figure 7.8: Figure showing the CC4 metamaterial responses both dry and in contact with Vaseline. The nominal thickness of the Vaseline is 100µm. Data has been normalised using a free space scan no smoothing or manipulation has been carried out on this data besides finding the magnitude of S21.

7.4.2 Cross Design Analyte Experiments

As the filter paper provides higher levels of contact between the analyte and the metamaterial further tests are carried out to examine the sensitivity of this method. Figure 7.9 shows the experimental response for the cross design in contact with filter paper and the filter paper soaked in a variety of analytes; alkanes, oils and water. As can be seen, hexane and octane resulted in similar peak frequencies to that of the dry paper (1.05 THz). This is likely to be due to the more volatile nature of these liquids causing a lack of adhesion with the metamaterial as the force holding the wet paper in contact with the metamaterial surface is the hydrostatic forces of the liquid. Therefore, if the liquid evaporates, even partially, it can cause the paper to lift off the metamaterial surface. The heavier molecule liquids are less volatile so able to keep contact with the surface which would explain the separate cluster of absorption peaks at 0.92-0.93 THz. As expected, the higher refractive index materials have a larger shift. The hexadecane peak is at a lower frequency than the undecane peak and similarly for sunflower oil as compared to olive oil. Finally, water does not exhibit a pronounced peak which could be attributed to the high absorbance of this material smearing any feature.

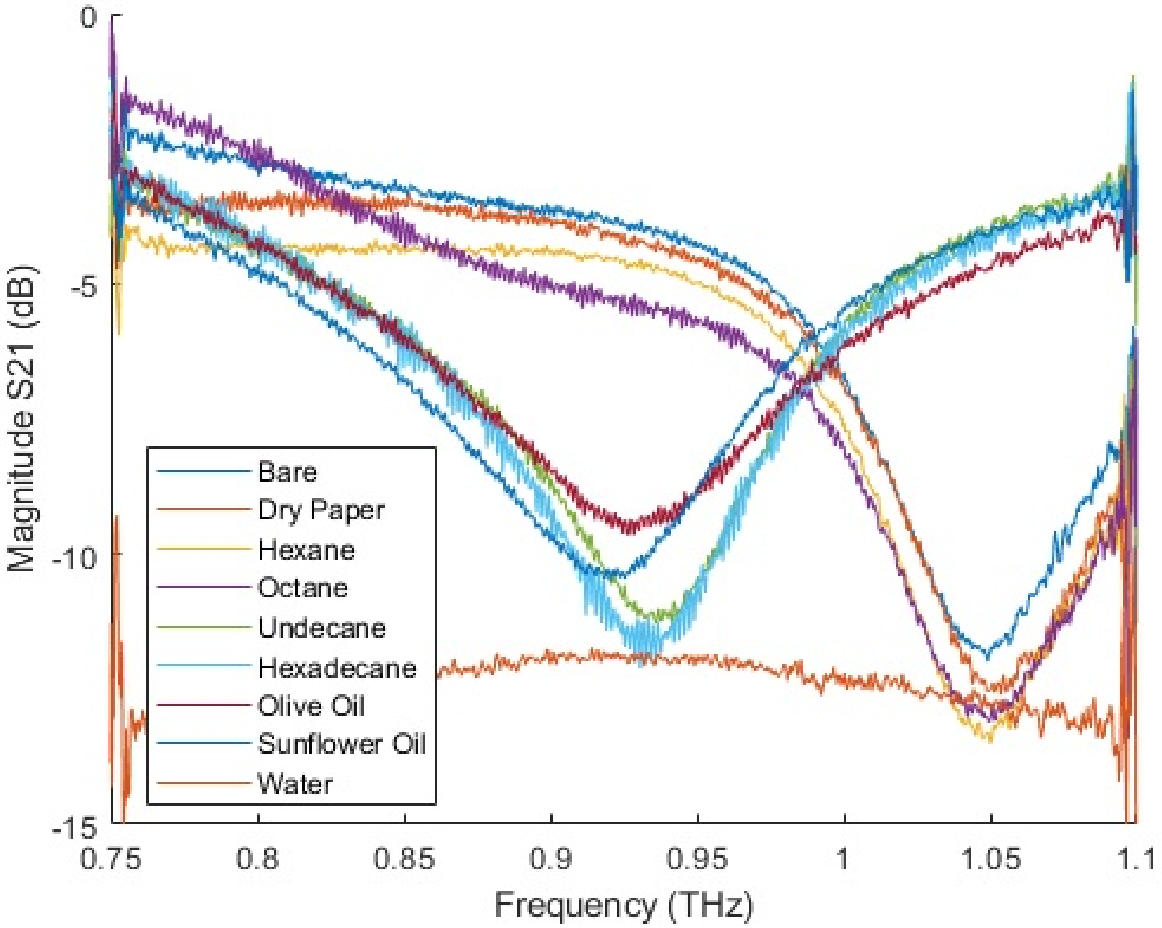

Figure 7.9: Figure of experimental response for the cross design with filter paper soaked in a range of analytes. Data has been normalised using a free space scan no smoothing or manipulation has been carried out on this data besides finding the magnitude of S21.

7.4.3 Isopropyl Alcohol (IPA)

To test polar solvents, other than water, IPA is considered. The scans in figure 7.10 show a shift between the dry and wet IPA scans. They also show that the shift remains relatively constant for one and two sheets with increased absorption. This is exactly as expected; the shift is based on the refractive index and the absorption is based on both the refractive index and thickness. There is a slight variation between the shift of the single sheet scans in both msf (metamaterial side first) and psf (plastic side first) orientations. This could indicate an issue with adhesion to the metamaterial surface, where some sections are not in good contact with the metamaterial the refractive index appears as an effective refractive index from the combination of the IPA soaked filter paper and air. Alternatively this could be due to the analyte thickness being too small to reach the saturation point where the shift is constant ([128] requires an excess of 15 µm for their n = 1.6 analyte) as the dry filter paper thickness is 12.5 µm if there is not enough liquid this could show a partial shift. In either case this should be avoided in future as it provides inaccurate results. Multiple wet scans can be taken, if the feature frequencies are the same for multiple scans the results can be assumed accurate. For example out of the four wet scans shown in figure 7.10, only the one sheet psf scan has a different feature frequency than the other three and therefore this should be ignored and the feature frequency of the other three scans should be taken as the true value (0.975 THz).

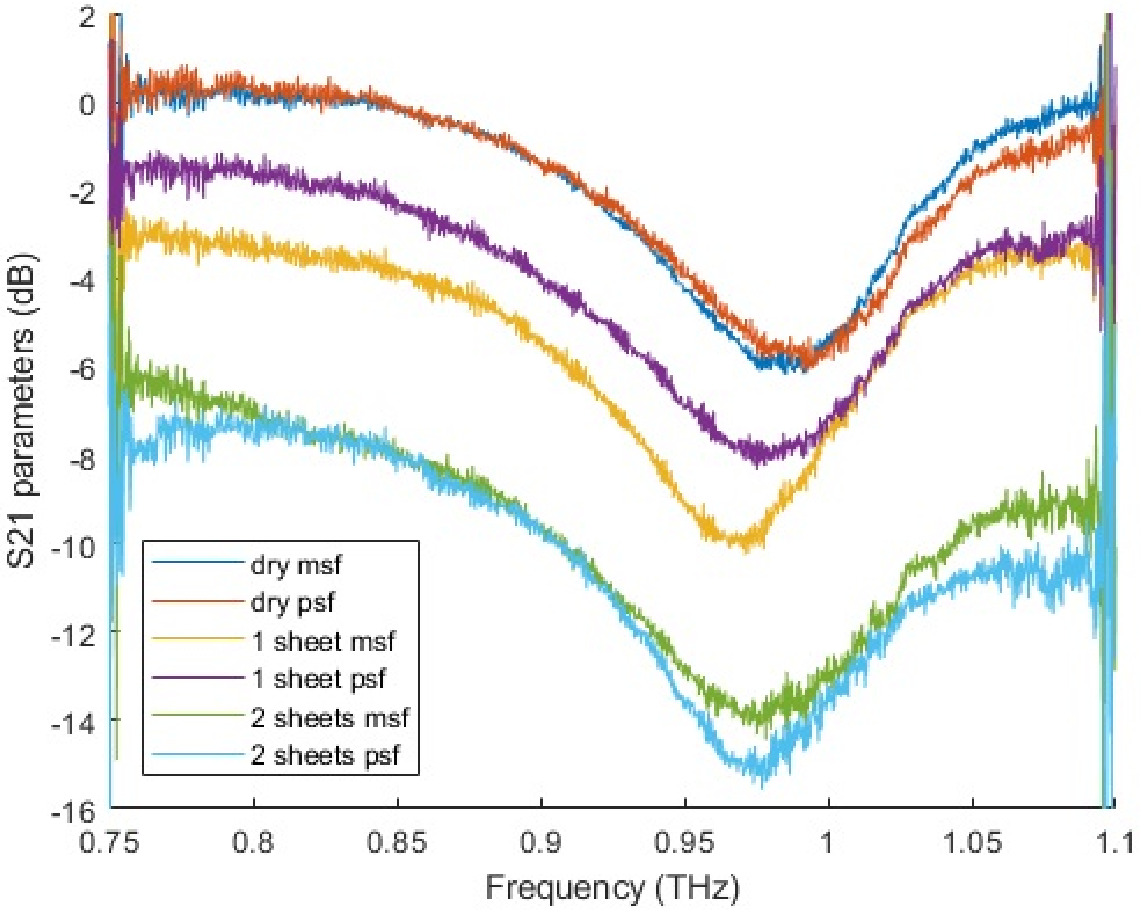

Figure 7.10: Figure showing the 4SQ5 metamaterial and its response dry, in contact with one sheet and in contact with two sheets of IPA soaked filter paper. The figure demonstrates that the trace for 1 sheet psf is not working correctly as it is not in line with the other three wet traces and so would be ignored as part of the devised protocol. Data has been normalised using a free space scan no smoothing or manipulation has been carried out on this data besides finding the magnitude of S21.

7.4.4 Water Responses

Wet and Dry Scans

Scans of each of the CC3, CC4 and 4SQ5 metamaterials, wet and dry, in two directions at a 90° rotation with respect to each other are taken. Figure 7.11 shows the responses for the 4SQ5 design. The figure shows that at 0° the 4SQ5 design does not exhibit a strong feature in the VNA region but the 90° orientation shows a strong -10 dB feature. This is consistent with the wet tests in each orientation. The frequency peak appears to have stayed at approximately the same frequency, which is not as expected. The increase in refractive index due to the water, from basic principles, should shift the feature down in frequency. This is also expected from previous simulations.

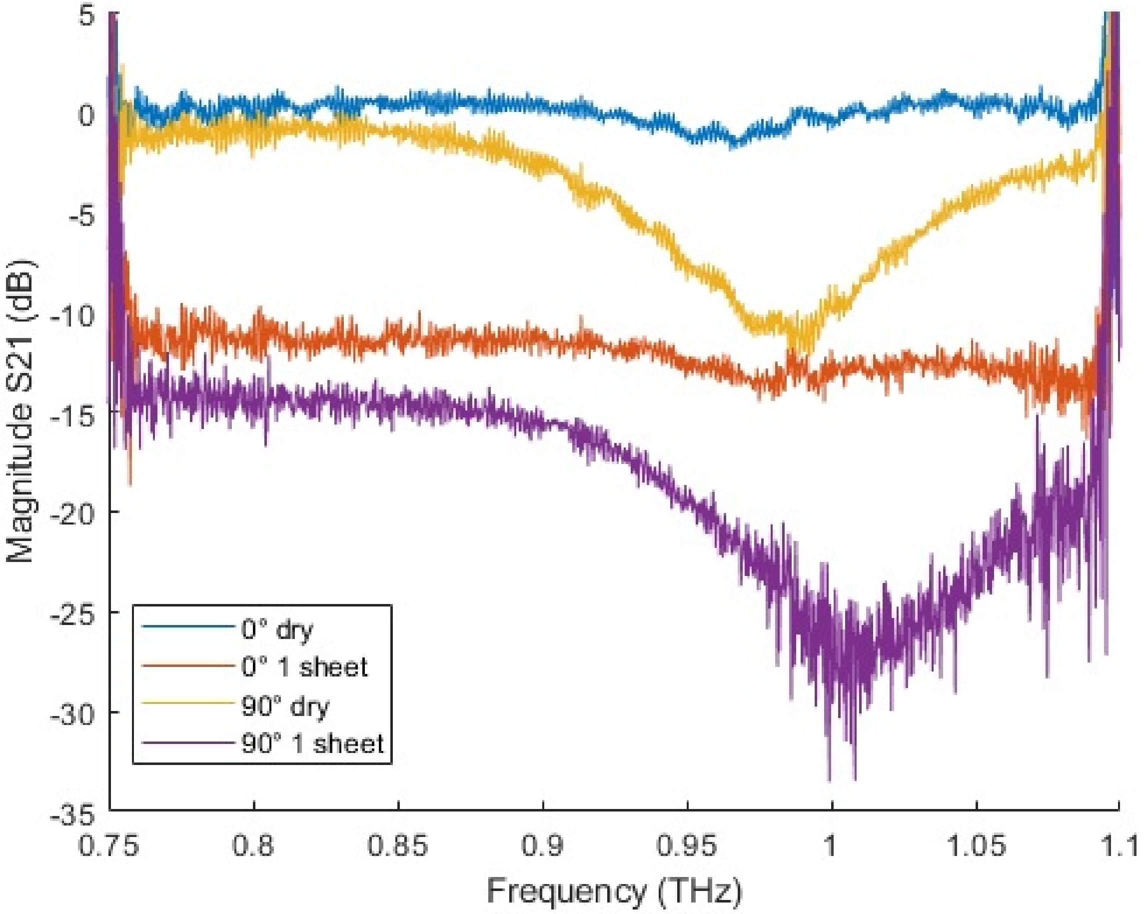

Figure 7.11: Figure showing the 4SQ5 metamaterial design both dry and in contact with 1 sheet of water soaked filter paper at 0° and 90° orientations. Data has been normalised using a free space scan no smoothing or manipulation has been carried out on this data besides finding the magnitude of S21.

Figure 7.12 shows the response for the CC3 metamaterial design, which shows a feature at both 0° and 90°. The feature at 0° is extremely small (< 5 dB) in comparison to the large 90° (45 dB). The feature remains present in both orientations when wet. Little to no shift is shown between the wet and dry scans of each orientation. This is unexpected, again, as the increase in refractive index should shift the peak to a lower frequency.

Figure 7.13 showing the CC4 experimental data shows a similar response to the CC3 results in figure 7.12. The 0° scans have a smaller feature than the 90° scans and both the orientations show a response for the wet scan which has little to no shift compared to their corresponding dry scans.

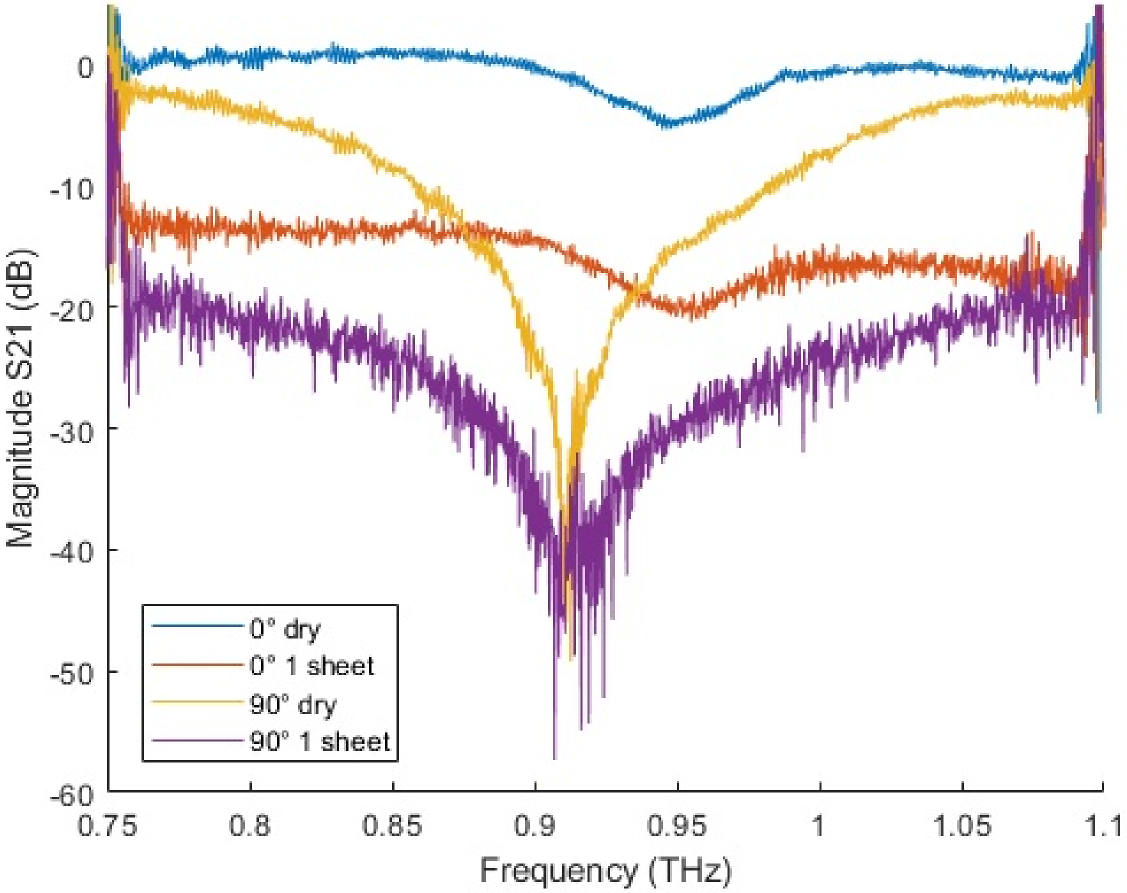

Figure 7.12: Figure showing the CC3 metamaterial design both dry and in contact with 1 sheet of water soaked filter paper at 0° and 90° orientations. Data has been normalised using a free space scan no smoothing or manipulation has been carried out on this data besides finding the magnitude of S21.

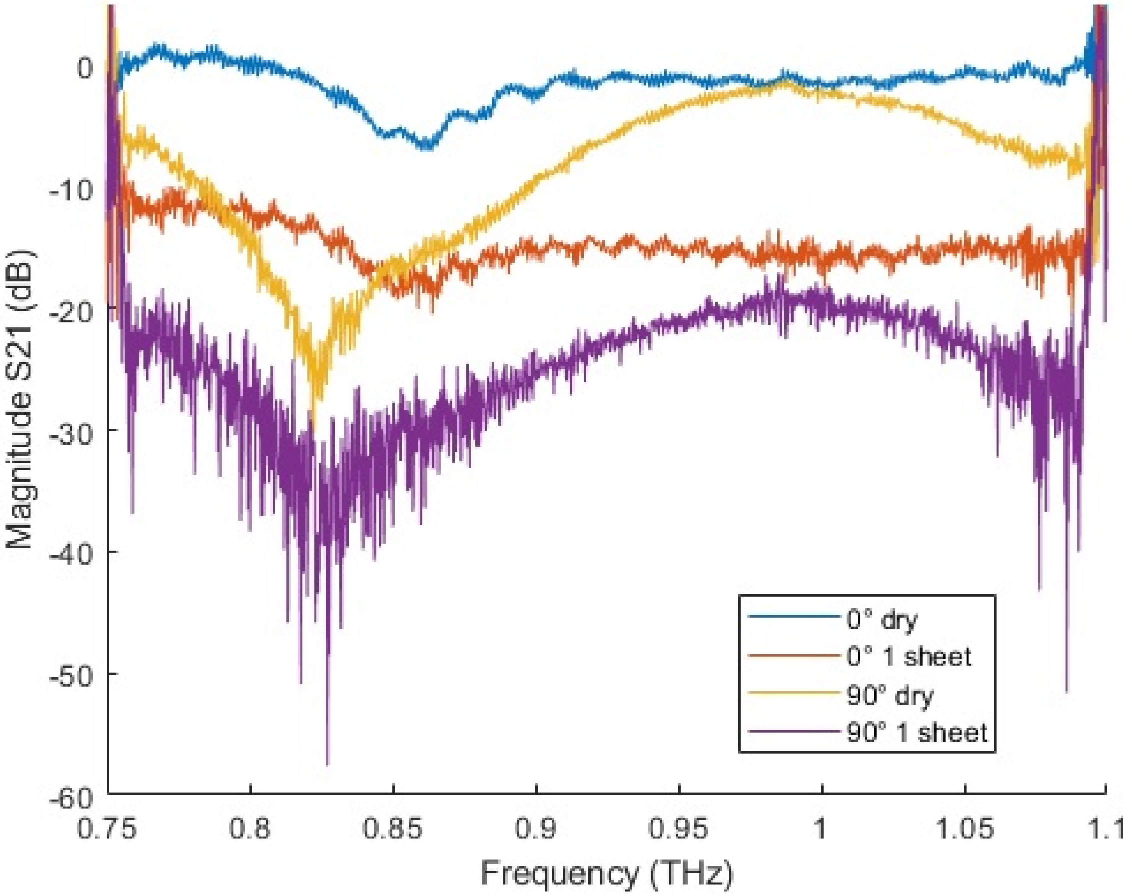

Figure 7.13: Figure showing the CC4 metamaterial design both dry and in contact with 1 sheet of water soaked filter paper at 0° and 90° orientations. Data has been normalised using a free space scan no smoothing or manipulation has been carried out on this data besides finding the magnitude of S21.

The lack of shift in each case here is thought to be due to poor adhesion between the metamaterial and water soaked filter paper. The frequency response of the metamaterial does not change but the addition of the water soaked filter paper increases absorption. This lack of adhesion could be as a result of the application method used in this section. To apply each of the filter paper sheets the filter paper is saturated with water then the excess water is removed using paper towels until there is no surface water on the filter paper. These tests show this is not an appropriate method of application as it does not provide sufficient adhesion with the metamaterial surface to detect a shift in feature frequency.

Filter Paper Drying Tests (Water)

The wet filter paper tests using the pat dry method were unsuccessful due to the application method. Therefore, further experiments are undertaken to assess the suitability of saturating the filter paper with water and continuously scanning until an appropriate level of wetness is achieved via air drying. The purpose of this method is to first ensure a good contact with the metamaterial by saturation then to reduce the amount of water in the filter paper to a measurable amount whilst continuously measuring. The initial measurements provide little to no information as the water layer is too thick and there is too much absorbance to clearly see any features. Over time, as the excess water evaporates from the filter paper without intervention, it is anticipated there will be some scans which have both a good contact with the metamaterial surface and also a low enough water content that the absorption is not too high to obscure the feature.

Figures 7.14 and 7.15 show the CC3 and CC4 metamaterial designs terahertz responses as the water soaked filter paper in contact with the metamaterial air dries. These figures show that the wet metamaterial responses, although they have varying degrees of absorption as the water evaporates, have a consistent feature position. The wet response has a lower feature frequency, ≈ 0.02 THz for the CC3 metamaterial and ≈ 0.01 THz for each peak in the CC4 response, this is the expected as the refractive index has increased from 1 (air) to $\approx$ 1.76 (filter paper and water).

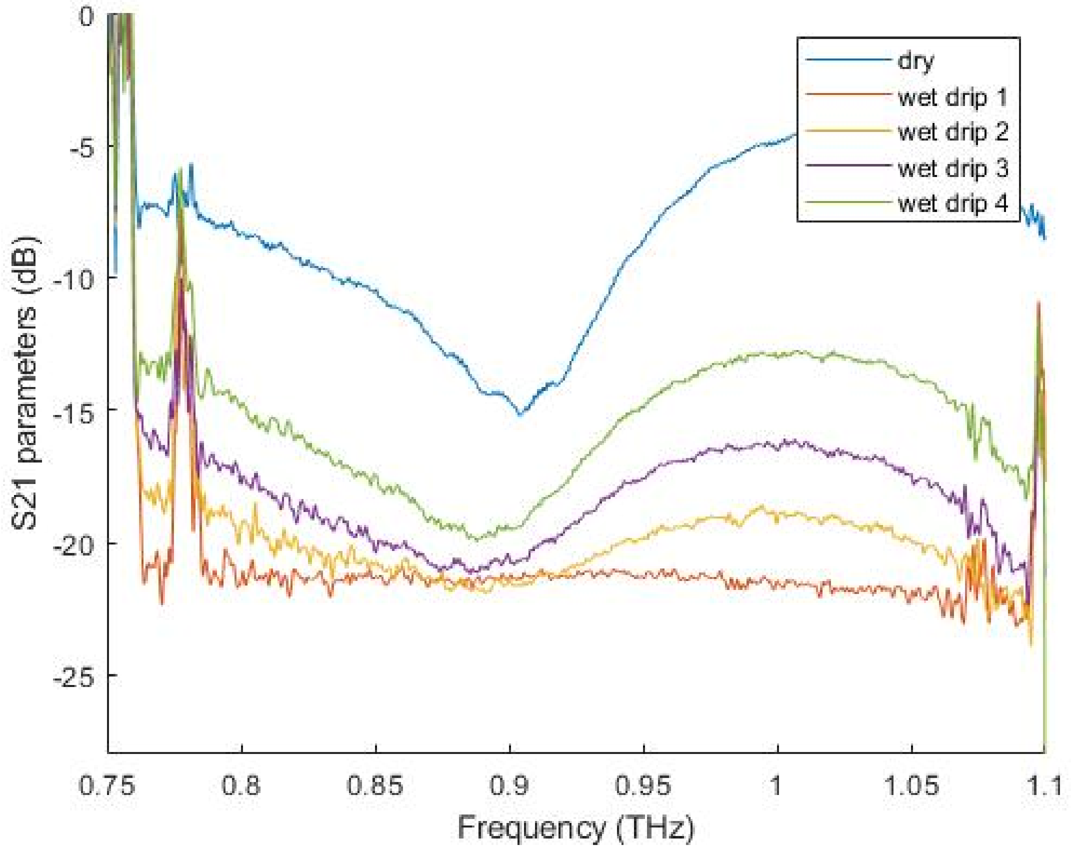

Figure 7.14: Figure showing measured response for CC3 metamaterial wet and whilst drying over time in comparison with its dry metamaterial counterpart. Data has been normalised using a free space scan no smoothing or manipulation has been carried out on this data besides finding the magnitude of S21.

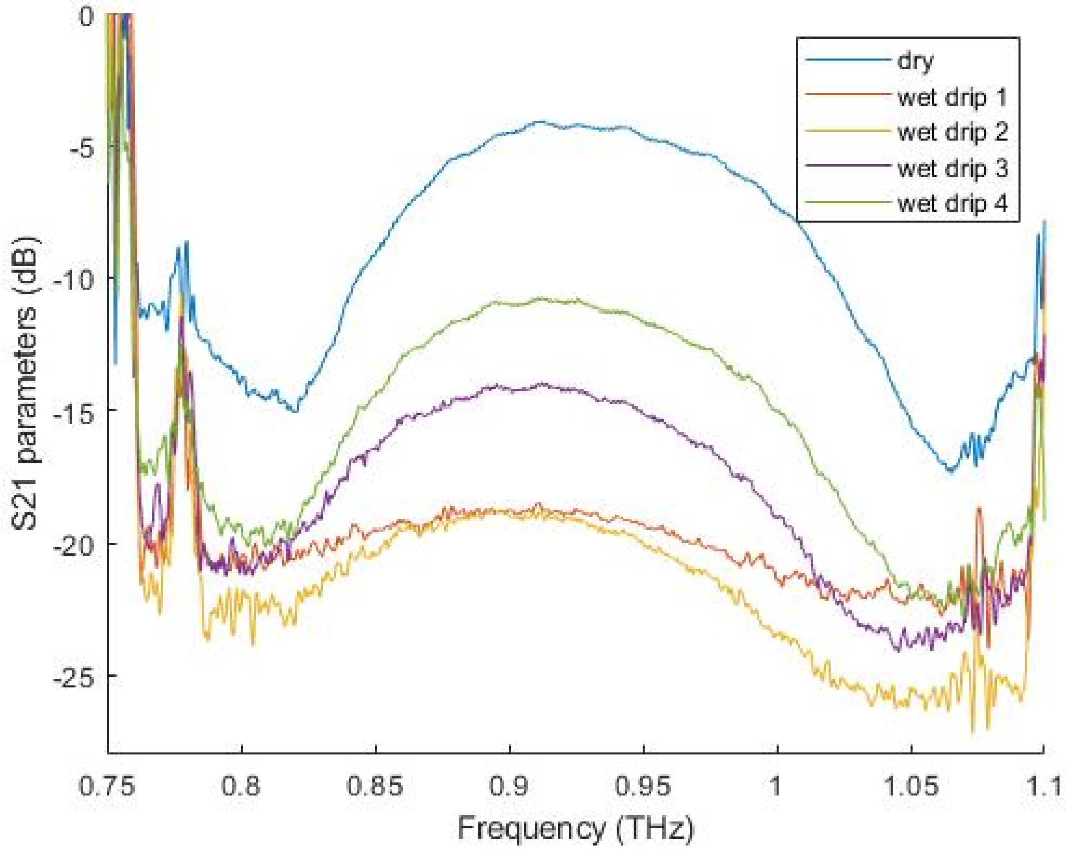

Figure 7.15: Figure showing measured response for CC4 metamaterial wet and whilst drying over time in comparison with its dry metamaterial counterpart. Data has been normalised using a free space scan no smoothing or manipulation has been carried out on this data besides finding the magnitude of S21.

Filter Paper Drying Tests (Water and Milk)

As the purpose for this metamaterial is to test blood serum, tests are conducted to determine whether the metamaterial can distinguish between different water based mixtures, ideally with a similar composition to serum. For these experiments, water soaked paper is used as a control. In place of serum, milk is used as it contains proteins in comparable concentrations to blood serum. The water and milk tests, are to determine whether the method can distinguish between non-protein containing and protein containing water-based liquids. Serum contains 6-8 $\mathrm{g\,dl^{-1}}$ of protein [130] while bovine milk contains 3.6 $\mathrm{g\,dl^{-1}}$ [124] although these are not an exact match milk provides a readily available mixture of comparable composition to serum.

Figure 7.16 shows the traces for the CC3 metamaterial in contact with both water and milk soaked filter paper sheets. Measurements have been taken over time and the last two measurements are displayed in the figure. This figure clearly shows only one of the traces exhibiting the recognisable feature of the CC3 metamaterial. This is the final water trace. The other scans all show reasonably flat responses. As can be seen in the contrast between the water 1 and water 2 traces, which correspond to the penultimate and final measurements taken over time as the paper dries. Each of the water scans prior to this resulted in similar traces straight across the VNA region with no distinct feature, similarly to all of the milk traces prior to this scan. This is thought to be due to insufficient adhesion to the metamaterial surface. In this case it is thought that there is a layer of pure milk or water between the wet paper and the metamaterial which could indicate the high refractive index has shifted the metamaterial peak out of range of the VNA. These scans illustrate the importance of dynamic drying tests to reduce the error from a single scan where the filter paper could contain too much analyte to measure a feature.

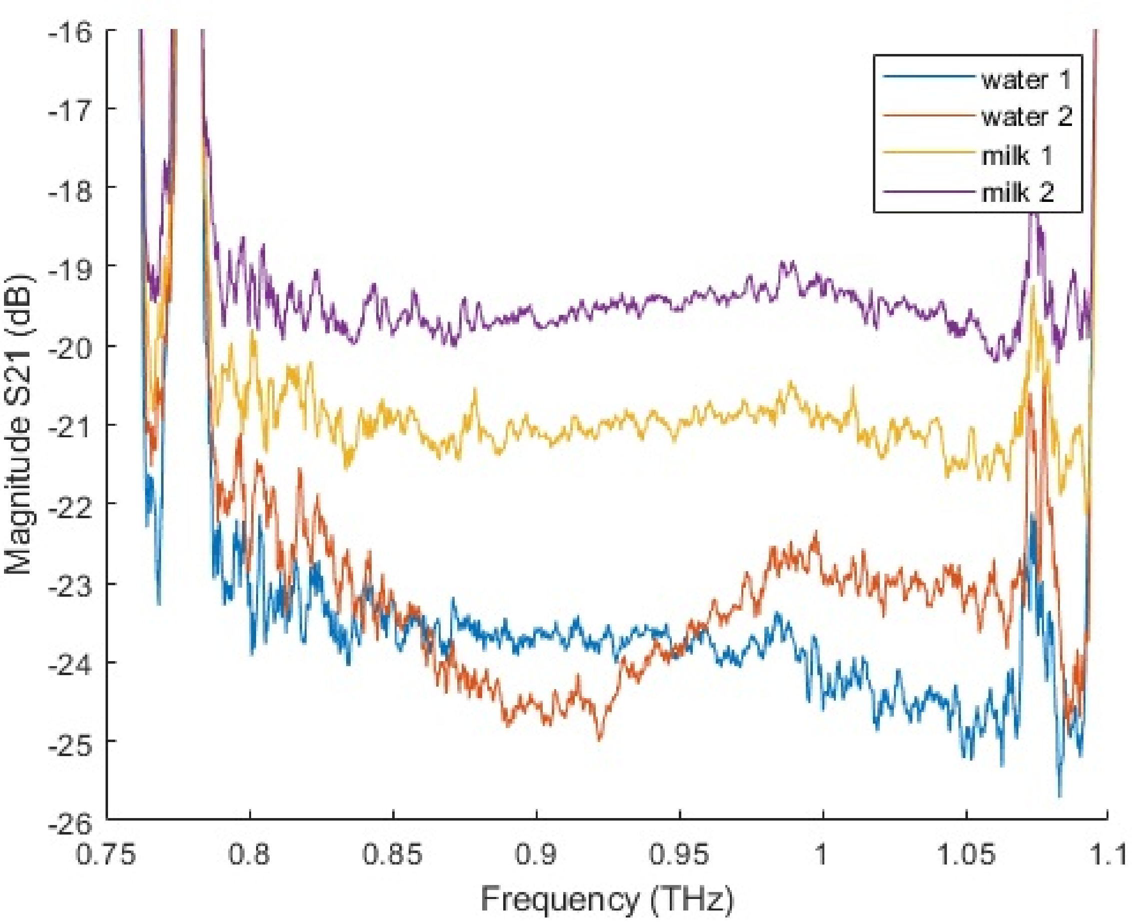

Figure 7.16: Figure showing measured response of the CC3 metamaterial in contact with milk and water soaked filter paper samples drying over time. Data has been normalised using a free space scan no smoothing or manipulation has been carried out on this data besides finding the magnitude of S21.

Figure 7.17 shows the penultimate and final measurements in time for the water and milk soaked filter paper in contact with the CC4 metamaterial. The desired amount of analyte is achieved in these scans as can be seen by the presence of features in all scans. The contrast between the the feature positions of water and milk scans is ≈ 0.01 THz for each of the two features. This is a positive result as this functions as proof of concept for the method.

As each scan is conducted independently, the absolute values of absorption cannot be taken into account. However, methods considering the rate of drying could be considered provided a controlled drying environment can be ensured.

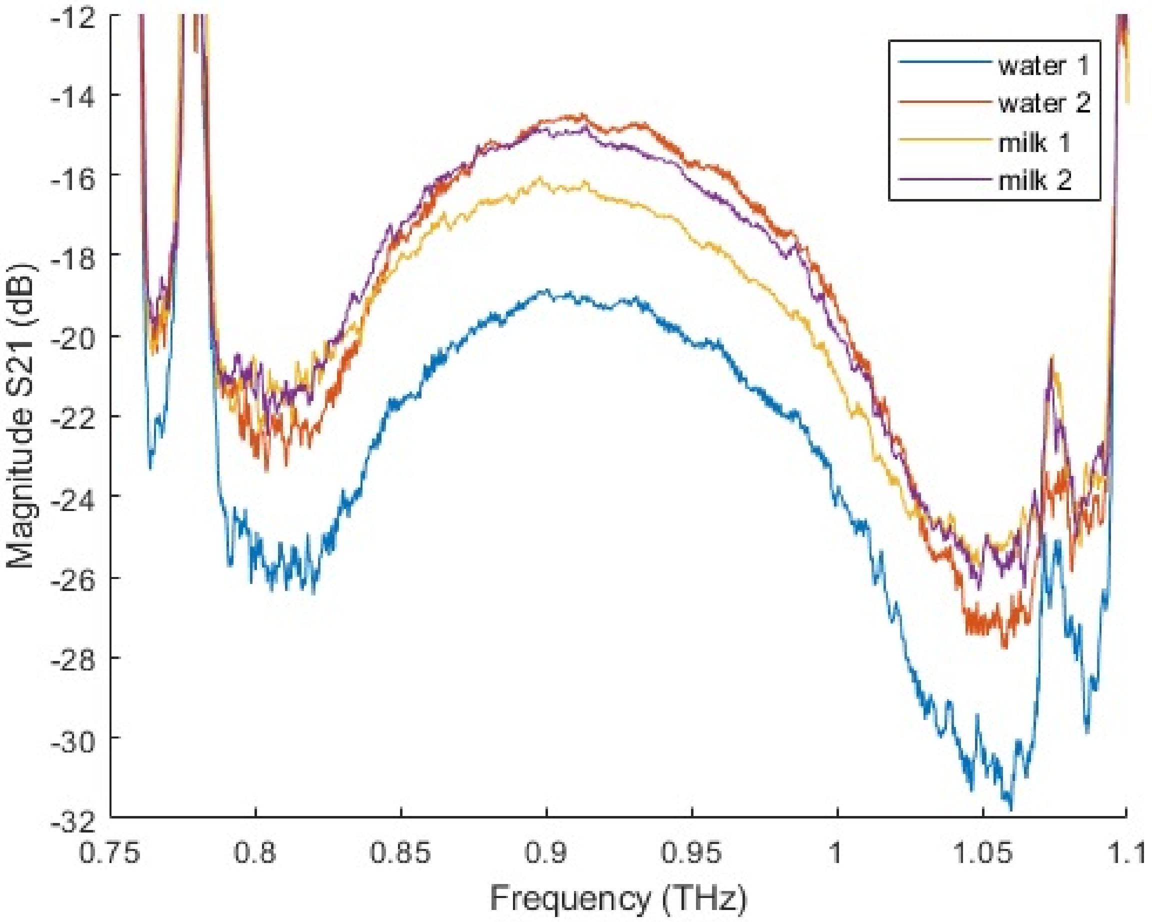

Figure 7.17: Figure showing measured response of the CC4 metamaterial in contact with milk and water soaked filter paper drying over time. Data has been normalised using a free space scan no smoothing or manipulation has been carried out on this data besides finding the magnitude of S21.

Finally, figure 7.18 shows the milk and water soaked filter paper scans for the 4SQ5 metamaterial. As demonstrated in the CC3 scans, the water 1 (penultimate water scan) does not show a feature thus is not dried enough at this scan. However, this is rectified in the final scan (water 2) and a feature can be seen. This feature is clearly distinct (0.92 THz) from the two features for the milk soaked filter paper scans (0.9 THz), which are both in line vertically therefore correct adhesion and metamaterial response saturation can be assumed.

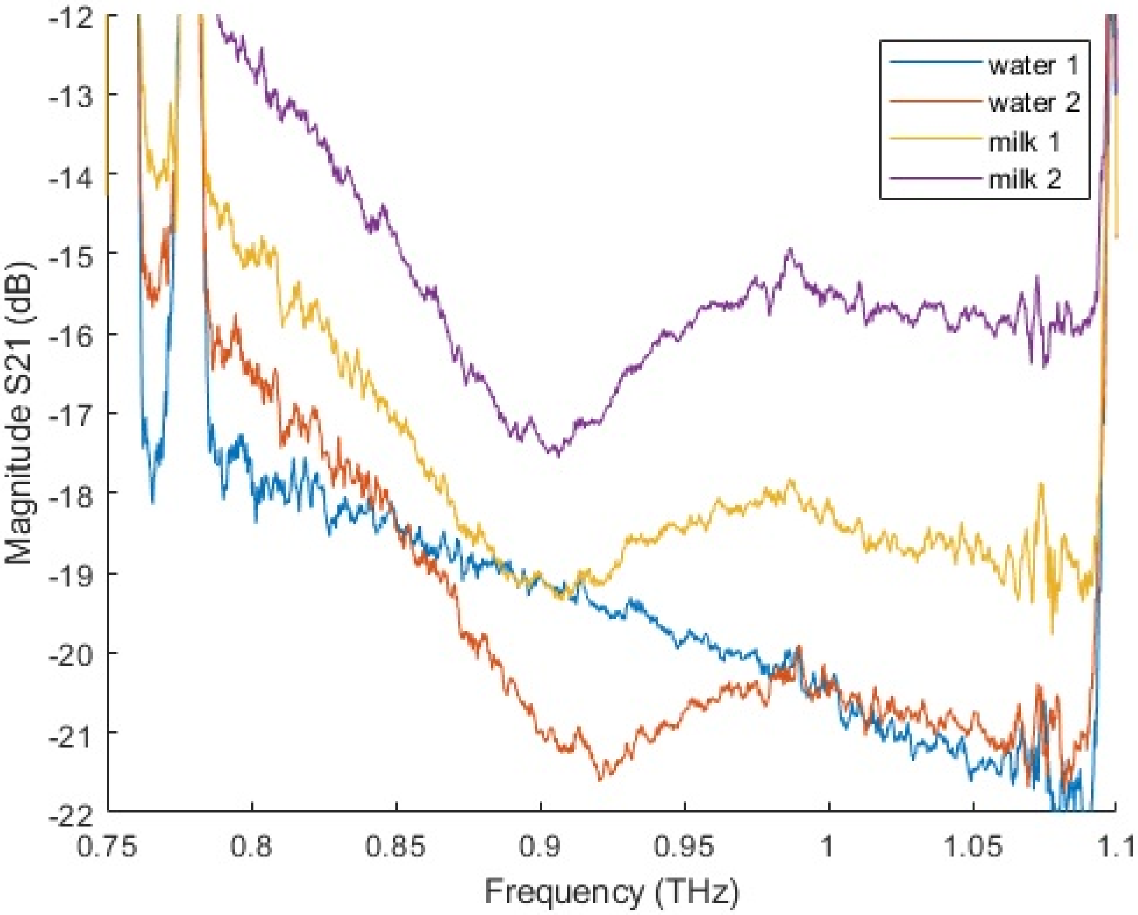

Figure 7.18: Figure showing measured response of the 4SQ5 metamaterial in contact with milk and water soaked filter paper drying over time. Data has been normalised using a free space scan no smoothing or manipulation has been carried out on this data besides finding the magnitude of S21.

These experiments stress the importance of testing at the required wetness level demonstrating the issue with measurements where the filter paper has excess liquid. Hence, it is important to ensure the scans are run for a sufficient amount of time to avoid the results as in figure 7.16. The initial wet dry paper scans showed the importance of not allowing the paper to be too dry. As the drip dry method starts with fully saturated filter paper and measures continuously this is avoided.

7.5 Final Design

The CC3 metamaterial with a central absorption peak for the VNA range was selected as the final design. It produced the most reliable design with respect to experimental response and compared with the CC4 and 4SQ5 designs, it produced the strongest single peak. The 4SQ5 design was shown and simulated to be the most sensitive. However, there have been issues with the fabrication and performance of the 4SQ designs in general and have been proven to be less reliable than the CC designs. The CC3 design has beneficial sensitivity as compared to the CC4 design and also enables the peak to be central ensuring it does not fall out of the VNA range during testing.

It was found from experiments that the largest aperture feasible for the device should be used. The angle should be kept stable in the orientation which is desired, for the CC3 design this is the 90° orientation. To mitigate fabrication consistency issues each metamaterial section is tested in the VNA prior to use.

The method of holding the liquid sample onto the metamaterial surface will be to use filter paper. Tests have shown that if the filter paper is too dry often a shift in feature frequency is not visible. This could be due to either poor adhesion with the metamaterial surface, the total analyte layer being too thin to reach saturation in the electromagnetic shift or a combination of both. When the filter paper is too wet the response is flat and shows no feature, this is thought to be due to a layer of pure analyte at the surface of the metamaterial shifting the feature out of range and/or the high absorption obscuring the feature. All of these issues can be found by taking multiple scans at different levels of wetness, if the feature position of multiple scans are the same then it can provide a level of confidence in the measurement that each of these problems are not occurring.

Chapter 8

Terahertz Detection of Tumour Markers

The methods described and developed in chapters 6 and 7 are applied to tumour marker detection of human serum samples. This chapter presents an overview of what we know about cancer in general including more specifically a brief overview of tumour markers and their use in cancer detection, diagnoses and treatment.

Following this, the final metamaterial design, as described in chapter 7, is used in a feasibility study to discover if the method developed in this thesis can detect tumour markers in human serum samples.

8.1 Introduction

There are almost 1000 new cases of cancer every day, with an estimated 2-3 million people living with cancer at any one time [131]. Cancer is a large group of over 100 diseases that progress with time and involve the uncontrolled division of the body's cells. Although cancer can develop in virtually any of the body's tissues the disease has its own unique features dependent upon the physical site. Cancer is initiated when any cell develops a mutation that causes it to be more likely to divide than it normally would. Once this cell divides, the ancestral cell all its descendants now have the mutation which causes them to grow and divide too often; this is known as hyperplastia. At some point, one of these cells mutates again, further increasing its tendency to divide. This cell and all of its descendants have mutated to divide excessively and also have an abnormal appearance this is known as dysplasia. After sufficient time, a third mutation will occur, this cell and its descendants will be very abnormal in both growth and appearance. By this stage, a tumour will have been formed by the build up of cells. However, it will still be contained within its tissue of origin and therefore is called in situ cancer. Once further mutations happen and the tumour is able to invade neighbouring tissues or shed cells into the blood or lymph the tumour is now said to be malignant as the cells may establish tumours at new sites across the body.

Cancer is responsible for 28% of all UK deaths and 45% of these deaths are from lung, bowel, breast or prostate cancer [132]. The mortality rate of cancer patients is dependent on the type of cancer as shown in table 8.1 for example the most common cancer types; breast, lung, prostate and bowel have a survival rates of 78% [132], 5% [132], 84% [132] and 57% [132] respectively.

Cancer type	**Incidences**	**Mortality's**	**Survival rate**
Anal cancer	1,438	399	57%
Bladder cancer	10,187	5,383	50%
Bone sarcoma	556	360	55%
Bowel cancer	42,042	16,384	57%
Brain tumours	11,725	5,250	14%
Breast cancer	55,213	11,563	78%
Cervical cancer	3,192	854	63%
Eye cancer	805	107	60%
Gallbladder cancer	1,040	606	15%
Head and neck cancers	11,945	4,047	19-59%
Hodgkin lymphoma	2,086	304	80%
Kidney cancer	12,866	4,619	50%
Leukaemia	9,918	4,712	46%
Liver cancer	5,906	5,417	
Lung cancer	47,235	35,620	5%
Melanoma skin cancer	15,970	2,285	90%

Continued on next page

Table 8.1 – *Continued from previous page*

Cancer type	**Incidences**	**Mortalities**	**Survival rate**
Mesothelioma	2,732	2,496	
Myeloma	5,657	3,079	33%
Non-hodgkin lymphoma	13,886	4,920	63%
Non-melanoma skin cancer	147,445	1,319	
Oesophageal cancer	9,101	8,004	12%
Ovarian cancer	7,470	4,227	35%
Pancreatic cancer	9,972	9,263	<1%
Penile cancer	639	134	38%
Prostate cancer	47,740	11,631	84%
Small intestine cancer	1,603	516	
Soft tissue sarcoma	3,272		45%
Stomach cancer	6,697	4,457	57%
Testicular cancer	2,364	57	98%
Thyroid cancer	3,527	382	85%
Uterine cancer	9,314	2,360	78%
Vaginal cancer	252	100	53%
Vulval cancer	1,318	460	53%

Table 8.1: Cancer sites and number of cases per year with number of deaths per year and survival rate as per their respective pages on [132].

8.1.1 Gender

There are many different factors which can affect an individual's chances of incidence and mortality from cancer. Gender is a strong factor that affects the types of cancer a person is able to get, is more likely to get, their bodily response to the cancer and even their response to treatment. In the US between 2009 and 2013, the incidence rate of cancer was 20% higher for men than for women and the mortality rate was 40% higher for men than for women [133]. A person's sex can affect cancer susceptibility while hormones can positively or negatively affect the development of various cancers [134]. The 1977 United States Food and Drug Administration excluded women in clinical research if they are considered to have ‘childbearing potential’ due to the risk of birth defects [135] however, there is accumulating evidence to show sex-specific differences in the toxicity and efficacy of chemotherapy [136, 137]. This lack of research can result in the incorrect dosing of women which can cause adverse reactions such as extreme side effects. Biological differences in men and women cause them to react differently to the same dose of a drug as there are differences in body mass, hepatic clearance, drug absorption, distribution in tissues, metabolism by liver enzymes and excretion via the kidney and intestine [138, 139]. Gender can therefore affect the overall risk of a person, for example the most common types of cancer in males is prostate cancer which is responsible for 26% of cancers in males at over 47,000 cases in 2016. As females do not have a prostate, they cannot get this type of cancer. Other male only cancers include testicular and penile cancer. The most common cancer for women in the UK is breast cancer where over 54,000 women are diagnosed each year; men can also get breast cancer but only 350 are diagnosed with the disease each year as shown in table 8.2. Women only cancers include vaginal, vulval, cervical, uterine and ovarian cancers. The types of cancer each gender can get, their individual risk for each type of cancer, along with the survival rate of each cancer type contribute to the imbalance of both incidences and deaths between the genders whilst the genetic makeup of both male and female patients can also define not only the cancer itself but also the response to therapy and chances of a smooth recovery.

8.1.2 Age

Another significant factor which affects the tendencies of cancer is age. Each year 53% of cancer deaths in the UK are in people aged 75 and over [132]. In general, the risk of getting cancer is increased with age, however the types of cancer people tend to get changes particularly with cancers resulting in mortality, hence, the higher mortality rate of older patients. The most common cancers diagnosed in children aged 0 to 14 were leukaemia and brain cancer with non-Hodgkin’s lymphoma for males and kidney cancer for females these account for 56.3% of the 1,459 child cancer diagnoses in England in 2017. In persons aged 15 to 44 years women were more likely to be diagnosed with cancer at

Cancer type	Female cases	Male cases
Breast cancer	54,541	355
Prostate cancer	0	47,640
Lung cancer	22,342	25,046
Bowel cancer	18,626	23,529
Melanoma skin cancer	8,294	8,080
Non-hodgkin lymphoma	6,265	7,729
Kidney cancer	4,714	8,041
Head and neck cancers	6,022	5,422
Bladder cancer	2,846	7,237
Pancreatic cancer	4,851	5,154
Uterian cancer	9,538	0
Leukaemia	3,789	5,714
Oesophageal cancer	2,824	6,249
Cancer of unknown primary	4,562	4,336
Ovarian cancer	7,526	0
Stomach cancer	2,213	4,367
Liver cancer	2,015	3,918
Myeloma	2,405	3,191
Thyroid cancer	2,634	973
Other sites	12,359	11,997

Table 8.2: Cancer incidence by gender [132].

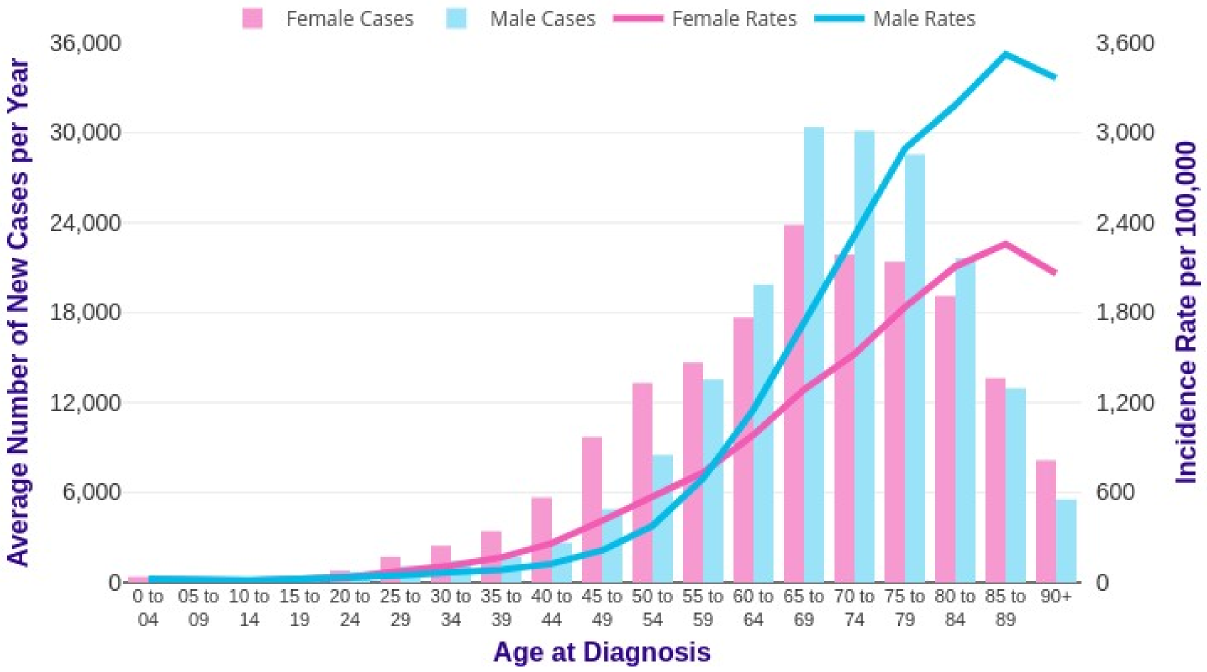

Figure 8.1: Graph of UK statistics for cancer incidences and rate with respect to gender and age [132].

11,953 incidences of which 4,221 were breast cancer as compared to men with a total of 6,663 incidences where testicular cancer was dominant with 1,369 cases. For males over 45 years of age, the most common cancer was prostate cancer, while for females breast cancer once again has the most instances [140]. For the elderly population (ages 75+) the most common cancer for males remained to be prostate cancer, however the percentage of male cancers has dropped slightly with increasing percentages of lung, bowel, bladder and non-hodgkin lymphoma [132]. Women ages 75 and over are similarly still most likely to suffer from breast cancer, however this likelihood has decreased from the previous group while bowel, lung, and pancreatic cancers rise. The overall incidence rates and number of cases for both males and females with age are shown in figure 8.1 where although the number of incidences for males and females decreases after age 70 (36% of new cancer cases are from people aged 75 and over) the cancer rate continues to increase to the highest incidences at ages 85-89 this is due to the size of the population at this age. The mortality rate has broadly decreased across all age groups however, the largest decrease of 63% is found in the 0-24 age range.

Age can even be an important factor in decision making processes for the treatment of cancer, older adults reported lower influence of support networks than younger adults and older groups were also more satisfied with their decision than younger and middle-aged adults [141].

8.1.3 Ethnic Group

A further significant factor in the likelihood of getting cancer is ethnic group; a study in England from 2002 to 2006 [142] showed that Asian, Chinese and mixed ethnic groups all had significantly lower incidence risk than White people. Black women have a slightly reduced risk of cancer than White women, however, there was no significant difference between Black and White men in terms of cancer incidence. The Asian ethnic group has significantly higher rates as compared to the White ethnic group for liver cancer across both sexes and all ages (1.5-3 times more likely in Asians than Whites). Higher rates are also found in mouth and cervical cancer for Asian women aged 65 or over. However, risk for Asian men or Asian women below 65 was either similar or significantly lower than the White group. Asians were at significantly lower risk of getting any of the four major cancers (breast, prostate, lung and colorectal) as well as many other cancer sites; bladder, brain and CNS, kidney, oesophagus, ovary, pancreas and malignant melanoma of the skin. Although Asian women have lower incidence rates for breast cancer, Asian women aged 15-64 had reduced survival at three years (89%) compared to White women (91%). In contrast, Asians had a significantly improved lung cancer survival rate for three years (20%) as compared to White people for all ages (11%). There were no significant differences for colorectal cancer survival between Asian and White people. Black people had higher rates of stomach cancer and myeloma for all ages. Black males are significantly more likely to get diagnosed with prostate cancer (1.1 to 3.4 times more likely than White males). Black females age 65 and over were more likely to get cervical cancer compared to Whites. Blacks people are at significantly lower risk of breast, lung, colorectal, bladder, brain and CNA, oesophagus, ovary, pancreas and malignant melanoma of the skin. Black women ages 15-64 years had reduced breast cancer survival at three years (85%) as compared to Whites (91%); there were no significant differences in those above 65 years old. Black males aged 65-99 with lung cancer had a much better three year survival rate (13%) than White males (8%). Chinese and mixed ethnic groups tended to have lower incidence rates than Whites for the four major cancer sites.

These results are similar to the US results, as can be seen in reference [143] incidence rates are significantly higher for African American and White men than for all other ethnic backgrounds in this study. The results are similar for females, however, the Hawaiian and Alaska Native groups also have similarly high incidence rates as seen in table 8.3.

Ethnicity	**Male Incidence**	**Female Incidence**	**Male Mortality**	**Female Mortality**
African American	560	326	319	168
Chinese	282	213	139	86
Filipino	274	224	105	63
Hawaiian	340	321	239	168
Japanese	322	241	133	88
Korean	266	180	N/A	N/A
Vietnamese	326	273	N/A	N/A
Alaska Native	372	348	225	179
American Indian	196	180	123	99
White	469	346	213	140
Hispanic	319	243	129	85

Table 8.3: Cancer incidence and mortality rates per 100,000 population by race, ethnicity and sex in the United States 1996 [143].

Stage of Detection with Ethnic Groups

There are also evident trends on the stage, treatment and survival across different ethnic groups. Reference [144] reports on a study in the south east of England assessed women diagnosed with breast cancer between 1998 and 2003. It found that White women had the highest incidence ratio of breast cancer among all ethnicities and so were used as the baseline group where other ethnic groups had incidence ratios as shown in table 8.4. This study also noted that White women are the most likely to have a stage noted at diagnosis and also least likely to be diagnosed with metastatic disease while Black women were the least likely to have a record of cancer surgery or hormone therapy but most likely to receive chemotherapy. An interesting conclusion in this study was that once adjusting the results for age, socioeconomic deprivation, disease stage and treatment received no significant variation between ethnic groups was found for breast cancer survival.

Ethnicity	**Incidence rate ratio**
White	1
Indian	0.68
Pakistani	0.59
Bangladeshi	0.23
Black Caribbean	0.8
Black African	0.66
Chinese	0.54

Table 8.4: Breast cancer incidence rate ratios in the South East of England between 1998 and 2003 [144].

Genetics

On a smaller scale, genetics can be a strong indicator of any individuals personal risk to cancer, we can identify this through trends in family history and more recently specific genes increasing the likelihood of certain cancers have been identified. Reference [132] shows the cancers known to have genes increasing the risk of cancer which can be tested for in the UK.

8.1.4 Environmental Causes

Along with all these genetic factors there are proven environmental factors which can increase the likelihood of having cancer for example there are widely known factors such as smoking, diet and obesity. Many specific cancers show trends with migration from lower risk countries to higher risk countries increasing the risk of the migrant therefore risk can be attributed to environmental factors [145].

Smoking

Smoking is widely known as one of the most prevalent causes of cancer attributing to 15% of cancers globally in 1985 [146]. Due to the death rates of the types of cancers caused by smoking, in the US, 30% of cancer deaths in 1981 are said to have been a direct cause of smoking [147]. A study on Korean men showed increased risk in mortality for current smokers compared to those who have never smoked for many cancers and a very strong relation for cancer of the oesophagus, larynx and lung full trends are shown in table 8.5.

Cancer	**Current Smoker versus never smoker**	**Former smoker versus never smoker**
Oesophagus	3.6	1.9
Stomach	1.6	1.4
Colon	1.1	1.1
Liver	1.2	1.3
Bile duct	1.5	1.1
Pancreas	1.4	1.3
Larynx	6.5	3.6
Lung	4.6	2.2
Prostate	1.2	1.0
Kidney	1.0	1.2
Bladder	1.9	1.6
Brain	1.1	1.1
Thyroid	1.2	1.6
Leukemia	1.3	1.4

Table 8.5: Cancer mortality rate in Korean men who smoke or have formerly smoked compared to Korean men who have never smoked [148].

Confirmed and suspected causes of cancer mentioned by the The international agency for research on cancer (IARC) [149] include tobacco which has been confirmed to cause many cancers including a range of consumption methods; smoking tobacco, smokeless tobacco, betel quid with tobacco and secondhand tobacco smoke. Betel quid without tobacco has also been shown to cause cancer of the oral cavity and the oesophagus.

Diet, Obesity and Physical Inactivity

Diet affects our risk of cancer incidence. For example low fruit and vegetable intake can increase the risk of colorectal, stomach, lung and oesophageal cancers [150]. There is also evidence that whole grains, dietary fibre, certain micro-nutrients and some fatty acids protect against some cancers where some other fatty acids and food preparation methods may increase risk [151]. Although many studies have previously been undertaken with a ‘cause and effect’ strategy finding which substances increase risk essentially through trial and error [152, 153], more recent work has been focusing on identifying the mechanisms responsible for increased cancer risk due to these dietary factors. These mechanisms are thought to be different for different cancer sites but could include insulin resistance and resultant chronic hyperinsulinaemia, increased bioavailability of steroid hormones and localized inflammation [154].

IARC [149] listed carcinogenic foods include: Chinese-style salted fish and processed meat with the consumption of red meat and traditional Asian pickled vegetables being suspected causes of cancer.

Along with diet, physical inactivity can also increase the risks of cancer, this also ties in with the increased risk due to obesity. Physical inactivity has shown increased risk of breast, colorectal and prostate cancer while obesity has shown a correlation for corpus uteri, colorectal, breast, gallbladder and kidney cancers [150]. The worldwide trend in obesity is suggesting that overeating may be the largest avoidable cause of cancer in nonsmokers [155] accounting for approximately 20% of all cancer cases [156]. Obesity has been shown to increase risk of cancer between 1.5 and 3.5 times that of non-obese subjects for post menopausal breast cancer, endometrium [157], colon and kidney and malignant adenomas of the oesophagus; further studies have shown that obesity may increase risk for pancreatic, hepatic and gallbladder cancer [158]. Again, while previous studies focused on cause and effect more recent work has been focused on the possible mechanisms relating obesity to cancer which is thought to be different for different cancer sites but could include insulin resistance and resultant chronic hyperinsulinaemia, increased production of insulin-like growth factors or increased bioavailability of steroid hormones.

Migrants and the Environment

Environmental factors such as diet can be seen clearly in migrants who can increase their risk by moving to higher risk countries e.g. migrants to Australia from Italy or Poland experience a rise in breast cancer risk particularly when migration occurs in childhood [159, 160]. Similar studies of Asians migrating to the United States show major increases in risk between first, second and third generations [161]. Migration has also been shown to increase risk of colorectal cancers implying that dietary and other environmental factors constitute a major component of risk [162]. Other main risk factors mentioned in [150] are smoking, alcohol use, unsafe sex, air pollution, indoor smoke from coal and contaminated health care injections.

Oesophegeal Cancer and the Environment

High risk areas for oesophageal cancer show various different environmental causes; tobacco and alcohol are the main agents in Europe and North America while chewing tobacco and betel are common causes in the Indian subcontinent. Hot beverages have also been shown to increase risk; drinking hot maté is likely the cause of high risk in Uraguay, southern Brazil and northern Argentina. One possible explanation of this risk is that yerba maté contains polycyclic aromatic hydrocarbons which are known to be carcinogenic. It has been found that drinking maté at colder temperatures does not increase this risk, there is not enough evidence currently to draw conclusions to the specific mechanism of this increased risk however, it can be assumed that it either has to do with the temperature of the drink or this in combination of the carcinogenic components [163]. Regular consumption of very hot drinks have also been shown to increase an individuals risk of oesophageal cancer when combined with the consumption of carcinogenic substances for example drinking very hot tea combined with the consumption tobacco and alcohol was shown to increase risk from a study of 450,000 participants in China [164]. This study found no increased risk for those who consumed very hot tea but did not smoke or drink. In addition, little risk was found for beverages consumed below the temperature of 65°C. A study conducted in northern Iran found that the risk of oesophegal cancer increases by 2.07 and 8.16 with drinking hot (60-65°C) and very hot (65+°C) tea respectively, interestingly most participants involved in this study have never consumed alcohol or tobacco [165]. Nutritional deficiencies are thought to cause the raised risk in central Asia, China and southern Africa. Other known contributory factors include foods such as pickled vegetables, nitrosamine-rich foods, mycotoxins, opium residues (Iran) or pipe stem residues (Traskei or southern Africa) [145].

Alcohol

Alcohol is another substance in common use across the world which is known to cause cancer. IARC has published and keeps up to date a list of confirmed and suspected carcinogenic substances [149] of which alcohol is a common feature across cancer types (oral cavity, pharynx, digestive tract, oesophagus, colon & rectum, liver & bile duct, larynx, breast).

Radiation and Workplace Hazards

Radioactive substances such as Plutonium, Radon-222, Thorium-232, Radium-224, Radium-226, Radium-228, Strontium-90, Phosphorus-32 and Radioiodines are either known to or suspected to cause cancer. Electromagnetic radiation in the form of X-rays, γ-rays and UV-radiation (which includes solar radiation) are all known to cause cancer.

There are many workplace health hazards associated with various industries where they work with substances which can cause cancer. These can take many forms from working with X-rays and γ-rays to working with radioactive substances or inhaling carcinogenic fumes. Working with industrial chemicals such as formaldehyde, strong inorganic mists and asbestos

Medical Causes

Hormonal therapy has been shown to increase the risk of certain cancers, e.g. estrogen-progestogen contraceptives and menapausal therapy are known to contribute to increased risk for breast, uterine, endometrium, ovarian and cancer of the cervix.

15.6% of the worldwide incidences of cancer can be attributed to the hepititis B and C viruses, the human papillomaviruses (HPV), Epstein-Barr virus (EBV), human T-cell lymphotropic virus I, human immunodeficiency virus (HIV), Helicobacter pylori, schistomes or liver flukes [166]. Hepititis B and C have been shown to increase the risk of liver cancer around 20 times [167] with more than 75% of cases worldwide and 85% of cases in less developed countries caused by these two viruses [168]. Stomach cancer has been shown to increase risk with the Helicobacter pylori infection being classed as carcinogenic to human beings increasing relative risk by 2.5 [169].

HPV is now accepted to be the most important cause of cervical cancer [170]. There are 100 different kinds of HPV which are responsible for almost all the cases of cervical cancer worldwide (99.7%). HPV16 and HPV18 account for approximately 70% of cervical cancer [171]. In the UK as of 2019 all the year 8 boys and girls ages 12-13 receive the HPV vaccine which protects against HPV 6, 11, 16 and 18 [172]. For the past decade the HPV vaccine has only been given to female children to protect from cervical cancer, however, since September 2019 it is also given to male children as HPV can cause other cancers such as anal, genital and head and neck cancers. HPV 6 and 11 are responsible for 90% of genital warts which the vaccine also protects against.

Socio-economic Factors

In addition to the biological differences in race affecting incidence and mortality rates, in places such as the United States (US), socio-economic factors can play a huge part, particularly in mortality rates as this is affected by access to healthcare. Across the US in 2017 [173] 91.5% of White and 92.7% of Asian people tend to have access to health insurance which is more than the 89.4% of Black and 83.9% of Hispanic people therefore just through sheer access to care the White and Asian groups are more likely to encounter a positive outcome.

Ethnic group and socioeconomic status can effect and socially influence environmental factors such as cigarette smoking, physical inactivity and obesity. Low and middle income countries now account for more than 50% of lung cancer deaths, this can be drawn down to the different historical smoking patterns and the fact that socioeconomic status is a strong indicator of the likelihood of smoking [174]. For example according to this study [175] for all races males have a 19.6% to 27.4% chance of being a smoker but for females this varies greatly with Asian Americans the lowest at 7.9% where American Indian/Alaskan Native women have a 38.6% chance of being a smoker. Hispanic men and women were most likely to have no leisure time physical activity while the American Indian/Alaskan

Natives were most likely to be obese.

8.1.5 Diagnostic Stage

Mortality rates of malignant tumours are known to significantly decrease with early stage diagnosis. Trends have been shown across many common cancers including prostate, breast, melanoma and lung cancers showing that for all of these cancer sites survival rates are highest at earlier stages of diagnosis which decrease rapidly by stage 4 diagnosis for both 1 and 5 year survival rates. For example 5 year breast cancer survival rates in women decrease from 98.8% at stage 1 to 90.1%, 72.2% and 27.9% at stages 2, 3, and 4 respectively therefore early stage diagnosis is imperative to decreasing the number of cancer deaths. In general, cancers with higher survival rates tend to have higher early diagnosis. For men in England, melanoma has 57.6% stage 1 diagnosis while prostate cancer has 30.4% stage 1 diagnosis. Melanoma has the highest survival rates for both 1 and 5 year survival, 97.4% and 89.2% respectively, while prostate cancer has 1 and 5 year survival rates of 96.5% and 87.1% [176]. For this reason, increased screening is an important factor in reducing overall death rates from cancer. For example yearly fecal occult-blood testing with rehydration of samples decreased the 13 year cumulative mortality from colorectal cancer by 33% [177].

8.1.6 Diagnostic Methods

Current diagnosis methods for cancer include lab tests for specific tumour markers, these alone do not confirm cancer as they are produced by normal cells and cancer cells alike but are generally produced in higher levels by cancer cells. However this is not always correct as higher levels can be produced by normal cells for other reasons e.g. pregnancy. Conversely, cancerous cells can produce low levels in some patients. Some cancers only present raised levels of tumour markers in small percentages of patients. Imaging tests are also used to see inside the body to see if a physical tumour is present. Such imaging tests could include a CT scan, MRI, nuclear scan, bone scan, PET scan, ultrasound or X-rays. These can identify masses within the body however, generally they cannot confirm if the tumour is malignant or benign. To diagnose a patient with cancer a biopsy is usually required. A biopsy is an invasive procedure and involves removing either a section or all of the abnormal cells this can sometimes remove the surrounding normal cells. Biopsies could be the removal of cells via a needle; for bone marrow, aspirations, spinal taps and some breast, prostate and liver biopsies, it could include an endoscopy of either the mouth, nose or anus which can be used to remove abnormal tissue to examine the colon, rectum, trachea, bronchi and lungs, alternatively surgery is required [178].

8.1.7 Tumour Markers and their Use

Tumour markers are more commonly used to estimate prognosis, detect remaining or reoccurring cancerous tissue after treatment, to assess the response of treatment and monitor whether the cancer has become resistant to treatment. Tumour markers are not commonly used in medical screening for cancer as the sensitivity and specificity of these tests are insufficient and generally would result in either few people being diagnosed this way that its not worth the additional testing or causing overdiagnosis and overtreatment resulting in undue stress and wastage of resources [179]. The prostate-specific antigen (PSA) which is used for prostate cancer has shown to have negligible effect on the mortality rate of prostate cancer. Although the number of diagnoses increased, it only prevented 1 death per 1000 men screened over 10 years [180]. Hence, this screening is not worth the resources and undue stress caused by the additional cancer diagnosis while the mortality rate is barely affected.

Many cancer symptoms e.g. lethargy, weight loss, jaundice etc. do not point to a specific locality nor do they give confidence to identify if the cause is a malignant tumour, therefore tumour markers are necessary in these cases [181].

One of the largest issues with using tumour markers for the diagnosis of malignancies is the sensitivity and specificity of these tests. The performance of the test is statistically measured by the result of a binary classification a ‘high’ amount of the specified tumour marker pertaining to a person who actually has the condition being tested for, in this case a malignant tumour and also the inverse (a ‘normal’ amount of the tumour marker would be for a healthy individual). There are many reasons for a false result even if the test can measure marker concentration perfectly. Tumour markers have a range of values considered ‘normal’ these commonly have a Gaussian distribution. The distribution of results from people with a malignancy also takes the form of a Gaussian distribution. The two Gaussians commonly have a large area of overlap. So although the mean of the 'normal' group is lower than the 'abnormal' group, identifying the group of an individuals test becomes difficult as the majority of results lie in the overlapping section demonstrated in figure 8.2.

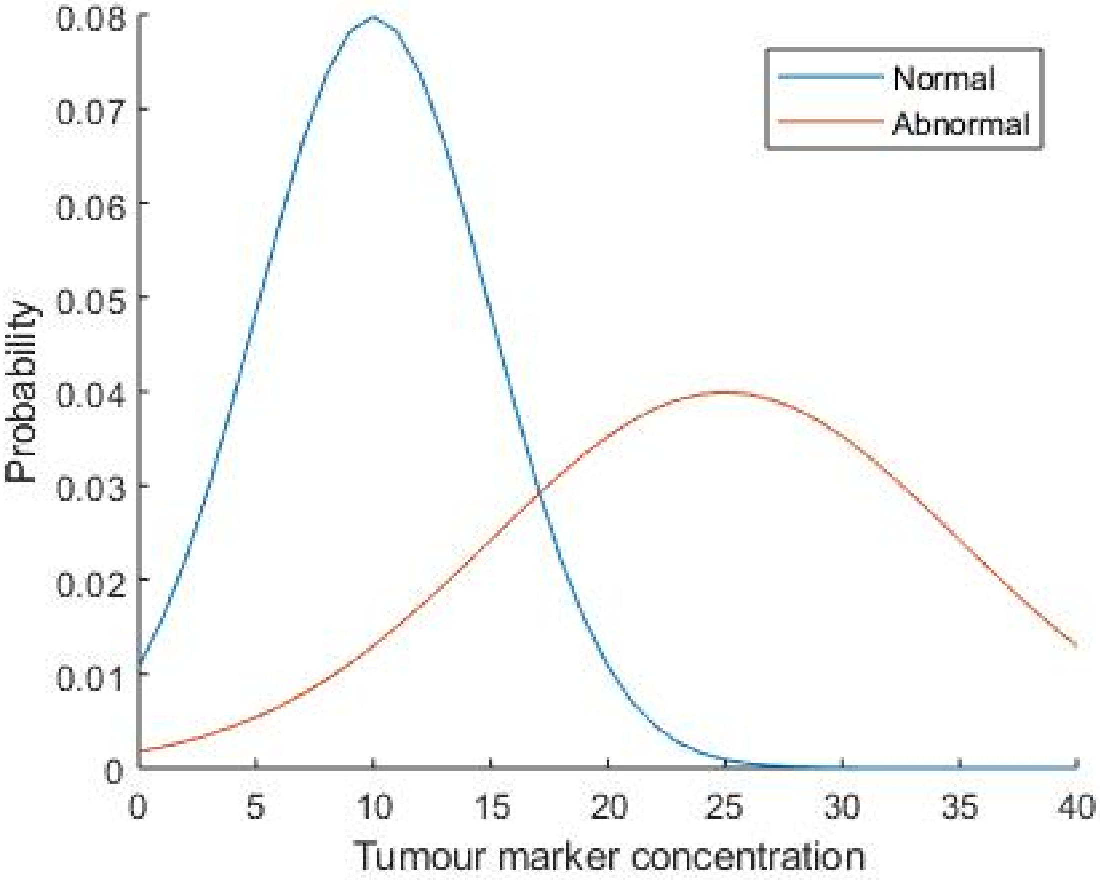

Figure 8.2: Figure demonstrating distributions of people considered 'healthy' or having a malignant tumour arbitrary numbers are used with no units as this is an example.

8.1.8 Sensitivity and Specificity of Tumour Markers

Sensitivity is defined as the number of true positives as a proportion of the samples resulting in a positive test result, a high sensitivity means that more people with high levels of the specific marker test positive for the presence of that specific marker. This is desirable as then more at risk patients or patients with early stage malignancies can be caught and receive the required treatment as fast as possible thus increasing their chances of survival. Specificity is a measure of the true negatives as a proportion of the negative test results hence, the percentage of healthy people who are correctly identified as not having the condition. This is desired to also be high as this reduces the number of healthy people being diagnosed with a malignancy causing undue stress and the wastage of medical resources on a healthy individual. A 100% sensitivity, 100% specificity test would always give the correct result in that it would be positive for patients with malignancies and negative for healthy patients. Commonly, diagnostics are carried out with additional testing following abnormal tumour marker results due to their relatively low sensitivity and specificity, however, tumour markers are commonly used in the monitoring of patients throughout treatment and to identify recurrent malignancies.

Unfortunately, 100% sensitivity and 100% specificity tests are impossible as there are many other reasons that certain markers would be raised. For example human chorionic gonadotropin (hCG) is used to test for pregnancy it is a very commonly raised biomarker in pregnant women and can also be used to test for cancer. Pregnancy has also been shown to increase levels of cancer antigen 15-3 (CA 15-3), squamous cell carcinoma (SCC) and cancer antigen 125 (CA 125) [182]. Similarly to pregnancy there are many other factors which can result in increased levels of tumour markers without the presence of malignant tumours e.g. hepatitis B, hepatitis C, alcohol consumption, tobacco smoking, menstral cycle, cirrhosis, pleural disease, inflammatory bowel disease, pancreatitis, gastric ulceration, alcoholic cirrhosis, lung infection, menapause and many more.

Conversely, not all patients with a specific malignancy exhibit raised levels of the particular marker expected for example CA 125 is only raised in approximately 50% of stage 1 epithelial ovarian cancers and 75-90% of patients with advanced disease [181] similarly, hCG is only raised in 45-60% of patients with billiary and pancreatic cancer and in 10-30% of most other cancers [183]. Hence, low sensitivity and specificity of these tests even if the actual test itself is able to determine the level of tumour marker with 100% accuracy the sensitivity and specificity are based on whether the test is able to cast the correct diagnosis. For this reason, it will always be impossible to achieve a 100% specificity and 100% sensitivity test with only the information of a single tumour marker's presence.

The sensitivity and specificity of tumour marker tests varies with cancer site. Additionally, for any given cancer a number of tumour markers can be present in serum samples. The sensitivities of various cancers to the tumour markers alpha fetoprotein (AFP), CA 125, cancer antigen 19-9 (CA 19-9) and carcinoembryonic antigen (CEA) are shown in table 8.6. Further to that, the sensitivity and specificity for a specific marker with respect to a specific cancer can also vary based on the stage the cancer is at for example CEA with stage I, II, III and IV colorectal cancer has sensitivities of 4%, 25%, 44% and 65% respectively therefore, early diagnosis becomes exceedingly difficult which is vital to reducing mortalities [184].

8.1.9 Multiple Marker Testing and the Work in this Thesis

It has been shown that studies combining multiple tumour markers with their respective statistical likelihood can reduce the uncertainty in diagnosing malignancies by tumour markers alone. The sensitivity of tests have been shown to increase by the use of multiple marker testing. Reference [185] shows sensitivities as high as 82%, 92% and 83% for digestive, urinary and skeletal tumours thus this method could be instrumental in the early detection of tumours while the loss in specificity can be tolerated. A recent study on combining tumour markers [33] shows not only increased sensitivities for ovarian, liver, stomach, pancreatic and esophageal cancers (69-98%) but also has a greater than 99% specificity and can locate the cancer to a small number of anatomic sites in 83% of patients. This is a promising result for the field if early detection can be carried out via tumour markers. Taking blood samples has no physical drawbacks on a healthy individual so the only consideration would be cost.

The main benefit of exploring tumour marker testing using metamaterials at terahertz frequencies is the future potential to test for multiple markers simultaneously. If this feasibility study shows promising results further work can be done to assess the possibility of testing for multiple markers simultaneously. Following this, statistical methods can be applied to increase the sensitivity and specificity of these tests. Hopefully providing more accurate testing than is currently available and possibly even higher throughput, lower unit costs and faster turnaround times.

Besides performance, another requirement of biological testing is to keep instruments

Cancer	**AFP**	**CA 125**	**CA 19-9**	**CEA**
Lung squamous cell carcinoma	8.3	41.7	8.3	58.3
Lung adenocarcinoma	3.7	51.9	3.7	40.7
Small cell lung carcinoma	0.0	41.7	8.3	58.3
Colon cancer	3.9	46.2	42.3	57.7
Rectal cancer	0.0	8.3	29.2	37.5
Liver cancer	48.4	41.9	41.9	19.4
Cholangiocarcinoma	5.3	31.6	68.4	47.4
Gallbladder carcinoma	4.8	47.6	71.4	47.6
Pancreatic cancer	3.9	42.3	57.7	61.5
Esophageal cancer	0.0	10.0	23.3	23.3
Gastric cancer	7.4	33.3	40.7	40.7
Breast cancer	2.9	14.7	14.7	26.5
Renal cancer	0.0	33.3	33.3	16.7
Bladder cancer	16.7	16.7	16.7	0.0
Bone cancer	3.6	30.0	13.3	30.0
Cervical cancer	0.0	9.1	0.0	3.0
Carcinoma of endometrium	5.3	26.3	31.6	15.8
Ovarian cancer	5.1	45.8	10.2	5.1
Carcinoma of fallopian tube	0.0	16.7	0.0	0.0

Table 8.6: Tumour markers AFP, CA 125, CA 19-9 and CEA showing their sensitivity (%) to various cancers [185].

sterile, hence it is highly desirable to make sample holders disposable; consequently, paper is ideal as it is combustible and biodegradable. These properties are driving interest in paper based sensors across the terahertz community [110].

In this chapter, a metamaterial fabricated on a low-cost substrate, as in chapters 7, is explored for the use of detecting tumour markers within serum samples. Reference [186] reported metamaterial biosensors for biomarkers using microfluidic techniques. A key part of this thesis is to extend the work as in [186] for the same biomarkers and additional markers, however, instead of using microfluidics here, paper is used to contain the fluid under test.

County Durham and Darlington NHS Trust currently tests for: AFP, CA 15-3, CA 19-9, CA 125, CEA, 5-hydroxyindoleacetic acid (5-HIAA), hCG, lactate dehydrogenase (LDH) and PSA. Their uses, turnaround time and number of samples tested per month are listed in table 8.7. These are the most commonly used markers which cover common cancer types so are sufficient to test for the majority of cancer cases. They do not cover all cancer types nor an exhaustive list of known tumour markers for each cancer type they provide a compromise between cost, simplicity and probabilistic advantage. Their sensitivities and specificities are generally not sufficient to be used for diagnosis. Common practice is to use them to refer patients for further tests or for monitoring the progress of therapy.

8.2 Methodology

The study outlined in this chapter aims to assess the feasibility of using a metamaterial terahertz sensor for the purpose of identifying tumour marker concentration in serum samples.

8.2.1 The Samples

A relationship between Durham University and Durham and Darlington NHS Trust has been built up for this research project and ethical approval from the research ethics committee (REC) of the NHS has been given for this project under the REC reference 19/HRA/4172.

Tumour marker	**Current use**	**Turnaround time**	**Average samples per month**
CEA	Follow-up after tumour resection	1 day	109
LDH	elevated in a wide variety of conditions including testicular tumours but bad prognostic marker in lymphoma	1 hour	100
CA 125	suspected or diagnosed ovarian cancer	1 day	76
CA 19-9	Gastric and hepatobiliary cancer, monitoring of pancreatic cancer	1 day	56
CA 15-3	for undiagnosed breast cancer	1 day	62
total-hCG	diagnostic of pregnancy, also raised in testicular tumours	1 hour	236
AFP	monitoring primary hepatic and testicular tumours and to lesser extent cirrhosis	1 day	21

Table 8.7: Tumour markers, their uses, turnaround times and average number of samples per month for County Durham and Darlington NHS Trust.

The samples used in this study are surplus serum remaining after testing at the hospital. Samples are able to be used for this study as the consent forms for the tests to be undertaken at the hospital allow surplus material to be used for research purposes. The conditions of this use are that the use of the serum is part of a PhD qualification, the samples are anonymous containing no cellular material and are only to be tested for the marker which was tested for at the hospital. All participants are between the ages of 18 and 100. Participants with known incurable blood-borne pathogens i.e. HIV, hepatitis B etc. were requested to be omitted to reduce the risk to the student.

AFP, total-hCG, CA 125, CA 15-3, CA 19-9, CEA and LDH are tested. A future scientific advantage of the terahertz metamaterial technique is that it could potentially be used to test for multiple markers simultaneously. Hence 5-HIAA and PSA have been excluded from this study, as they are only known to increase for a single type of common cancer, carcinoid and prostate respectively.

8.2.2 The Method

A small number of samples were tested to assess if the method could distinguish between different levels of markers. 15 samples per proposed marker (CEA, LDH, CA 125, CA 19-9, CA 15-3, total-hCG and AFP). 3 negative samples per marker were used as a control.

The samples were collected at the hospital and stored at -80°. These were transported via a freezer box to the freezer at Durham (-30°) where they were kept until testing.

The device consisted of a section of PEN substrate with the CC3 metamaterial design in aluminium. The metamaterial was held in contact with filter paper using a physical restraint on one corner. Each sample was large enough to cover a $\frac{1}{2}$ inch beam width. An acetate plate with a hole for the beam was used to hold the sample as shown in figure 8.3. The horizontal plate utilised gravity to ensure adhesion between the paper and metamaterial surface during testing.

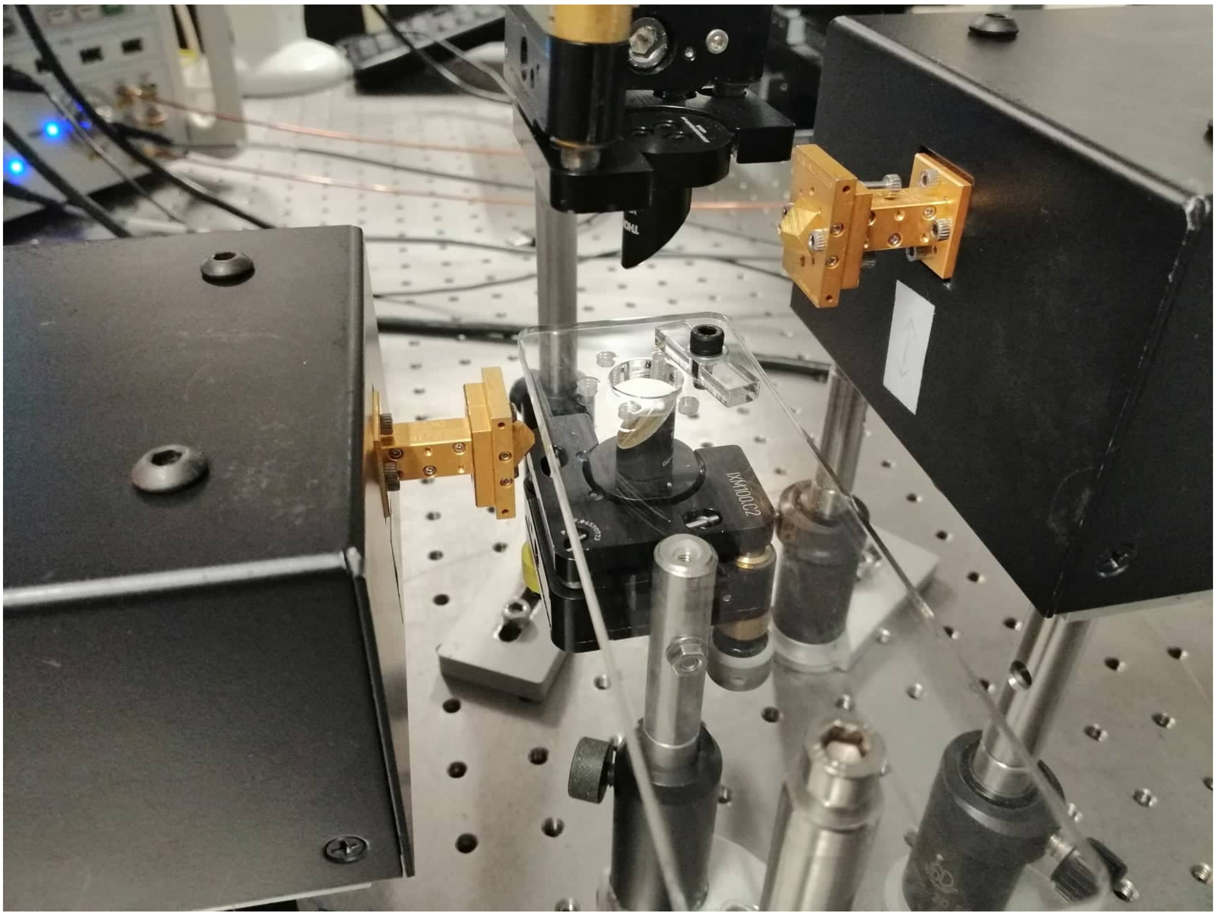

Figure 8.3: Photo of experimental setup for serum tests. The beam is set vertically through a hole in the acetate holder. The holder has a gap for the sample to lay over and an additional acetate block which is screwed in place to hold down the sample.

Once ready to test, the sample was removed from the freezer to thaw then placed into a plastic bag to isolate the serum from the handler. 5 empty scans and 5 scans of the dry metamaterial and filter paper were taken for each sample. A syringe was used to deposit 0.03 ml of serum onto the filter paper. A series of 40 scans were taken. Each scan takes 90 s resulting in a full wet measurement time of 60 min (excluding the initial empty and dry scans). 1201 points were taken per scan at a range of 0.75-1.1 THz with an IFBW of 50 Hz.

8.3 Tumour Markers

In this section, human serum samples are tested using the VNA and CC3 metamaterial. As the marker tests fundamentally function by measuring refractive index there are countless other factors which could affect the results of the tests in addition to the marker concentration. The refractive indices of most of the components of blood have yet to be characterised in isolation within the terahertz region. Hence, it would be unreasonable to implement compensation for any of these factors as there are still many other unknowns. It would be unreasonable to test each sample, prior to testing using the VNA, for an exhaustive list of other components such as glucose, hormone, hydration and platelet levels. In addition to this, the effect on the VNA's response with respect to many other components within the blood is unknown. To make the measurements here fair and unbiased, these tests are conducted blind to all possible blood components except tumour marker concentration.

Some brief background information is presented for each of the measured tumour markers and then the data is presented. Three figures are presented for each of the tumour markers explored. Each of these figures has been handled identically for each of the markers. The data traces in each of these figures is grouped into bands of concentration as a visual aid to help identify any trends but each individual sample is shown.

The received data exhibited a significant amount of noise which makes the identification of trends in unprocessed data challenging. An full set of data is presented for the first marker to demonstrate the process used and following this only the processed data is presented for the other markers.

8.3.1 CEA

Carcinoembryonic antigen (CEA) is a set of glycoproteins, it is usually produced in gastrointestinal tissue during fetal development. It is commonly present in healthy adults up to 20 ng/mL. CEA levels can be increased due to smoking, even in the absence of cancer. Increased CEA levels can be found in colorectal, medullary thyroid, breast, gastrointestinal, liver, lung, ovarian, pancreatic and prostate cancers it is usually used to measure response to treatment as opposed to diagnosis or screening. The reference values of CEA in people in various clinical conditions are shown in table 8.8. Results of 0-5 $\mathrm{ng\,l^{-1}}$ are considered negative.

	CEA distribution (ng/mL)				
Clinical condition	0-2.5	2.6-5.0	5.1-10.0	10.1-20.0	>20.0
Healthy Nonsmokers	98.2	1.8	0	0	0
Healthy Smokers	87.3	8.0	4.7	0	0
Colorectal cancer	37.6	10.8	7.2	6.4	38.0
Lung cancer	46.2	15.8	10.8	7.0	20.2
Breast cancer	68.3	14.9	7.7	2.3	6.8
Gastric cancer	60.0	17.1	8.6	5.7	8.6
Ovarian cancer	82.8	11.4	2.9	2.9	0
Pancreatic cancer	44.2	20.9	16.3	7.0	11.6
Liver cancer	50.0	16.7	0	33.3	0
Lymphoproliferatice	80.0	20.0	0	0	0
Other cancers	75.0	10.0	10.0	5.0	0

Table 8.8: Expected distrobution of CEA as per the Siemens AVIDA Centaur, AVIDA Centaur XP and AVIDA Centaur XPT datasheet [187].

Figure 8.4 shows the raw dataset for CEA. As can be seen in this figure little to no conclusions about this data can be drawn by visual inspection, hence additional processing has been applied to remove the excessive noise.

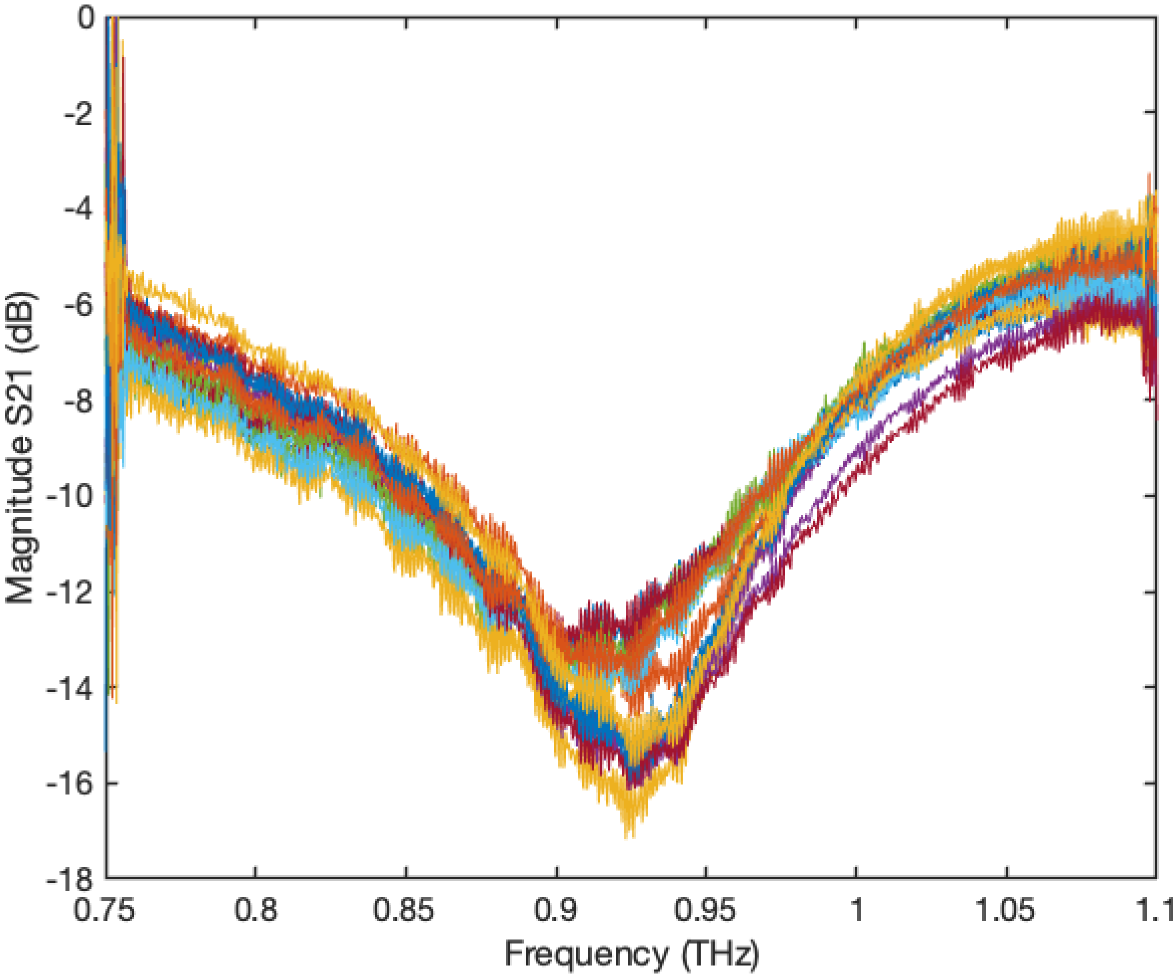

Figure 8.4: Graph displaying all results for CEA an average of five scans have been taken and normalised using an average of five empty scans. No smoothing has been applied.

Figure 8.5 has systematically removed noise by taking the wet results and normalising with the empty scans following this, points which differ by over 0.01 (absolute measured value) from the previous point are removed. This eliminates any large noise values from the data. Finally, smoothing has been applied across 120 measured frequency points. This results in a very smooth dataset with only the main feature clearly visible. However, again, it is difficult to draw conclusions from this figure.

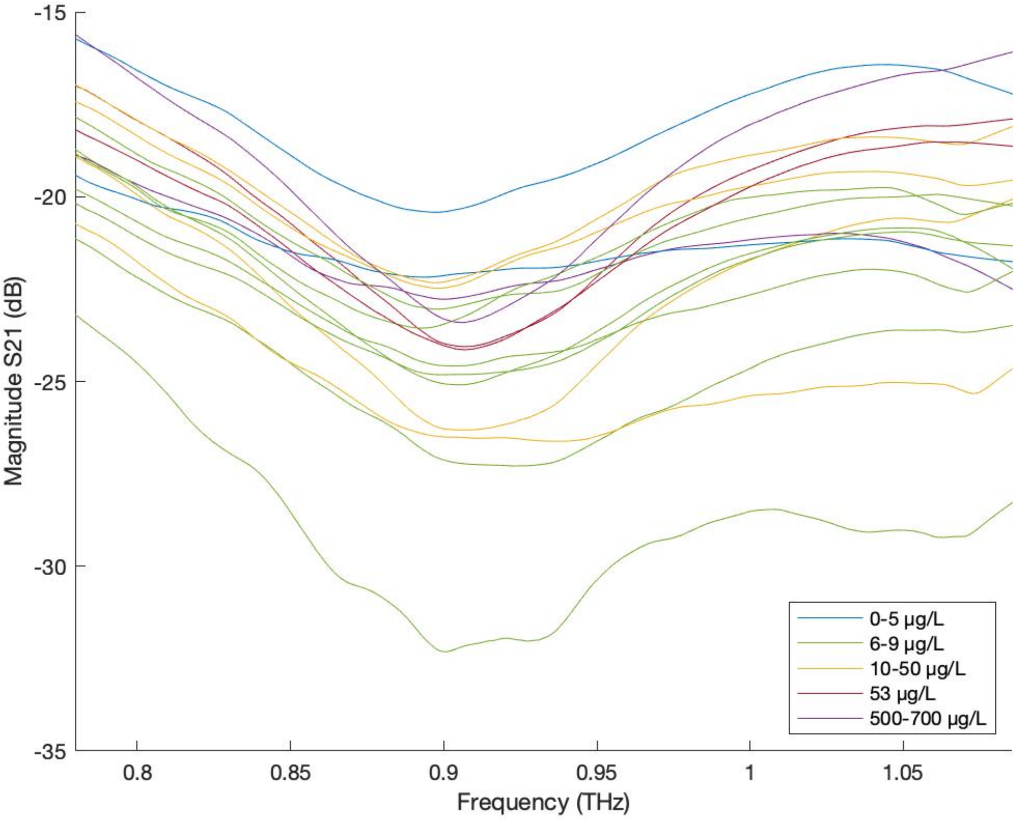

Figure 8.5: Graph displaying all results for CEA as in figure 8.4 removing points which differ by over 0.01 absolute value from the previous point and smoothing over 120 points has been applied. Results are grouped to similar levels of CEA.

As an alternative the wet results are presented normalised by the dry results in figure 8.6 (not the empty scans). This accounts for any variation in peak position due to fabrication inconsistencies and presents only the difference. Clipping for a difference between values of greater than 0.05 (absolute measured value) as in the previous figure is applied and a reduced smoothing of 15 points is applied.

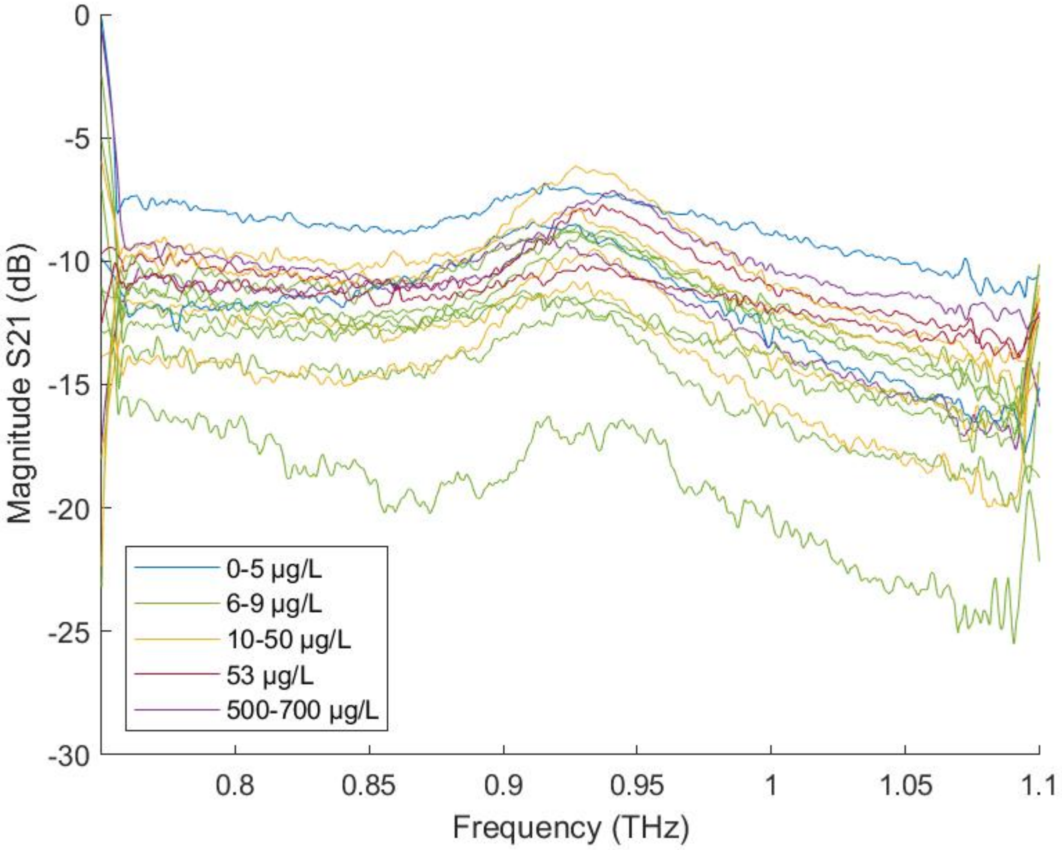

Figure 8.6: Graph displaying the results for CEA normalised with a dry metamaterial scan as opposed to an empty scan. Points differing from the previous point by over 0.05 absolute value have been removed and smoothing over 15 points has been applied.

Again, little to no information could be drawn from this figure, although improved from the previous figure by enabling more information to be viewed with significantly reduced smoothing, it does not provide an easy method of detecting trends between the plots.

Finally, it was decided to take a more computational approach using a polynomial peak fitting tool. Similarly to the work presented in section 4.3 a fitting tool is used to model the trace and this model is used to isolate the peak position. This graph is generated by removing points which differ by over 0.01 (absolute measured value) as before, then a 100th order polynomial fit is made. The frequency of the minimum point is then plotted against marker concentration. Upon close inspection of figure 8.7 it can be seen that for the negative (blue), low (green) and medium (yellow) concentration samples although each individual sample may or may not remain inline with the previous, the bulk group position is seen to increase as the marker concentration increases. This style of figure will be used to present the remaining tumour marker information.

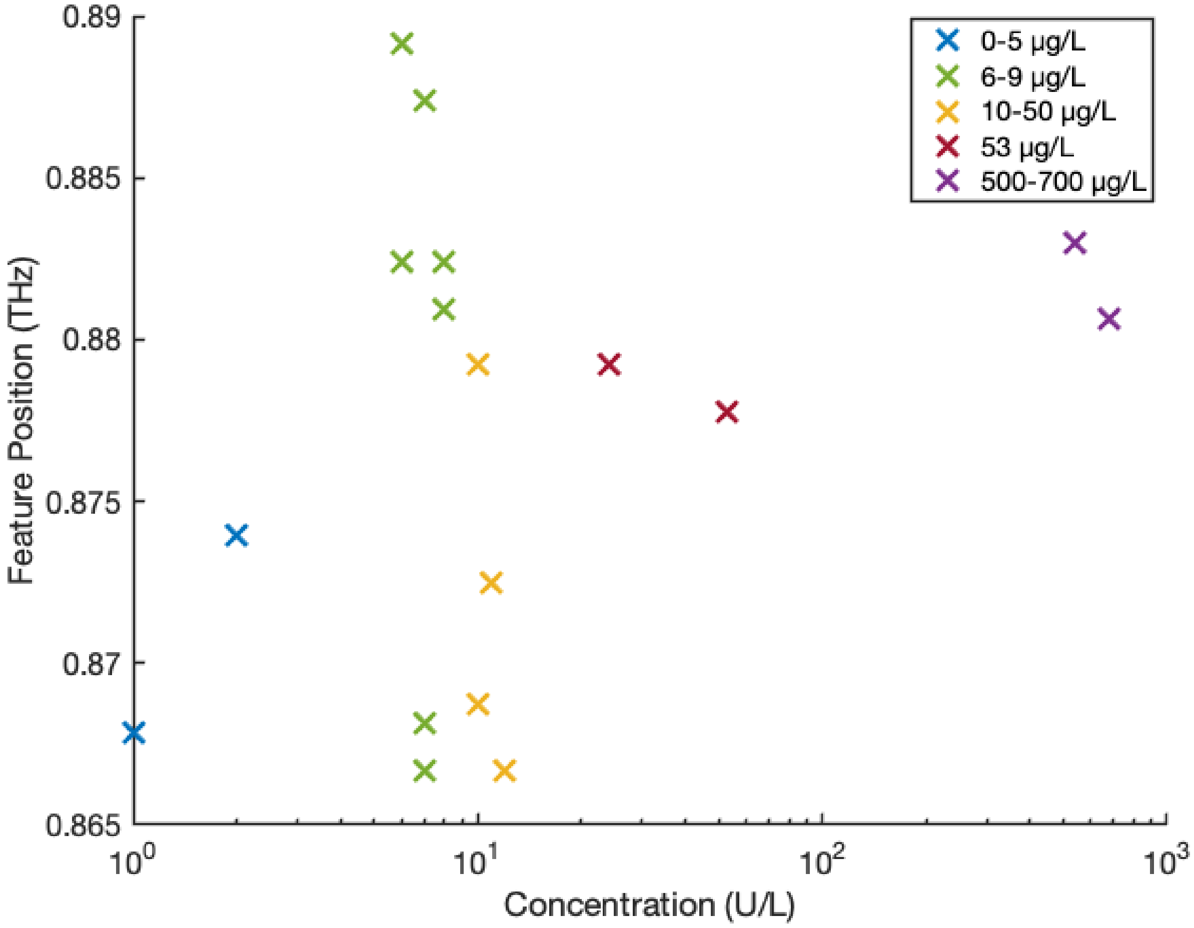

Figure 8.7: Graph displaying the calculated polynomial fit absorption peak positions for CEA.

8.3.2 LDH

Lactate dehydrogenase (LDH) is an enzyme that the body uses in the process of turning sugar into energy. It is commonly found in most body tissues but has a very low concentration in the blood unless there are damaged or destroyed tissues. LDH is generally used to identify the location and severity of tissue damage which includes kidney disease, liver disease and cancer. LDH is not usually used in the diagnosis of cancer but is commonly used to monitor the response to treatment in testicular cancer, ovarian cancer, lymphoma, leukaemia, melanoma and neuroblastoma.

For LDH the 'normal' level is 240-480 U/l, however, results of lower than 240 U/l are classed as negative for these tests conducted at the hospital so for the purpose of these experiments results less than 480 U/l are considered negative. Similarly to CEA, the polynomial fit peak position results (figure 8.8) show a group trend across the negative (blue), low (green) and medium (yellow) concentration groups. This trend does not follow for the high (red) and very high (purple) concentration groups.

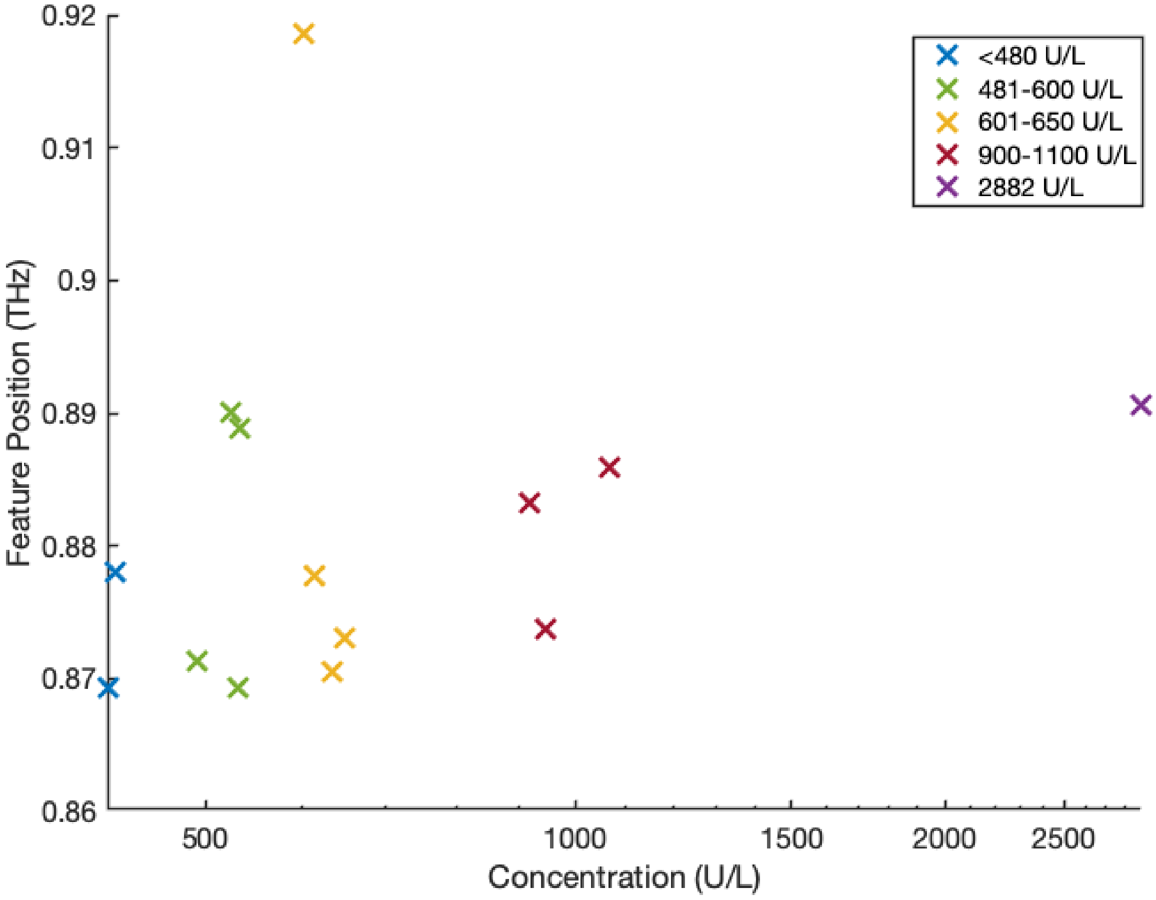

Figure 8.8: Graph displaying the calculated polynomial fit absorption peak positions for LDH.

8.3.3 CA 125

Cancer antigen 125 (CA 125) is a glycoprotein of over 200 KD. Elevated levels of CA 125 are found in pregnant women. Again, CA 125 is not used in the diagnosis of cancer or cancer screening as it can also be elevated in menstruation and non-cancerous conditions such as uterine fibroids. Ovarian, endometrial, peritoneal and fallopian tube cancers can cause elevated CA 125 serum levels. CA 125 tests are used in the monitoring of treatment for these cancers, testing for recurrence and in the screening of high risk patients such as those with the BCRA1 or BCRA2 gene mutation. Results of 0-30 kU/l are considered negative.

	CA 125 distribution (U/mL)	
Clinical condition	<35	>35
Premenopausal women	98	2
Postmenopausal women	100	0
Pregnancy	86.7	13.3
Ovarian cancer	20.7	79.3
Breast cancer	68	32
Lymphoma	100	0
Colorectal cancer	50	50
Lung cancer	90	10
Prostate cancer	100	0

Table 8.9: Expected distribution of CA 125 as per the Siemens AVIDA Centaur, AVIDA Centaur XP and AVIDA Centaur XPT datasheet [188].

Figure 8.9 showing the polynomial fitted peak positions shows somewhat of an increase in group frequency between the negative (blue), low (green) and medium (yellow) positions. This is not carried onto the high (red) and very high (purple) groups but the same trend can be seen through these groups independently. Also, with the large range across each of these groups it is possible that the high or very high groups follow this trend but the small number of samples happen to be at the low end of the range. This does not show a convincing trend but instead the possibility that this method could work with further development.

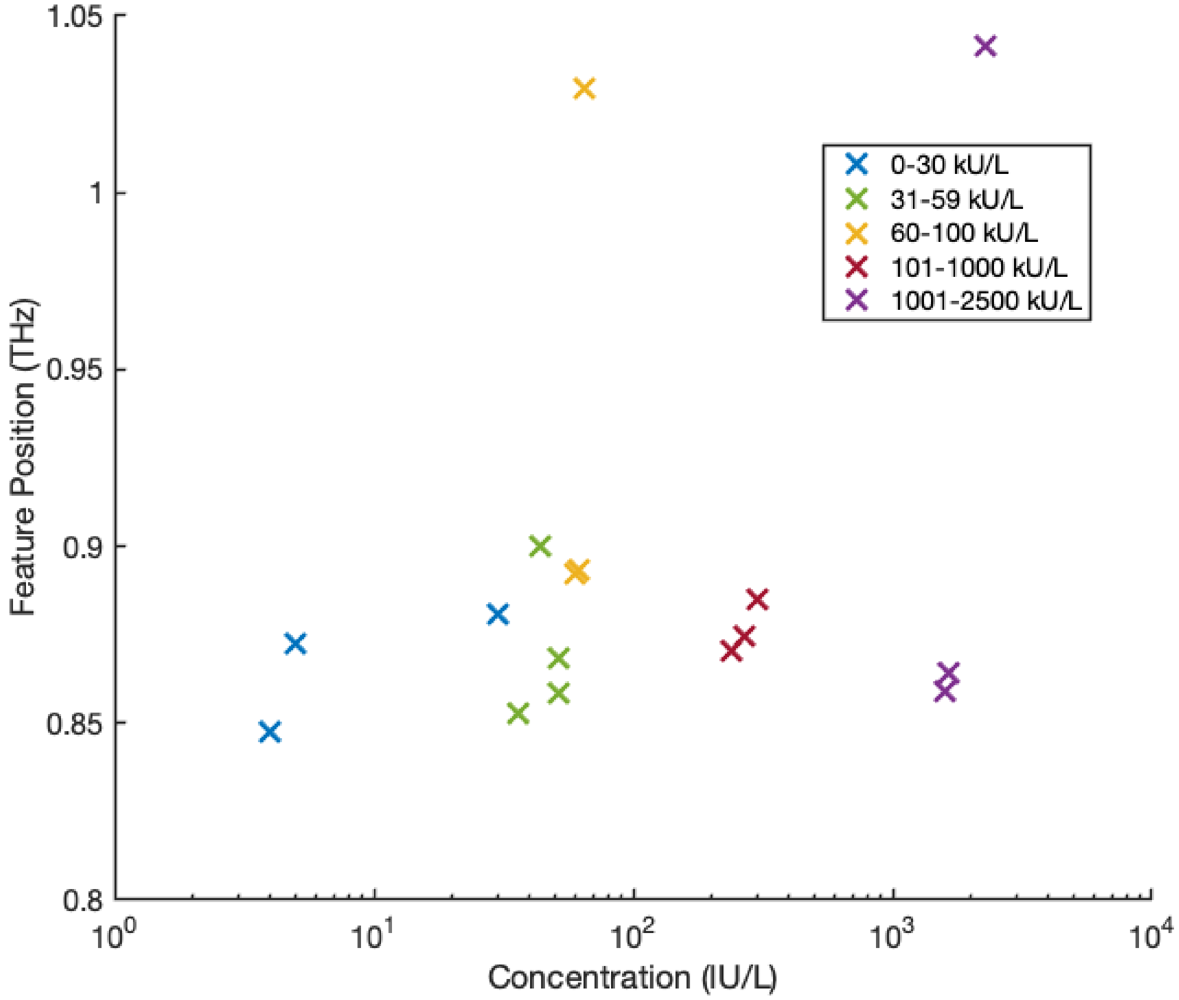

Figure 8.9: Graph displaying the calculated polynomial fit absorption peak positions for 125.

8.3.4 CA 19-9

Cancer antigen 19-9 (CA 19-9) is a glycoprotein with a molecular weight of 210 KD. Normal levels of CA 19-9 are below 37 U/ml. CA 19-9 is elevated in most pateints with advanced pancreratic cancer but it is also elevated in colorectal, lung and gallbladder cancer as well as benign diseases such as gall stones, pancreatitis, cyctic fibrosis and liver disease. Results of <37 kU/l are considered negative.

The CA 19-9 polynomial fit calculated absorption peak graph (figure 8.10) shows a good correlation of decreasing frequency with increasing marker concentration if the low (green) samples are excluded. Realistically, it is not reasonable to ignore these samples

	CA 19-9 distribution (U/mL)	
Clinical condition	<37	>37
Healthy people	96.3	3.7
Pancreatic cancer	25	75
Colorectal cancer	34	66
Biliary cancer	40	60
Breast cancer	66.7	33.3
Esophageal cancer	87	13
Gastric cancer	66.7	33.3
Liver cancer	45	55
Lung cancer	73	27
Ovarian cancer	100	0

Table 8.10: Expected distrobution of CA 19-9 as per the Siemens AVIDA Centaur, AVIDA Centaur XP and AVIDA Centaur XPT datasheet [189].

however it may be worth investigation to see if there is any reason for this deviation from the trend or to consider if the trend between the other concentration groups is real or just coincidental.

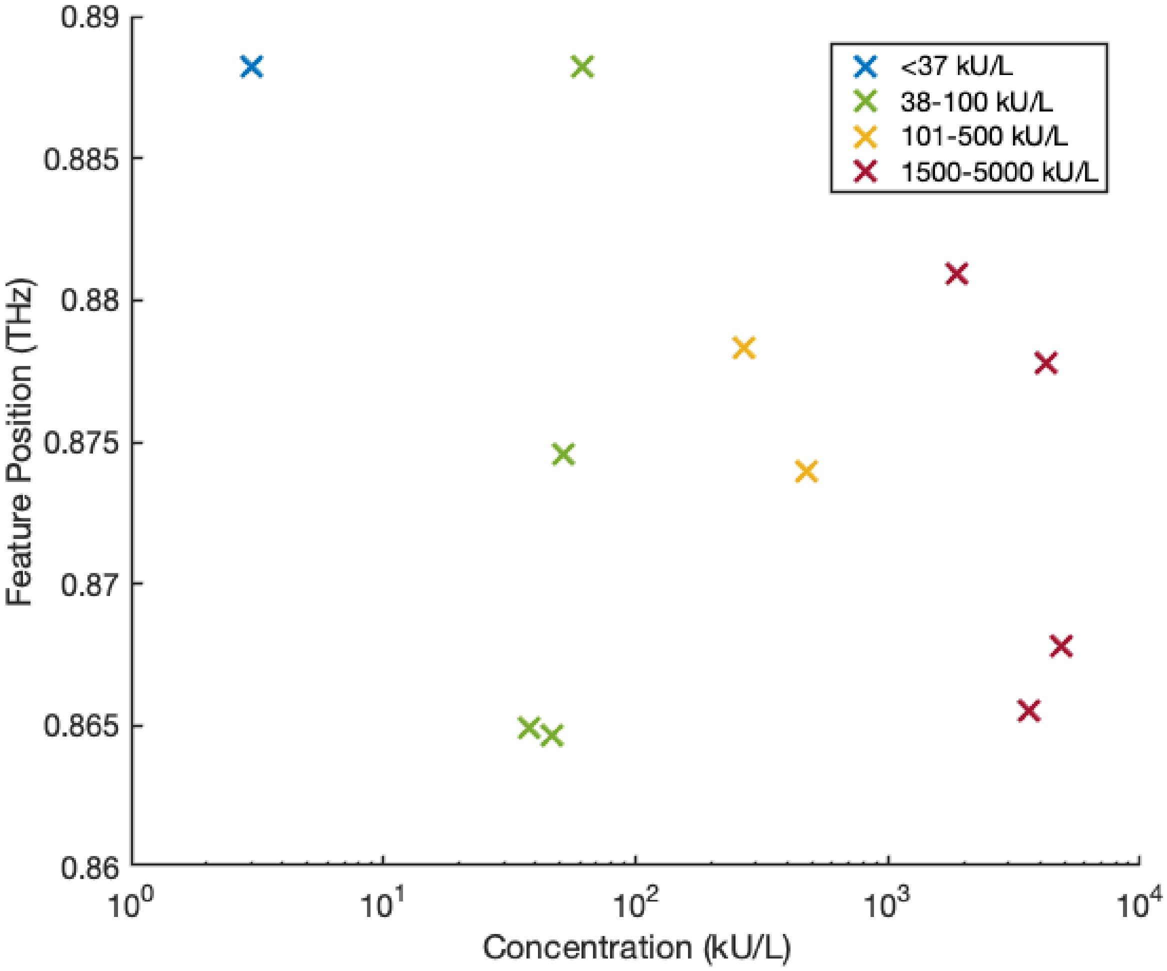

Figure 8.10: Graph displaying the calculated polynomial fit absorption peak positions for CA 19-9.

8.3.5 CA 15-3

Cancer antigen 15-3 (CA 15-3) is a heterogeneous glycoprotein with a molecular weight of 300 KD. The sensitivity for CA 15-3 is low as it is also elevated in pregnanacy and breastfeeding along with a wide range of benign diseases: benign breast diseases, liver cirrhosis, endometriosis, lupus, pelvic inflammatory disease, sarcoidosis, tuberculosis, acute hepatitis and chronic hepatitis. CA 15-3 is most commonly used to monitor the treatment of breast cancer but can also be elevated in colorectal cancer, liver cancer, lung cancer, pancreatic cancer and prostate cancer distributions are shown in table 8.11. Results of 0-32 kU/l are considered negative.

	CA 15-3 distribution (U/mL)			
Clinical condition	0-32.4	>32.4-60	>60-100	>100
Healthy Females $<$ 50 years	99.5	0.5	0	0
Healthy Females $>$ 50 years	98	1.5	0.5	0
Stage I Breast cancer	90.0	10.0	0	0
Stage II Breast cancer	95.5	0	0	4.5
Stage III Breast cancer	77.8	11.1	11.1	0
Stage IV Breast cancer	25.0	30.0	10.0	35.0
Cervix/Uterus cancer	37.5	37.5	0	25
Colorectal cancer	100.0	0	0	0
Liver cancer	100.0	0	0	0
Lung cancer	80.0	0	0	20.0
Ovarian cancer	66.7	16.7	16.7	0
Pancreatic cancer	62.5	12.5	12.5	12.5

Table 8.11: Expected distrobution of CA 15-3 as per the Siemens AVIDA Centaur, AVIDA Centaur XP and AVIDA Centaur XPT datasheet [190].

Figure 8.11 shows that the mathematically modelled and calculated absorption peak positions follow somewhat of a decrease in absorption peak position frequency across all groups. The individual measurements do not show a strong trend as there is a large amount of variation presumably due to the large amount of noise within the system, however, across multiple measurements an overall trend can be seen.

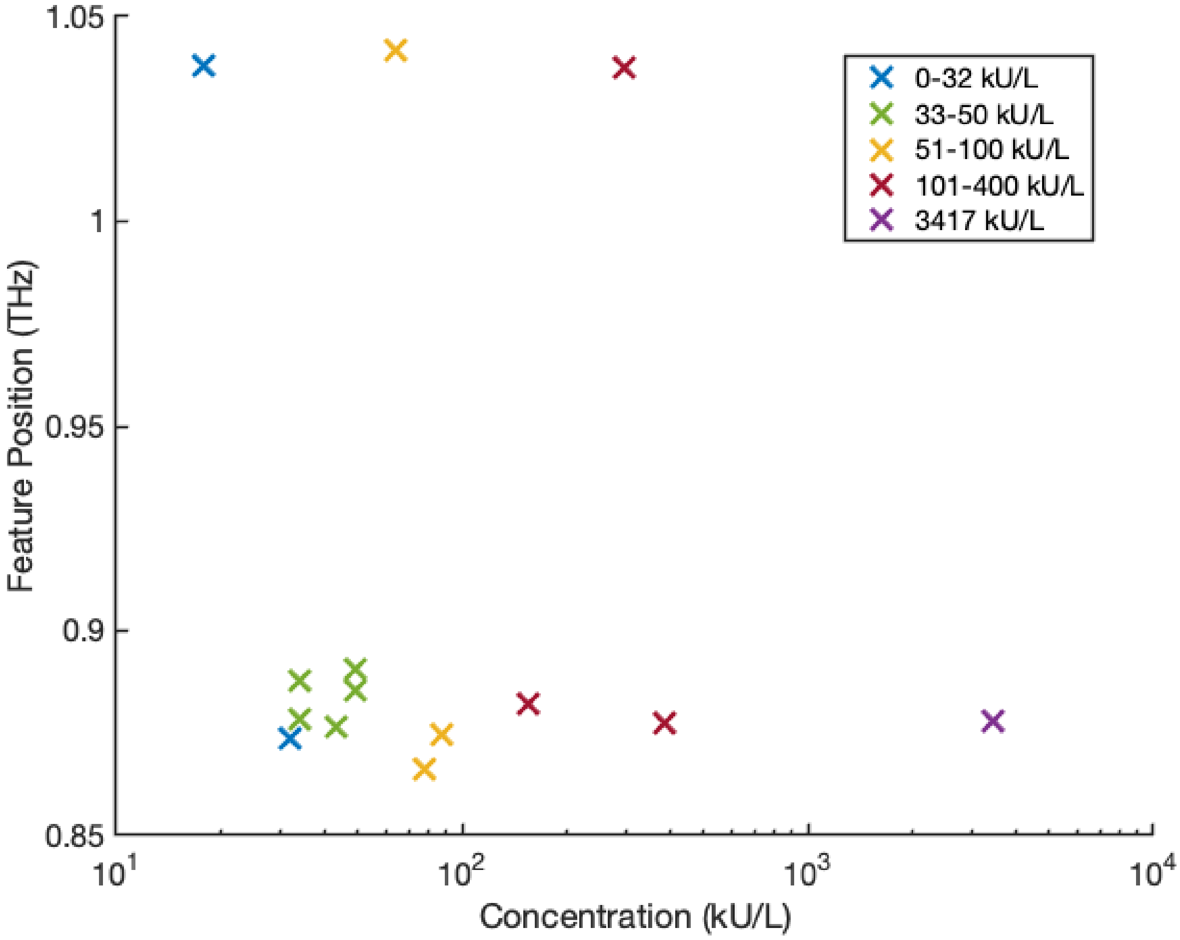

Figure 8.11: Graph displaying the calculated polynomial fit absorption peak positions for CA 15-3.

8.3.6 Total-hCG

Human chorionic gonadotropin (hCG) is a glycoprotein of molecular weight 37.5 KD it is most commonly produced in high concentrations by placental trophoblasts. During pregnancy, serum concentrations increase rapidly peaking at 8-10 weeks [192]. The proteins are heterodimers consisting of an α and a β subunit. The α subunit is common to the glycoprotein hormone family including the luteinizing hormone, follicle-stimulating hormone and thyroid-stimulating hormone it contains 92 amino acids. However, each of their β subunits are distinct and determine the biological activity they also display extensive homology. β hCG consists of 145 amino acids and is around 23.5 KD, hence the α subunit is 14 KD. hCG can be used as both a diagnosis and monitoring tool for germ cell, liver, breast, lung, skin and stomach cancers. It can also be used in the monitoring or diagnosis of benign diseases such as gestational trophoblastic disease (GTD), cirrhosis, duodenal ulcer and inflammatory bowel disease. Elevated hCG levels can also be due to the use of certain drugs such as anticonvulsants, antiparkinsonian agents, hypnotics and tranquilizers. Generally the tests are unrealiable and more commonly used for GTD as opposed to the diagnosis or monitoring of cancer. Results of 0-4 IU/l for males are considered negative and 0-5 IU/l for females are considered not pregnant.

For hCG, the negative (blue), low (green), medium (yellow) and high (red) concentration groups all appear to be around the same position in frequency and vary randomly with respect to concentration as shown in figure 8.12. It suggests there is little to no correlation between marker concentration and peak position for this marker and that, in terms of the feasibility study, testing for this marker using a terahertz VNA is not worth pursuing.

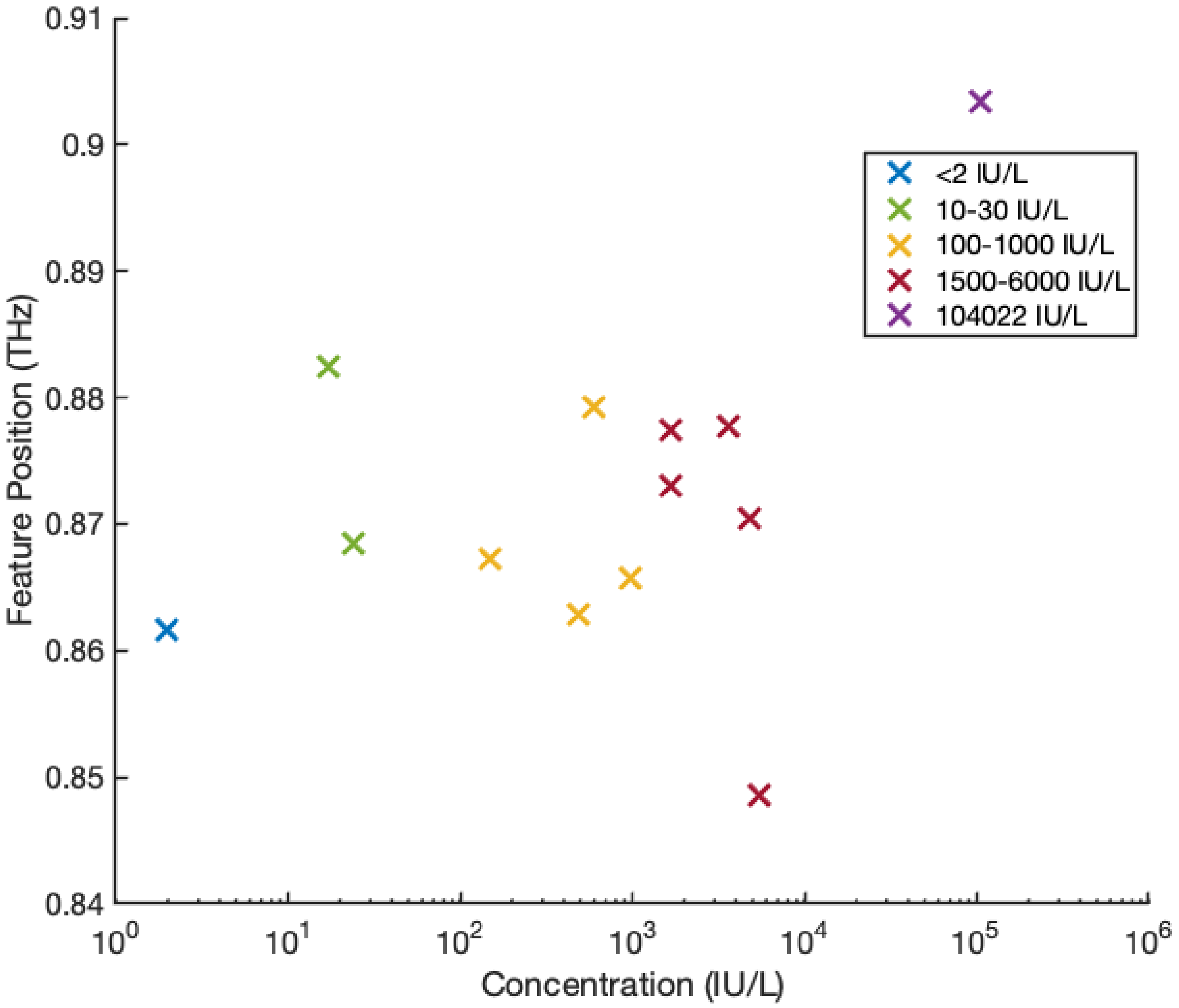

Figure 8.12: Graph displaying the calculated polynomial fit absorption peak positions for hCG.

8.3.7 AFP

Alpha fetoprotein (AFP) is a single chain glycoprotein, it has a molecular weight of 65 KD. Normal levels of AFP are below 15 ng/ml for adults but are commonly above 500 ng/ml in cases of malignancy. It is not only expressed in malignancy but also during intra uterine or early postnatal life. It is made by a fetus's liver and yolk sac and is the main protein during the first three months of development however it should only be found in adults in low levels. AFP is mainly found in liver cancer but is also used in nonseminomatous germ cell tumours, testicular cancer or cancers of the brain, mediastinum or blood. Benign diseases which can introduce elevated levels of AFP into the blood are cirrhosis or chronic hepatitis. AFP can be used for both diagnosis and monitoring purposes. Expected AFP values for various clinical conditions are shown in table 8.12. Results of 0-7 $\mathrm{ng\,ml^{-1}}$ for males are considered negative.

	AFP distribution (ng/mL)				
Clinical condition	0-8.0	8.1-20.0	20.1-500.0	500.1-1000.0	>1000.0
Healthy males	98.0	1.8	0.2	0	0
Healthy females	98.7	1.3	0	0	0
Testicular seminoma	90.3	7.3	2.4	0	0
Testicular non-seminoma	51.5	9.3	27.5	2.4	9.3
Primary liver cancer	36.3	13.7	25.0	5.0	20.0
Secondary liver cancer	84.9	8.6	5.4	0	1.1
Gastrointestinal cancer	84.4	12.5	3.1	0	0
Genitourinary cancer	92.5	7.5	0	0	0
Pancreatic cancer	88.8	5.6	5.6	0	0
Other cancers	83.8	6.1	3.0	2.0	5.1

Table 8.12: Expected distrobution of AFP as per the Siemens AVIDA Centaur, AVIDA Centaur XP and AVIDA Centaur XPT datasheet [191].

Finally, only a few samples for AFP were available due to the low number of tests and even lower number of positive samples received at the hospital. So only six samples are shown, unfortunately the 11 $\mathrm{ng\,ml^{-1}}$ sample did not produce a clear feature. This result was found in the previous chapters (e.g. pages 153-156) and thought to be due to the filter paper being too wet where there may be a thin layer of pure liquid in contact with the metamaterial instead of the soaked filter paper. Figure 8.13 shows an indication there may be a correlation particularly given the small number of samples no conclusions can be drawn here about the effectiveness of this method but it would be worth further investigation based on the results of this small feasibilty study.

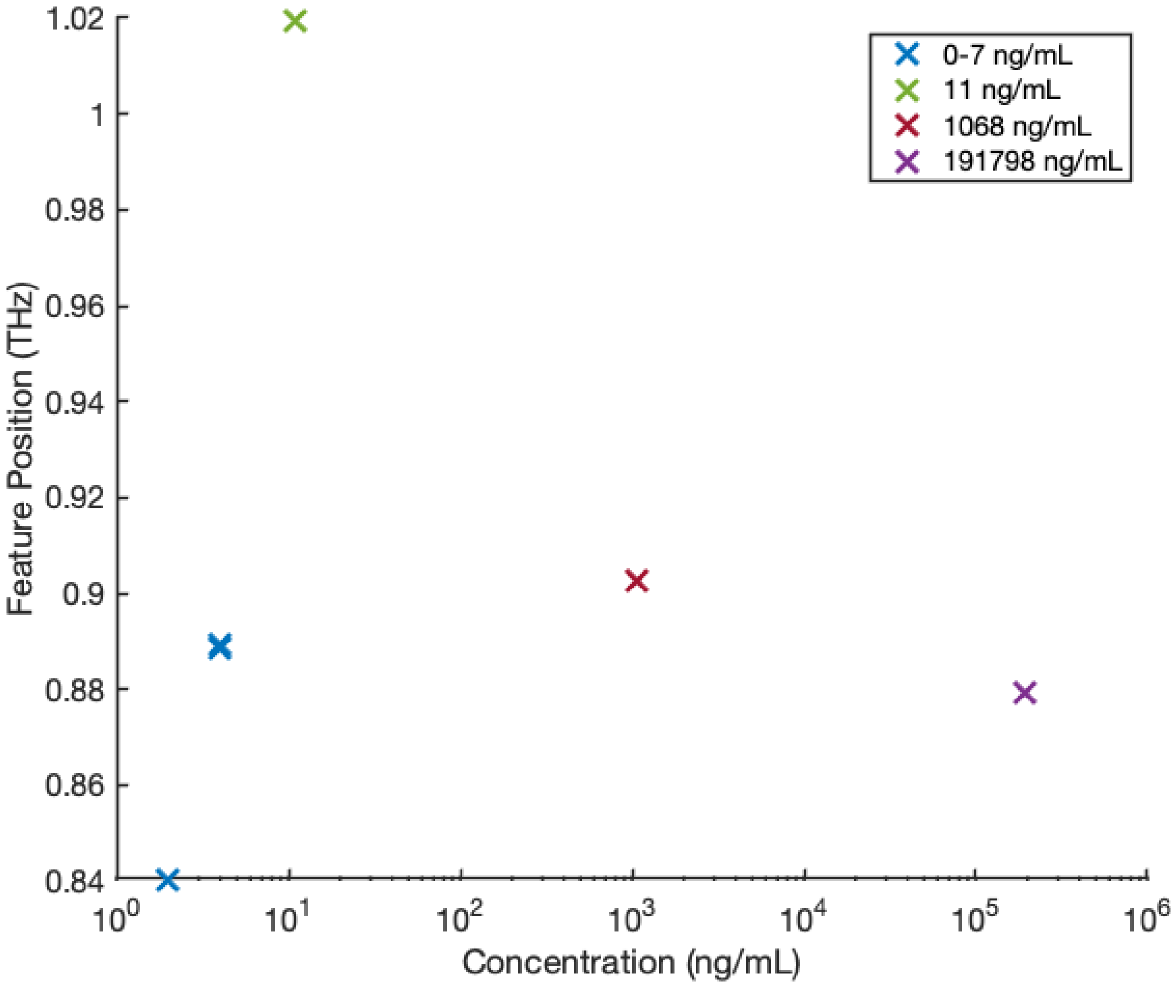

Figure 8.13: Graph displaying the calculated polynomial fit absorption peak positions for AFP.

8.3.8 Envelope Assessment

As an additional method of determining differences between each of the traces the envelopes of the S-parameter data have been taken. The complex S-parameter data is processed using a MATLAB program to calculate these enveloped. The data is fed into an empty array of twice the data length where the S-parameter data takes up the initial points leaving the second half of the array zeros. The inverse fast-fourier-transform (FFT) has been taken. The resulting complex number is used to calculate the envelope using equation 8.3.1 as follows:

$$envelope = \sqrt{re(ifft)^2 + im(ifft)^2} \tag{8.3.1}$$

where the real and imaginary parts of the inverse FFT are squared, summed and the square root is taken.

The resulting envelope for most tumour markers gave two distinct features as displayed in figure 8.14 which shows the envelopes for the CA 19-9 marker. Investigations into the two different features showed that these could be attributed to a difference in the system between measurements. Markers CEA and LDH showed only the feature on the left.

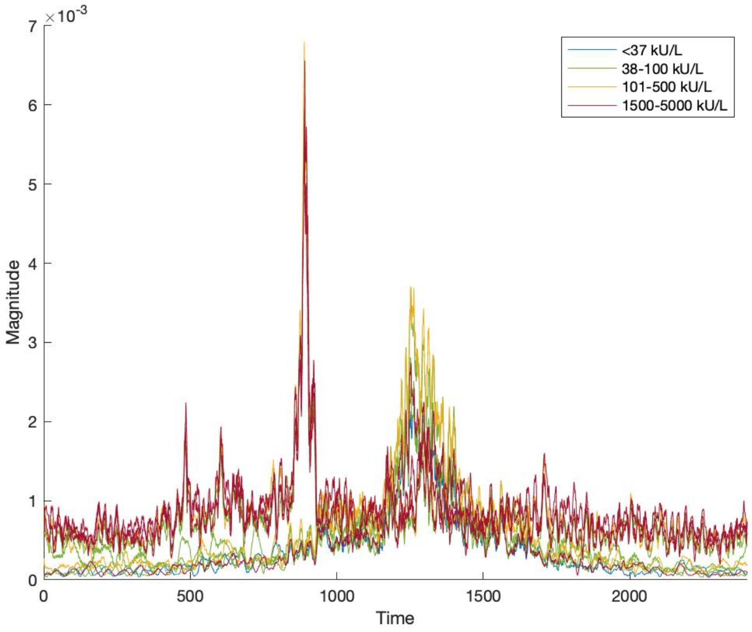

Figure 8.14: Graph displaying envelopes for CA 19-9. Results are grouped to similar levels of concentration.

The markers were collected in two installments, initially 77 samples were collected. The samples were tested in number order but have been numbered in clusters e.g. 17 of each sample have been reserved so samples 1-17 correspond to AFP samples, 18-34 correspond to hCG and so on for CA 125, CA 19-9, CA 153, CEA and LDH. The initial 77 samples fell across all markers leaving gaps in each of the clusters which were to be filled with the second installment from the hospital. It would appear that part way through installment 1, between testing marker 78 and 79, there was a significant change in the VNA performance which has affected each of the samples tested following this. Hence, all the samples from the later tested markers (CEA and LDH) show to have a similar envelope as demonstrated in figure 8.15 which shows the envelopes for CEA and some of the samples for each of the other markers exhibit this behaviour as they have been collected in installment 2 and tested after the change in the VNA.

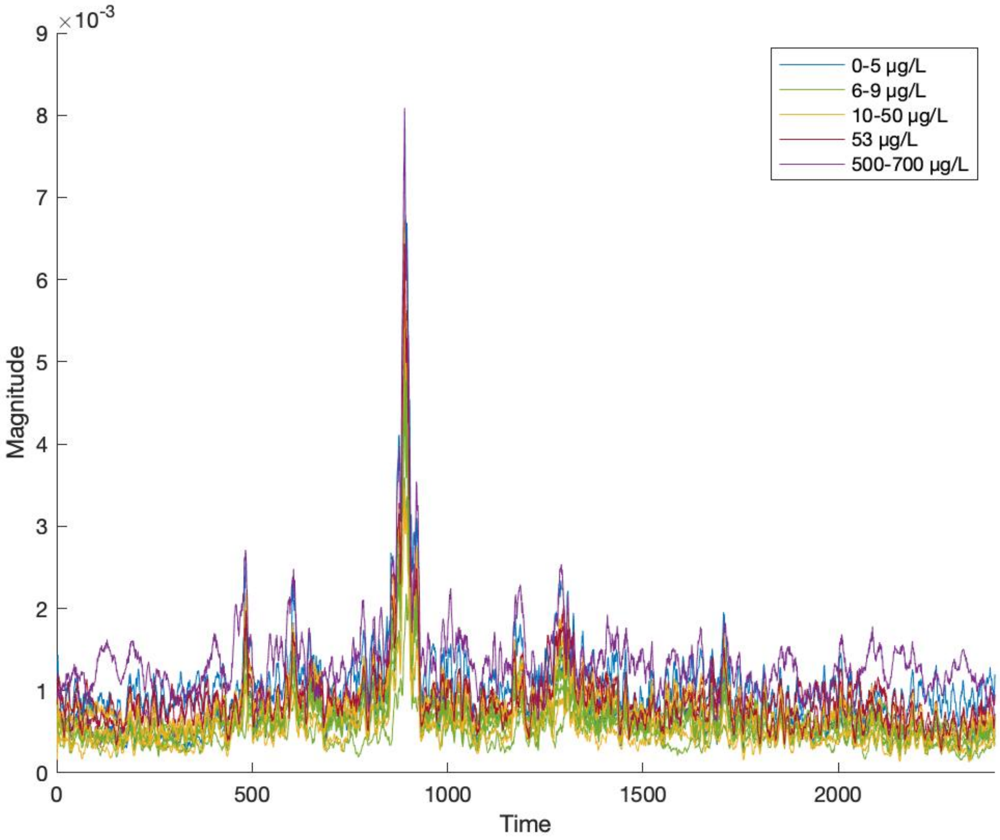

Figure 8.15: Graph displaying envelopes for CEA. Results are grouped to similar levels of concentration.

The empty scans took one of two appearances as shown in figure 8.16, which displays the empty scans taken immediately prior to each of the CA 19-9 scans. After assessing the empty scans for the CEA and LDH markers only one of these modes was found as shown in figure 8.17, which shows the empty scans for CEA. It is therefore assumed that the two distinct envelope features are due to these two noise modes and not as a result of the data. This has been confirmed by cross referencing the empty scans with the envelopes for each of the other samples.

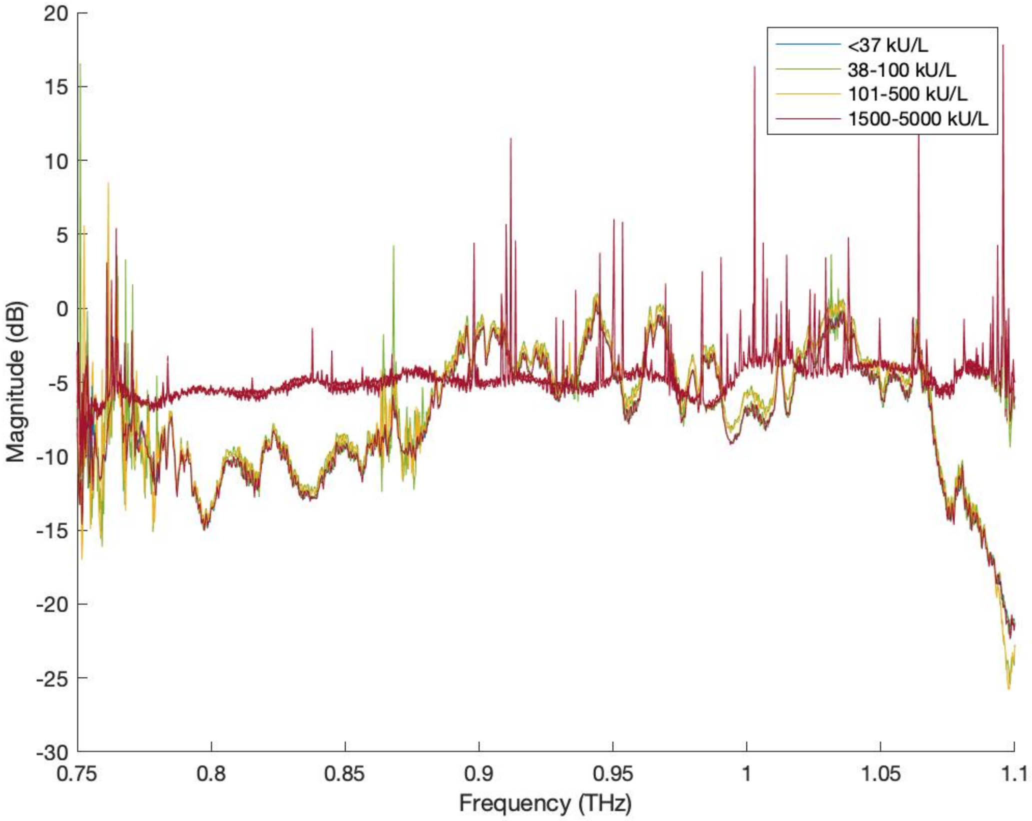

Figure 8.16: Graph displaying empty scans before each of the CA 19-9 scans have been taken.

Finally, the envelope of the raw data normalised by the dry results is calculated. However, the two distinct features are still present. Figure 8.18 is an example of the CA 125 envelopes calculated from the wet results normalised using the dry scan.

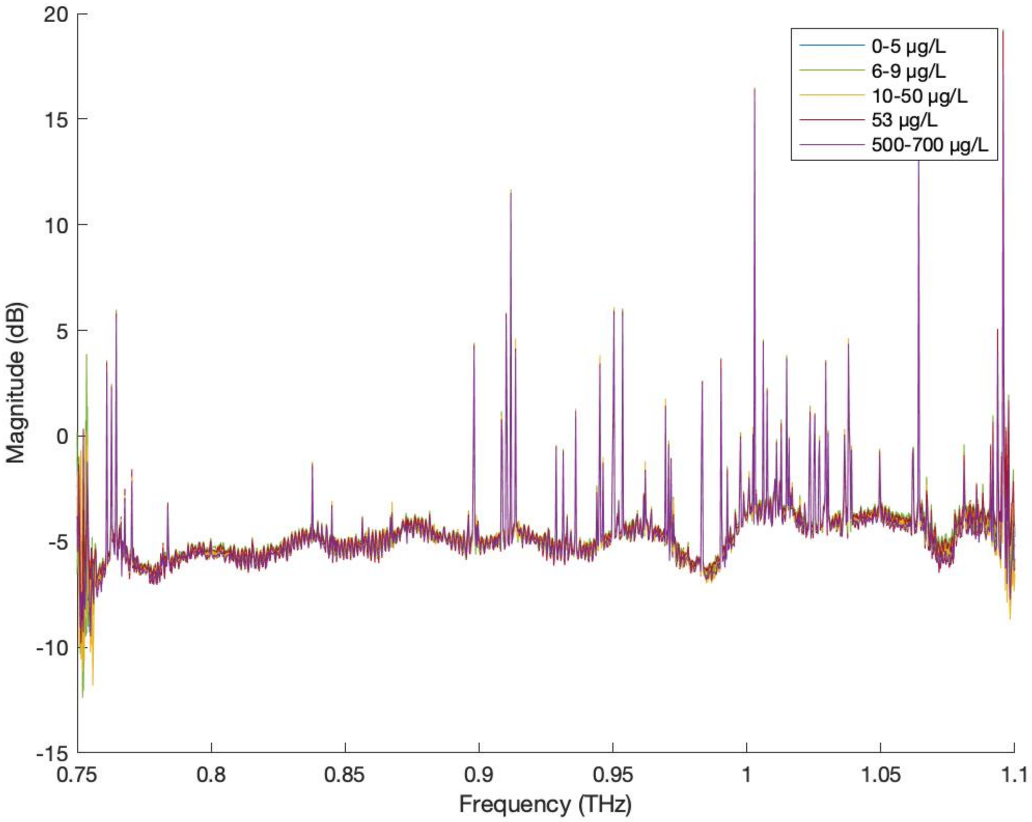

Figure 8.17: Graph displaying empty scans before each of the CEA scans have been taken.

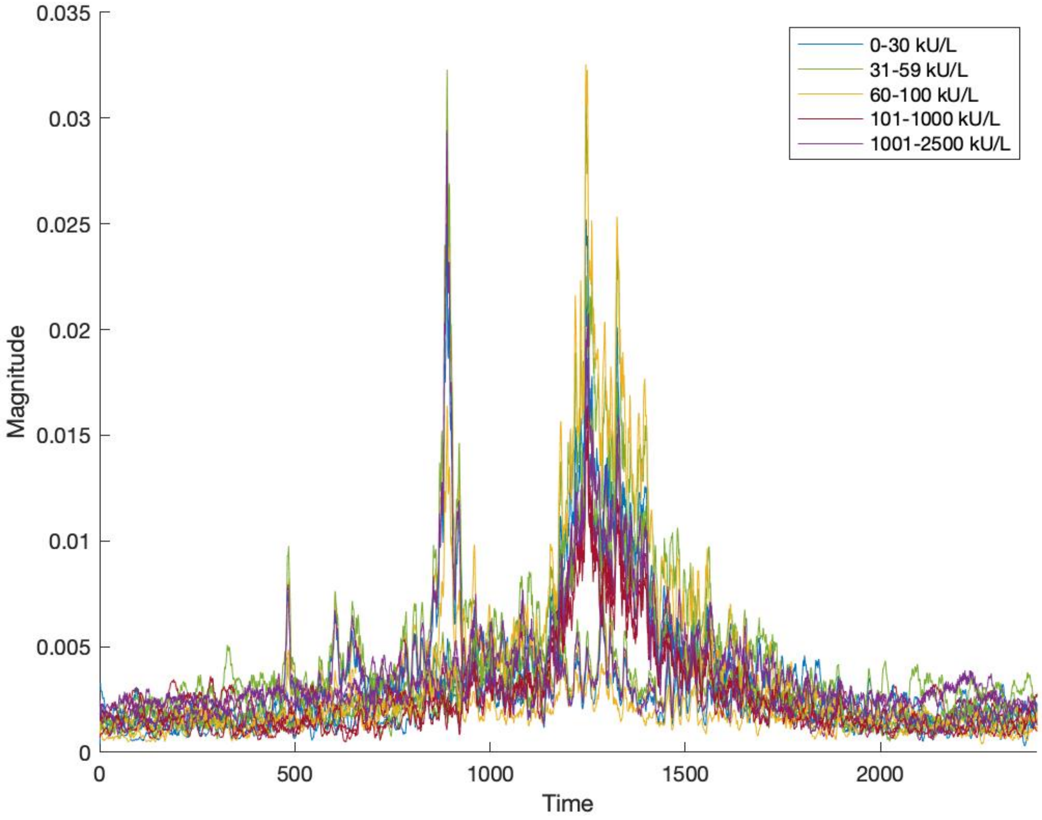

Figure 8.18: Graph displaying empty scans before each of the CA 125 scans have been taken.

8.3.9 Trends Across Markers

The high level of noise in the data makes it difficult to see the trends with marker concentrations. For each individual scan there is noise across the full trace with some frequencies experiencing particularly strong noise. Dependent on the frequency position of the noise, this may even cover the feature position. Thus resulting in difficult or perhaps inaccurate extraction of feature position data and the incorrect calculation of the feature shift. The data presents traces from groups of similar tumour marker concentration which have been averaged together.

Figure 8.19 shows traces which consist of the average of all ‘negative’ scans for each tumour marker. The maximum number of negative samples for each marker is 3 and for some markers this is lower. This small sample size means that some variation is expected, however there is more statistical confidence of the true value than an individual sample. The absorption is ignored as this is dependent on the volume of liquid in the sample. The volume of liquid dosed onto the filter paper is controlled at 0.03 ml and the filter paper size is controlled but the evaporation rate can vary based on the volume of air in the bag and the temperature in the room. This figure shows that the absorption peak position is similar for all markers which is an extremely positive result. From this it can be inferred that the variation in metamaterial fabrication and common blood composition, for example blood glucose level, have little to no effect on the feature position. This is an ideal result as this can imply that any shift in measurements is likely dependent on the marker under test. This shows that the method is robust across multiple samples even with a small sample size of three or less.

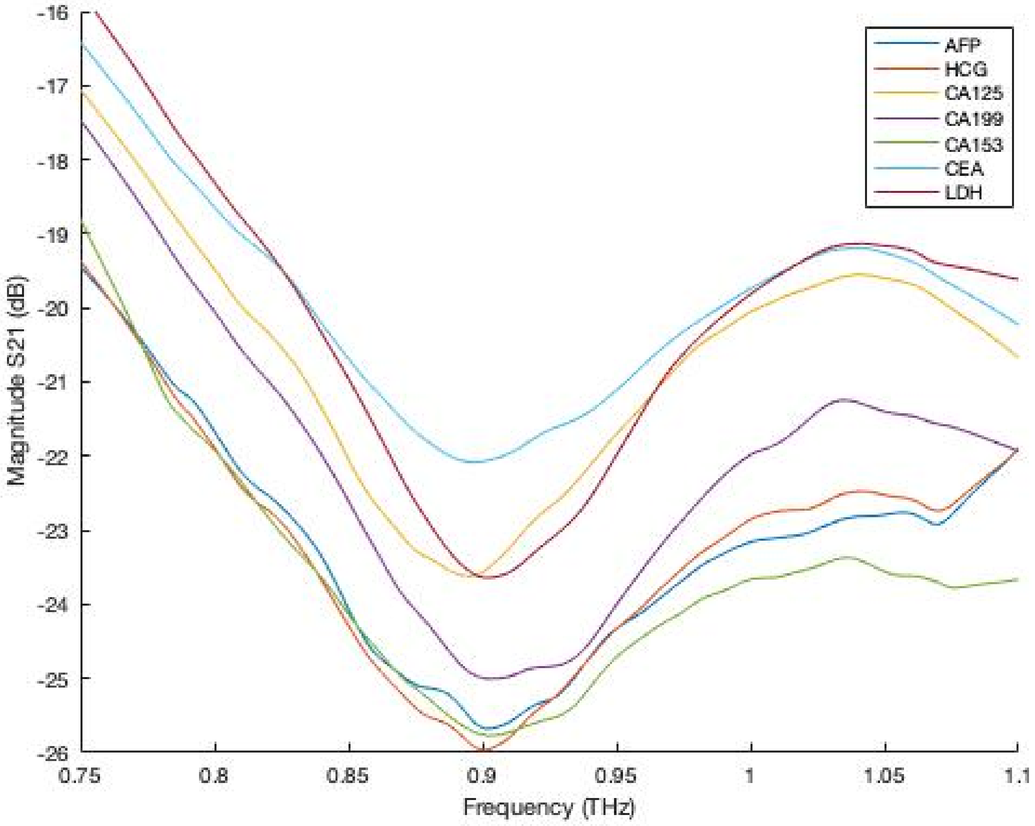

Figure 8.19: Graph displaying average of all ‘negative’ results for each marker.

To compare, the ‘high’ and ‘very high’ sample groups have been averaged together and plotted in figure 8.20 for each of the markers. This graph shows a much wider variation in the feature frequency than the negative samples. It should be noted that there are generally more than three high and very high samples for each marker. As there is a wider variation in the feature position of the averaged trace it shows that a trend can be seen which distinguishes the negative samples between some of the higher value samples for some markers. This means that, although it is difficult to spot in individual samples, there is evidence to say that there may be a measurable correlation due to the marker concentration using this method.

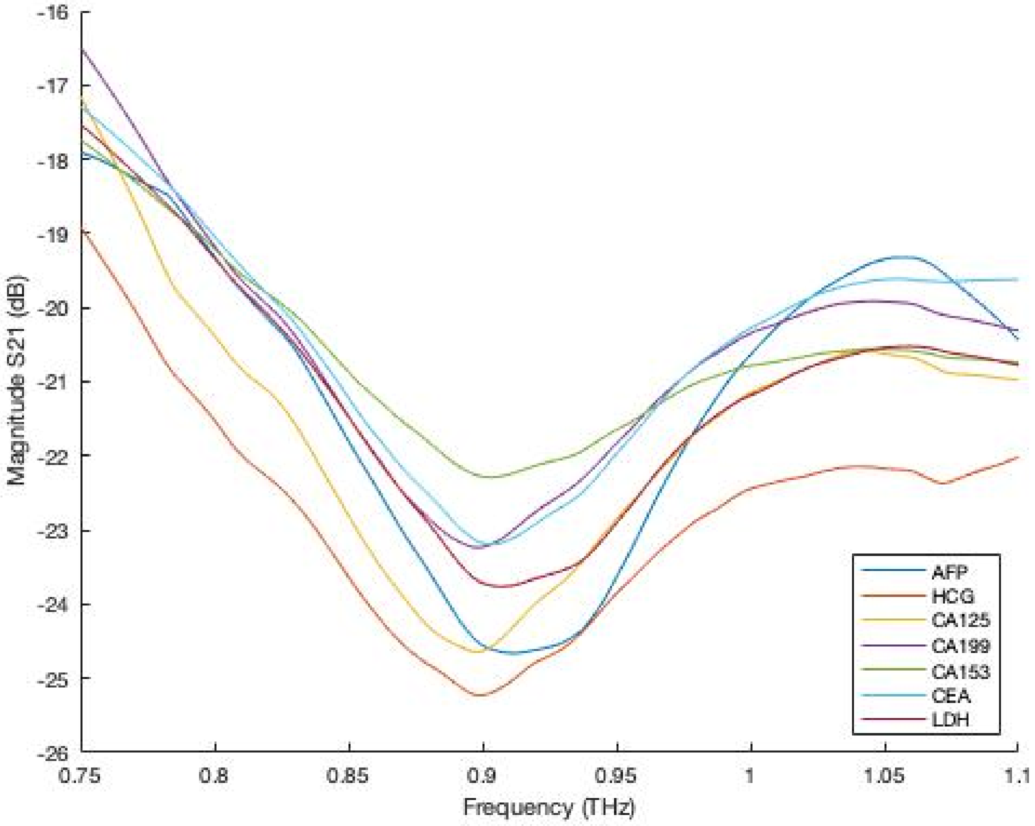

Figure 8.20: Graph displaying average 'high' and 'very high' results for each marker.

Further investigation would be required to confirm this trend is based on marker concentration and not another coincidental factor. In addition, further work would be required to make this method suitable for individual measurement testing for example repeat measurements could be taken for each sample and averaged to give a more confident measurement. This would reduce the impact of the method by increasing both measurement time and cost but it reduces the effect of noise.

8.4 Conclusion

Within this chapter the majority of the results do not to show conclusive findings due to the large volume of noise in this data. In addition to the high level of noise, there also appears to be two distinct noise modes which were taken chronologically before and after an unknown event occurred whilst measuring samples. As each of the samples was mostly measured in order with the exception of a few samples for each marker which had not yet been collected in the initial set, this resulted in a small selection of mode 1 and 2 samples in five of the measured markers with only mode 2 noise for two markers (CEA and LDH).

Various formats of the data have been explored from polynomial fitting to inverse FFT's none of the manipulations showed an obvious trend from marker to marker however, some of the markers showed a trend in grouped averages. The variation between individual measurements is too great to be able to distinguish between the different concentrations but it is possible that the averages of multiple traces was able to distinguish between higher and lower grouped concentrations. A future trial could test each sample multiple times and take the average potentially enabling this technique to distinguish between concentrations of individual samples. However, this would extend measurement times and increase measurement cost reducing the benefit of the method. It is important to note that due to the large level of noise and small number of samples averaged it is possible the differences in averaged samples could be due to another factor however it is worth investigating.

Chapter 9

Conclusions and Future Work

Terahertz technology has been rapidly developing over the past few decades, thus material characterisation is required at this frequency to be able to use these materials for upcoming terahertz technology development. A common characterisation metric for materials is refractive index, this is an inherent property of a material describing its response to a certain frequency of radiation at a certain temperature.

Chapter 3 presented a range of experimental techniques used within this thesis. It outlined the basics of beam handling and some VNA configurations including measurements in both transmission and reflection. The beams formed by the horn antennas used upon exit of the extender heads and translated through parabolic mirrors were explored. MATLAB was presented as an automated system for VNA control. The chapter describes how MATLAB was used to instruct the VNA how, when and what measurements to take by SCPI commands. The VNA control in MATLAB can be integrated with the control of external systems for example moving stages. Moving stages can also be controlled using a MATLAB program and SCPI commands. This allows for a multitude of fully automated measurement possibilities. A test case was presented using a variety of experimental setups to demonstrate the capabilities of the system.

Refractive index measurements of liquids at terahertz frequencies was explored in chapter 4. Two novel cuvette measurement methods were presented which use rotational stages enabling the VNA system to extract material data. The rotational cuvette method was unable to distinguish between individual alkanes but has a mean error of only 0.017 refractive index units so is still a useful technique dependent on the application. The split cuvette method was able to distinguish between even small refractive index differences. As the split cuvette method uses a reference liquid to measure absolute refractive index values it relies on the accurate knowledge of the reference liquids refractive index. The split cuvette can measure refractive index of a liquid across a boundary layer. It can also detect the effective refractive index of a liquid mixture. The split cuvette provides a fast and effective method of measuring refractive index data. The self-referencing system and fast measurements speed lend the method to use for in-flow testing e.g. in the petrochemical industry. Further research into the split cuvette is recommended using a non-square based custom cuvette which utilises the mathematical relationship where the measured component (the exit angle of the beam from the cuvette) can have an increased value based on the inverse tangent of the split angle of the cuvette. This increases the precision given an identical rotational stage.

Chapter 5 introduced the use of paper and explored the properties of paper at terahertz frequencies. The phase retardation and absorption of standard copy paper was measured at 57° and 0.96 dB per sheet respectively. This information was used to generate paper Fresnel lens designs. The beams formed through the paper lenses were presented. The findings showed that a single sheet binary Fresnel lens produced an $\approx$6 dB increase in power received at the focal point. It was found experimentally that multi-tiered designs provide minimal increase in received power and only produce an overall positive contribution for a small number of sheets due to the increased absorption from the increased number of sheets. To enhance the use of multi-tiered devices it is recommended that different paper is used which has reduced absorption by either using thinner sheets or a material with different additives or density. It was found that efficiency of a lens is greatly increased by the overall phase retardation through the full stack of paper sheets being a multiple of 180° for example a three sheet binary Fresnel lens increases the 6 dB response of a single sheet to 10 dB. Soaking the paper lenses in liquid was explored as a method of increasing the phase retardation of the paper sheet whilst also reducing the fluctuation of lens performance due to humidity by preventing the absorption of water from the air into the lens. It is speculated that measuring the refractive index of the liquid soaked into the paper sheet could be possible by plotting the responses while increasing the number of sheets. This should result in a decaying sinusoidal response where the sinusoidal component is related to the phase retardation of the soaked paper and the decay is related to the absorption of the liquid and paper. This information, combined with the known characteristics of dry paper can be used to calculate the refractive index of the liquid. This was attempted but it was found that the absorption of soaked copy paper was too high to measure a large enough range in number of sheets to accurately characterise the sinusoidal response. It may be possible for this to work using thinner paper sheets by reducing the absorption per sheet allowing for more sheets to be measured before reaching the noise floor.

A range of metamaterial designs were presented in chapter 6 along with the simulation and fabrication methods used. Lumerical, a 3D Maxwell solver, was used to alter the feature frequency of the designs found in literature to within the range of 0.75-1.1 THz. Two cross based designs and five split ring designs were presented. One of the cross designs and two of the split ring designs produced features within the VNA region. Chapter 7 explored the experimental performance of these designs finding that using filter paper to hold a test liquid in contact with the metamaterial is the most appropriate method, that the direction of measurement has no effect on the results and that the technique requires sufficient contact and a certain level of wetness. The metamaterial response was impaired if the filter paper was too dry, the mechanism for this is thought to be due to insufficient contact between the filter paper and the metamaterial surface. If the metamaterial was too wet the result was also null, it is speculated that when the filter paper is too wet, a thin layer of liquid lies between the metamaterial surface and the soaked filter paper. Chapter 7 also proposed a final design for the metamaterial to be used in chapter 8.

Chapter 8 presented a body of background information surrounding cancer and more specifically tumour marker use within cancer diagnosis and treatment. A study using human serum samples was presented. There was no proven correlation between tumour marker concentration and any measured metric from each of the markers tested. However, there were some indications that a trend may be found with further investigation. CEA and LDH showed a possible trend in the lowest three concentration groups. This trend was only detectable through observing all the results within each concentration group as the range within each group is large and has a significant overlap. CA-125 showed the same indication for the lowest three concentration groups and also a similar trend between the highest two concentration groups but with a discontinuity between these. This may be a feature of the correlation or may be an indication that this is not actually a true trend and just a conjecture due to the small number of samples. CA 19-9 showed a clear trend when excluding one of the concentration groups, again, this may be a feature of the trend at this particular concentration or may be an indication that this is an incorrect conclusion to draw but given only the small number of samples it is currently unconfirmed. CA 15-3 showed a trend across all groups, this trend is only visible looking at the collective data and no individual point as the range for each concentration group is large and overlaps with neighbouring groups. Conversely, the hCG results, with the exception of a single outlier, showed only random deviation from a mean value and no clear trend. Unfortunately, due to a lack of samples from the NHS no clear conclusion can be given surrounding the AFP responses. No obvious trend was evident, but as there were only a few samples it cannot be concluded that there is no relationship to be found. It is recommended that additional research is conducted for the CEA, LDH, CA-125, CA 19-9 and CA 15-3 to confirm or reject the suggested possible relations between absorption peak position frequency and marker concentration.

Bibliography

[1] J. M. Chamberlain, *Where optics meets electronics: recent progress in decreasing the terahertz gap*, Phil. Trans. R. Soc. Lond. A, **362**, pp 199-213, doi: 10.1098/rsta.2003.1312, (2003).

[2] E. Castro-Camus and M. B. Johnston, *Conformational changes of photoactive yellow protein monitored by terahertz spectroscopy*, Chemical Physics Letters, **455**, pp 289-292, doi: 10.1016/j.cplett.2008.02.084, (2008).

[3] J. Xu, K. W. Plaxco and S. J. Allen, *Probing the collective vibrational dynamics of a protein in liquid water by terahertz absorption spectroscopy*, Protein Science, **15**, pp 1175-1181, doi: 10.1110/ps.062073506, (2006).

[4] B. M. Fischer, M. Walther and P. U. Jepsen, *Far-infrared vibrational modes of DNA components studied by terahertz time-domain spectroscopy*, Physics in Medicine and Biology, **47**, (21), (2002).

[5] M. Brucherseifer, M. Nagel, P. H. Bolivar and H. Kurz, *Label-free probing of the binding state of DNA by time-domain terahertz sensing*, Appl. Phys. Lett., **77**, (4049), doi: 10.1063/1.1332415, (2000).

[6] M. Franz, B. Fischer, D. Abbott and H. Helm, *Terahertz study of chiral and racemic crystals*, 2006 Joint 31st International Conference on Infrared Millimeter Waves and 14th International Conference on Teraherz Electronics, doi: 10.1109/ICIMW.2006.368438, (2006).

[7] M. Walther, B. M. Fischer and P. U. Jepsen, *Noncovalent intermolecular forces in polycrystalline and amorphous saccharides in the far infrared*, Chemical Physics, **288**, (2-3), pp 261-268, doi: 10.1016/S0301-0104(03)00031-4, (2003).

[8] B. Born, A. J. Kim, S. Ebbinghaus, M. Gruebele and M. Havenith, *The terahertz dance of water with the proteins: the effect of protein flexibility on the dynamical hydration shell of ubiquitin*, Faraday Discussions, **141**, pp 161-173 doi: 10.1039/B804734K, (2009).

[9] B. Born, H. Weingärtner, E. Bründermann and M. Havenith, *Solvation dynamics of model peptides probed by terahertz spectroscopy. Observation of the onset of collective network motions*, J. Am. Chem. Soc., **131**, (10), pp 3752-3755, doi: 10.1021/ja808997y, (2009).

[10] S. Ebbinghaus, S. J. Kim, M. Heyden, X. Yu, U. Heugen, M. Gruebele, D. M. Leitner and M. Havenith, *An extended dynamical hydration shell around proteins*, PNAS, **104**, (52), pp 20749-20752, doi: 10.1073/pnas.0709207104, (2007).

[11] D. M. Leitner, M. Gruebele and M. Havenith, *Solvation dynamics of biomolecules: modeling and terahertz experiments*, HFSP J., **2**, (6), pp 314-323, doi: 10.2976/1.2976661, (2008).

[12] D. A. Schmidt, O. Birer, S. Funkner, B. P. Born, R. Gnanasekaran, G. W. Schwaab, D. M. Leitner and M. Havenith, *Rattling in the cage ions as probes of sub-picosecond water network dynamics*, J. Am. Chem. Soc., **131**, (51), doi: 10.1021/ja9083545, (2009).

[13] M. C. Kemp, P. F. Taday, B. E. Cole, J. A. Cluff, A. J. Fitzgerald and W. R. Tribe, *Security applications of terahertz technology*, Terahertz for Military and Security Applications, **5070**, doi: 10.1117/12.500491, (2003).

[14] M. R. Scarfí, M. Romanó, R. Di Piertro, O. Zeni, A. Doria, G. P. Gallerano, E. Giovenale, G. Messina, A. Lai, G. Campurra, D. Coniglio and M. D'Arienzo, *THz exposure of whole blood for the study of biological effects on human lymphocytes*, Journal of Biological Physics, **29**, doi: 10.1023/A:1024440708943, (2003).

[15] R. H. Clothier and N. Bourne, *Effects of THz exposure on human primary keratinocyte differentiation and viability*, Journal of Biological Physics, **29**, pp 179185, doi: 10.1023/A:1024492725782, (2003).

[16] E. Berry, *Risk Perception and Safety Issues*, Journal of Biological Physics, **29**, pp 263267, doi: 10.1023/A:1024461313486, (2003).

[17] H. Liu, H. Zhong, N. Karpowicz, Y. Chen and X. Zhang, *Terahertz spectroscopy and imaging for defense and security applications*, Proceedings of the IEEE, **95**, (8), doi: 10.1109/JPROC.2007.898903, (2007).

[18] V. Vaks, *High-Precise Spectrometry of the Terahertz Frequency Range: The Methods, Approaches and Applications*, Journal of Infrared, Millimeter, and Terahertz Waves, **33**, pp 4353, doi: 10.1007/s10762-011-9846-x, (2012).

[19] W. R. Tribe, D. A. Newnham, P. F. Taday and M. C. Kemp, *Hidden object detection: security applications of terahertz technology*, Proc. SPIE 5354, Terahertz and Gigahertz Electronics and Photonics III, doi: 10.1117/12.543049, (2004).

[20] J. F. Federici, B. Schulkin, F. Huang, D. Gary, R. Barat, F. Oliveira and D. Zimdars, *THz imaging and sensing for security applications - explosives, weapons and drugs*, Semicond. Sci. Technol., **20**, doi: 10.1088/0268-1242/20/7/018, (2005).

[21] J. Dong, A. Locquet, M. Melis and D. S. Citrin, *Global mapping of stratigraphy of an old-master painting using sparsity-based terahertz reflectometry*, Scientific Reports, doi: 10.1038/s41598-017-15069-2, (2017).

[22] C. L. Koch-Dandolo, T. Filtenborg, K. Fukunaga, J. Skou-Hansen and P. U. Jepsen, *Reflection terahertz time-domain imaging for analysis of an 18th century neoclassical easel painting*, Appl. Opt., doi: 10.1364/AO.54.005123, (2015).

[23] C. Seco-Martorell, V. López-Domínguez, G. Arauz-Garofalo, A. Redo-Sanchez, J. Palacios and J. Tejada, *Goya's artwork imaging with terahertz waves*, Optics Express, doi: 10.1364/OE.21.017800, (2018).

[24] C. L. K. Dandolo and P. U. Jepsen, *Wall painting investigation by means of non-invasive terahertz time-domain imaging (THz-TDI): inspection of subsurface structures buried in historical plasters*, J. Infrared. Milli. Terahz. Waves, doi: 10.1007/s10762-015-0218-9, (2016).

[25] J. Bianca Jackson, J. Bowen, G. Walker, J. Labaune, G. Mourou, M. Menu and K. Fukunaga, *A survey of terahertz applications in cultural heratage conservation science*, IEEE Transactions on Terahertz Science and Technology, **1**, doi: 10.1109/TTHZ.2011.2159538, (2011).

[26] G. Pastorelli, T. Trafela, P. F. Taday, A. Portieri, D. Lowe, K. Funkunaga and M. Strlič, *Characteriastion of historic plastics using terahertz time-domain spectroscopy and pulsed imaging*, Anal. Bioanal. Chem., doi: 10.1007/s00216-012-5931-9, (2012).

[27] P. Dondi, L. Lombardi, M. Malagodi and M. Licchelli, *Automatic identification of varnish wear on historical instruments: the case of Antonio Stradivari violins*, Journal of Cultural Heritage, **22**, doi: 10.1016/j.culher.2016.05.010, (2016).

[28] K. Su, Y. Shen and A. Zietler, *Terahertz sensor for non-contact thickness and quality measurement of automobile paints of varying complexity*, IEEE Transactions on Terahertz Science and Technology, **4**, doi: 10.1109TTHZ.2014.2325393, (2014).

[29] T. Yasui, T. Yasuda, K. Sawanaka and T. Araki, *Terahertz paintmeter for non-contact monitoring of thickness and drying progress in paint film*, Appl. Opt., **44**, doi: 0003-6935/05/326849-08$15.00/0, (2005).

[30] P. H. Siegel, *Terahertz technology in biology and medicine*, IEEE Transactions on Microwave Theory and Techniques, **52**, doi: 10.1109/TMTT.2004.835916, (2004).

[31] H. Lindley-Hatcher, A. I. Hernandez-Serrano, Q. Sun, J. Wang, J. Cebrian, L. Blasco and E. Pickwell-MacPherson, *A robust protocol for in vivo THz skin measurements*, J. Infrared, Millimeter, and Terahertz Waves, **40**, (9), pp 980-989, doi: 10.1007/s10762-019-00619-8, (2019).

[32] J. P. Laib and D. M. Mittleman, *Temperature-Dependent Terahertz Spectroscopy of Liquid n-alkanes*, J. Infrared Milli. Terahz. Waves, **31**, pp 1015-1021, doi: 10.1007/s10762-010-9678-0, (2010).

[33] J. D. Cohen, L. Li, Y. Wang, C. Thoburn, B. Afsari, L. Danilova, C. Douville, A. A. Javed, F. Wong, A. Mattox, R. H. Hruban, C. L. Wolfgang, M. G. Goggins,

M. D. Molin, T. Wang, R. Roden, A. P. Klein, J. Ptak, L. Dobbyn, J. Schaefer, N. Silliman, M. Popoli, J. T. Vogelstein, J. D. Browne, R. E. Brand, J. Tie, P. Gibbs, H. Wong, A. S. Mansfield, J. Jen, S. M. Hanash, M. Falconi, P. J. Allen, S. Zhou, C. Bettegowda, L. A. Diaz Jr., C. Tomasetti, K. W. Kinzler, B. Vogelstein, A. M. Lennon and N. Papadopoulos, *Detection and localization of surgically resectable cancers with a multi-analyte blood test*, Science, **359**, pp 926-930, doi: 10.1126/science.aar3247, (2018).

[34] C. Thacker, A. Cooray, J. Smidt, F. De Bernardis, K. Mitchell-Wynne, A. Amblard, R. Auld, M. Baes, D. L. Clements, A. Dariush, G. De Zotti, L. Dunne, S. Eales, R. Hopwood, C. Hoyos, E. Ibar, M. Jarvis, S. Maddox, M. J. Michałowski, E. Pascale, D. Scott, S. Serjeant, M. W. L. Smith, E. Valiante and P. Van Der Werf, *H-atlas: the cosmic abundance of dust from the far-infrared background power spectrum*, The Astrophysical Journal, **768**, 58, doi: 10.1088/0004-637X/768/1/58, (2013).

[35] R. Köhler, A. Tredicucci, F. Beltram, H. E. Beere, E. H. Linfield, A. G. Davies, D. A. Ritchie, R. C. Lotti and F. Rossi, *Terahertz semiconductor-heterostructure laser*, Nature, **9**, (417), doi: 10.1038/417156a, (2002).

[36] M. Brandstetter, C. Deutsch, M. Krall, H. Detz, D. C. MacFarland, T. Zederbauer, A. M. Andrews, W. Schrenk, G. Strasser and K. Unterrainer, *High power terahertz quantum cascade lasers with symmetric wafer bonded active regions*, Appl. Phys. Lett., **103**, (171113), doi: 10.1063/1.4826943, (2013).

[37] L. Li, L. Chen, J. Zhu, J. Freeman, P. Dean, A. Valavanis, A. G. Davies and E. H. Linfield, *Terahertz quantum cascade lasers with >1 W output powers*, Photonics, **50**, (4), pp 309-311 doi: 10.1049/el.2013.4035, (2014).

[38] B. S. Williams, S. Kumar, Q. Hu and J. L. Remo, *High-power terahertz quantum-cascade lasers*, Electronics letters, **42**, (2), pp 1-2, doi: 10.1109/CLEO.2006.4628285, (2006).

[39] C. Walther, M. Fischer, G. Scalari, R. Terazzi, N. Hoyler and J. Faist, *Quantum cascade lasers operating from 1.2 to 1.6 THz*, Appl. Phys. Lett., **91**, (131122), doi: 10.1063/1.2793177, (2007).

[40] S. Kumar, C. W. I. Chan, Q. Hu and J. L. Reno, *A 1.8-THz quantum cascade laser operating significantly above the temperature of* $\hbar\omega/\kappa_B$, Nature Physics, **7**, pp 166-171, doi: 10.1038/nphys1846, (2011).

[41] J. R. Freeman, J. Madéo, A. Brewer, S. Dhillon, O. P. Marshall, N. Jukam, D. Oustinov, J. Tignon, H. E. Beere and D. A. Ritchie, *Dual wavelength emission from a terahertz quantum cascade laser*, Appl. Phys. Lett., **96**, (051120), doi: 10.1063/1.3304783, (2010).

[42] M. A. Belkin, F. Capasso, F. Xie, A. Belyanin, M. Fischer, A. Wittmann and J. Faist, *Room temperature terahertz quantum cascade laser source based on intracavity difference-frequency generation*, Appl. Phys. Lett., **92**, (201101), doi: 10.1063/1.2919051, (2008).

[43] J. T. Lü and J. C. Cao, *Terahertz generation and chaotic dynamics in GaN NDR diode*, Semicond. Sci. Technol., **19**, pp 451-456, doi: 10.1088/0268-1242/19/3/028, (2004).

[44] O. Cojocari, B. Mottet, M. Rodriquez-Girones, S. Biber, L. Marchand, L. P. Schmidt and H. L. Hartnagel, *A new structural approach for uniform sub-micrometer anode metallization of planar THz schottky components*, Semicond. Sci. Technol., **19**, pp 537-542, doi: 10.1088/0268-1242/19/3/045, (2004).

[45] G. W. Chantry, *Long-wave optics: The Science and Technology of Infrared and Near-Millimeter Waves*, Academic Press, Volume 2, (1984).

[46] M. Y. Tretyakov, S. A. Volokhov, G. Y. Golubyatnikov, E. N. Karyakin and A. F. Krupnov, *Compact tunable radiation source at 180 - 1500 GHz frequency range*, Int. J. Infrared Milli., **20**, (8), pp 1443-1451, doi: 10.1023/A:1021748301525, (1999).

[47] A. Dobroiu, M. Yamashita, Y. N. Ohshima, Y. Morita, C. Orani and K. Kawase, *Terahertz imaging system based on a backward-wave oscillator*, Appl. Optics, **43**, (30), pp 2076-2078, doi: 10.1364/AO.43.005637, (1997).

[48] C. Paoloni, D. Gamzina, R. Letizia, Y. Zheng and N. C. Luhmann Jr., Millimeter wave travelling wave tubes for the 21st century, Journal of Electromagnetic Waves and Applications, **35**, (5), pp 567-603, doi: 10.1080/09205071.2020.1848643, (2021).

[49] B. Steer, A. Roitman, P. Horoyski, M. Hyttinen, R. Dobbs and D. Berry, *Advantages of extended interation klystron technology at millimeter and sub-millimeter frequencies*, 2007 16th IEEE International Pulsed Power Conference, doi: 10.1109/PPPS.2007.4345972, (2007).

[50] M. Blank, P. Borchard, S. Cauffman, K. Felch, M. Rosay and L. Tometich, *Experimental demonstration of a 527 GHz gyrotron for dynamic nuclear polarization*, 2013 Abstracts IEEE International Conference on Plasma Science (ICOPS), doi: 10.1109/PLASMA.2013.6635226, (2013).

[51] W. J. van der Zande, R. T. Jongma, L. van der Meer and B. Redlich, *FELIX facility: free electron laser light sources from 0.2 to 75 THz*, 2013 38th International Conference on Infrared, Millimeter, and Terahertz Waves (IRMMW-THz), doi: 10.1109/IRMMW-THz.2013.6665600, (2013).

[52] G. Cinque, M. Frogley, K. Wehbe, J. Filik and J. Pijanka, *Multimode InfraRed Imaging and Microspectroscopy (MIRIAM) Beamline at Diamond*, Synchrotron Radiation News, **24:5**, pp 24-33, doi: 10.1080/08940886.2011.618093, (2011).

[53] T. A. G. Bondaz, A. Laurain, J. V. Moloney and J. G. McInerney, *Generation and stabilization of continous-wave THz emmission from a bi-color VECSEL*, IEEE Photonics Technology Letters, **31**, (19), pp 1569-1572, doi: 10.1109/LPT.2019.2938169, (2019).

[54] L. L. Slocombe and R. A. Lewis, *Electrival versus optical: comparing methods for detecting terahertz radiation using neon lamps*, Journal of Infrared, Millimeter and Terahertz Waves, **39**, pp 701-713, doi: 10.1007/s10762-018-0495-1, (2018).

[55] P. Shumyatsky and R. R. Alfano, *Terahertz sources*, J. of Biomedical Optics, **16(3)**, doi: 10.1117/1.3554742, (2011).

[56] P. R. Smith, D. H. Auston, M. C. Nuss, *Subpicosecond photoconducting dipole antennas*, IEEE Journal of Quantum Electronics, **24**, (2), pp 255-260, doi: 10.1109/3.121, (1988).

[57] S. Kono, M. Tani, P. Gu and K. Sakai, *Detection of up to 20 THz with a low-temperature-grown GaAs photoconductive antenna gated with 15 fs light pulses*, Appl. Phys. Lett., **77**, (4104), doi: 10.1063/1.1333403, (2000).

[58] S. S. Dhillon, M. S. Vitiello, E. H. Linfield, A. G. Davies, M. C. Hoffmann, J. Booske, C. Paoloni, M. Gensch, P. Weightman, G. P. Williams, E. Castro-Camus, D. R. S. Cumming, F. Simoens, I. Escorcia-Carranza11, J. Grant, S. Lucyszyn, M. Kuwata-Gonokami, K. Konishi, M. Koch, C. A. Schmuttenmaer, T. L. Cocker, R. Huber, A. G. Markelz, Z. D. Taylor, V. P. Wallace, J. A. Zeitler, J. Sibik, T. M. Korter, B. Ellison, S. Rea, P. Goldsmith, K. B. Cooper, R. Appleby, D. Pardo, P. G. Huggard, V. Krozer, H. Shams, M. Fice, C. Renaud, A. Seeds, A. Sthr, M. Naftaly, N. Ridler, R. Clarke, J. E. Cunningham and M. B. Johnston, *The 2017 terahertz science and technology roadmap*, J. Phys. D: Appl. Phys., **50**, 043001, doi: 10.1088/1361-6463/50/4/043001, (2017).

[59] N. Vieweg, F. Rettich, A. Deninger, H. Roehle, R. Dietz, T. Gbel and M. Schell, *Terahertz-time domain spectrometer with 90 dB peak dynamic range*, Journal of Infrared, Millimeter and Terahertz Waves, **35**, pp 823832, doi: 10.1007/s10762-014-0085-9, (2014).

[60] W. Withayachumnankul and M. Naftaly, *Fundamentals of measurement in terahertz time-domain spectroscopy*, Journal of Infrared, Millimeter and Terahertz Waves, **35**, (8), pp 610-637, doi: 10.1007/s10762-013-0042-z, (2013).

[61] J. V. Rudd, D. Zimdars and M. Wannuth, *Compact, fiber-pigtailed, terahertz imaging system*, Proc. SPIE 3934, Commercial and Biomedical Applications of Ultrafast Lasers II, pp 27-35, doi: 10.1117/12.386344, (2000).

[62] Virginia Diodes Inc., [online]. Available: $https://vadiodes.com/en/products/vector-network-analyzer-extension-modules$. [Accessed: 18/06/2022].

[63] P. F. X. Neumaier, K. Schmalz, J. Borngräber, R. Wylde and H. W. Hübers, *Terahertz gas-phase spectroscopy: chemometrics for security and medical applications*, Analyst, **140**, pp 213-222, doi: 10.1039/C4AN01570C, (2014).

[64] W. Sun, B. Yang, X. Wang, Y. Zhang and R. Donnan, *Accurate determination of terahertz optical constants by vector network analyzer of Fabry-Perot response*, Optics Letters, **24**, (38), pp 5438-5441, doi: 10.1364/OL.38.005438, (2013).

[65] J. L. Hesler, Y. Duan, B. Foley and T. W. Crowe, *THz vector network analyzer measurements and calibration*, 21st International Symposium on Space Terahertz Technology, (2010).

[66] J. Hammler, A. J. Gallant and C. Balocco, *Free-space permittivity measurement at terahertz frequencies with a vector network analyser*, IEEE Transactions on Terahertz Science and Technology, **6**, (6), pp 817-823, doi: 10.1109/TTHZ.2016.2609204, (2016).

[67] S. Yang, P. Liu, M. Yang, Q. Wang, J. Song and L. Dong, *From flexible and strechable meta-atom to metamaterial: a wearable microwave meta-skin with tunable frequency selective and cloaking effects*, Scientific Reports, doi: 10.1038/srep21921, (2016).

[68] S. Cheon, K. D. Kihm, H. G. Kim, G. Lim, J. S. Park and S. Lee, *How to reliably determine the complex refractive index (RI) of graphene by using two independent measurement constraints*, Nature Scientific Reports, doi: 10.1038/srep06364, (2014).

[69] R. Datta, C. D. Munson, M. D. Niemack, J. J.McMahon, J. Britton, E. J. Wollack, J. Beall, M. J. Devlin, J. Fowler, P. Gallardo, J. Hubmayr, K. Irwin, L. Newburgh, J. P. Nibarger, L. Page, M. A. Quijada, B. L. Schmitt, S. T. Staggs, R. Thornton and L. Zhang, *Large-aperture wide-bandwidth anti-reflection-coated silicon lenses for millimeter wavelengths*, Appl. Opt., **52(36)**, pp 8747-8758, doi: 10.1364/AO.52.008747, (2013).

[70] J. D. Wheeler, B. Koopman, P. Gallardo, P. R. Maloney, S. Brugger, G. Cortes-Medellin, R. Datta, C. D. Dowell, J. Glenn, S. Golwala, C. McKenney, J. J. McMahon, C. D. Munson, M. Niemack, S. Parshley and G. Stacey, *Anti-reflection coatings for submillimeter silicon lenses*, Millimeter, Submillimeter, and Far-Infrared Detectors and Instrumentation for Astronomy VII, **9153**, doi: 10.1117/12.2057011, (2014).

[71] R. M. Woodward, B. E. Cole, V. P. Wallace, R. J. Pye, D. D. Arnone, E. H. Linfield and M. Pepper, *Terahertz pulse imaging in reflection geometry of human skin tissue*, Physics in Biology and Medicine, **47**, doi: 10.1088/0031-9155/47/21/325, (2002).

[72] D. Churchley, R. J. M. Lynch, F. Lippert, J. S. O. Eder, J. Alton and C. Gonzalez-Cabezas, *Terahertz pulsed imaging study to assess remineralisation of artificial caries lesions*, Journal of Biomedical Optics, **16**, (2), doi: 10.1117/1.3540277, (2011).

[73] J. A. Zeitler, Y. Shen, C. Baker, P. F. Taday, M. Pepper and T. Rades, *Analysis of coating structures and interfaces in solid oral dosage forms by three dimensional terahertz pulsed imaging*, Journal of Pharmaceutical Sciences, **96**, (2), doi: 10.1002/jps.20789, (2007).

[74] *Nominal Horn Specifications*, Virginia Diodes, Inc., (2011). [online]. Available: $https : //www.datasheetarchive.com/whats_new/09b80abf8efc3bdc011593e0ed99fac8.html$ [Accessed: 18/06/22].

[75] *Skin Effect Depth Calculator*, Chemandy Electronics, (2020). [online]. Available: $https : //chemandy.com/calculators/skin - effect - calculator.htm$. [Accessed: 18/06/2022].

[76] J. W. Jung, K. S. Kim, J. H. Shin, Y. J. Kwon, J. H. Hwang and S. Y. Lee, *Fingernail configuration*, Arch, Plast. Surg., **42(6)**, pp 753-760, doi: 10.5999/aps.2015.42.6.753, (2015).

[77] I. H. Libon, M. Hempel, S. Seitz, N. E. Hecker, J. Feldmann, A. Hayd, G. Zundel, D. Mittleman and M. Koch, *THz spectroscopy of polar liquids*, Proc. SPIE 3617, Terahertz Spectroscopy and Applications, doi: 10.1117/12.347127, (1999).

[78] *SU-8 2000, Permanent Epoxy Negative Photoresist, Processing guidelines for: SU-8 2025, SU-8 2035, SU-8 2050 and SU-8 2075*, Microchem, [online]. Available: *https* : //*kayakuam.com/wp* − *content/uploads*/2019/09/*SU* − 82000*DataSheet*2025*thru*2075*Ver*4.*pdf*. [Accessed: 18/06/2022].

[79] J. E. Pedersen and S. R. Keiding, *THz time-domain spectroscopy of non-polar liquids*, IEEE Journal of Quantum Electronics, **28**, 10, pp 2518-2522, doi: 10.1109/3.159558, (1992).

[80] B. Zhang, J. Hendrickson, N. Nader, H. Chen and J. Guo, *Metasurface optical antireflection coating*, Appl. Phys. Lett., **105**, doi: 10.1063/1.4904827, (2014).

[81] J. T. Kindt and C. A. Schmuttenmaer, *Far-Infrared Dielectric Properties of Polar Liquids Probed by Femtosecond Terahertz Spectroscopy*, J. Phys. Chem., **100**, 10373-10379, doi: 10.1021/jp960141g, (1996).

[82] T. Ikeda, A. Matsushita, M. Tatsuno, Y. Minami, M. Yaaguchi, K. Yamamoto, M. Tani and M. Hangyo, *Investigation of inflammable liquids by terahertz spectroscopy*, Appl. Phys. Lett., **87**, 034105, doi: 10.1063/1.1999847, (2005).

[83] S. Gorenflo, U. Tauer, I. Hinkov, A. Lambrecht, R. Buchner and H. Helm, *Dielectric properties of oil-water complexes using terahertz transmission spectroscopy*, Chemical Physics Letters, **421**, pp 494-498, doi: 10.1016/j.cplett.2006.01.108, (2006).

[84] L. Thrane, R. H. Jacobsen, P. Uhd Jepsen and S. R. Keiding, *THz reflection spectroscopy of liquid water*, Chemical Physics Letters, **240**, doi: 10.1016/0009-2614(95)00543-D, (1995).

[85] P. U. Jepsen, J. K. Jensen and U. Møller, *Characterisation of aqueous alcohol solutions in bottles with THz reflection spectroscopy*, Optics Express, **16**, pp 9318-9331, doi: 10.1364/OE.16.009318, (2008).

[86] R. Mendis, V. Astlet, J. Liu and D. M. Mittleman, *Terahertz microfluidic sensor based on a parallel-plate waveguide resonant cavity*, Applied Physics Letters, **95**, 171113, doi: 10.1063/1.3251079, (2009).

[87] J. Li, Z. Tian, Y. Chen, W. Cao and Z. Zheng, *Distinguishing octane grades in gasoline using terahertz metamaterials*, Applied Optics, **51**, 16, pp 3258-3262, doi: 10.1364/AO.51.003258, (2012).

[88] F. Fan, S. Chen, X. Wang, P. Wu and S. Chang, *Terahertz refractive index sensing based on photonic column array*, IEEE Photonics Technology Letters, **27**, 5, pp 478-481, doi: 10.1109/LPT.2014.2382128, (2015).

[89] J. Ornik, J. Lehr, M. Reuter, D. Jahn, F. Beltran-Mejia, J. C. Balzer, T. Kleine-Ostmann and M. Koch, *Repeatability of material parameter extraction of liquids from transmission terhertz time-domain measurements*, Optics Express, **28**, 19, pp 28178-28189, doi: 10.1364/OE.403159, (2020).

[90] B. Gorshunov, A. Volkov, I. Spektor, A. Prokhorov, A. Mukhin, M. Dressel, S. Uchida and A. Loidl, *Terahertz BWO-spectroscopy*, International Journal of Infrared and Millimeter Waves, **26**, 9, doi: 10.1007/s10762-005-7600-y, (2005).

[91] E. Arik, H. Altan and O. Esenturk, *Dielectric properties of ethanol and gasoline mixtures by terahertz spectroscopy and an effective method for determination of ethanol content of gasoline*, J. Phys. Chem., **118**, 17, pp 3081-3089, doi: 10.1021/jp500760t, (2014).

[92] M. Borecki, P. Prus and M. L. Korwin-Pawlowski, *Capillary Sensor with Disposable Optrode for Diesel Fuel Quality Testing*, Sensors, **19**, 9, doi: 10.3390/s19091980, (2019).

[93] R. K. Verma, P. Suwalka and J. Yadav, *Detection of adulteration in diesel and petrol by kerosene using SPR based fiber optic technique*, Optical Fiber Technology, **43**, pp 95-100, doi: 10.1016/j.yofte.2018.04.011, (2018).

[94] J. E. Greivenkamp, *Field Guide to Geometrical Optics*, SPIE Field Guides, doi: 10.1117/3.547461 (2004).

[95] A. Siemion, P. Kostrowiecki-Lopata, A. Pindur, P. Zagrajek and M. Sypek, *Paper on Designing Costless THz Paper Optics*, Hindawi Advances in Materials Science Engineering, doi: 10.1155/2016/9615698, (2016).

[96] S. O. Thompson, *Paper manufacturing and early books*, Annuals of the New York Academy of Sciences, **314**, pp 167-176, doi: 10.1111/j.1749-6632.1978.tb47791.x, (1978).

[97] M. Reid and R. Fedosejevs, *Terahertz birefringence and attenuation properties of wood and paper*, Applied optics, **45**, doi: 0003-6935/06/122766-07$15.00/0, (2006).

[98] T. Hattori, H. Kumon and H. Tamazumi, *Terahertz Spectroscopic Characterisation of Paper*, 35th international conference on infrared, millimeter and terahertz waves, **35**, doi: 10.1109/ICIMW.2010.5612460 (2010).

[99] A. Holland, *Papermaking Additives and Fillers*, (2012). [online]. Available: $https://www.georgeweil.com/blog/papermaking-additives-and-fillers/$. [Accessed: 17/06/2022].

[100] W. M. Bundy and J. N. Ishley, *Kaolin in paper filling and coating*, Applied Clay Science, **5**, pp 397-420, doi: 10.1016/0169-1317(91)90015-2, (1991).

[101] A. Siemion, A. Siemion, M. Makowski, J. Suszek, J. Bomba, A. Czerwiński, F. Garet, J. Coutaz and M. Sypek, *Diffractive Paper Lens for Terahertz Optics*, Optics lett., **37**, pp 4320-4322, doi: 10.1364/OL.37.004320, (2012).

[102] A. Siemion, A. Siemion, J. Suszek, A. Kowalczyk, J. Bomba, A. Sobczyk, N. Palka, P. Zagrajek, A. Kolodziejczyk and M. Sypek, *THz Beam Shaping Based on Paper Diffractive Optics*, IEEE Transactions on Terahertz Science and Technology, **6**, pp 568-575 doi: 10.1109/TTHZ.2016.2575440, (2016).

[103] R. Lees, P. S. Stefanova, A. K. Klein, C. Balocco and A. J. Gallant, *Paper based optical components for the THz region*, 43rd international conference on infrared, millimeter and terahertz waves, **43**, doi: 10.1109/IRMMW-THz.2018.8510036, (2018).

[104] B. Scherger, M. Scheller, N. Vieweg, S. T. Cundiff and M. Koch, *Paper terahertz wave plates*, Optics Express, **19**, 25, pp 24884-24889, doi: 10.1364/OE.19.024884, (2011).

[105] V. Vassilev, B. Stoew, J. Blomgren and G. Andersson, *A mm-Wave Sensor for Remote Measurement of Moisture in Thin Paper Layers*, IEEE Transactions in Terahertz Science and Technology, **5**, pp 770-778, doi: 10.1109/TTHZ.2015.2462716, (2015).

[106] H. Chen, J. Zhou, J. F. O'Hara and A. J. Taylor, *A numerical investigation of metamaterial antireflection coatings*, International Journal of Terahertz Science and Technology, **3**, (2), pp 66-73, doi: 10.11906/TST.066-073.2010.06.06, (2010).

[107] Z. Jakšić, S. Vuković, J. Matovic and D. Tanasković, *Negative refractive index metasurfaces for enhanced biosensing*, Materials, **4**, 1, pp 1-36, doi: 10.3390/ma4010001, (2011).

[108] A. Salim and S. Lim, *Review of recent metamaterial microfluidic sensors*, Sensors, **18**, 1(232), doi: 10.3390/s18010232, (2018).

[109] I. Al-Naib, *Biomedical sensing with conductively coupled terahertz metamaterial resonators*, IEEE Journal of Selected Topics in Quantum Electronics, **23**, (4), doi: 10.1109/JSTQE.2016.2629665, (2017).

[110] H. Tao, L. R. Chieffo, M. A. Brenckle, S. M. Siebert, M. Liu, A. C. Strikwerda, K. Fan, D. L. Kaplan, X. Zhang, R. D. Averitt and F. G. Omenetto, *Metamaterials on paper as a sensing platform*, Adv. Mater., **23**, pp 3197-3201, doi: 10.1002/adma.201100163, (2011).

[111] K. Ling, M. Yoo, W. Su, K. Kim, B. Cook, M. M. Tentzeris and S. Lim, *Microfluidic tunable inkject-printed metamaterial absorber on paper*, Optics Express, **23**, (1), pp 110-120, doi: 10.1364/OE.23.000110, (2015).

[112] A. Sadeqi, H. R. Nejad and S. Sonkusale, *Low-cost metamaterial-on-paper chemical sensor*, Optics Express, **25**, (14), pp 16092-16100, doi: 10.1364/OE.25.016092, (2017).

[113] P. Naulleau, *2.17 - Optical Lithography*, Comprehensive Nanoscience and Nanotechnology (Second Edition), Lawrence Berkeley National Laboratory, Academic Press, pp 387-398, doi: 10.1016/B978-0-12-803581-8.10433-3, (2019).

[114] D. Ma, S. Chon, S. Cho, Y. Lee, M. Yoo, D. Kim, D. Y. Lee and J. K. Lim, *A novel photolithographic method for fabrication of flexible micro-patterned glucose sensors*, Journal of Electroanalytical Chemistry, **876**, 114720, doi: 10.1016/j.jelechem.2020.114720, (2020).

[115] MicroChemicals, *Aluminium Etching*, (2013). [online]. Available: $https : //www.microchemicals.com/technical_information/aluminium_etching.pdf$. [Accessed: 17/06/2022].

[116] C. Wang, X. Li, Y. Huang, W. Xu, R. Zhou, R. Wang, L. Xie and Y. Ying, *Metallic mesh devices-based terahertz parallel-plate resonators: charachteristics and applications*, Optics Express, **26**, (19), pp 24992-25002, doi: 10.1364/OE.26.024992, (2018).

[117] I. A. Naib, C. Jansen, N. Born and M. Koch, *High Q-factor planar terahertz metamaterials*, 35th International Conference on Infrared, Millimeter, and Terahertz Waves, doi: 10.1109/ICIMW.2010.5612801, (2010).

[118] I. Al-Naib, R. Singh, C. Rockstuhl, F. Lederer, S. Delprat, D. Rocheleau, M. Chaker, T. Ozaki and R. Morandotti, *Excitation of a high-Q subradiant resonance mode in mirrored single-gap asymmetric split ring resonator terahertz materials*, Appl. Phys. Lett., **101**, 071108, doi: 10.1063/1.4745790, (2012).

[119] V. A. Fedotov, M. Rose, S. L. Prosvirnin, N. Papasimakis and N. I. Zheludev, *Sharp trapped-mode resonances in planar metamaterials with a broken structural symmetry*, Phys. Rev. Lett., **99**, (14), 147401, doi: 10.1103/PhysRevLett.99.147401, (2007).

[120] R. Singh, W. Cao, I. Al-Naib, L. Cong, W. Withayachumnankul and W. Zhang, *Ultrasensitive terahertz sensing with high-Q fano resonances in metasurfaces*, Appl. Phys. Lett., **105**, (17), 171101, doi: 10.1063/1.4895595, (2014).

[121] S. J. M. Rao, Y. K. Srivastava, G. Kumar and D. R. Chowdhury, *Modulating fundamental resonance in capacitive coupled asymmetric terahertz metamaterials*, Scientific Reports, **8**, 16773 doi: 10.1038/s41598-018-34942-2, (2018).

[122] J. Zhou, X. Rao, X. Liu, T. Li, L. Zhou, Y. Zheng and Z. Zhu, *Temperature-Dependent optical and dielectric properties of liquid water studied by terahertz time-domain spectroscopy*, AIP Advances, **9**, 035346, doi: 10.1063/1.5082841 (2019).

[123] J. T. Busher, Serum Albumin and Globulin, *Clinical methods: the history, physical, and laboratory examination. 3rd edition.*, Walker HK, Hall WD, Hurst JW, editors., (1990).

[124] S. H. Davoodi, R. Shahbazi, S. Esmaeili, S. Sohrabvandi, A. M. Mortazavian, S. Jazayeri and A. Taslimi, *Health-related aspects of milk proteins*, Iran J. Pharm. Res., **15(3)**, pp 573-591, (2016).

[125] Y. Tang, L. Xing and P. Wang, *Preperation of a hydrophilic nitrocellulose membrane*, IOP Conf. Series: Materials Science and Engineering, **677**, 022035, doi: 10.1088/1757-899X/677/2/022035, (2019).

[126] The Protein Man, *PVDF or nitrocellulose - which membrane is best?*, G-Biosciences, (2014). [online]. Available: *https : //info.gbiosciences.com/blog/bid/*203026*/pvdf − or − nitrocellulose − which − membrane − is − best*. [Accessed: 17/06/2022].

[127] E. R. Tovey and B. A. Baldo, *Protein binding to nitrocellulose, nylon and PVDF membranes in immunoassays and electroblotting*, Journal of Biochemical and Biophysical Methods, **19**, pp 169-184, doi: 10.1016/0165-022x(89)90024-9, (1989).

[128] Y. Wang, Z. Han, Y. Du and J. Qin, *Ultrasensitive terahertz sensing with high-Q toroidal dipole resonance governed by bound states in the continuum in all-dielectric metasurface*, Journal of Nanophotonics, **10**, 4, pp 1295-1307, doi: 10.1515/nanoph-2020-0582, (2021).

[129] M. Naftaly, N. Ridler, J. Molloy, N. Shoaib and D. Stokes, *A comparison method for THz measurements using VNA and TDS*, 2015 40th International Conference on Infrared, Millimeter, and Terahertz waves (IRMMW-THz), doi: 10.1109/IRMMW-THz.2015.7327635, (2015).

[130] J. T. Busher, *Clinical Methods: The History, Physical, and Laboratory Examinations. 3rd edition.*, Chapter 101 Serum Albumin and Globulin, Walker HK, Hall WD, Hurst JW, editors., (1990). [online]. Available: *https : //www.ncbi.nlm.nih.gov/books/NBK*204/. [Accessed: 17/06/2022].

[131] Macmillan Cancer Support, *Statistics fact sheet*, (2017). [online]. Available: *https : //www.macmillan.org.uk/*$_i$*mages/cancer − statistics − factsheet*$_t$*cm*9 − 260514.*pdf*. [Accessed: 17/06/2022].

[132] Cancer Research UK, *Cancer statistics for the UK*, [online]. Available: *https : //www.cancerresearchuk.org/health − professional/cancer − statistics − for − the − uk*. [Accessed: 17/06/2022].

[133] R. L. Siegel, K. D. Miller and A. Jemal, *Cancer statistics, 2017*, Ca. cancer J. Clin., **67**, pp 7-30, doi: 10.3322/caac.21387, (2017).

[134] H. Kim, H. Lim and A. Moon, *Sex differences in cancer: edidemiology, genetics and therapy*, Biomol. Ther., **26**, pp 335-342, doi: 10.4062/biomolther.2018.103, (2018).

[135] R. B. Merkatz, R. Temple, S. Sobel, K. Feiden and D. A. Kessler, *Women in clinical trials of new drugs – a change in food and drug administration policy*, N. Engl. J. Med., **329**, pp 292-296, doi: 10.1056/NEJM199307223290429, (1993).

[136] C. Tran, S. R. Knowles, B. A. Liu and N. H. Shear, *Gender differences in adverse drug reactions*, J. Clin. Pharmacol., **38**, pp 1003-1009, doi: 10.1177/009127009803801103, (1998).

[137] G. D. Anderson, *Sex and racial differences in pharmacological response: where is the evidence? pharmacogenetics, pharmacokinetics, and pharmacodynamics*, Journal of women's health, **14**, (1), pp 19-29, doi: 10.1089/jwh.2005.14.19, (2005).

[138] M. Rademaker, *Do women have more adverse drug reactions?*, Am. J. Clin. Dermatol., **2**, (6), pp 349-351 doi: 0.2165/00128071-200102060-00001, (2001).

[139] V. Regitz-Zagrosek, *Geschlechterunterschiede in der pharmakotherapie*, Bundegesundheitsbl., **57**, pp 1067, doi: 10.1007/s00103-014-2012-6, (2014).

[140] Office for National Statistics, *Cancer registration statistics, England: 2017*, (2017). [online]. Available: $https://www.ons.gov.uk/peoplepopulationandcommunity/healthandsocialcare/conditionsanddiseases/bulletins/cancerregistrationstatisticsengland/2017$. [Accessed: 17/06/22].

[141] J. L. Krok-Schoen, A. L. Palmer-Wackerly, P. M. Dailey, J. C. Wojno and J. L. Krieger, *Age differences in cancer treatment desicion making and social support*, Journal of Aging and Health, **29**, (2), pp 187-205, doi: 10.1177/0898264316628488, (2016).

[142] National cancer intellegence network, *Cancer incidence and survival by major ethinic group, england, 2002 - 2006*, (2009). [online]. Available: $http://www.ncin.org.uk/view?rid = 75$. [Accessed: 17/06/22].

[143] S. L. Parker, K. J. Davis, P. A. Wingo, L. A. G. Ries and C. W. Heath, *Cancer statistics by race and ethnicity*, Ca Cancer J. Clin., **48**, (1), pp 31-48, doi: 10.3322/canjclin.48.1.31, (1998).

[144] R. H. Jack, E. A. Davies and H. Møller, *Breast cancer incidence, stage, treatment and survival in ethnic groups in south east england*, British Journal of Cancer, **100**, pp 545-550, doi: 10.1038/sj.bjc.6604852, (2009).

[145] D. M. Parkin, *Global cancer statistics in the year 2000*, Oncology, **2**, (9), pp 533-543, doi: 10.1016/S1470-2045(01)00486-7 (2001).

[146] D. M. Parkin, P. Pisani, A. D. Lopez and E. Masuyer, *At least one in secen cases of cancer is caused by smoking. Global estimcates for 1985*, International Journal of Cancer, **59**, (4), pp 494-504, doi: https://doi.org/10.1002/ijc.2910590411 (1994).

[147] R. Doll and R. Peto, *The causes of cancer: quantitive estimates of avoidable risks of cancer in the unites states today*, Journal of the National Cancer Institute, **66**, (6), pp 1192-1308, doi: 10.1093/jnci/66.6.1192 (1981).

[148] S. H. Jee, J. M. Samet, H. Ohrr, J. H. Kim and I. S. Kim, *Smoking and cancer risk in korean men and women*, Oncology, **2**, (9), pp 533-543, doi: 10.1016/S1470-2045(01)00486-7 (2001).

[149] International Agency for Research on Cancer, *List of classifications by cancer site*, (2019). [online]. Available: $https://monographs.iarc.fr/agents-classified-by-the-iarc/$. [Accessed: 17/06/22].

[150] G. Danaei, S. V. Hoorn, A. D. Lopez, C. J. L. Murray and M. Ezzati, *Causes of cancer in the world: comparative risk assessment of nine behavioural and environmental risk factors*, The Lancet, **366**, (9499), pp 19-25, doi: 10.1016/S0140-6736(05)67725-2 (2005).

[151] P. Greenwald, C. K. Clifford and J. A. Milner, *Diet and cancer prevention*, European Journal of Cancer, **37**, pp 948-965, doi: 10.1016/s0959-8049(01)00070-3, (2001).

[152] D. Divisi, S. Di Tommaso, S. Salvemini, M. Garramone and R. Crisci, *Diet and cancer*, Acta. Biomed., **77**, pp 118-123, (2006).

[153] W. C. Willett, *Diet and cancer*, The Oncologist, **5**, pp 393-404, doi: 10.1634/theoncologist.5-5-393, (2000).

[154] E. E. Calle and R. Kaaks, *Overweight, obesity and cancer: epidemiological evidence and proposed mechanisms*, Nature Reviews Cancer, **4**, pp 579-591, doi: 10.1038/nrc1408, (2004).

[155] E. E. Calle and M. J. Thun, *Obesity and cancer*, Oncogene, **23**, pp 6365-6378, doi: 10.1038/sj.onc.1207751 (2004).

[156] K. Y. Wolin, K. Carson and G A. Colditz, *Obesity and cancer*, The Oncologist, **15**, (6), pp 556-565, doi: 10.1634/theoncologist.2009-0285 (2009).

[157] A. S Furberg and I. Thune, *Metabolic abnormalities (hypertension, hyperglycemia and overweight), lifestyle (high energy intake and physical inactivty) and endometrial cancer risk in a norweigian cohort*, Int. J. Cancer, **104**, pp 669-676, doi: 10.1002/ijc.10974 (2003).

[158] T. Pischon, U. Nöthlings and H. Boeing, *Obesity and cancer*, Proceedingd of the nutrition society, **67**, pp 128-145, doi: 10.1017/S0029665108006976 (2008).

[159] J. Tyczyński, W. Tarkowski, D. M. Parkin and W. Zatoński, *Cancer mortality among polish migrants to australia*, European Journal of Cancer, **30**, (4), pp 478-484, doi: 10.1016/0959-8049(94)90423-5 (1994).

[160] D. M. Parkin and M. Khlat, *Studies of cancer in migrants: rationale and methodology*, European Journal of Cancer, **32A**, (5), pp 761-771, doi: 10.1016/0959-8049(96)00062-7, (1996).

[161] R. G. Ziegler, R. N. Hoover, M. C. Pike, A. Hildesheim, A. M. Y. Nomura, D. W. West, A. H. Wu-Williams, L. N. Kolonel, P. L. Horn-Ross, J. F. Rosenthal, M. B. Hyer, *Migration patterns and breast cancer risk in asian-american women*, Journal of the national cancer institute, **85**, (22), pp 1819-1827, doi: 10.1093/jnci/85.22.1819 (1993).

[162] D. M. Parkin, F. Bray, J. Ferlay, P. Pisani, *Global cancer statistics, 2002*, CA Cancer J. Clin., **55**, pp 74-108, doi: 10.3322/canjclin.55.2.74, (2005).

[163] E. Oranuba, H. Deng, J. Peng, S. M. Dawsey and F. Kamangar, *Polycyclic aromatic hydrocarbons as a potential source of carcinogenicity of mate*, J. Envrion. Sci. Health C. Environ. Carcinog. Ecotocicol. Rev., **37**, (1), pp 26-41, doi: 10.1080/10590501.2019.1555323 (2019).

[164] C. Yu, H. Tang, Y. Guo, Z. Bian, L. Yang, Y. Chen, A. Tang, X. Zhou, X. Yang, J. CHen, Z. Chen, J. Lv and L. Li, *Hot tea consumption and its interations with alcohol and tobacco use on the risk for esophageal cancer: a population-based cohort study*, Ann. Intern. Med., **168**, (7), pp 489-497, doi: 10.7326/M17-2000 (2018).

[165] F. Islami, A. Pourshams, D. Nasrollahzadeh, F. Kamangar, S. Fahimi, R. Shakeri, B. Abedi-Ardekani, S. Merat, H. Vahedi, S. Semnani, C. C. Abnet, P. Brennan, H. Møller, F. Saidi, S. M. Dawsey, R. Malekzadeh and P. Boffetta, *Tea drinkning habits and oesophageal cancer in a high risk area in northern Iran: population based case-control study*, BMJ, **338**, b929, doi: 10.1136/bmj.b929 (2009).

[166] P. Pisani, D. M. Parkin, N. Muñoz and J. Ferlay, *Cancer and infection: estimates of the attributable fraction in 1990*, Cancer Epidemiology, Biomarkers and Prevention, **6**, pp 387-400, (1997).

[167] D. M. Parkin, *The global health burden of infection-associated cancers in the year 2002*, Int. J. Cancer, **118**, pp 3030-3044, doi: 10.1002/ijc.21731, (2006).

[168] F. Donato, P. Boffetta and M. Puoti, *A meta-analysis of epidemiological studies on the combines effect of hepatitis B and C virus infections in causing hepatocellular carcinoma*, Int. J. Cancer, **75**, pp 347-354, doi: 10.1002/(sici)1097-0215(19980130)75:3<347::aid-ijc4>3.0.co;2-2, (1998).

[169] J. Danesh, *Helicobacter pylori infection and gastric cancer: systematic review of the epidemiological studies*, Ailment. Pharmacol. Ther., **13**, pp 851-856, doi: 10.1046/j.1365-2036.1999.00546.x, (1999).

[170] J. M. Walboomers, M. V. Jacobs, M. M. Manos, F. X. Bosch, J. A. Kummer, K. V. Shah, P. J. F. Snijders, J. Peto, C. J. L. Meijer and N. Muñoz, *Human papillomavirus is a necessary cause of invasive cervical cancer worldwide*, J. Pathol., **189**, pp 12-19, doi: 10.1002/(SICI)1096-9896(199909)189:1<12::AID-PATH431>3.0.CO;2-F, (1999).

[171] D. R. Lowry and J. T. Schiller, *Prophylactic human papillomavirus vaccines*, The Journal of Clinical Investigation, **116**, (5), pp 1167-1173, doi: 10.1172/JCI28607 (2006).

[172] NHS, *HPV vaccine overview*, (2017). [online]. Available: $https://www.nhs.uk/conditions/vaccinations/hpv-human-papillomavirus-vaccine/$. [Accessed: 17/06/22].

[173] E. R. Berchick, E. Hood and J. C. Barnett, *Health Insurance Coverage in the United States: 2017*, (2018). [online]. Available: $https://www.census.gov/content/dam/Census/library/publications/2018/demo/p60-264.pdf$. [Accessed: 17/06/22].

[174] L. A. Torre, R. L. Siegel and A. Jemal, *Lung cancer statistics*, Lung cancer and personalised medicine, Advances in Experimental Medicine and Biology, Editors: A. Ahmad, S. Gadgeel, **893** doi: 10.1007/978-3-319-24223-1_1, (2015).

[175] E. Ward, A. Jemal, V. Cokkinides, C. K. Singh, C. Cardinez, A. Ghafoor and M. Thun, *Cancer disparities by race/ethnic and socioeconomic status*, CA Cancer J. Clin., **54(2)**, pp: 78-93, doi: 10.3322/canjclin.54.2.78, (2004).

[176] S. John and J. Broggio, *Cancer survival in England: national estimates for patients followed up to 2017*, Office for national statistics, (2019).

[177] J. S. Mandel, J. H. Bond, T. R. Church, D. C. Snover, M. Bradley, L. M. Schuman and F. Ederer, *Reducing mortality from colorectal cancer by screening for fecal occult blood*, The New England Journal of Medicine, **328**, (19), pp 1365-1371, doi: 1010.1056/NEJM199305133281901, (1993).

[178] National Cancer Institute, *How cancer is diagnosed*, (2019). [online]. Available: *https : //www.cancer.gov/about − cancer/diagnosis − staging/diagnosis*. [Accessed: 17/06/22].

[179] National Cancer Institute, *Tumour Markers*, (2021). [online]. Available: *https : //www.cancer.gov/about − cancer/diagnosis − staging/diagnosis/tumor − markers − fact − sheet*. [Accessed: 17/06/22].

[180] D. Ilic, M. Djulbegovic, J. H. Jung, E. C. Hwang, Q. Zhou, A. Cleves, T. Agoritsas and P. Dahm, *Prostate cancer screening with prostate-specific antigen (PSA) test: a systematic review and meta-analysis*, BMJ, **362**, k3519, doi: 10.1136/bmj.k3519 (2018).

[181] E. L. Moss, J. Hollingworth and T. M. Reynolds, *The role of CA 125 in clinical practice*, J. Clin. Pathol., **58**, pp 308-312, doi: 10.1136/jcp.2004.018077, (2004).

[182] S. N. Han, A. Lotgerink, M. M. Gziri, K. V. Calsteren, M. Hanssens and F. Amant, *Physiologic variations of serum tumor markers in gynecological malignancies during pregnancy: a systematic review*, BMC Medicine, **10**, 86, doi: 10.1186/1741-7015-10-86, (2012).

[183] U. Stenman, H. Alfthan and K. Hotakainen, *Human chorionic gonadotropin in cancer*, Clinical Biochemistry, **37**, pp 549-561, doi: 10.1016/j.clinbiochem.2004.05.008, (2004).

[184] M. G. Fakih and A. Padmanabhan, *CEA monitoring in colorectal cancer. What you should know*, Oncology, **20**, (6), pp 579-587, (2006).

[185] X. Li, J. Lu, H. Ren, T. Chen, L. Gao, L. Di, Z. Song, Y. Zhang, T. Yang, A. Thakur, S. Zhou, Y. Yin and M. Chen, *Combining multiple serum biomarkers in tumor diagnosis: A clinical assessment*, Molecular and Clinical Oncology, **1**, pp 153-160, doi: : 10.3892/mco.2012.23 (2013).

[186] Z. Geng, X. Zhang, Z. Fan, X. Lv and H. Chen, *DA route to terahertz metamaterial biosensor integrated with microfluidics for liver cancer biomarker testing in early stage*, Scientific Reports, **7**, 16378, doi: 10.1038/s41598-017-16762-y (2017).

[187] ADVIA Centaur ®, ADVIA Centaur ®XP, ADVIA Centaur ®XPT, Immunoassay Systems, *CEA*, Siemens, (2015).

[188] ADVIA Centaur ®, ADVIA Centaur ®XP, ADVIA Centaur ®XPT, Immunoassay Systems, *CA 125II*, Siemens, (2018).

[189] ADVIA Centaur ®, ADVIA Centaur ®XP, ADVIA Centaur ®XPT, Immunoassay Systems, *CA 19-9*, Siemens, (2018).

[190] ADVIA Centaur ®, ADVIA Centaur ®XP, ADVIA Centaur ®XPT, Immunoassay Systems, *CA 15-3*®, Siemens, (2018).

[191] ADVIA Centaur ®, ADVIA Centaur ®XP, ADVIA Centaur ®XPT, Immunoassay Systems, *AFP*, Siemens, (2018).

[192] ADVIA Centaur ®, ADVIA Centaur ®XP, ADVIA Centaur ®XPT, Immunoassay Systems, *Total hCG*, Siemens, (2015).